New analogue-type resistive switching memristive devices for artificial synapse applications

Thoai-Khanh Khuu

THÈSE

Pour obtenir le grade de

DOCTEUR DE L'UNIVERSITÉ GRENOBLE ALPES

École doctorale : EEATS - Electronique, Electrotechnique, Automatique, Traitement du Signal (EEATS)
Spécialité : Nano électronique et Nano technologies
Unité de recherche : Laboratoire des Technologies de la Microélectronique

Nouvelles dispositifs mémoires résistives à commutation analogue pour applications en tant que synapses artificielles

New analogue-type resistive switching memristive devices for artificial synapse applications

Présentée par :

Thoai-Khanh KHUU

Direction de thèse :

Ahmad BSIESY PROFESSEUR DES UNIVERSITES, Université Grenoble Alpes	Directeur de thèse
Monica BURRIEL LOPEZ CHARGE DE RECHERCHE HDR, CNRS	Co-encadrante de thèse
Serge BLONKOWSKI Ingénieur Docteur, CEA-Leti	Co-encadrant de thèse
Eric JALAGUIER Ingénieur Docteur, CEA-Leti	Co-encadrant de thèse

Rapporteurs :

Ulrike LUDERS
DIRECTEUR DE RECHERCHE, CNRS, ENSICAEN
Damien DELERUYELLE
PROFESSEUR DES UNIVERSITES, INSA LYON

Thèse soutenue publiquement le **29 juin 2023**, devant le jury composé de :

Ahmad BSIESY PROFESSEUR, Université Grenoble Alpes	Directeur de thèse
Ulrike LUDERS DIRECTEUR DE RECHERCHE, CNRS, ENSICAEN	Rapporteure
Damien DELERUYELLE PROFESSEUR DES UNIVERSITES, INSA LYON	Rapporteur
Alain SYLVESTRE PROFESSEUR DES UNIVERSITES, UNIVERSITE GRENOBLE ALPES	Président du jury et examinateur
Simon JEANNOT INGENIEUR DOCTEUR, STmicroelectronics	Examinateur

Abstract

To overcome the constraints that the traditional von Neumann computing architectures and the end of Moore's law pose, neuromorphic computing is one of the promising solutions. The construction of these brain-inspired systems requires specific electronic devices capable of artificially producing synaptic behaviors. Valence change memory (VCM) with analogue switching capabilities is one of the exciting candidates for artificial synapse applications, as its resistance (or conductance), which represents the synaptic weight, can be modulated in a continuous manner. In oxide-based VCM, oxygen drift involves in the redox reaction, which triggers the change in resistance.

In this context, in our group lanthanum nickelate ($La_2NiO_{4+\delta}$, L2NO4), a mixed ionic electronic oxide well known for its ability to store and transport oxygen thanks to its interstitial oxygen, is deposited by pulsed-injection metal-organic chemical vapor deposition (PI-MOCVD) and studied as a memristive layer. In this thesis, we first managed to transfer the Ti\L2NO4/Pt planar memristive devices from single-crystal substrates to Si-based substrates, i.e., using $Si_3N_4/SiO_2/Si$. However, such devices show small HRS/LRS ratios and require very high operating voltages (up to ± 40 V), and an additional heating step (rapid thermal annealing, RTA) to activate the switching.

Then, Ti/L2NO4/Pt memristive devices were constructed in vertical configuration for the first time. The L2NO4 films were deposited on another Si-based substrate, i.e., $Pt/TiO_2/SiO_2/Si$. The deposition of L2NO4/Pt was optimized to get a pure L2NO4 phase, as well as flatter L2NO4 thin films and to avoid Pt dewetting. L2NO4 (optimized or non-optimized)-based memristors combined with Ti electrodes show HRS/LRS ratios, in a range from 6 to 10 with dynamic resistance relaxation. The activation of the switching by RTA in Ti/L2NO4/Pt devices was not reproducible and required a finer control of the temperature. The formation of a TiO_x interlayer at the Ti/L2NO4 interface was shown by TEM, which is assumed to play a crucial role in the switching of these devices.

In the third stage of the thesis, TiN/L2NO4/Pt vertical memristive devices were built for the first time. After the 'soft-forming' step, they exhibit bipolar RS with gradual SET and RESET transitions. A HRS/LRS ratio close to 40 was measured with good reproducibility. Highly multilevel resistance states can be obtained by using different voltage amplitudes, pulse amplitudes (pulse height) or pulse duration (pulse length). Potentiation/depression was artificially reproduced by applying many sweeps/pulses in the same polarity with data retention characteristics up to (at least) 6 hours, opening the door to use TiN/L2NO4/Pt devices as the long-term artificial synapses.

Finally, the RS mechanism was also investigated by XANES and TEM in different modes and conditions. *Operando* XANES at Ni-K edge and *in situ* TEM equipped with EELS at Ti-$L_{2,3}$ edges allow us to get better insights into the underlying switching mechanism in TiN/L2NO4/Pt devices. A TiN_xO_y interlayer is spontaneously formed during the microfabrication of TiN_x electrode. Changes in the Ni oxidation state and the oxidation/reduction of TiN_xO_y interlayer could be reproducibly measured during the device operation, as the device was cycled in both voltage polarities, confirming a valence-change mechanism taking place. At the end, a simplified switching model is proposed based on the coexistence of filamentary and interfacial switching in these TiN/L2NO4/Pt memristive devices.

Content

List of Figures

List of Tables

Nomenclature

Acronyms and Abbreviations

AFM	Atomic Force Microscopy
ALU	Arithmetic and Logic Unit
CC	Current Compliance
CMOS	Complementary Metal Oxide Semiconductor
CPU	Central Processing Unit
CVD	Chemical Vapor Deposition
ECM(s)	Electrochemical Memory(ies)
EDS	Energy Dispersive Spectroscopy
EELS	Electron-Energy Loss Spectroscopy
EPMA	Electron Probe MicroAnalysis
ESRF	European Synchrotron Radiation Facility (Grenoble, France)
FIB	Focused-Ion Beam
GB(s)	Grain boundary(ies)
GIXRD	Grazing-incidence X-ray Diffraction
HAADF	High-Angle Annular Dark Field
HRS	High Resistance State
HRTEM	High Resolution Transmission Electron Microscopy
ICDD-PDF	International Centre for Diffraction Data – Powder Diffraction File
IR	Initial Resistance
L2NO4	$La_2NiO_{4+\delta}$
LRS	Low Resistance State
MIEC	Mixed Ionic Electronic Conductor

MIM	Metal-Insulator-Metal
MOM	Metal-Oxide-Metal
MU	Memory Unit
NVM(s)	Non-Volatile Memory(ies)
PCMO	Praseodymium calcium manganite, $Pr_{1-x}Ca_xMnO3$
PIMOCVD	Pulsed Injection Metal Organic Chemical Vapor Deposition
PTA	Plateform Technologique Amont
ReRAM(s)	Redox Random Access Memory(ies)
ROI	Region of Interest
RRAM(s)	Resistive Random Access Memory(ies)
RS	Resistive Switching
RT	Room Temperature
RTA	Rapid Thermal Annealing
SEM	Scanning Electron Microscopy
SN	$Si_3N_4/SiO_2/Si$ substrate
STEM	Scanning Transmission Electron Microscopy
TCM(s)	Thermochemical Memory(ies)
TEM	Transmission Electron Microscopy
TLM	Transmission Line Measurement
VCM(s)	Valence Change Memory(ies)
XRD	X-Ray Diffraction

Acknowledgment

It is quite difficult to express how much important this PhD is in my life. From feeling afraid of public speaking to delivering a scientific talk in an international conference and, finally, a public defense in front of so many people. This throughback somehow demontrates how much I grew and learned over the duration of the PhD, which lasted over a thousand days.

Completing this doctoral journey has been a transformative and enriching experience, and it would not have been possible without the support, guidance, and encouragement of numerous individuals and organizations. I am deeply grateful to those who have played an instrumental role in shaping this thesis and my personal growth.

Foremost, I express my heartfelt gratitude to my esteemed supervisors: Ahmad Bsiesy, Eric Jalaguier, Mónica Burriel and Serge Blonskowki for their intellectual guidance, support and invaluable insights throughout this research endeavor. Your mentorship has refined my research skills and instilled in me a profound understanding of academic rigor and scholarly dedication. Especially, Mónica, from the bottom of my heart, thank you for giving me the opportunity of the internship and the PhD, as well as your kindness, availability and devotion in both scientific and non-scientific activities during my stay in Grenoble.

I extend my sincere appreciation to the jury members: Alain Sylvestre, Ulrike Luders, Damien Deleruyelle and Simon Jeannot for their perceptive feedback, rigorous evaluations, and thought-provoking discussions that have immensely enriched the quality of this thesis. Your collective expertise has been essential in shaping this research and enhancing its scientific contributions. Especially, Alain, I would like to thank you for your kindness, constructive feedback and valuable suggestions not only in the defense but also in the CSI (comitté de suivi de thèse) meetings.

I would like to thank Gauthier Lefèvre, David Cooper, Carmen Jiménez, Hervé Roussel, Florence Robaut, Rachel Martin, Valentine Bolcato, Laetitia Rapenne, Isabelle Gélard and Fabrice Wilhelm for their support with the deposition and characterization techniques, as well as the interpretation of the results.

Many results shown in this thesis were carried out in LMGP laboratory. I want to acknowledge the LMGP direction (Carmen Jiménez and Franz Bruckert) and the HR team (Annie Ducher, Michèle San Martin and Josiane Viboud) for providing and running smoothly an incredible working environment.

I want to deeply thank the Nanoionic team, both past members (Klaasjan, Raquel, Ragnar, Dolors) and present members (Adeel, Alex, Quentin,…) for your kindness and assistance. I have learned a lot from

you since the beginning of my thesis and I believe that, teamwork is the most valuable skill that I developed as a result of our teamwork.

My gratitude extends to my colleagues in the laboratory: anh Hương, Huy, anh Chiêu, Hải, Ibtihel, Shruti, Pétros, Alexandre,… who have shared their knowledge, insights, and camaraderie throughout this journey. The exchange of ideas and collaborative spirit within our academic community has been a constant source of inspiration and motivation.

I am thankful to my family and friends in Vietnam for their unwavering support, understanding, and encouragement during the highs and lows of this academic pursuit. Your belief in me has been a driving force, and your presence has provided solace and joy beyond words. Cảm ơn!

I would like to acknowledge the financial support provided by LabEx Minos, which enabled me to conduct my research and disseminate my findings. Your investment in my work has been instrumental in its realization.

Lastly, I extend my gratitude to all those unnamed individuals who have contributed to this journey in their own unique ways. Whether through a thought-provoking conversation, a timely word of encouragement, or a simple act of kindness, your impact has been deeply felt and cherished.

The completion of this PhD thesis marks the milestone of a profound intellectual and personal journey. The invaluable contributions and support of those mentioned above have been the bedrock upon which this work stands. While this page of acknowledgments captures a fraction of the gratitude I feel, please know that your influence will resonate throughout my academic and professional career.

With deepest appreciation,

Ho Chi Minh city (Vietnam), July 2023

Chapter 1: Introduction

1.1. Memristive devices for neuromorphic computing

1.1.1. The need for non-von Neumann computation architecture

Artificial intelligence (AI) is a new branch of computer science, which has recently become very popular, as it could offer many benefits in different aspects of our lives. Due to the vast potential of AI, it is believed that its popularity will continue to rise in the upcoming years, making it one of the most important technologies of the future. However, in certain cognitive operations of AI (such as speech recognition, face detection, sentiment analysis, risk assessment, etc.), the traditional computing architecture (von Neumann paradigm) is inefficient in terms of performance and power consumption because large amounts of data and computational resources are required. Indeed, these operations are mostly based on the software approach, meaning their algorithms are still running on CMOS-based von Neumann computation architecture. Compared to natural systems such as our brains, AI computing with current technology is still unnatural in terms of configuration, thus leading to the difficulty or impossibility of being executed, especially for the cases that require real-time processing or fault tolerance. The limitations of present AI technology are becoming more and more obvious as the von Neumann bottleneck and the end of Moore's law are approaching [1], while the need for AI computing keeps growing exponentially.

For the past few decades, Gorden Moore's prediction in the early 60's, i.e. that the number of transistors on a chip would double approximately every two years [2], has held true. However, the miniaturisation of transistors is reaching the atomic scale, leading to a slow improvement in computing performance and an increase in the production cost of advanced microchips. This is known as the end of Moore's law. On the other hand, in von Neumann architecture, all calculations are performed in the arithmetic logic unit (ALU), which is physically separated from the memory unit and known as another challenge for the future of computing. Indeed, as these units are linked by data paths, resulting in a physical limitation in the number and speed of the calculations that can be performed at the same time, namely the von Neumann bottleneck (Figure 1.1). To overcome these two challenges, non-von Neumann computing architectures are therefore required.

One promising approach is to develop a system that relies on more closely-related natural neural network structures. In this context, neuromorphic computing, which is inspired by the functioning of the human brain, emerges as a potential candidate. The large interconnectivity of neurons and synapses in our brain allows us to perform millions of complex operations simultaneously using less energy than a regular

computer, while performing the same number of operations. Neuromorphic computing architectures surpass the classical von Neumann architectures because they are based on a massively parallel network of computational elements that are interconnected on a matrix-like grid (Figure 1.1), and the bottleneck can be avoided.

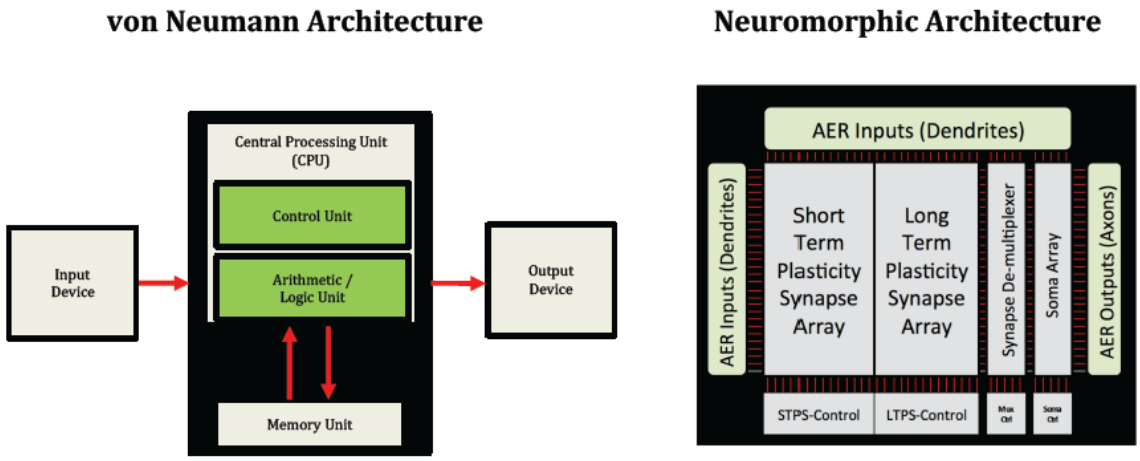

Figure 1.1: Comparison of high-level conventional (von Neumann) and neuromorphic computer architectures. The so-called von Neumann bottleneck is the data path between the CPU and the memory unit. In contrast, a neural network-based architecture combines synapses and neurons into a fine-grain distributed structure that scales both memory (synapse) and computing (soma) elements as the systems increase in scale and capacity, thus avoiding the bottleneck between computing and memory. Reprinted from reference [3].

1.1.2. Analog memristive device: a new artificial synapse concept

Biological neural networks (such as the human brain) are made of an enormous amount of neurons, which are specialized cells that control our memories, emotions, learning and other crucial functions by sending and receiving electrical signals. Each of them has three main organizational components: i) a soma, ii) dendrites that receive signals from other neurons or and iii) an axon that sends signals to other neurons, as seen in Figure 1.2a. The neuron is the central component and is responsible for generating intrinsic electric impulses and combining them with synaptic inputs to generate outputs in the form of action potentials. This response is exclusively produced when the sum of the inputs exceeds a certain threshold, as illustrated in Figure 1.2b. Such behavior is known as the leaky integrate and fire (LIF) model and is widely used as learning algorithm in artificial neural networks (ANNs). Neuristor (or artificial neuron) is the term used to describe electronic devices that mimic neuron functions. Volatile resistive switching-based memories would be one of the potential candidates for such neuristor applications [1].

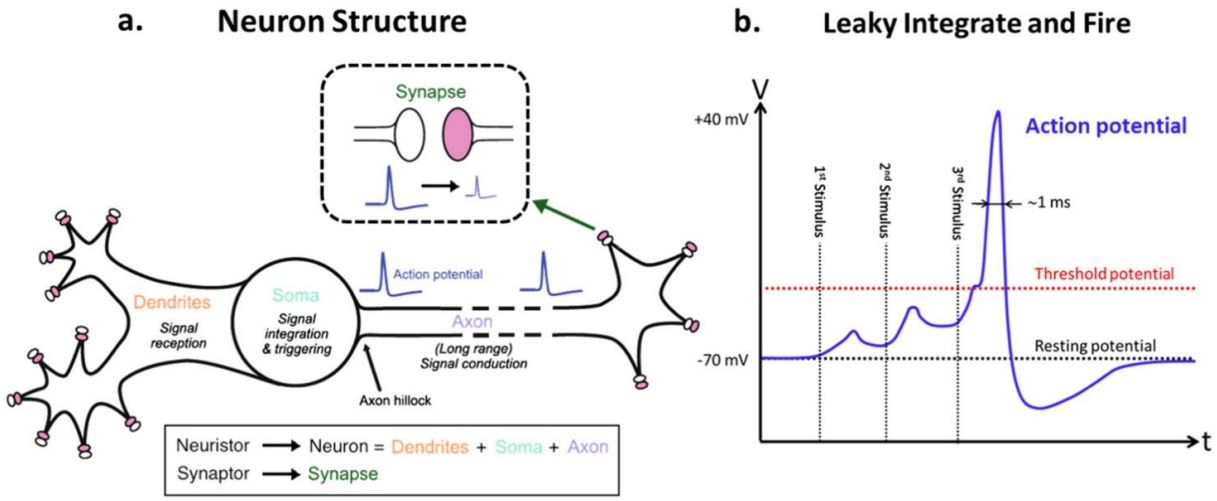

Figure 1.2: a) Sketch of a neuron and its synapses in a biological neural network. b) Voltage spiking illustrating the leaky-integrate and fire (LIF) behavior. Reproduced from reference [1].

Synapse is another critical component of the neural network which is responsible for connecting the neurons (by connecting an axon of the pre-neuron to a dendrite of the post-neuron with the intention of carrying electric impulses) and adjusting the transmitted-signal strength, often known as the "synaptic weight" or "synaptic strength". Synaptic plasticity is the term used to describe the ability to change synaptic strength, which is believed to be one of the key functions of memory and learning. In this case, electronic devices that have the ability to mimic synaptic behaviors are referred-to as synaptors (or artificial synapses).

To realize brain-inspired computing, algorithms based on CMOS transistors that can mimic the behavior of synapses and simulate the functions of neurons were firstly tested. Then, hardware implementation of such brain-like computing is increasingly preferred since it allows for better energy consumption and physical space. Even if significant attempts are being made to create a system that can replicate the brain's structure and functioning mechanism on a solid-state platform, there is still a long way to go. Thus, ANNs have been created and effectively used in many applications. Using crossbar array of ReRAM, ANNs are made of many layers which contain nodes (neurons) to perform specific tasks. Generally, in each layer the input is applied to the first row of the memory array and the conductance of each memory cell is used to multiply the input values. The resulting values are summed up along each column and passed through an activation function to produce the output. The output of a layer can be used as the input for the next layer.

SNNs are a type of ANNs which mimic the bio-neuron behavior by using electrical pulses (or spikes) to transmit information. In SNNs, signals are encoded by the synaptic strength between neurons and the timing and frequency of these pulses. In fact, depending on the previous pulses (history-dependent),

they can vary throughout time rather than remain constant. Spike-timing-dependent plasticity (STDP) refers to the processes by which synaptic weights modify their values based on the relative timing of electric spike activity [4], as seen in Figure 1.3. When the pre-neuron activates just before the post-neuron at a given synapse, the synaptic weight is strengthened and this process is known as potentiation. In contrast, depression refers to the reduction in synaptic weight that occurs when the post-neuron becomes active just before the pre-neuron. STDP is also another key function that artificial synapses must have to create an effective neuromorphic system.

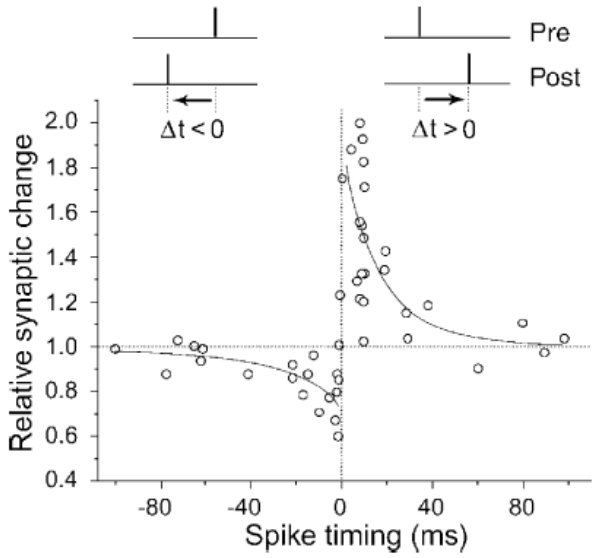

Figure 1.3: Scheme showing spike-timing dependent plasticity (STDP). Pre-neuron triggered before post-neuron causes synaptic potentiation. Post-neuron triggered before pre-neuron causes synaptic depression. Reproduced from reference [4].

Recently, many types of memory devices (such as resistive random access memories, RRAMs; phase change memories, PCMs; electrochemical memories, ECMs, etc.) have been proposed as exciting candidates for artificial synapse applications in SNNs [5-7]. In particular, they should undergo spike-based learning in real time under biologically inspired learning rules such as STDP [8, 9]. However, to ensure learning accuracy and energy efficiency, in addition to the required functions that have just been mentioned, these synaptic devices should present a number of properties, as detailed below. This paragraph is inspired and adapted from reference [9].

- Device size: this is one of the most important factors. Compact devices allow for a higher density in connections, meaning that more devices can be packed in space. This is crucial because, as previously mentioned, neuromorphic systems require an enormous amount of artificial neurons and synapses (10^{11} neurons and 10^{15} synapses) [10], even though the number

of artificial synapses in neuromorphic computing hardware is not expected to be as high. Nowadays, the crossbar array configuration is believed to be the most densely-packed 2D structure, and offers the implementation of the memristors structure, as shown in Figure 1.4. This geometry offers large interconnectivity as each capacitor-like structure has two terminals (corresponding to the dendrite and axon of the neuron in biological systems), so that every axon of the pre-neuristor can connect to every dendrite of the post-neuristor. In the inset, a so-called synaptor is shown, being similar to a memory cell composed of a memristive layer (metal oxide) sandwiched between two metallic electrodes. Details of resistive switching will be introduced in the following section.

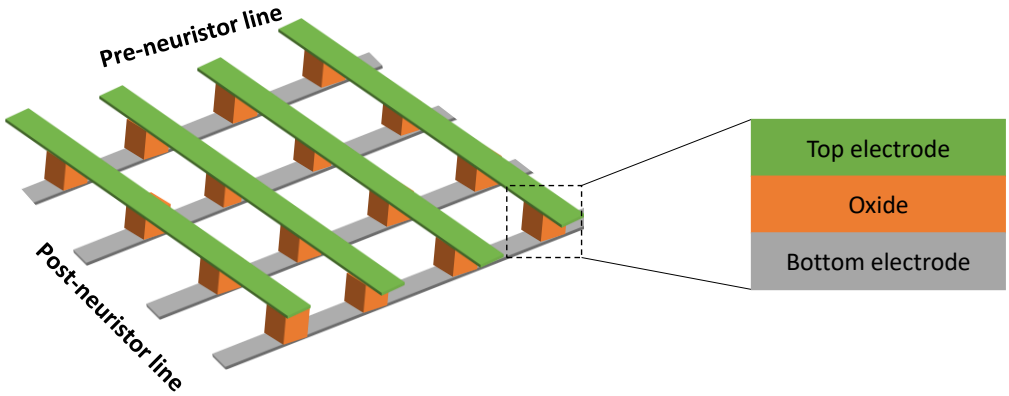

Figure 1.4: Crossbar array architecture to implement hardware-based neural networks. It consists of a synaptic-matrix device in between a pre-neuristor layer and a post-neuristor layer.

- Multilevel resistance states: synaptic plasticity is a key feature in neural networks that memristive devices should be able to reproduce in the form of multiple levels of resistance/conductance. Multiple resistance states also allow for improving the learning precision of the network (by offering a finer-grained control of the synaptic weights), and reducing power consumption (by reducing the number of electronic elements used in the system).
- Programming window: this term is also known as HRS/LRS ratio. Higher HRS/LRS ratios improve the signal-to-noise ratio, thus improving the accuracy and reliability of the device performance.
- Asymmetry and linearity in synaptic-weight updating: the synaptic weight updating is expected to be linear; however, in reality, it is found to be non-linear in most resistive artificial synapses, as shown in Figure 1.5a-b. In general, based on the applications that the update rule is used for, either symmetric or asymmetric weight update can still be efficient.

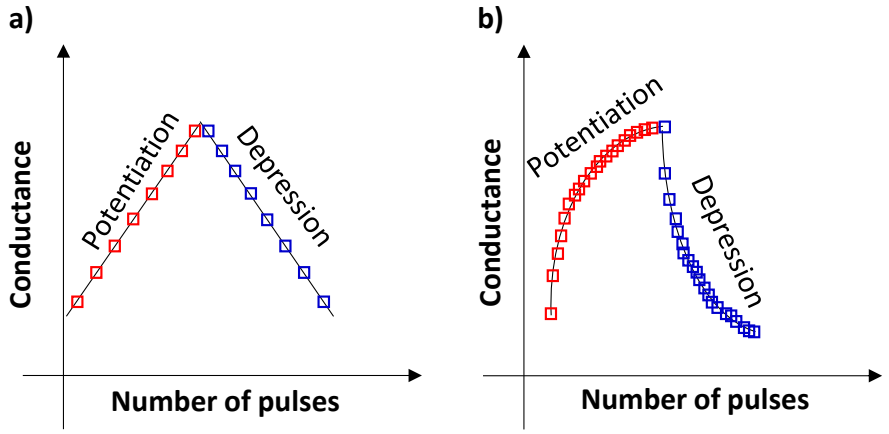

Figure 1.5: Illustration of plasticity in artificial neural networks: a) Ideal conductance modulation with the pulse number showing the illustrated linear and symmetric weight updating. b) Non-linear and asymmetric weight updating.

- Programming energy consumption: in biological neural networks, the estimation of energy consumption is approximately 1 – 10 fJ per synaptic event. In most memory devices, the typical programming voltage and current are around 1 V and 10 μA, respectively, with the switching speed can be around 100 ns. The energy consumption is thus in the range of picojule. Therefore, more efforts on improving memory device energy are incensed.
- Retention and endurance: typically, the synaptic weights should be stored reliably over ten years at chip operating temperatures (85°C). The synapses should be able to maintain their performance over thousands of repeated programming cycles (for example, 10^4 cycles for training the MNIST data set) [11].

The synaptic weight update can be regarded as the conductance update in the memristive device, which can be artificially produced by the increase or decrease of conductance, respectively [12]. Since analogue resistive switching non-volatile memories (NVM) allow for the imitation of synaptic plasticity (Figure 1.5), they usually regarded as the be the best choice for the application of artificial synapses [13].

1.1.3. Resistive switching

1.1.3.1. Phenomenon and the first discovery

Resistive switching (RS) is defined as the phenomenon that occurs in a capacitor-like "metal-insulator (or semiconductor)-metal" (MIM) structure (Figure 1.6a) when a certain field (or current) is applied to one of the electrodes. Upon an appropriate electrical stimulus, the resistance of the MIM can be switched between a low resistance state (LRS) and a high resistance state (HRS) [14]. Figure 1.6b illustrates the

I-V and R-V characteristics of a memristive device with multilevel resistance states. V_{SET} stands for the voltage required to switch from HRS to LRS, while V_{RESET} stands for the voltage required for the opposite switching (LRS to HRS). The two programmed resistance states can be regarded as values "0" and "1" of the binary information storage system. The programmed resistance states can be measured by a small readout voltage (V_{read}). In addition to the HRS and LRS, intermediate resistance states can be obtained in some cases by controlling either the V_{SET} and V_{RESET} values, the voltage sweep rate, the current compliance or the pulse amplitude/duration of V_{SET} and V_{RESET} (in the case of the external bias is applied in the form of pulses).

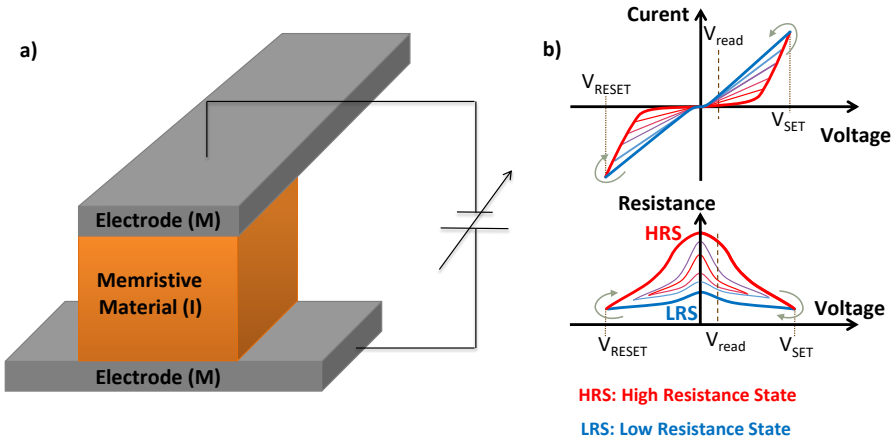

Figure 1.6: a) Sketch of a MIM memristive cell in vertical configuration. b) illustration of the current-voltage and resistance-voltage characteristics of a multilevel memristive cell.

The first discovery of RS was made by Leon Chua in 1971 and the memristor was theorized in the same year as the fourth fundamental element of circuits, alongside the resistor, capacitor and inductor [15].

1.1.3.2. Classification

Based on the switching voltage polarity, the RS process can be categorized into two types: unipolar and bipolar. Unipolar RS depends only on the amplitude of the voltage applied to switch the device reversibly between HRS and LRS, while bipolar RS also depends on the polarity (SET and RESET events occur for opposite polarities).

Based on the location of the switching mechanism that governs the device operation, the subcategories of filament-based RS and interface-based RS have been established, as sketched in Figure 1.7a-b. In filamentary switching, the formation/disruption of conductive filaments (CFs) at localized regions is responsible for the switching. Typically an electroforming step is required and serves as a 'soft breakdown' to activate the device. The electroforming occurs at a higher voltage than the operation voltage. When the filament is connected/disrupted, the memristive cell is in LRS/HRS, respectively. It

should be noted that various types of filamentary RS can occur: switching with multiple CFs, switching with a change in the CF size, and switching with a change in the CF composition [12]. In interface-type switching, RS is induced by a gradual change of the chemical nature at the whole area of the metal electrode/memristive-layer interface. For example, the redox reaction at the Ti electrode/PCMO oxide induces RS in Pt/Ti/$Pr_{1-x}Ca_xMnO_3$ (PCMO)/$SrRuO_3$/$SrTiO_3$ and Ti/PCMO/Pt vertical heterostructures, where the further oxidation/reduction of Ti dictates the resistance state of the device [16-18]. Typically, interfacial RS is experimentally demonstrated as area-dependent and forming-free, although often a so-called "initialization" process is required prior to device operation. In some cases, the coexistence of filament and interface switching mechanisms is present in the memory device [19-22].

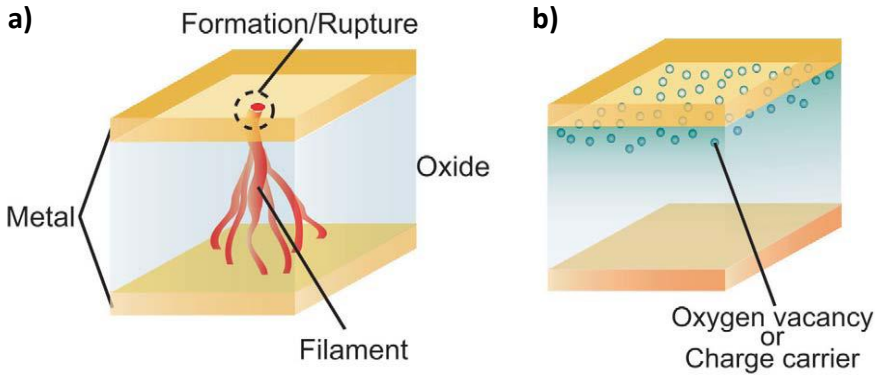

Figure 1.7: Sketch of the a) filamentary and b) interfacial resistive switching. Reproduced from reference [23].

Moreover, based on the physical origin of the observed RS, the two types of RS mentioned above (filamentary and area-dependent) can be further classified into many subcategories: thermochemical memory (TCM), electrochemical memory (ECM), valence change memory (VCM), phase change memory (PCM), etc. More detailed information about the different mechanisms can be found in the review articles [24-28]. Understanding the underlying mechanisms of resistive switching is important as it offers fundamental insights into the behavior of materials and the physics governing the switching, which allows researchers to create models and to have a suitable design for improving device performance when the devices are integrated into reliable hardware artificial synapses.

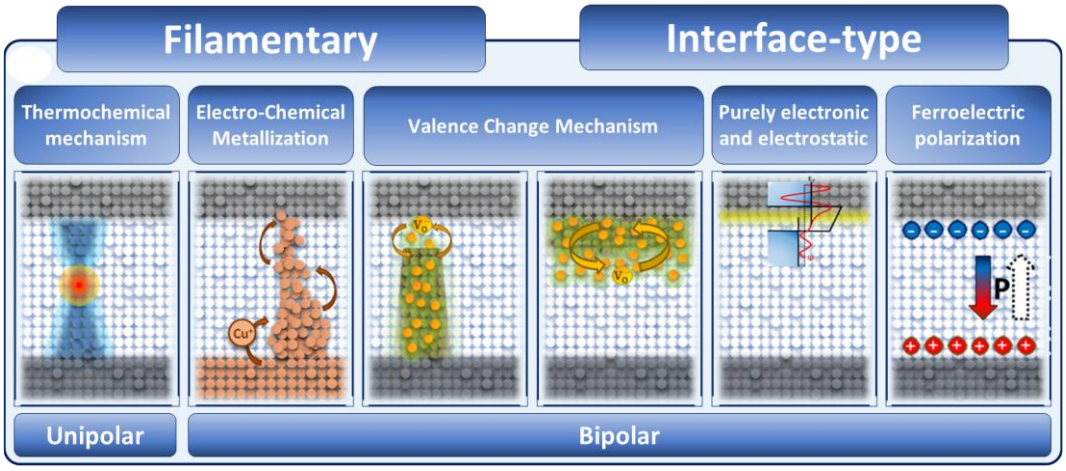

Figure 1.8: Classification with an illustration of RS mechanisms in filamentary and interfacial switching. Reprinted from reference [24].

The following subsection will be dedicated to VCMs, which are expected to be the switching mechanisms taking place in the devices studied in this thesis.

1.1.3.3. Valence change memories (VCMs)

This subsection is inspired by section *4. Valence change memory* of the review article from R. Waser [29]. The reader is referred to the source reference and/or other review articles [14, 25, 30, 31] for more details of VCM.

VCMs are electrochemical systems based on a MIM heterostructure in which the reversible redox reactions control the resistance change of the devices. In the MIM structure, typically there is an active electrode where the redox-based switching occurs and an ohmic electrode. Both filament-type and interface-type RS can occur in VCMs, as schematized in Figure 1.9. Filament-type RS in VCMs involves the formation and rupture of localized conductive filaments made of oxygen vacancies in an oxide matrix, with the concomitant changes in the oxidation state of the cation sublattice.

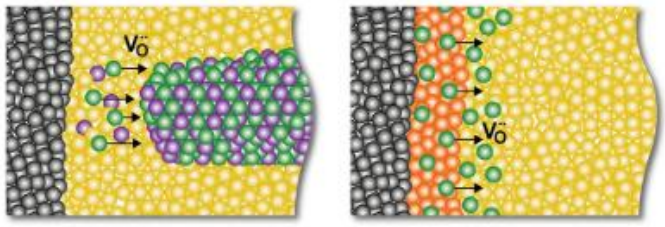

Figure 1.9: (left) Sketch of a filamentary VCM cell. Black spheres: high work function metal; yellow spheres: metal oxide in the fully oxidized state; green spheres: oxygen vacancies; purple spheres: metal oxide in a reduced valence state. (right) Sketch of an interface-type VCM cell. Orange spheres: metal oxide tunnel barrier. Reproduced from Dittmann *et al* [31].

Considering firstly filamentary RS based in an n-type oxide, a field-induced change in the Schottky barrier is usually held responsible for the change in resistance, as illustrated in Figure 1.10. At the active interface (between the n-type oxide and the active electrode), the filament made of vacancy-rich n-type oxide is named plug, while a potential barrier (between the electrode and the plug) is called disc. At HRS, the energy barrier is high with the presence of oxygen-deficient disc. After SET, LRS is obtained with the disc is filled by oxygen vacancies and the depletion width is dramatically decreased.

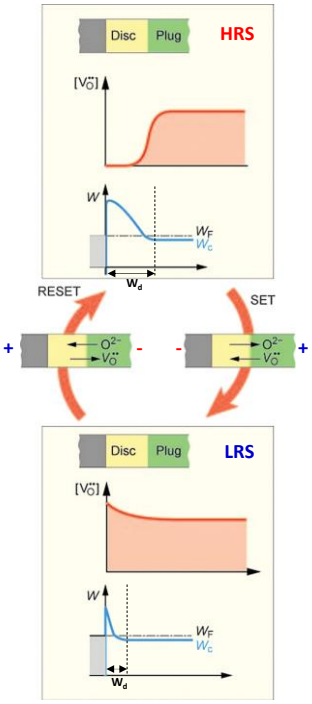

Figure 1.10: Oxygen vacancy concentration profile and Schottky junction between a n-type oxide and a metal in HRS and LRS programmed by SET and RESET processes. Plug and disc are illustrated for filamentary RS. Reproduced and adapted from reference [29].

For example, a Pt/ZrOx/Zr structure which consists of an n-type conducting material (ZrO_x) sandwiched between two metallic electrodes (Pt and Zr), is shown in Figure 1.11 (see the inset). The Pt electrode serves as the active electrode and Zr is the ohmic electrode. A typical I-V curve showing the RS behavior of the memristive cell is displayed at the center of the schematic. In Figure 1.11a, the plug is made of ZrO_x with a potential barrier (between the electrode and the plug). In this stage, the device is at HRS (OFF state). When the applied negative voltage reaches V_{SET}, oxygen vacancies are released from the plug and attracted towards the active electrode (Pt) into the disc (Figure 1.11b) at the active interface. It leads to the connection of the filament, which turns the memristor into its LRS (ON state, Figure 1.11c). In the opposite polarity, when the applied voltage is positive during the RESET process, the active interface repels the oxygen vacancies, which as a result, turns the memristor back into the HRS (Figure 1.11d). Since the RS is based on the oxygen ion (negatively-charged species) moving upon the electric field, the obtained I-V curve is bipolar. The switching polarity, as seen in Figure 1.11, is therefore called counter-eight-wise.

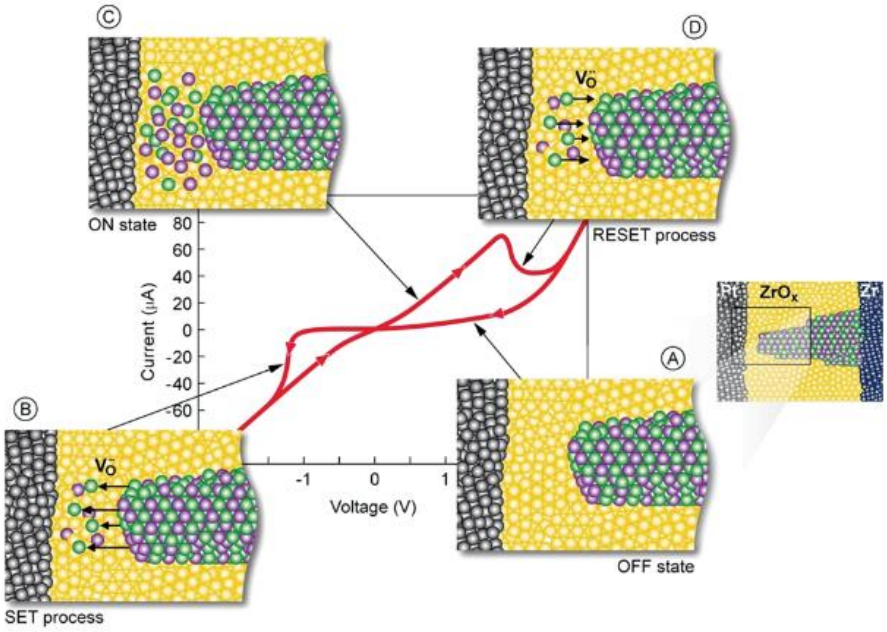

Figure 1.11: Schematic of the current–voltage characteristic of a Pt/ZrOx/Zr VCM cell, recorded with a triangular voltage sweep. The insets A to D show the different stages of the switching procedure. Only the active interface and part of the conducting filament are shown. The green spheres indicate oxygen vacancies, the purple spheres indicate Zr ions in a lower valence state. Please note that only oxygen vacancies are mobile while Zr ions are immobile and may only change their valance state. (a) HRS; (b) SET process; (c) LRS; (d) RESET process. The definition of the disc and plug part of the filament is shown in a sketch on the right. Reproduced from reference [29].

Interface-type RS also occurs due to the field-induced change of Schottky barrier at the active interface, but this effect takes place over the whole electrode area. Under the applied electric field, oxygen drift takes place and locally varies the active-metal/oxide interface properties, such as the depletion with (W_d) as sketched in Figure 1.10. Moreover, in some cases, the accumulation of oxygen at the active electrode can lead to the formation of an interlayer, especially metals whose oxide has low free energy of oxidation (large negative value). Therefore, the total resistance of the memristive devices can be eventually increased due to the series resistance added from the interlayer.

p-type oxide has also been exploited as a memristive layer in addition to n-type ones. In this case, a similar RS mechanism As for n-type oxide-based VCMs is held true, but in the opposite switching sense. For example, in the case of p-type oxides (such as PCMO and L2NO4), when contacting with a high work function metal (such as Pt, Au, etc.), ohmic current-voltage (I-V) characteristics are expected (Schottky contact if a n-type oxide is used). On the contrary, contacting a low work function metal (such as Ti, TiN, etc.), leads to a band bending and thus creates a Schottky barrier with highly nonlinear and rectifying I-V characteristics. The work function reported values for several metals of interest are: Pt (5.9-6.2 eV) [32], Ti (4.3 eV) [33], TiN (4.3-4.65 eV) [34]. Many studies have reported on the use of oxidizable electrodes such as Ti [35], Al [36, 37], and TiN [38] to accommodate oxygen (electrode acts as oxygen reservoir layer), which plays a key role in the RS properties of the final device.

In most MIM systems, an electroforming process is required prior to the RS operation. Electroforming consists of the application of a high voltage, much larger than the V_{SET}, to trigger a large change in the resistance of the pristine memristor. After the forming process, the device can be programmed using lower voltages than that of the electroforming. According to R. Waser *et al* [29], the electroforming process generally reduces the oxide, leading to the formation of filaments inside the memristive layer. During the forming process, very high local temperatures occur because of the relatively high currents. This process may lead to a change in morphology. It is worth noting that this forming voltage decreases by reducing the oxide film thickness. In many cases, when the film thickness becomes lower than 3 nm (a critical film thickness) [39], the forming process might not be necessary. Consequently, these forming-free memristors would decrease the fabrication cost.

Due to their flexibly adjustable ionic and electronic transport properties, perovskites and perovskite-related oxides, such as $GdBaCo_2O_{5+\delta}$ [40], $GdBaCo_2O_{5+\delta}/LaNiO_3$ [41], $LaNiO_{3+\delta}$ [38, 42], $La_2NiO_{4+\delta}$ [43], Fe-doped $SrTiO_3$ [20] or $La_{1-x}Sr_xMnO_{3-y}$ [44] could potentially facilitate valence change RS with multiple resistance states.

1.2. Lanthanum nickelate-based memristive devices

In this context, $La_2NiO_{4+\delta}$ (L2NO4) stands out among the various switching materials suggested for use as switching oxides in memristive devices [43, 45, 46] due to its mixed-ionic electronic conduction properties and capability to accommodate a broad range of oxygen stoichiometry without decomposing

1.2.1. Crystal structure and phase diagram

In the Ruddlesden-Popper (RP) $La_{n+1}Ni_nO_{3n+1}$ series, which can be described as the intergrowth of n perovskite layers of $LaNiO_3$ between individual LaO rock-salt type layers, La_2NiO_4 is the first member with n = 1, as can be seen in Figure 1.12.

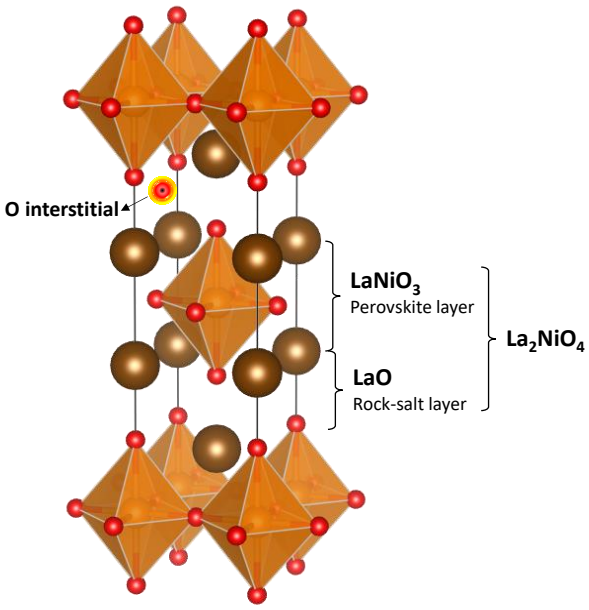

Figure 1.12: Representation of the $La_2NiO_{4+\delta}$ structure showing the location of oxygen interstitial point defect. Adapted from reference. [43]

We consider first the stoichiometric $La_2NiO_{4.00}$, tetragonal structure (*I*4/*mmm*), which is stable at high temperature (T > 700 K) [47] due to a good mismatch between $LaNiO_3$ and LaO units. At lower temperatures (80 K < T < 700 K), the structure is distorted to release the stress between compressed NiO_2 planes and stretched LaO layers. This results in different Ni-O and La-O bond lengths which lead to L2NO4 structural variety (i.e., orthorhombic *Bmab*). If we keep decreasing the temperature (T < 80K), two new phases can appear: tetragonal $P4_2/ncm$ and orthorhombic *Pccn* [48, 49]. All these phases are usually called: HTT (High Temperature Tetragonal), LTO (Low Temperature Orthorhombic), LTT (Low Temperature Tetragonal) and LTLO (Low Temperature Less Orthorhombic) in the literature.

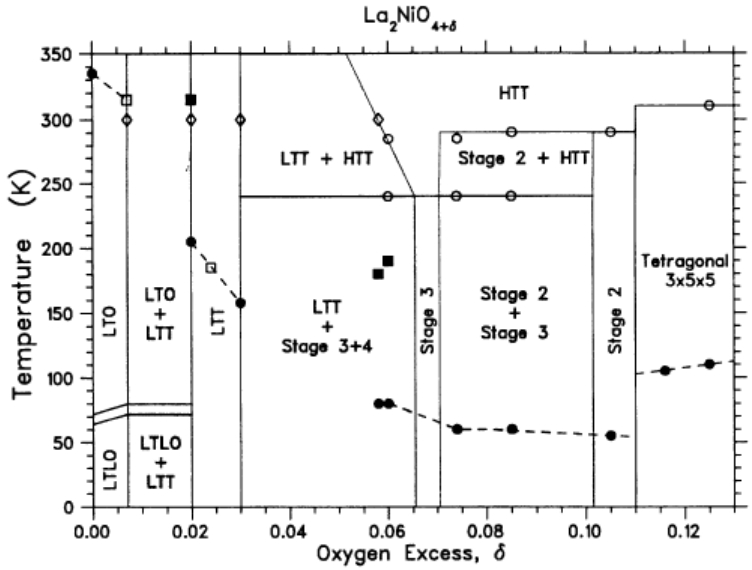

Figure 1.13: Phase diagram for $La_2NiO_{4+\delta}$ with $0.00 < \delta < 0.13$. Reprinted from reference [50].

However, in reality, obtaining stoichiometric ($\delta=0$) and homogeneous La_2NiO_4 is rather tricky. Indeed, for samples in powder, they may quickly absorb oxygen at room temperature. For thin films, based on the synthesis method and oxygen partial pressure used, the oxygen stoichiometry of L2NO4 can be varied.

We now consider over-stoichiometric $La_2NiO_{4+\delta}$, for which the maximum value of δ reported in the literature varies from 0.16 to 0.25 [48, 51, 52]. At room temperature, the *Bmab* orthorhombic (LTO) structure has been reported for L2NO4 samples where $0.00 \leq \delta \leq 0.05$ [53]. Beyond $\delta = 0.05$, there is a miscibility gap where the coexistence of *Bmab* orthorhombic and *F/mmm* orthorhombic because of the interstitial oxygen segregation into oxygen-rich domains (*F/mmm*) and oxygen-poor domains (*Bmab*). Finally, the tetragonal *F*4/*mmm* phase exists at ambient temperature in the range of over-stoichiometry $0.06 < \delta < 0.15$ [48]. Although there are many discrepancies between the proposed diagrams, the most typical one is shown in Figure 1.13.

1.2.2. Ionic and electronic conductivity in L2NO4

Skinner *et al* demonstrated that the Ni-$O_{appical}$ of NiO_6 octahedral extends when losing interstitial oxygen (located in the La_2O_2 layers) [54]. Additionally, they showed how the Ni-O and La-O bonds continuously make up for the interstitial oxygen lost by adjusting their bond length to keep the lattice volume minimal. The consistent finding is also reported in the literature [53], where Ni-$O_{appical}$ shortening was reported to occur when an interstitial oxygen atom is present. The most prevalent mechanism of oxygen diffusion along *a-b* plane in L2NO4 reported in the literature [55, 56] is interstitially transport. The findings show that oxygen diffusion is significantly anisotropic with

activation energies of (0.3 – 0.9 eV) and (2.9 – 3.5 eV) for the *a*-*b* plane and *c* (out-of-plane) directions, respectively. This oxygen anisotropy is caused by the structural anisotropy of L2NO4.

L2NO4 is a p-type semiconductor [57]. As the electrical conduction mechanism, Kharton *et al* proposed the hopping of hole carriers between mixed valence Ni cations [58]. The activation energy of this hopping conduction is in the range of 50-100 meV [59, 60]. A maximum resistivity of 12.5 mΩ.cm for L2NO4 in polycrystalline bulk ceramics and films was reported [61-66].

To maintain the overall charge-neutrality inside the lattice of $La_2NiO_{4+\delta}$, the positively-charged carrier (hole, $h^{\cdot}$) must electrically compensated with negatively-charged oxygen interstitial ions (O_i''), as illustrated in the equation below:

$$\frac{1}{2}O_2 + V_i^x \rightleftarrows O_i'' + 2h^{\cdot}$$

Based on this equation, the higher the oxygen content, the higher the concentration of charge carriers (electronic holes). O_i'' can be viewed in this context as an acceptor dopant, which results in the p-type conductivity observed in L2NO4. This particular doping mechanism, in which oxygen defects produce more charge carriers, is often referred to as "self-doping", even though in other materials, the doping is accomplished by adding a very small percentage of impurity atoms. What is more, it is thought that the shortening of the Ni-$O_{appical}$ bond length (at least for $0.13 < \delta < 0.18$) [53] is responsible for charge transfer from the interstitial defect to the NiO_2 layer, and thus is the origin of electronic conduction in L2NO4. Therefore, high oxygen interstitial doping gives rise to high conductivity in L2NO4. At extremely low δ doping levels, the presence of oxygen vacancies in the NiO_2 layers may prevent the charge transfer between Ni and $O_{equatorial}$, and thus significantly increase the material's resistivity, which would explain the insulating behavior of stoichiometric $La_2NiO_{4.00}$.[49]

1.2.3. Recent studies on L2NO4-based memristive devices

From a material point of view, L2NO4 offers numerous interesting properties. First of all, as previously mentioned, L2NO4 is a mixed ionic-electronic conductor (MIEC) in which structure a large range of oxygen over-stoichiometry can be incorporated, unlike other oxides used as memristive layers, where oxygen vacancies are the main structural point defects [67]. What is more, L2NO4 possesses capabilities of oxygen transport and oxygen storage without decomposition. Its structural and electronic properties strongly depend on the concentration of interstitial oxygen defects, which is considered a "self-doping" phenomenon. The doping level (δ) thus becomes a key factor for using L2NO4 as a memristive layer in VCM-based memristors, which can be easily tuned by post-thermal treatment in various atmospheres.

Recently, the electroforming-free analogue switching capabilities of standard L2NO4-based devices (as-deposited films grown on $SrTiO_3$ single-crystal substrates) were reported. These devices were developed both using single layers of $La_2NiO_{4+\delta}$ [43] and $La_2NiO_{4+\delta}/LaNiO_{3-\delta}$ bilayers.[46] The single-layer planar devices (Ti\200µm-L2NO4/Pt), built with an active Ti electrode and an inert Pt electrode, demonstrated gradual SET and RESET transitions as well as memory transience, making them appropriate for use in the short-term artificial synapses, as seen in Figure 1.14a-b.

Maas *et al.* [68] experimentally demonstrated the existence of a TiOx interlayer in the pristine Ti\L2NO4/Pt planar memristive devices. This spontaneous oxidation of Ti can be attributed to the high affinity for oxygen of the electrode material (Ti). In these interfacial VCM-based Ti\L2NO4/Pt planar memristive devices, there was no electroforming process required during the operation of the memristor. Instead, an 'initialization step' is needed to turn the device into HRS. This 'initialization step' was carried out at voltages similar to the ones used for device operation. The change of resistance can be attributed to the change of a Schottky barrier at the metal/semiconductor junction. The applied electric field attracts/repels the oxygen ions (well-known as a drift of ions), leading to the accumulation at the electrode interface. Therefore, it changes the depletion width of the main carriers and the electronic conductivity of L2NO4. Besides the change in the Schottky junction characteristics, the accumulation of oxygen around the electrode can cause the formation of interlayers.

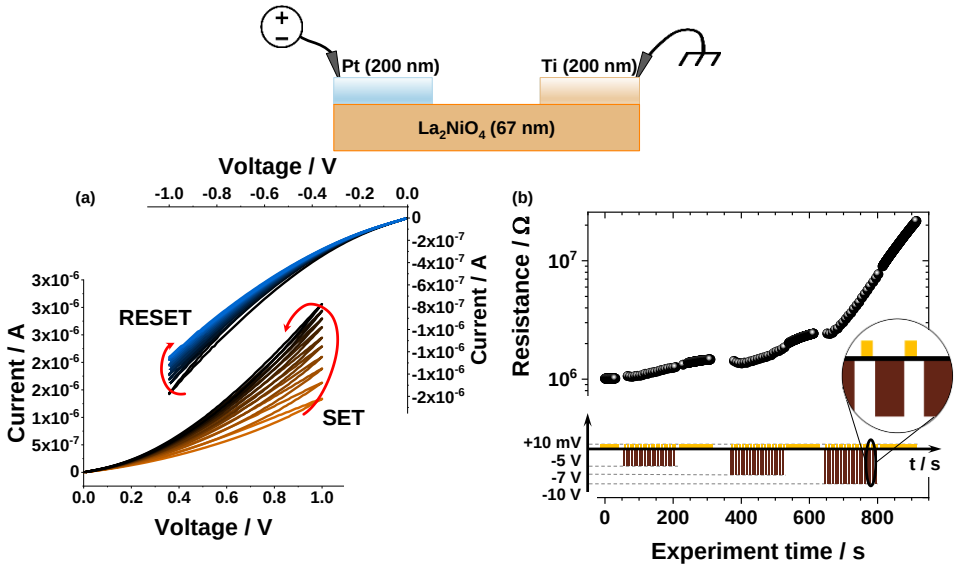

Figure 1.14: a) I-V characteristics of the Ti\as-deposited epitaxial-L2NO4/Pt memristive device under ten consecutive positive and negative voltage sweeps. b) Evolution of resistance controlled by 20 pulses of -5 V, -7 V and -10 V, respectively. A pulse duration of 3s was applied. The sketch of the device is present on top of the figure. Adapted from reference [43].

In addition, Maas and *et al.* showed that annealed epitaxial L2NO4 thin films in oxidizing or reducing conditions have clear effects on their structural and electrical properties, as shown in Figure 1.15a-c [45]. Oxygen-annealed L2NO4 (highest oxygen concentration) films have the largest out-of-plane cell parameter and the smallest resistivity, in which the presence of oxygen interstitial ions is believed to be crucial.

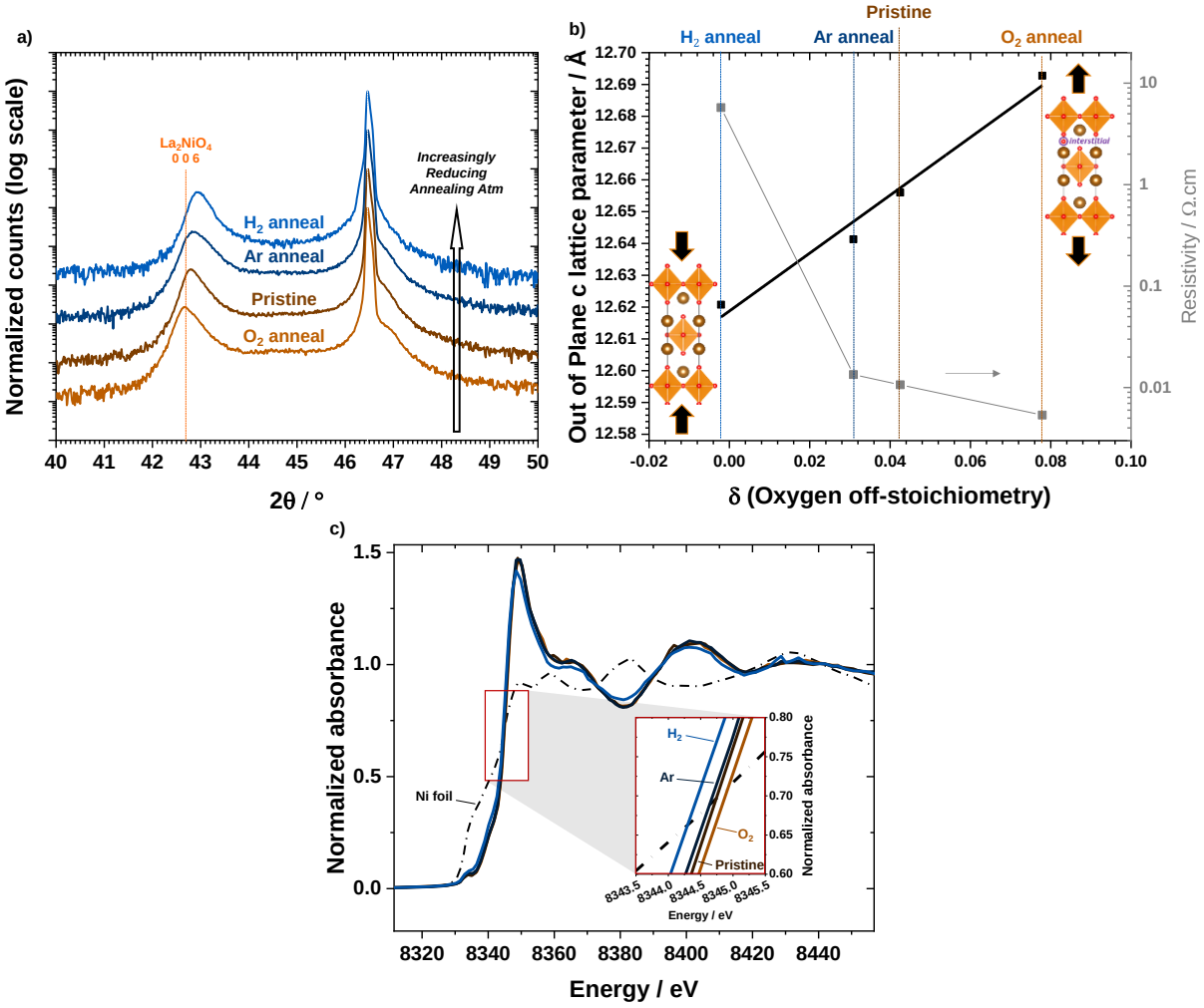

Figure 1.15: Structural and electrical properties of different annealing-L2NO4 thin films. These samples were epitaxially grown on $SrTiO_3$ single-crystal substrate. a) XRD diagrams. b) Lattice parameter estimated from XRD patterns and measured resistivity as a function of oxygen off-stoichiometry. c) XANES spectra at Ni-K edge. Adapted from reference [45].

These L2NO4 films with three different oxygen stoichiometries were used to construct memristive devices and their I-V characteristics are shown in Figure 1.16. The sample with the highest oxygen concentration shows the biggest opening of the I-V curve (largest hysteresis), suggesting the memristive

properties of L2NO4-based devices can be controlled by adjusting the additional oxygen ions in the form of interstitial defects through a post-anneal treatment.

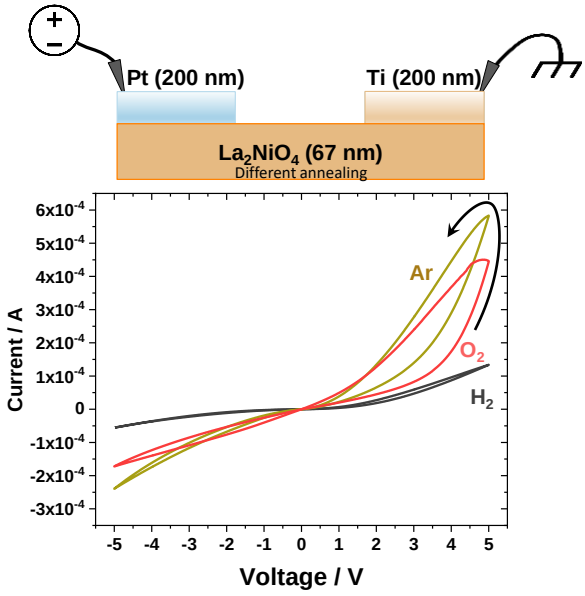

Figure 1.16: I-V characteristics of Ti\ different annealing expitaxial-L2NO4/Pt memristive devices: (top) sketch of the device, (bottom) hysteretic I-V characteristics showing gradual SET and RESET events. Adapted from reference [45].

However, to use these promising memristive devices in embedded technologies, the compact low-energy-consumption vertical configuration integrated on Si-based substrates is greatly preferred. The vertical configuration is commonly used for memristive devices due to its reduced dimensions, compactness and easiness for device fabrication, as well as compatibility for integration in crossbar array architectures [69]. Therefore, silicon-based substrates, i.e., Pt/TiO_2/SiO_2/Si and Si_3N_4/SiO_2/Si were used for all of the work carried out during this thesis, and most of the work was focused on the vertical configuration.

1.3. Aims and scope of the thesis

As stated in the previous section, Ti\L2NO4/Pt planar devices fabricated on $SrTiO_3$ had shown interesting properties for both resistive switching and neuromorphic computing applications. The aims of this thesis are:

i) to transfer such devices to Si-based substrates

ii) to construct and evaluate L2NO4-devices in a vertical configuration

iii) to optimize the device characteristics by materials optimization (electrode composition and size, oxygen content in L2NO4) and device operation optimization (soft initialization, operation conditions, etc.)

iv) to elucidate the switching mechanisms taking place during the operation

Two types of device configurations (planar and vertical) were studied in this thesis for the Ti/polycrystalline L2NO4/Pt stacks. Then, for the vertical devices, two types of oxidizable electrodes (Ti and TiN) were assessed. The memristive properties of all these devices were evaluated, as well as the structural and chemical properties of the different layers. Finally, the chemical changes during the operation of the optimized TiN/L2NO4/Pt memristive devices were studied in depth by various *in situ* and *operando* characterization techniques.

Chapter 1 introduces beyond-von Neumann computation architecture, resistive switching phenomena and the main characteristics of L2NO4-based memristive devices.

Chapter 2 briefly describes the experimental process for the growth of L2NO4 thin films using PIMOCVD (pulsed injection metal-organic chemical vapor deposition), the techniques used for structural/chemical characterization of the L2NO4 thin films and of the memristive devices, the detailed process of device microfabrication in the cleanroom and the electrical characterization of the devices.

Chapter 3 is devoted to L2NO4-based memristive devices that use Ti as top electrode and it is split into three sections. In the first section, L2NO4 thin films were deposited on Si_3N_4 substrates based on the earlier work's protocol (using the deposition conditions of epitaxial L2NO4 thin films grown-on single crystal substrates) and the L2NO4/Si_3N_4 samples obtained were then used to construct Ti\L2NO4/Pt planar devices. They exhibit resistive switching characteristics only by applying a very high electric field and after a thermal treatment. Thus, the second section focuses on the integration of Ti/L2NO4/Pt vertical devices to avoid these high energy-consumption problems. For that, platinized substrates (Pt) were used as the bottom conducting electrode. The deposition temperature of L2NO4 on Pt was optimized to avoid Pt dewetting. The precursor solution was also optimized to obtain highly-pure L2NO4 films. The optimized L2NO4/Pt samples were used to fabricate Ti/L2NO4/Pt vertical devices for the first time. Many RTAs were then carried out on larger devices to trigger the RS, the role of RTA was studied, and is presented in the third section. The second part of chapter 2 is adapted from the recently published article [70].

Chapter 4 concentrates on the study of TiN/L2NO4/Pt memristive devices, which were built for the first time during this PhD thesis. The structural and chemical characterization of L2NO4/Pt thin films and resistive switching properties of TiN/optimized L2NO4/Pt vertical devices with different oxygen

stoichiometry (δ) L2NO4, was assessed. Moreover, the suitability of using such devices as long-term artificial synapses was evaluated.

Chapter 5 is dedicated to advanced characterization techniques (TEM and XANES) in *ex situ, in situ* and *operando* modes for a better comprehension of the operation of the device and the electrochemical processes taking place.

Finally, the main conclusions of this work are summarized and future prospects are discussed in Chapter 6.

Chapter 2: Deposition and Characterization Techniques

This chapter is dedicated to the description of the experimental techniques used during the thesis and is divided into four main sections. The first one describes the experimental methodology to grow L2NO4 thin films. The second section presents the techniques used for the structural and chemical characterization of the L2NO4 thin films grown on different substrates. The third part details the micro-fabrication of memristive devices in the cleanroom and specifies the characteristics of the devices in planar and vertical configuration. The final section presents the different types of electrical characterization carried out for the L2NO4-based devices.

2.1. Pulsed injection metal-organic chemical vapor deposition

Metal-organic chemical vapor deposition (MOCVD) is a chemical vapor synthesis method which uses metal-organic precursors in the vapor phase during the deposition. In industrial applications, MOCVD is well-known as a low-cost method that enables the deposition of homogeneous films over large wafer areas. Among the different types of MOCVD, pulsed injection MOCVD (PIMOCVD) uses a precursor solution prepared by mixing metals in the form of metal-organic compounds in a solvent, which is then injected as small drops into the evaporation zone, which is next transferred towards the reaction zone to generate the targeted thin film material. All the lanthanum-nickelate thin films used in this thesis were synthesized by PIMOCVD [71]. In PIMOCVD, the stoichiometry of the film can be adjusted under fixed deposition conditions by changing the precursor solution's composition, and the film thickness can be regulated by the number of droplets.

First of all, the substrates used for the deposition require a cleaning process consisting of immersing them in 1) acetone, 2) isopropanol and 3) deionized water. Three beakers containing each solvent were put in an ultrasonic bath and the substrates were cleaned in each beaker for at least 10 seconds. This cleaning process allows for the elimination of undesired contamination on the substrate surface, for example, dust or organic particles. Dust was also observed on the surface of $Pt/TiO_2/SiO_2/Si$ substrate used in this thesis, which could be contaminated during the substrate cutting. Then there were two ways of fixing the substrates on the sample holder. The first is to use silver paste. However, the silver paste needs a few hours to be dried and can diffuse inside the substrates during the deposition, so the alternative is to use steel masks. Using steel masks for the deposition of L2NO4 on Pt also facilitates the contact of the Pt bottom electrode in electrical measurements without the need of etching, as the

region is covered by the mask is L2NO4-free after the deposition. After fixing the substrates on the sample holder (upside down), the precursor solution was prepared by mixing $La(tmhd)_3$ (tris(2,2,6,6-tetramethyl-3,5-heptanedionato)lanthanum(III)) and $[Ni(tmhd)_2]$ (bis(2,2,6,6-tetramethyl-3,5-heptanedionato)nickel(II)) precursors from Strem Chemicals in a solution of m-xylene (1,3-dimethylbenzene) from Alfa Aesar. It is worth emphasizing that the preparation of precursor solution was performed just before the deposition to avoid its degradation over time. The precursor solution is kept in Ar inert air whenever possible. For all of the depositions presented in this thesis, the volume of the precursor solution was kept at 20 mL, and a precursor concentration solution of 0.02 mol/L was used. Different solutions with varying La/Ni ratios (R) were prepared throughout the thesis. The R-value used for each sample is detailed in each case.

Figure 2.1 shows the PIMOCVD process and the involved growing steps. The prepared solution is poured into the injector, which is connected to a computer where the injection program can be controlled (e.g. opening time of electrovalve, frequency of pulses, number of pulses, etc.). An opening time of 2 ms and a frequency of 1 Hz are always used. The solution micro-droplets are formed by a high-speed electrovalve and injected into the circuit. A flow of oxygen and argon mixture transports them to the substrate surface. During the travelling, the droplets are vaporized by the heating line.

After reaching the reaction area, there are many kinetic processes involved: gas phase reaction, adsorption of precursors, gas-solid reaction, nucleation and growth of L2NO4 films. The by-products are removed from the boundary region and carried away by the gas flow. After coming out of the reactor, they are trapped in a liquid N_2 flask. During the deposition, a pressure of 5 Torr and the atmosphere of mixed oxygen-argon are always used (for all samples in this thesis). After deposition, the reactor is cooled down naturally by Ar atmosphere (similar to the heating).

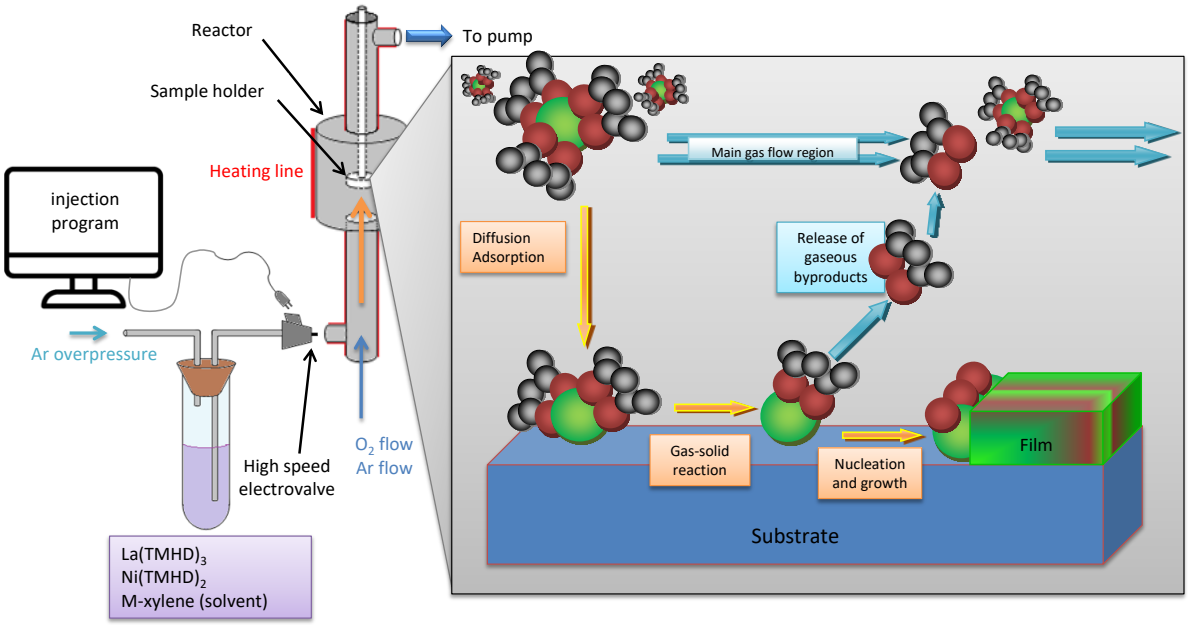

Figure 2.1: Schematic of the PI-MOCVD reactor used for the deposition of lanthanum-nickelate thin films and the main steps that happened during the deposition.

2.2. Thin film characterization techniques

2.2.1. X-ray diffraction

X-ray diffraction was used to determine the phases present in the thin films, as well as to calculate the cell parameters of the L2NO4 phase. As standard Bragg Brentano θ-2θ configuration does not allow obtaining high-quality peaks of the polycrystalline thin films (the majority of the signal comes from the substrate), a 5-circle RIGAKU Smartlab diffractometer in grazing incidence mode was used instead for phase identification. The incidence angle was 0.4° with monochromatic CuKα (λ = 1.5406 Å). The collected signal was carried out with a step of 0.06° and 0.25° per minute. The cell parameters of L2NO4 thin films were refined using the fitting in DIFFRAC.SUITE TOPAS software from Bruker.

2.2.2. Raman spectroscopy

The Raman spectra presented in this thesis were measured using a Jobin Yvon/Horiba Labram spectrometer equipped with a liquid N_2-cooled CCD detector. The green laser (λ = 514 nm) with a spot size of 1 μm^2 and an objective x100 was used. The spectra were then calibrated to the theoretical position of 520.7 cm^{-1} of a silicon sample at room temperature, which was measured the same day.

2.2.3. Scanning electron microscopy

The morphology of polycrystalline L2NO4 was studied by scanning electron microscopy (SEM). SEM images in this thesis were acquired in a high vacuum in a SEM FEG ZEISS GemeniSEM 300 with the conditions: operating energy of 3 kV, a working distance of 4 mm.

2.2.4. Atomic force microscopy

The topography of L2NO4 thin films was obtained by using a Bruker Dimension 3100 atomic force microscope (AFM) in tapping mode for the sample presented in section 3.1.1, while the AFM images of the other samples in this thesis were measured by AFM using a D3100 Veeco Instrument in tapping mode with a Si_3N_4 tip probe.

2.2.5. Electron probe microanalysis

The overall cationic composition of the L2NO4 films grown on $Si_3N_4/SiO_2/Si$ and $Pt/TiO_2/SiO_2/Si$ substrates was analyzed by electron-probe microanalysis (EPMA) using a CAMECA SX50 spectrometer. For individual sample, two different acceleration voltages (12 keV and 16 keV) were acquired and the data analysis was carried out using the Strategem software. The measurements were acquired by Rachel Martin and Florence Robault (CMTC – Consortium des Moyens Technologies Commun, Grenoble INP).

2.2.6. Transmission Electron Microscopy

Transmission electron microscopy (TEM) was used in this thesis for the cross-section structure of the device stack with multiple goals:

- To verify the quality of the devices after the micro-fabrication process in the cleanroom
- To study the TiO_x interlayer of the L2NO4-based devices in combination with the Ti electrode
- To study the switching mechanisms by *ex situ* and *in situ* TEM of the TiN/L2NO4/Pt devices

Samples presented in chapter 3, section 5.1 and Figure 4.4

Lamella preparation and TEM observations were carried out by Dr. Gauthier Lefèvre (CEA-Leti) using FIB milling in a FEI dual-beam Helios 450S. A thin layer of Pt was evaporated on top of the sample as a protective layer. Rough milling was at 30 kV and fine milling was at 2-8kV. After the FIB process, all of the lamellae were cleaned with an oxygen-argon plasma to remove hydrocarbon contamination.

The TEM observation of the lamellae was performed at 200 kV using a probe-corrected Tecnai Osiris FEI microscope equipped with the Super-X detector system for Energy Dispersive X-ray Spectroscopy (EDX) chemical composition analysis.

The TiN/L2NO4(Ar-annealed)/Pt lamella presented in Figure 4.5

The TEM lamella was prepared by Florence Robaut (CMTC) using a xenon ion beam in a Thermo Fisher FIB Helios 5 dual-column SEM-plasma microscope. The lamella was protected by a film of W several microns thick. It was thinned at 30 kV with a decreasing ion current from 100 to 20 pA and a beam angle of 2° to the lamella faces. Final thinning of both lamella faces was performed at 5 kV, 20 pA with a tilt angle of 5°.

The TEM observations were carried out by Dr. Laetitia Rapenne (LMGP). This lamella was observed at 200 kV in a JEOL JEM 2010 LaB6 TEM with a resolution of ~0.19 nm. Complementary STEM-EDS (scanning transmission electron microscopy equipped with energy dispersive spectroscopy) was carried out in a JEOL 2100F FEG microscope at 200 kV with a 0.2 nm resolution in scanning mode.

Samples presented in section 5.2 of *in situ* TEM:

Lamellae and TEM observations were carried out by Dr. David Cooper (CEA-Leti). The lamellae were prepared by using focused ion beam (FIB) milling in a FEI Strata 400S. A thin layer of tungsten was deposited on top of the sample as a capping layer to avoid damage during the lamella preparation. The milling consisted of several main steps, including fast milling at 30-16 kV and a lower energy clean at 2 kV.

The lamella was then mounted in a Nanofactory sample holder (see Figure 2.2), which has a piezo-controlled motor, allowing for the movement of the lamellae in the nanometer range. The Pt bottom electrode was grounded with this system. For *in situ* contacting, a movable tungsten tip landed on the top of the TiN electrode. It should be noted that the electrical contact is far away from the regions where we did the TEM observations to have better observations.

Figure 2.2: Photo of the Nanofactory sample holder used for *in situ* TEM measurements. Reproduced from Villepreux's PhD thesis [72].

Just before the experiments, the sample was exposed to an oxygen-argon plasma cleaning. The TEM measurements were performed in ultra-high vacuum using a double-aberration-corrected FEI Titan Ultimate TEM equipped with a high-brightness electron source and a Gatan Tridiem energy filter equipped with Dual EELS. A beam current of 200 pA was used. The specimen was electrically biased using a Keithley2600 sourcemeter located outside of the TEM chamber.

2.2.7. X-ray Absorption Spectroscopy

Due to the presence of a thick substrate, XANES measurements at the Ni-K edge and Ti-K edge were performed in X-ray fluorescence mode. However, due to the lower intensities obtained in this mode compared to the transmission mode, the measurement time has to be extended in order to increase the signal-to-noise ratio and obtain X-ray absorption spectra with sufficient statistics.

- All the XANES measurements presented in this thesis were carried out at the ESRF Synchrotron (Grenoble, France), at the ID12 beamline and during two different beamtimes: MA-4802 and MA-5230. For convenience, we have divided the beamtime of MA-5230 into two shifts of measurements (namely shift 1 and shift 2), which correspond to the first and last days of measurements. Depending on the beamtime and shift, either a $Ni_{18}Mn_{88}$ alloy or a Ni foil was measured and used as calibration references for the position of the Ni edge. Our measurements were corrected by shifting the XANES curves by ΔE to lower energy and the precise ΔE is detailed in Table 2.1 depending on beamtime and shift. In addition, the XANES spectrum of a NiO powder was also measured to be used as calibration of the Ni oxidation state. The measurements of the foils and powder have been corrected for the self-absorption effect and are shown in Figure 2.3a. The corrected positions of the Ni-K edges for each sample were obtained by the first derivative method and are reported in Figure 2.3b. As can be observed, the two values measured for the Ni-K edge of the NiO powder, corresponding to Ni (II), are close to the

calibration curve established from Woolley's work [73]. Thus, we use this calibration curve to estimate the Ni oxidation state in this work (polynomial fitting curve shown in Figure 2.3b). The detailed data of our measurements and calibration references are also reported in Table 2.1. For measurements in beamtime MA-4802 and the other measurements in this thesis,Pt was grounded and voltage was applied on TiN.

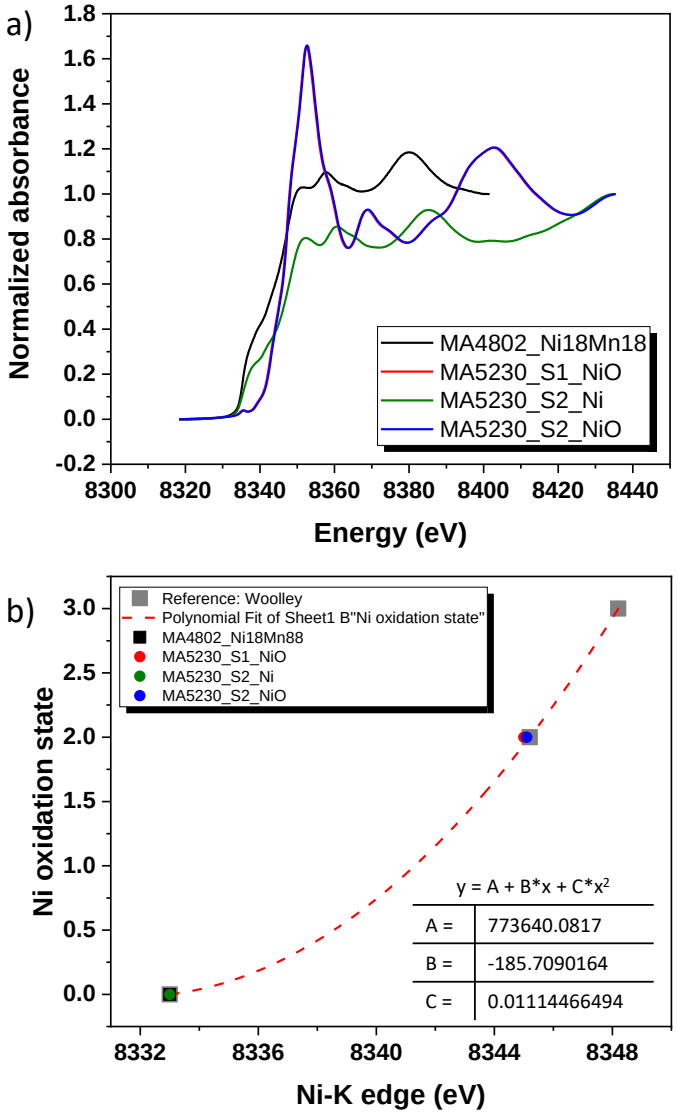

Figure 2.3: a) XANES measurements of reference materials after the self-absorption correction. b) calibration curve between the Ni oxidation state and the Ni-K edge energy reproduced from Woolley's work [73] and the Ni-K edge position measured in a), *y* represents Ni oxidation state and *x* stands for Ni-K edge energy. The polynomial fitting curve is plotted by the dashed line and fitting parameters are shown in the graph.

Table 2.1: XANES measurement details in this work and Woolley's work for the calibration curve

Beamtime		Material	Ni oxidation state	Ni-K edge position (eV)	ΔE (eV)
MA-4802		$Ni_{18}Mn_{88}$ alloy	0	8335.3	2.3
MA-5230	Shift 1	NiO	2	8347.3	2.1
	Shift 2	Ni foil	0	8335.3	2.3
		NiO	2	8347.4	2.2
Woolley *et al.*		Ni foil	0	8333.0	
		NiO	2	8345.2	
		$LaNiO_3$	3	8348.2	

***ΔE: difference between the measured values and those reported in reference [73], the correction applied to all measurements of each beamtime.

XANES spectra at the Ni-K edge and at the Ti-K edge were acquired for L2NO4 thin films (under different conditions) and for L2NO4-based memristive devices (with and without electrical bias) to evaluate the Ni and Ti oxidation state changes. When obtaining the Ni oxidation state (y), the oxygen off-stoichiometry (δ) can be estimated by the charge balance in $La_2NiO_{4+\delta}$:

$$(3 \text{ x } 2) + y + (4 + \delta) \times (-2) = 0 \rightarrow \delta = \frac{y-2}{2}$$

Two different setups and measurement conditions were used:

- **<u>Under vacuum:</u>** For the reference samples ($Ni_{18}Mn_{88}$ alloy, Ni foil and NiO powder) and the L2NO4 thin films annealed in different atmospheres (different oxygen stoichiometry) which were used as references, their XANES spectra were acquired in grazing incidence configuration using the entire samples (10x10 mm^2) under vacuum at room temperature, using a practically constant beam current of 196 mA. The fluorescence yield was collected in backscattering geometry (detector plane at 90° to the beam direction), with a silicon photodiode utilized as the detector.
- **<u>In open air:</u>** For the L2NO4/Pt samples with memristive devices, the XANES spectra were acquired for selected regions (focusing the beam) at atmospheric pressure in the open air at room temperature (Figure 2.4). The fluorescence yield was collected using two silicon drift detectors in a backscattering configuration. To minimize elastic scattering, a 10 μm Cr foil was

used. For accurate XANES mapping, a beam size smaller than the electrode area was used (the precise beam size will be detailed in each result). For the external electrical bias, a Keithley 2410 sourcemeter was employed. Exceptionally, voltage was applied on Pt contact, and TiN contact was grounded for the measurements in beamtime MA-5230. For measurements in beamtime MA-4802 and the other measurements in this thesis,Pt was grounded and voltage was applied on TiN.

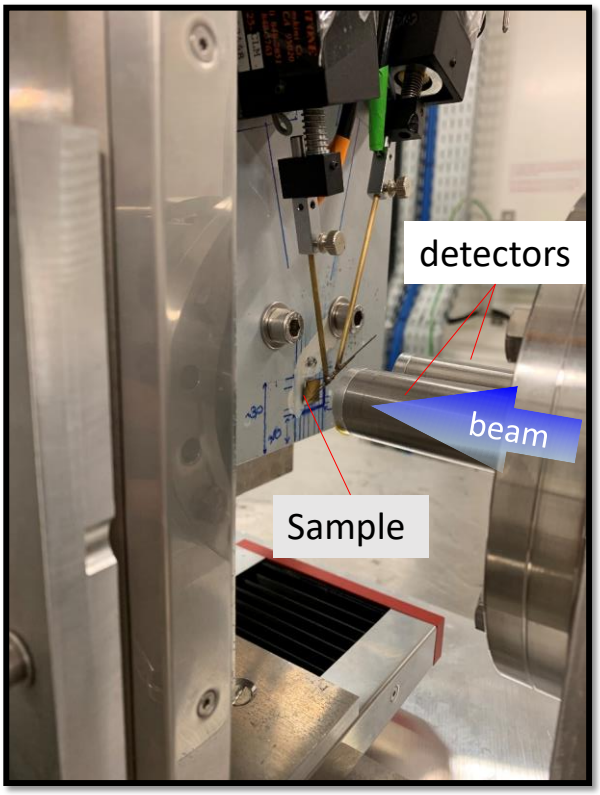

Figure 2.4: Experimental setup of XANES in the open air showing the sample is fixed on the state, two micromanipulators are used to contact the device of interest, the beam is perpendicular to the sample surface

Different samples and devices were measured by XANES in this thesis and the information of the chapter and chapter/section where they appear is reported in Table 2.2.

Table 2.2: Information of the L2NO4 samples measured by XANES and the corresponding measurements

PhD thesis section	Conditions	Mode	Beamtime	Description	Device	Electrode
3.3.3	Atmosphere	*Ex situ*	5230-S2	As-deposited 3-min RTA 10-min RTA	Ti/L2NO4/Pt	No bias
4.1.2	Vacuum	*Ex situ*	5230-S1	As-deposited O_2 anneal Ar anneal	No electrode (L2NO4/Pt)	No bias
5.1.2.1	Atmosphere	ROI1, ROI2	5230-S1	As-deposited	TiN/L2NO4/Pt (C6 for ROI1)	No bias
	Atmosphere	*Ex situ*	4802	As-deposited (pristine, HRS, LRS devices)	TiN/L2NO4/Pt (C2, C12, C13)	No bias
5.1.2.2	Atmosphere	*In situ*	4802	As-deposited Cycled device	TiN/L2NO4/Pt (D4)	TiN: biased Pt: GND
5.1.2.3	Atmosphere	*Operando*	5230-S1	As-deposited Cycled device	TiN/L2NO4/Pt (C6)	Pt: biased TiN: GND

2.3. Micro-fabrication of memristive devices

2.3.1. Main steps of device fabrication in the cleanroom

The micro-fabrication of electrodes was carried out at the PTA (Plateforme de Technologie Amont) cleanroom facilities in Grenoble. The workflow in Figure 2.5 corresponds to the fabrication of one type of electrode (either Ti, TiN or Pt). Therefore, in the case of planar devices, the following process needs to be performed twice. The steps involved are described below:

1. Beforehand, the samples are cleaned to remove dust and organic particles. This process allows to obtain a homogenous resin layer in the next step. The cleaning process consisted of immersing and shaking the samples into acetone, isopropanol and deionized (DI) water consecutively. Finally, the sample is dried using a nitrogen flow.
2. 200 µL of a positive photoresist (AZ 1512 HS) is used to cover the sample surface (1x1 cm^2) thanks to the spin coater. The program of the spin coating is 4000 RPM for 60 s with an acceleration of 2000 RPM/s. Then, the coated sample is baked on a 100°C-plate for 90 s to harden the photoresist. The expected thickness of the coated layer is 1 µm.
3. A digital mask where the required patterns (shape and size of electrodes) are designed is prepared in advance. This mask was then imported to the laser lithography computer, and the patterns were transferred to the sample using 100% energy of 15 mW. Writing head III is used (which allows for a resolution of 5 µm). The exposed areas of the photoresist become soluble when put in the developer. The lithography equipement used is µPG 101 from HEIDELBERG Instruments. Careful alignment must be carried out for the second electrode layer in the case of planar devices to ensure the devices' geometry is correctly fabricated.
4. The sample is then passed to the development step: the patterned sample is immersed and shaken in the proper developer for 35 s, and then in DI water for 45 s. This process allows for the removal of the laser-exposed areas.
5. The samples now have two regions: resin and resin-free. The Ti and Pt metals are then deposited in a high vacuum on their surfaces by the MEB550 evaporator from Plassys. Prior to the deposition, the samples are exposed to a mild Ar^+ etching step at 250-300 V to remove the residuals from the previous steps. Deposition rates are 0.1 nm/s and 0.5 nm/s for 25 nm of Ti and 75 nm of Pt, respectively. In the case of the TiN electrodes, the deposition of TiN was carried out by Valentine Bolcato in the BCAi cleanroom. The reactive sputtering equipment is PVD 100 Alliance Concept. The deposition rate is 0.2 nm/s for 100 nm of TiN.
6. The final step is lift-off, where the resin is AZ 1512 HS dissolves in acetone, revealing the desired patterns. The sample is immersed and shaken in acetone for 3 minutes. This process is made under soft sonication. A pipette is sometimes required to help remove the resist by creating bubbles.

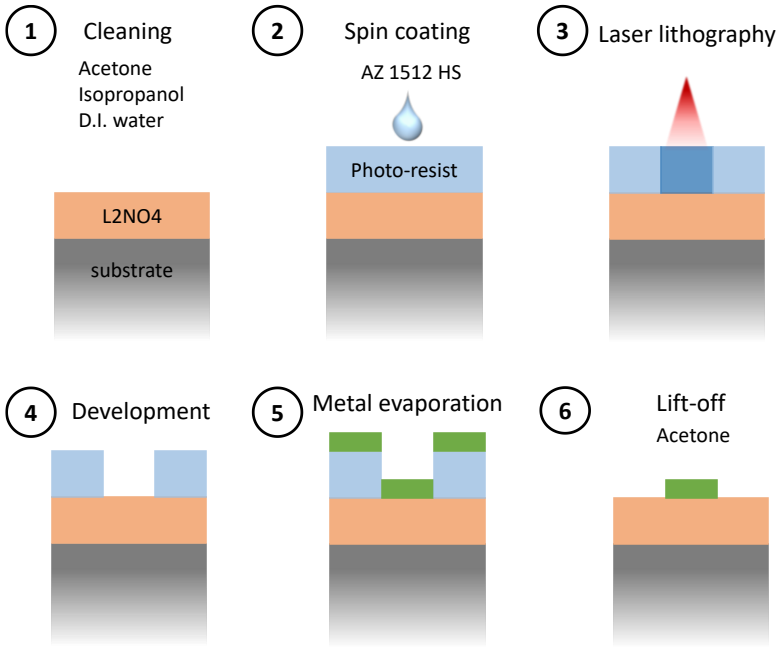

Figure 2.5: Main steps of the micro-fabrication of memristive devices. Acetone, isopropanol and deionized (D.I) water are used for cleaning. Positive photo-resin is coated before exposure in laser lithography. In the case of planar devices where two different electrodes are placed on top of L2NO4, the workflow from 1 to 6 has to be repeated twice.

2.3.2. Ti\L2NO4/Pt planar memristive devices

In this thesis, Ti\L2NO4/Pt is hereafter referred to as "top-top" configuration or planar device. As shown in the top part of Figure 2.6 the planar Ti\L2NO4/Pt devices were fabricated using non-optimized L2NO4 thin films (see section 3.1) with two types of different electrodes: i) 25 nm of Ti on the bottom + 75 nm of Pt on top, where Ti acts as an active electrode and Pt acts as a protective layer, and ii) 100 nm of Pt, where Pt acts as a passive electrode. Figure 2.3 also reveals the reproduction of the real sample, as well as the mask used for laser lithography during the micro-fabrication, showing three regions of interest. Region 1 is a series of Pt bar-shaped contacts used for transmission line measurements (TLM, see subsection 2.4.2 for more details). The Pt bars are separated by different distances (1000, 500, 200, 100, 50, 20 and 10 µm). Region 2 shows the electrodes where their area is constant (S = 200x200 μm^2) and the distance between Ti and Pt electrodes (d) is variable to study the effect of d in memristivity. Reversely, region 3 shows the electrodes with constant d but variable S to study the impact of S in memristivity behaviors.

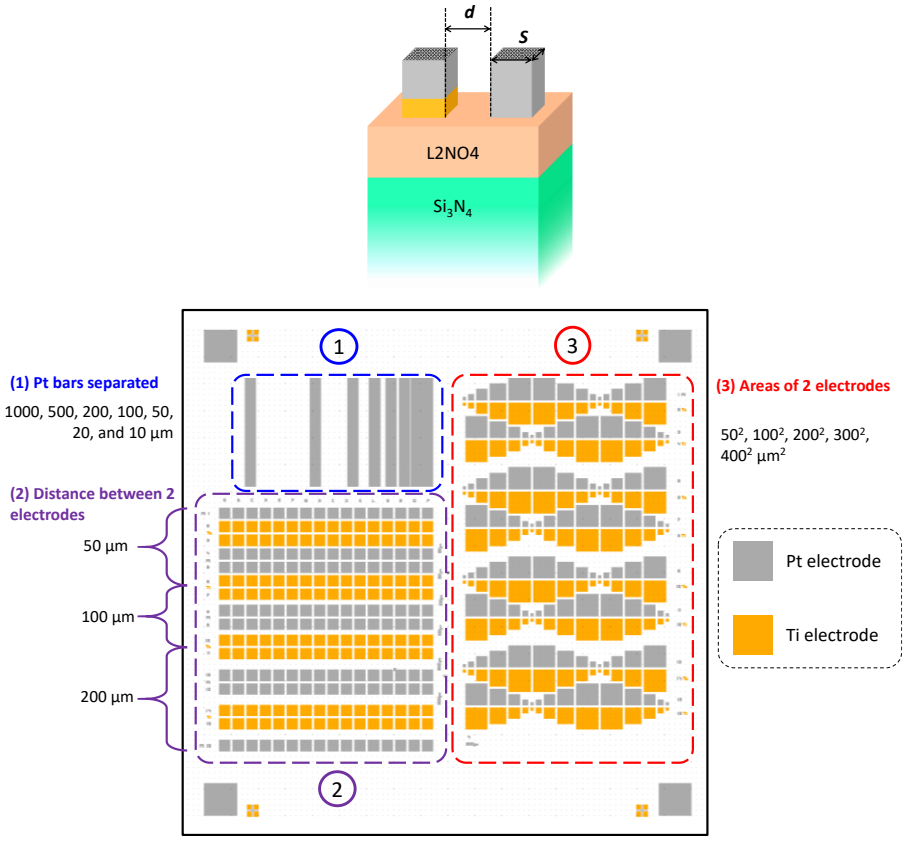

Figure 2.6: Electrode map (also the digital mask used in laser lithography for planar devices) reproducing the real sample configuration and showing three regions for specific measurements. 1) Pt bar-shaped contacts (2000x200 µm^2) for TLM. 2) Memristive devices with different distances between two electrodes (*d*), while the electrode area (*S*) is kept similar (200x200 µm^2). 3) Memristive devices with different *S*, while the *d* is constant (50 µm). The top part shows the sketch of a planar memristive device

2.3.3. Ti/L2NO4/Pt vertical memristive devices

In the thesis, Ti/L2NO4/Pt is hereafter referred to as "top-bottom" device (vertical geometry). Ti/L2NO4/Pt devices are made of both optimized L2NO4 and non-optimized L2NO4 (see section 3.2). Metal contacts (M) can be either (25 nm of Ti + 75 nm of Pt) or 100 nm of TiN (chapter 4). Figure 2.7 represents the real L2NO4 sample with M electrodes on top. The side sizes of squared electrodes are 200, 150, 50, 100 and 20 µm from left to right, respectively, in each region (1 or 2). These regions also represent the layers used for laser lithography during cleanroom micro-fabrication. Typically one layer is used for each L2NO4/Pt sample, but both layers can be employed if two different materials of top electrodes are required.

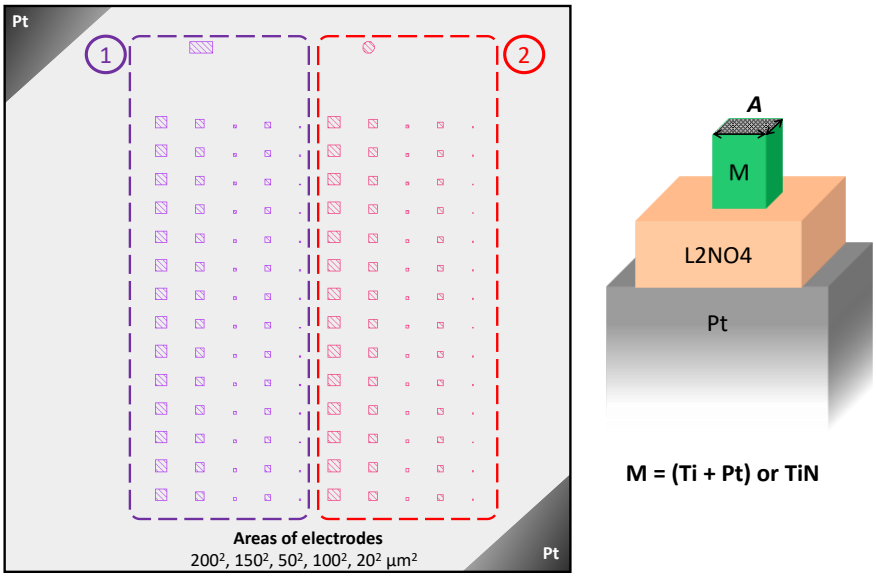

Figure 2.7: Sketch of the L2NO4 sample with TiN electrodes in the center and Pt corners (serve as bottom electrodes) reproducing the real sample configuration. Layers 1 and 2 (included in the digital mask used in laser lithography for vertical devices) are exactly similar and designed for different electrode materials. The dimensions of the side of the squared contacts are 200, 150, 50, 100 and 20 µm from left to right, respectively. The right part shows the sketch of a vertical memristive device.

2.4. Electrical characterization

2.4.1. Standard electrical measurements

Electrical measurements of L2NO4-based memristive devices were carried out using a semiconductor parameter analyzer Keithley 4200 equipped with a source measure unit (SMU), a pulse measure unit (PMU) and two external micromanipulators (connected to two tungsten probes). In the Ti\L2NO4/Pt, Ti/L2NO4/Pt and TiN/L2NO4/Pt devices, the bias was applied to the (Ti+Pt) or TiN electrode and the Pt electrode was grounded (unless otherwise stated).

Four types of electrical measurements were performed (Figure 2.8), as summarized below:

a) Bipolar I-V sweeps: each sweep consists of two half-cycles (0 V → $+V_{max}$ → 0 V → $+V_{read}$) and (0 V → $-V_{max}$ → 0 V → $+V_{read}$). The voltage step is 0.01 V for V_{max} range (1 V – 10 V) and 0.1 V for V_{max} amplitude higher than 10 V. The read voltage ($+V_{read}$) was 0.1 V and 0.01 V for devices in top-top (planar) and top-bottom (vertical) configuration, respectively. The HRS and LRS are obtained by extracting the current at $+V_{read}$ for the reading sweeps.

b) Resistance hysteresis switching loops (RHSL) are acquired by pulsed measurements. They are performed by applying a staircase of writing pulses followed by the read pulses. This test allows for obtaining HRS, LRS and intermediate resistance states (switching window)

c) Depression/potentiation measurements consisted of two trains of pulses: the first train included 50 consecutive $+V_{max}$ pulses (depression), and the second train consisted of 50 consecutive $-V_{max}$ pulses (potentiation). A read pulse is applied right after each $+V_{max}$ pulse or $-V_{max}$ pulse to read the resistance values.

d) Depression measurements based on three trains of pulses with a fixed voltage amplitude (V_{max}) and three different pulse durations were carried out to study the effect of pulse length on the plasticity behavior (depression curves).

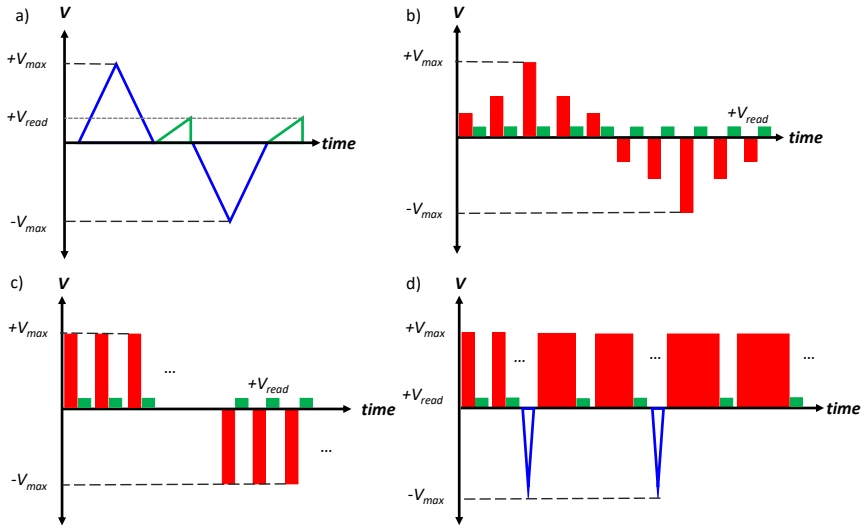

Figure 2.8: Diagrams representing the electrical characterization sequences used to characterize the L2NO4-based devices. a) Bipolar I-V sweep. b) Resistance switching hysteresis loops (RSHL) allows for reading the resistance value after each writing pulse. c) Depression/potentiation measurements where consecutive writing pulses with a fixed voltage ($+V_{max}$ or $-V_{max}$) are applied. A reading pulse is carried out after an individual write pulse. d) Depression measurements with a fixed $+V_{max}$ where the duration of the pulse is changed to study its effect on plasticity (depression curves).

2.4.2. Transmission length measurements (TLM)

Transmission length measurements (TLM) allow for calculating the contact resistance, L2NO4 thin-film resistivity and transfer length. The illustration of the TLM is shown in Figure 2.9. The total resistance of a Pt\L2NO4/Pt planar device is given by the following relationships:

$$R_{total} = R_{semi} + 2R_m + 2R_c$$

Equation 1

Where R_{total}, R_{semi}, R_m and R_c are the total resistance of the device, the resistance of the L2NO4 film between the devices, the resistance of the Pt metal electrode and the Pt/L2NO4 contact resistance, respectively. As the conductivity of Pt metal is very high, the contribution of R_m to R_{total} can be considered negligible. Moreover, expressing the R_{semi} as a function of the L2NO4 resistivity: $R_{semi} = \frac{\rho_{semi}.d}{e.l}$ can turn Equation 1 into Equation 2:

$$R_{total} = \frac{\rho_{semi}.d}{e.l} + 2R_c$$

Equation 2

Where *d* is the distance between two bar-shaped Pt contacts, *e* is the L2NO4 thickness and *l* is the length of the electrode. R_C can be expressed by the specific contact resistivity ρ_C (expressed in $\Omega.cm^2$):

$$R_C = \frac{\rho_C}{L_T.l}$$

Where L_T (transfer length) is the average distance a charge carrier travels beneath the Pt metal contacts before being injected into the semiconductor (L2NO4 in this case). The transfer length can be expressed as a function of ρ_C and R_S (from equivalent circuit considerations):

$$L_T = \sqrt{\frac{\rho_C}{R_S}}$$

Equation 3

When combining Equation 2 and Equation 3, the total resistance of the device becomes:

$$R_{Total} = \frac{\rho_{Semi}}{e.L}(d + 2L_T)$$

Equation 4

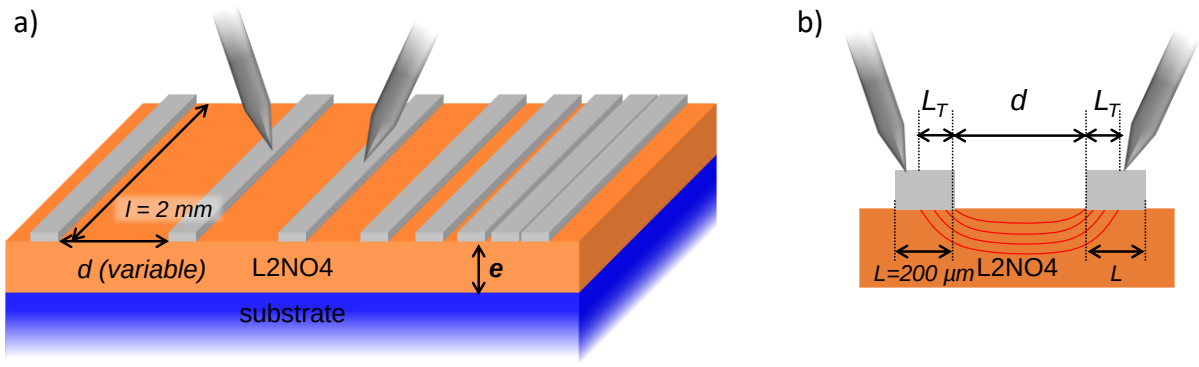

Figure 2.9: a) illustration of bar-shaped Pt array for TLM. *d* is the distance between two contacts. *e* is the thickness of L2NO4 thin film. *l* is the length of the electrode. b) cross-section showing the current flow for a given *d*. L is the transfer length.

Hence, it is possible to predict the resistance of the device (y, R_{total}) by a linear regression established by the distance between two electrodes (x, *d*). The linear regression is expressed as follow: y = m.x + a or y = m.(x + b) where:

- the slope, $m = \frac{\rho_{Semi}}{e.L}$
- the y-axis intercept, a = 2.R_C
- the x-axis intercept, b = 2.L_T

Chapter 3: Ti/$La_2NiO_{4+\delta}$/Pt Memristive Devices integrated on Si-based Substrates

As stated in section 1.2.3, Ti\epitaxial L2NO4/Pt devices showed very interesting memristive properties. However, their integration in a Si-compatible substrate was still missing. The current chapter focuses on the integration of L2NO4-based memristive devices in planar and vertical configurations using Ti as the active electrode and Pt as the inert electrode. Two types of devices were built and measured on two different substrates: Ti\L2NO4/Pt devices in planar configuration fabricated on Si_3N_4 substrates (section 3.1) and Ti/L2NO4/Pt devices in vertical configuration grown on Pt substrate (sections 3.2). An additional thermal treatment process was required in some cases to activate the resistive switching characteristics of the devices. Section 3.3 reports the role of this heat treatment.

3.1. Ti\L2NO4/Pt planar memristive devices integrated on Si_3N_4 substrates

In this section, the L2NO4 films were prepared by PI-MOCVD using the deposition conditions of monocrystalline L2NO4 from the previous study. These conditions were optimized to obtain epitaxial L2NO4 films grown on single-crystal substrates ($SrTiO_3$ or $LaAlO_3$).

3.1.1. Deposition of L2NO4 films on Si_3N_4 substrates

For Ti\L2NO4/Pt planar devices, we first deposited L2NO4 on a $Si_3N_4/SiO_2/Si$ (SN) substrate. Si_3N_4 (top layer) is an insulating material, and it is widely used for many applications in the semiconductor field. The growth conditions of L2NO4 on the SN substrate using PI-MOCVD technique are summarized in Table 3.1.

Table 3.1: Deposition conditions used for the growth of L2NO4 thin films on SN by PI-MOCVD

Parameter	Value
Injection frequency (Hz)	1
Number of pulses	2000
Temperature (°C)	650
Ratio of (La/Ni) in solution - R	5.00

The GIXRD pattern obtained for the L2NO4/SN thin film is shown in Figure 3.1a. All the intense diffraction peaks can be attributed to the L2NO4 tetragonal phase with preferential orientations of (101) and (110). A small diffraction peak corresponding to the La_2CO_5 phase is observed at 27° and marked by a red circle. The presence of the La_2O_3 phase is confirmed by the electron probe microanalysis (EPMA), which reveals a cationic La/Ni ratio of 2.75 (pure L2NO4 phase in thin film should give a ratio of 2.00). The surface morphology of the L2NO4/SN sample can be observed in the SEM image (Figure 3.1b), showing the film is composed of small grains (tens of nanometers). A dense, polycrystalline and homogenous film without porosity nor cracking, suitable for memristive device fabrication, is observed. The AFM image shown in Figure 3.1c indicates that a relatively flat L2NO4 film was obtained, with a film surface root-mean-square (RMS) roughness value of 2.23 ± 0.02 nm and an average grain size of 15.8 ± 0.4 nm.

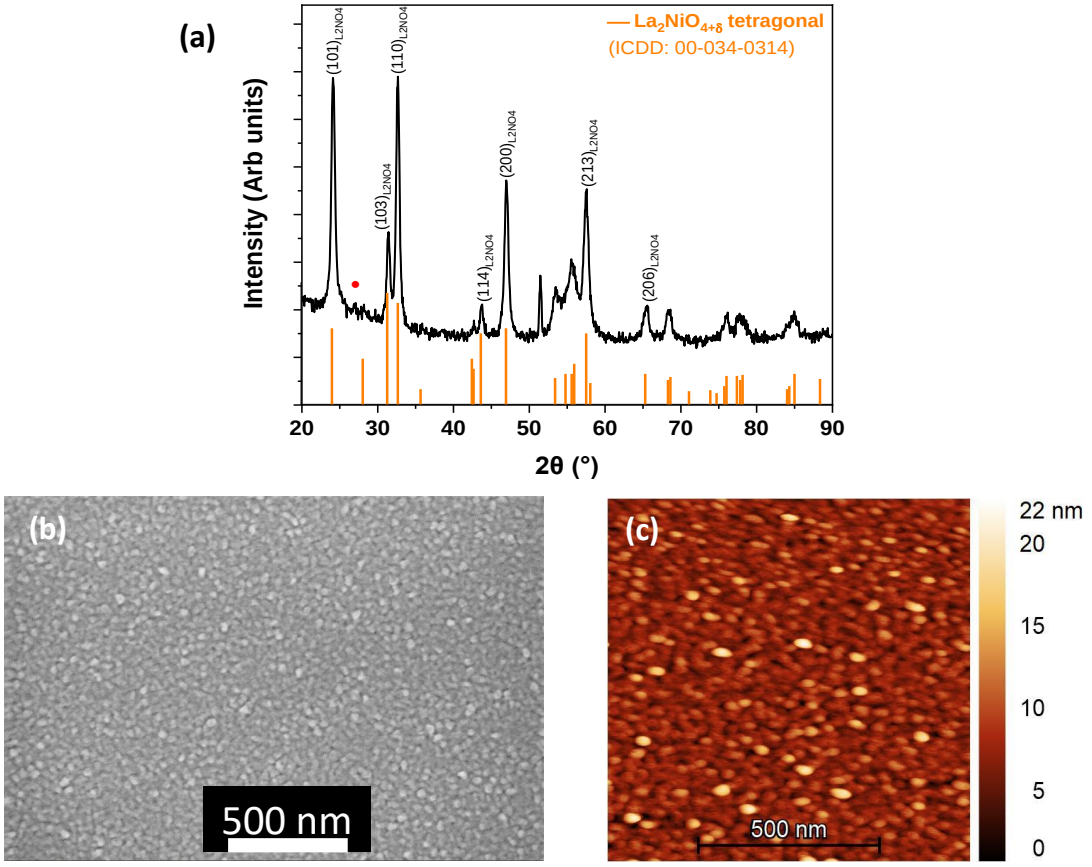

Figure 3.1: Structural characterization of the L2NO4 thin film grown on SN substrate: a) GIXRD pattern, the diffraction peak of La_2CO_5 impurity phase is marked by a red circle, orange drop lines correspond to $La_2NiO_{4+\delta}$ in tetragonal *I4/mmm* structure (ICDD: 00-034-0314) added for comparison. b) SEM surface image and c) AFM surface image.

3.1.2. Structural characterization of Ti\L2NO4/Pt memristive devices in planar configuration

To deposit the square top electrodes (Pt/Ti and Ti), a microfabrication process consisting of spin coating, laser lithography, metal evaporation and lift-off was carried out twice (for Pt/Ti and Pt electrodes), as described in subsection 2.3.1. After the microfabrication of the metal electrodes, TEM measurements were carried out across two lamellae prepared from a Ti\L2NO4/Pt device, as indicated in Figure 3.2a. The sketch of the device shows the inert electrode on the left side consisting of 100 nm of Pt placed on top of L2NO4, and on the right side, the active electrode consisting of 25 nm of Ti covered by 75 nm of Pt (capping layer). The two lamellae, located one at each electrode (lamellae 1 and 2), cross the whole device stack from the top electrodes to the SN substrate at the bottom.

To verify whether the device was well fabricated, STEM images coupled to EDX (Figure 3.2b and Figure 3.2c) were carried out. In both lamellae, L2NO4 film is continuous, dense and homogeneous. These observations indicate the high-quality growth of L2NO4 on the SN substrate and the successful fabrication of two types of electrodes (Pt/Ti and Ti) on the L2NO4 film. When looking at the EDX maps, sharp-chemical interfaces within the layer stacks were observed. No cation diffusion is observed between the layers during the deposition nor fabrication. However, a thin layer of SiO_2 (or SiO_xN_y) can be observed at the top of SN substrate. This can be explained by the oxidation of the SN substrate during the heating process in the reactor or during the deposition. However, this SiO_xN_y interlayer is not expected to affect the electrical properties of the memristive devices since both SiO_xN_y and Si_3N_4 act as insulating layers. Hence, when biasing the devices, the current is not expected to pass through the substrate but through the whole volume of the L2NO4 film. In addition, the presence of oxygen at the Ti/L2NO4 interface is detected, suggesting the presence of a TiO_x interlayer. This oxidation occurs spontaneously during the Ti top electrode evaporation and was also observed in previous studies carried out in the group on Ti\L2NO4/Pt memristive devices grown epitaxially on $SrTiO_3$ single crystal substrates [43, 45, 68] and in other oxide-based memristive systems [16, 35, 74].

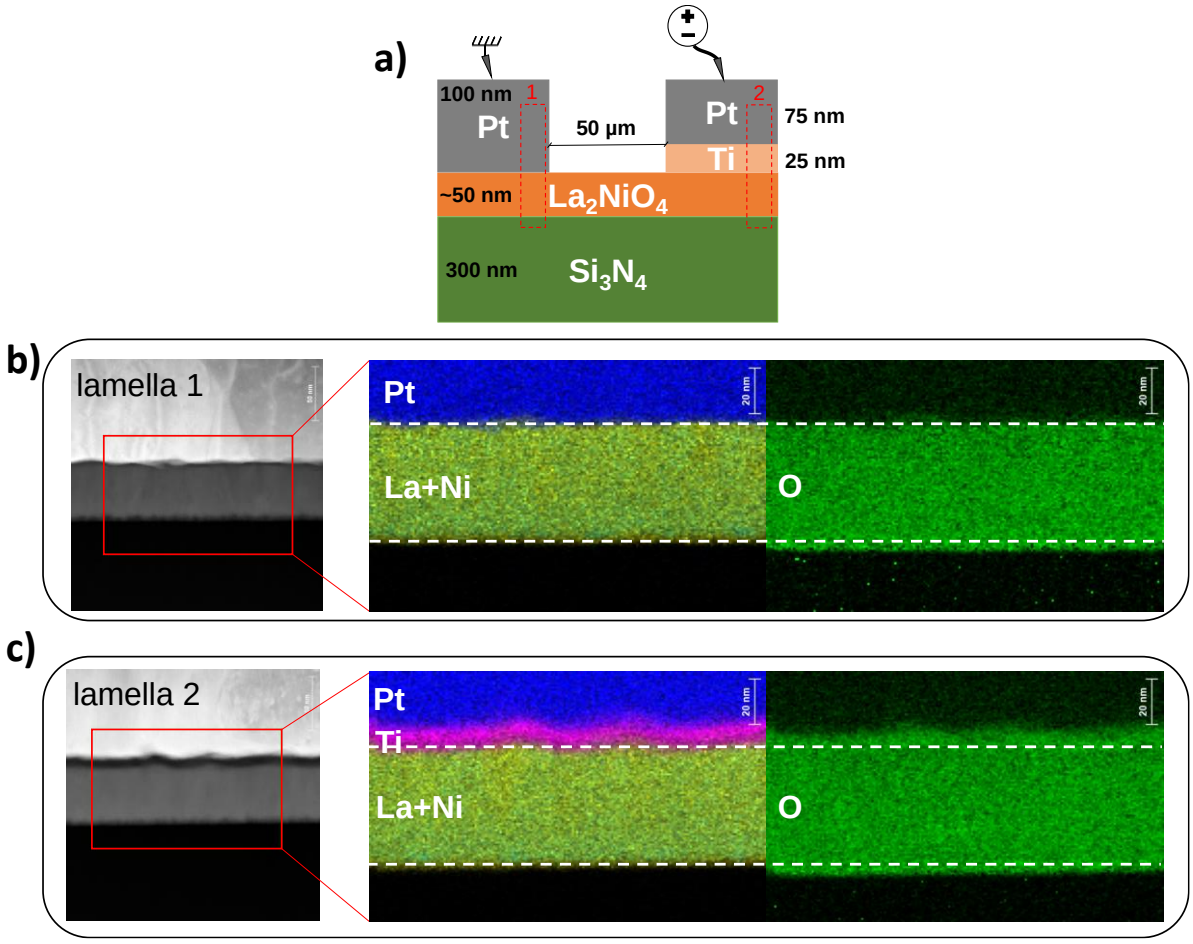

Figure 3.2: (a) Sketch of a Ti/L2NO4\Pt memristive device integrated on a SN substrate indicating the location of lamella 1 (Pt/L2NO4/SN stack) and lamella 2 (Pt/Ti/L2NO4/SN stack). STEM images and the corresponding EDX elemental maps color-coded as follows: Pt (blue), mixture of La and Ni (yellow) and O (green) for (b) lamella 1 and (c) lamella 2, showing the presence of oxygen in at the top of the SN layer and at the bottom of the Ti electrode.

The EDX chemical depth profiles of the two lamellae shown in Figure 3.3a and b (from bottom Si_3N_4 to top Pt layer) confirm the possible presence of a SiO_2 layer at the top part of SN substrate. Figure 3.3b shows that oxygen is present in the Ti electrode, mainly in the bottom half part, with a high oxygen concentration at the Ti/L2NO4 interface that then sharply decreases towards the Pt capping layer, confirming the presence of TiO_x.

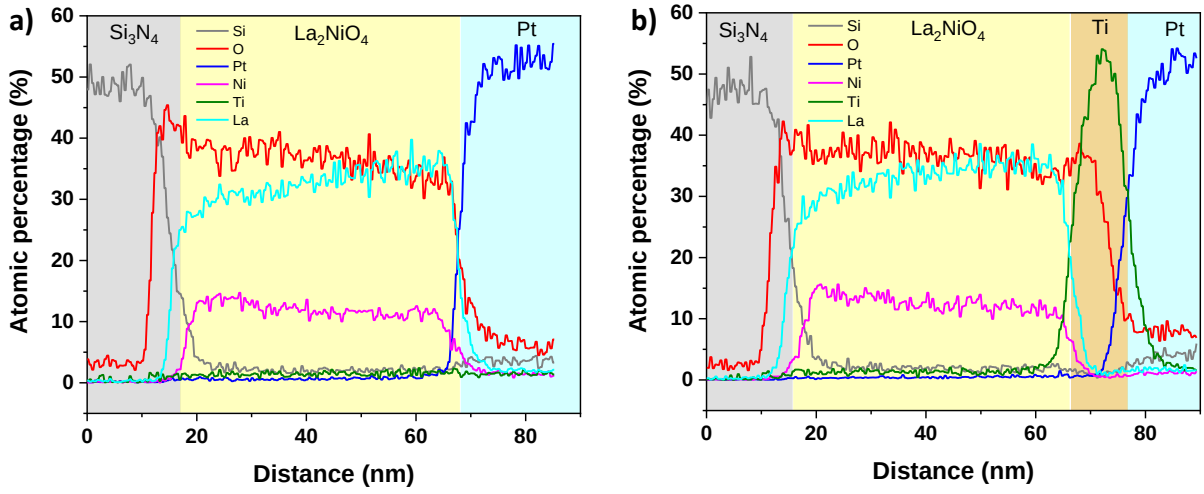

Figure 3.3: EDX elemental profiles of (a) lamella 1: Pt/L2NO4/SN stack and (b) lamella 2: Pt/Ti/L2NO4/SN stack, showing the presence of oxygen at the L2NO4/SN and Ti/L2NO4 interfaces.

3.1.3. Electrical characterization of Ti\L2NO4/Pt planar memristive devices

Ti\L2NO4/Pt memristive devices in planar configuration have different motifs, as shown in section 2.3.2. The L2NO4 resistivity (ρ_{L2NO4}) and the Pt/L2NO4 contact resistance (R_c) were obtained by transmission line measurements (TLM). The Pt bar-shaped contacts were prepared during the microfabrication at the same time as the Pt squared pads (region 1 of the sketch shown in Figure 2.3). The sketch shown in Figure 3.4a represents the cross-section of the pattern used in the test. The distance between two Pt electrodes (*d*) is varied for each measurement. Six resistances were measured corresponding to six devices (*d* values: 0.02, 0.05, 0.1, 0.2, 0.5 and 1.0 mm), as shown in Figure 3.4b. The TLM results with the fitting are shown in Figure 3.4c, yielding a contact resistance R_C of 74.5 ± 32.2 kΩ and the resistivity ρ_{L2NO4} of 4.2 ± 0.2 Ω.cm.

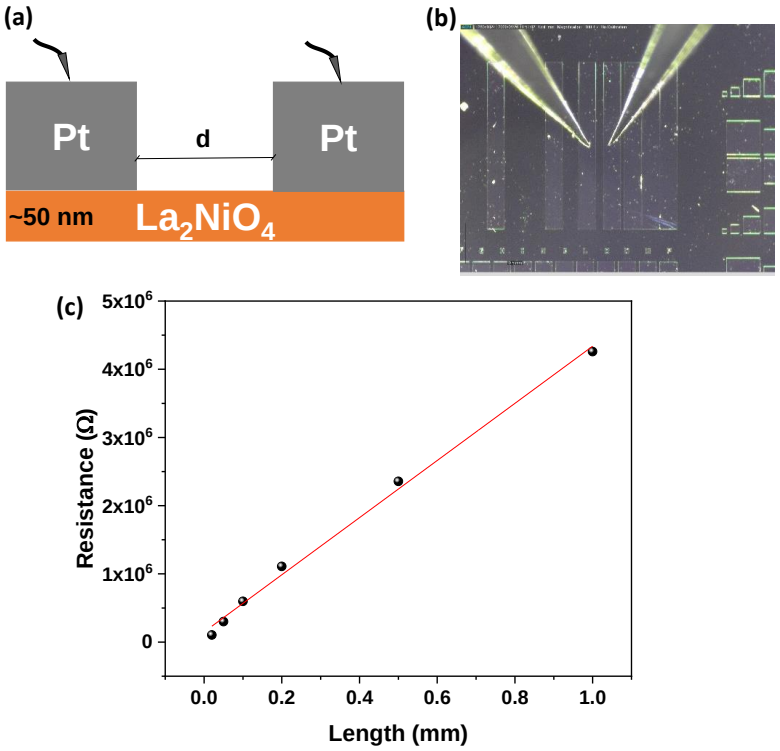

Figure 3.4: a) Sketch shows a side-view of the Pt contacts. The L2NO4 film thickness *e* is around 50 nm. b) Photo of Pt bar-shaped contacts separated by *d* (distance between Pt bars). The length of the Pt bar is 2 mm. c) The resistance vs length TLM results with a linear fit used to estimate the contact resistance and L2NO4 resistivity.

Here we focus on region 2 of Figure 2.3, and have selected devices of different electrode areas (*S*) (i.e., 400x400, 300x300, 200x200, 100x100 and 50x50 μm^2) with a fixed distance between electrodes of d = 50 µm. The initial resistance of these devices was measured by a unipolar read sweep (0 → 0.1 V), and calculated from the current measured at 0.1 V. Figure 3.5a shows that the initial resistance varies between 1 to 7 MΩ as the devices increase in size, as expected, with small device-to-device variability. Figure 3.5b presents the relationship between the average resistance value for each electrode size and the electrode area, showing the larger the electrode area, the lower the initial resistance obtained. A slope of -0.41 is obtained, revealing the initial resistance is weakly dependent on the electrode area. This effect can be explained because the contribution of the L2NO4 sheet resistance in the device's initial resistance is non-negligible. The total resistance of a planar memristive device was calculated using an equivalent circuit, as shown in Figure 3.5c. The resistance equations below illustrate how this approach reveals the dependence of each element on the device geometry. The resistance of the Ti and Pt electrodes is considered negligible as these metals have low resistivity. Thus, the total resistance of the device is simplified to the sum of four resistances (see Equation 5): Ti/L2NO4 interface ($R_{Ti/L2NO4}$),

reduced L2NO4 under Ti layer ($R_{L2NO4'}$), L2NO4 between two electrodes (R_{L2NO4}) and Pt/L2NO4 interface ($R_{Pt/L2NO4}$). If we consider the device size of L = 200 μm, the $R_{Pt/L2NO4}$ of around 1.9 kΩ and R_{L2NO4} of around 420 kΩ can be calculated by the Pt/L2NO4 contact resistivity and L2NO4 resistivity (estimated by TLM). Therefore, $R_{Pt/L2NO4}$ is negligible compared to the total resistance of the 200^2 μm^2 device (around 600 kΩ). Eventually, the device resistance mainly depends on the other three elements.

$$R_{total} = R_{Ti} + R_{Ti/L2NO4} + R_{L2NO4'} + R_{L2NO4} + R_{Pt/L2NO4} + R_{Pt}$$

Equation 5

Each of these resistances is related to the lateral electrode size in the following way:

$$R_{Ti/L2NO4} = \frac{\rho_{L2NO4}}{L^2} \rightarrow \propto R_{Ti/L2NO4} \propto \frac{1}{L^2}$$

$$R_{L2NO4'} = \frac{\rho_{L2NO4'} \cdot \frac{L}{2}}{e.L} \rightarrow R_{L2NO4'} \propto \frac{L}{L}$$

$$R_{L2NO4} = \frac{\rho_{L2NO4}.d}{e.L^2} \rightarrow R_{L2NO4} \propto \frac{1}{L}$$

The interface resistance ($R_{Ti/L2NO4}$) is inversely proportional to the electrode area (S or L^2). The second resistance ($R_{L2NO4'}$) does not scale with the electrode size (slope = 0). The reduced L2NO4 will be discussed in the next section. The third resistance (R_{L2NO4}) scales inversely with the electrode side (L). The obtained slope (-0.41) in log R - log S in Figure 3.5a seems to indicate that the elements governing the total resistance are those related to the L2NO4 film, as if it were the interface resistance (electrode area) contribution, a slope of -1 would have been expected.

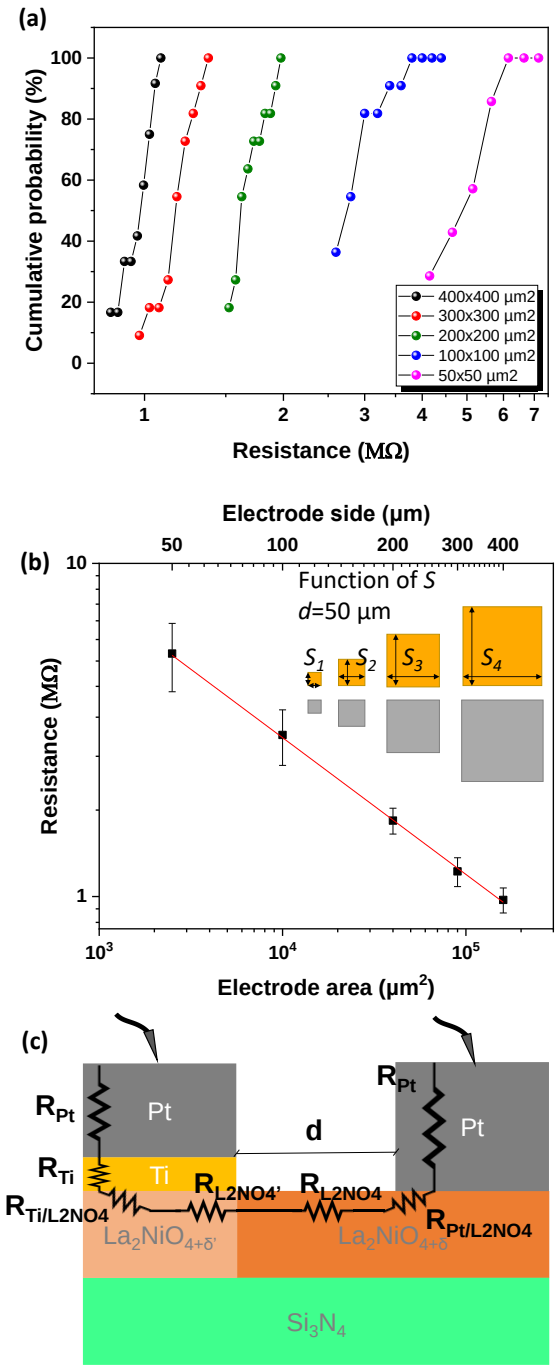

Figure 3.5: (a) Cumulative probability plot of the initial resistance state of the devices with different electrode pad size. (b) Electrode area dependence study for Ti\L2NO4/Pt memristive devices in planar configuration. (c) schematic of a Ti\L2NO4/Pt planar device with its equivalent circuit. $La_2NiO_{4+\delta'}$ stands for the reduced lanthanum-nikelate region under Ti electrode ($\delta' < \delta$).

The electrical characteristics of the Pt\L2NO4/Ti planar devices (in any *S*) were initially ohmic (see Figure 3.6) and did not show resistive switching (RS) properties, i.e. no hysteresis in the I-V curves

(three devices in the pristine state were measured). Hence, an additional heat treatment step was performed, i.e., rapid thermal annealing (RTA), consisting of a flash annealing (~30 s at 300 °C) of the device in an inert Ar atmosphere in order to partially oxidize the Ti electrode and/or homogenize the TiO_x layer (by supplying energy to the oxygen ions in L2NO4 to diffuse into Ti). After the RTA, rectifying I-V characteristics were obtained (see Figure 3.6). The effect and role of the RTA will be discussed in more depth in subsection 3.3.1.

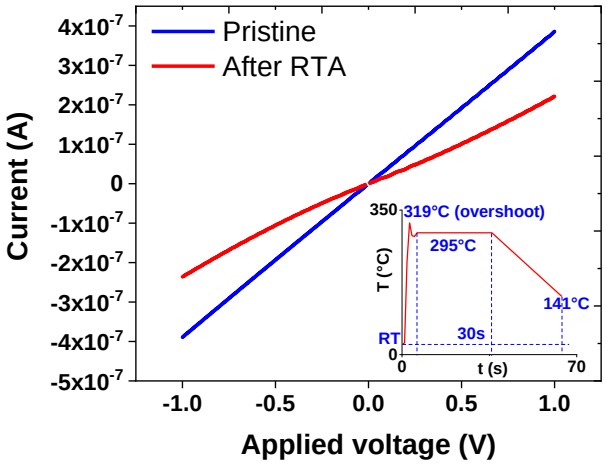

Figure 3.6: I-V characteristics of Ti\L2NO4/Pt planar memristive devices before and after the RTA process. The evolution of temperature during the RTA as a function of time is illustrated in the inset.

After RTA, hysteretic memristive behavior was observed in five Ti\L2NO4/Pt devices (out of the 13 measured devices). Figure 3.7a-d show the I-V and R-V characteristics of a representative device with d = 50 µm and S = 200x200 µm^2. The I-V curves suggest that the L2NO4-based memristor in planar configuration shows a small hysteresis from V_{max} = 10 V, and thus resistive switching I-V characteristics. With increasing V_{max} (i.e, 15 V, 20 V, 25 V, 30 V and 40 V), the ratio of HRS/LRS increases gradually from 1.24 (V_{max} = 15 V) to 1.66 (V_{max} = 40 V). In the last I-V sweep (at V_{max} = 40 V), the limit of sourcemeter was reached, thus the real voltage applied is smaller than 40 V. As will be later shown, the required operating voltage of Ti\L2NO4/Pt is higher than that of the devices in the vertical configuration (see subsection 3.2.3).

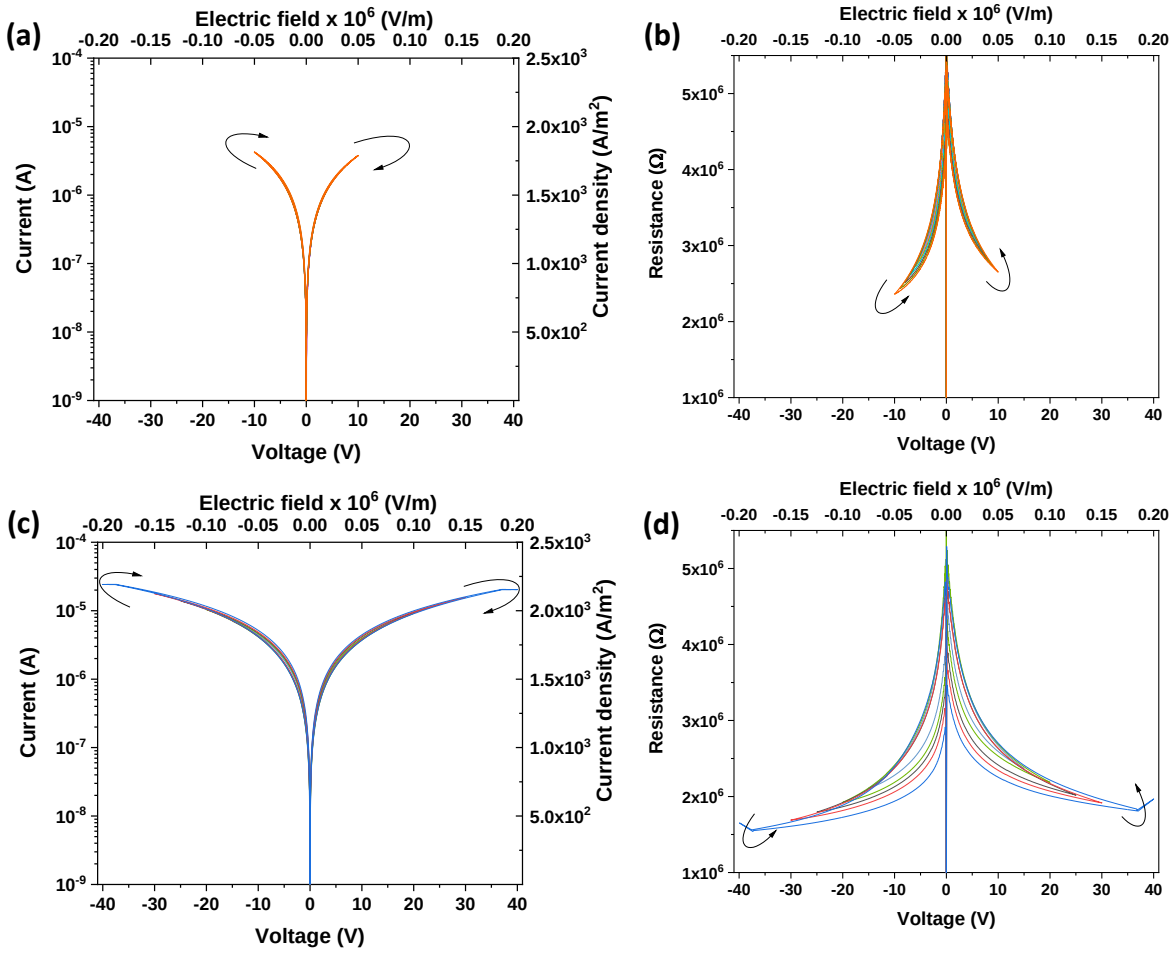

Figure 3.7: a), c) Current-voltage (I-V) and b), d) resistance-voltage (R-V) characteristics of a Ti\L2NO4/Pt memristive device carried out at a), b) small voltage amplitude range (1 – 10 V, step of 1 V) and c), d) large voltage amplitude range (15 – 30 V, step of 5 V and 40 V).

The RTA process is always necessary as an activation process to increase the device resistance and trigger the RS. This constitutes a disadvantage from the device performance point of view. Moreover, not all of the devices were 'activated' after the RTA. On top of that, the activated devices operate at very high voltages and with a small opening window. What is more, from the structural characterization, we observed L2NO4 is not pure with the current deposition conditions. That is why the following section is dedicated to the integration of L2NO4-based vertical memristive devices on platinized substrates (to serve as bottom electrodes), starting firstly with the optimization of thin films. Devices in the vertical configuration are expected to have smaller operation voltages due to the much smaller distance between electrodes that results in higher fields.

3.2. Ti/L2NO4/Pt vertical memristive devices integrated on platinized substrates

This section is adapted from the paper "$La_2NiO_{4+\delta}$-Based Memristive Devices Integrated on Si-Based Substrates", Thoai-Khanh Khuu, Gauthier Lefèvre, Carmen Jimenez, Hervé Roussel, Adeel Riaz, Serge Blonkowski, Eric Jalaguier, Ahmad Bsiesy and Mónica Burriel, *Adv. Mater. Technologies*, vol. 7, no. 11, p. 2200329, 2022. [70]

3.2.1. Optimization of L2NO4 growth on platinized substrates

Typically, high temperatures (≥ 650 ºC) are usually required for the deposition of crystalline layered oxide structures, which experimentally lead to the dewetting of the Pt bottom electrode. In order to avoid this limitation, in this work, we explore the optimization of the deposition conditions in two steps: i) by decreasing the deposition temperature (T) to find the best compromise to avoid the Pt dewetting while maintaining the crystallinity of the film, and ii) by varying the precursor solution composition to obtain stoichiometric, homogenous and highly dense L2NO4 films. The deposition conditions used for the two optimization series are detailed in Figure 3.8. In the first step, the La/Ni ratio in the precursor solution (R) was fixed to 5.00, while the deposition temperature T was varied from 650 °C to 600 °C, with a step of 25 °C. Secondly, T was fixed at 600 °C and R was varied from 5.00 to 4.00, with steps of 0.25. In this section, the frequency of 1 Hz and 2000 pulses of the injection were used, as in the previous section.

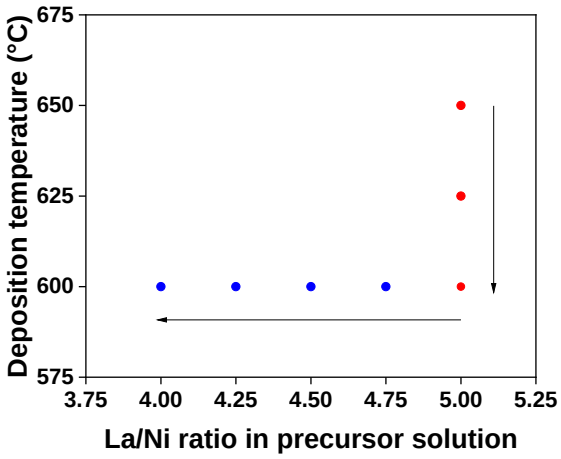

Figure 3.8: L2NO4 thin film growth conditions used for the optimization series by varying the temperature and the precursor solution composition

In addition, to be embedded in realistic devices in the future, the fabrication process should be CMOS-BEOL (back-end-of-line) compatible where the temperature is required to be lower than 450 °C. To

overcome this challenge, the deposition of amorphous L2NO4 thin film at 400 °C followed by a fast laser crystallization treatment [75-77] is considered as a promising approach. Another route to avoid heating above 450 °C would be to build amorphous L2NO4-based memristive devices. However, as the functional properties (electronic and ionic transport) of the amorphous films are expected to be different, their memristive properties might largely differ from the crystalline counterpart. The effects of the deposition temperature and solution composition on the growth of L2NO4 films will be discussed in the following sections.

3.2.1.1. Effect of the temperature on the growth of polycrystalline L2NO4 films

The influence of the deposition temperature in the film composition, crystallinity and morphology is assessed for deposition temperatures between 600 and 650 °C with a constant R of 5.00 (red dots in Figure 3.8). These sample's La/Ni ratios were measured by the electron probe microanalysis (EPMA) technique, which increase with increasing deposition temperature, as shown in Figure 3.9a. A clear linear relationship between these two parameters was obtained. The growth rates are 1.3 nm/min and 1.5 nm/min for depositions at 600 °C and 650 °C, which result in films of 43 ± 3 nm and 50 ± 3 nm by using 2000 pulses, respectively.

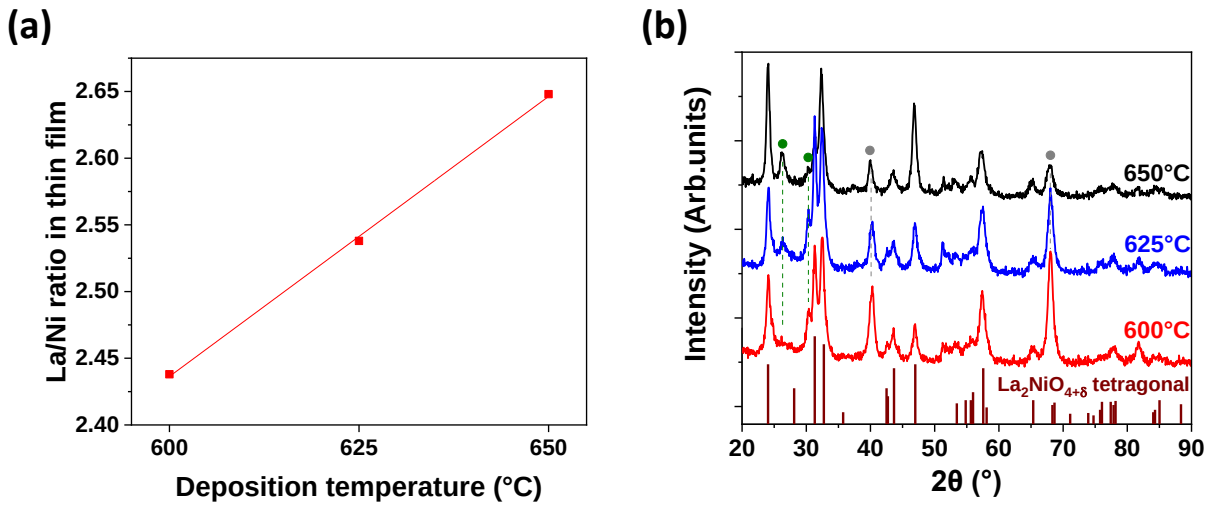

Figure 3.9. a) La/Ni atomic ratio measured by EPMA for the L2NO4 films as a function of the PI-MOCVD deposition temperature. b) GI-XRD patterns of L2NO4 films deposited on Pt at different temperatures using a La/Ni ratio of 5.00 in the precursor solution. The position of the tetragonal *I4/mmm* peaks for $La_2NiO_{4+\delta}$ (ICDD: 00-034-0314) has been added at the bottom for comparison. The positions for Pt peaks (gray dots) and impurity La_2CO_5 phase (green dots) are indicated.

The grazing incidence X-ray diffraction (GI-XRD) patterns obtained for these three films are shown in Figure 3.9b. The Pt substrate peaks are indicated by gray dots. The main diffraction peaks observed are

attributed to the L2NO4 tetragonal phase (space group *I4/mmm*, ICDD: 00-034-0314) in polycrystalline form (randomly oriented), with small peaks corresponding to the La_2CO_5 phase. The intensity of the impurity phase decreases as the deposition temperature decreases, in agreement with the decrease of La/Ni ratio in films (Figure 3.9a). Moreover, an amorphous thin film can be obtained by lowering the deposition down to 500 °C, while at 550 ºC a mixture of the L2NO4 and $La_3Ni_2O_7$ phases is obtained, with a contribution of the La_2CO_5 phase (see Figure 3.10).

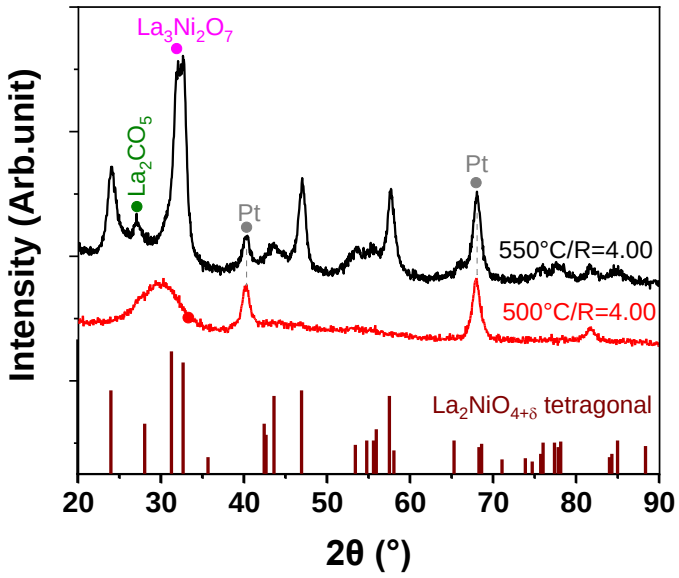

Figure 3.10: GI-XRD patterns of L2NO4 films deposited on Pt at 550 °C (black diffractogram) and 500 °C (red diffractogram) using a La/Ni ratio of 4.00 in the precursor solution. The position of the tetragonal *I4/mmm* peaks for $La_2NiO_{4+\delta}$ (ICDD: 00-034-0314) has been added at the bottom for comparison. The positions for Pt peaks (gray dots), undesired phases: La_2CO_5 (green dots) and ($La_3Ni_2O_7$) are indicated.

The top-view scanning electron microscopy (SEM) images of films deposited at 650, 625 and 600 °C are shown in Figure 3.11a, Figure 3.11b and Figure 3.11c, respectively. Their surface morphology is quite similar, formed by randomly oriented grains with small grain sizes of the order of 25 - 45 nm. All films are homogeneous, polycrystalline and dense. Moreover, no cracking nor pinholes were observed for any of the samples. It can be seen that the grain size is largest for the 650 °C deposition and decreases for the lower deposition temperatures.

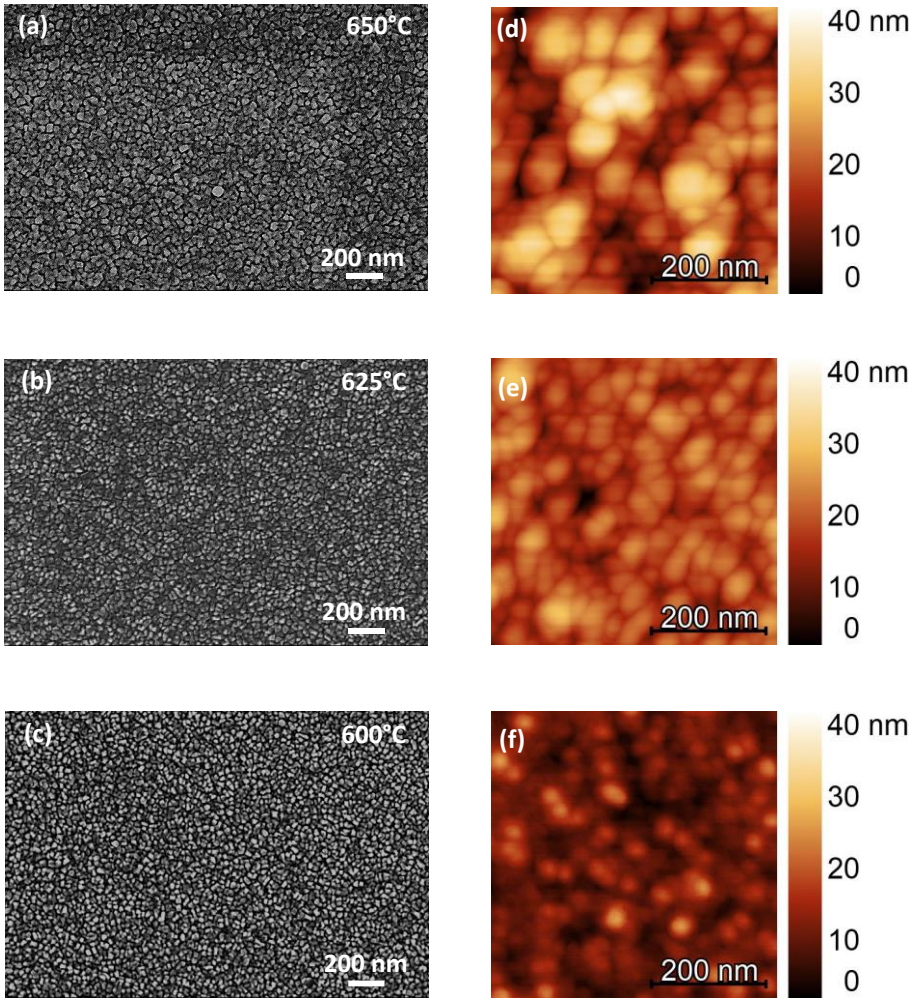

Figure 3.11. a-c) SEM top-surface and d-f) AFM images of the L2NO4 films deposited on Pt at 650 °C, 625 °C and 600 °C, respectively.

The corresponding atomic force microscopy (AFM) images of these L2NO4 samples can be found in Figure 3.11d, Figure 3.11e and Figure 3.11f. The sample deposited at 650 °C presents larger particle sizes (RMS of 42.1 nm), compared to the films deposited at lower temperatures. At this temperature, the small grains cluster to form larger ones, resulting in a film with a larger roughness. At lower temperatures, the size of the individual particles is similar (RMS of 23.4 - 24.0 nm), and smaller than that observed for the sample grown at 650 °C, in agreement with the SEM observations. The L2NO4 films deposited at 625 °C and 600 °C are flatter, as measured by the RMS surface roughness, which decreases from 6.6 to 3.4 nm and, when the temperature is reduced from 650 °C to 600 ºC (see Table 3.2). The higher roughness of the L2NO4 film deposited at 650 °C can be explained by the L2NO4 grain coarsening and by the evolution of Pt grains during the deposition under a relatively high temperature. The improvement (decrease) of surface roughness when decreasing the deposition temperature is also

confirmed by the scanning transmission electron microscopy (STEM) cross-sectional images of L2NO4 films deposited at 600 °C (Figure 3.14a) and at 650 °C (Figure 3.15)

Table 3.2. RMS surface roughness and average grain size of the L2NO4 films grown at different temperatures

Deposition temperature (°C)	RMS (nm)	Average grain size (nm)
650	6.6	42.1
625	3.6	24.0
600	3.4	23.4

3.2.1.2. Effect of the solution composition on the growth of polycrystalline L2NO4 films

Due to the smaller film roughness and flatter surface, 600 °C was selected as the deposition temperature to grow the L2NO4 films. However, with R = 5.00 the films still present the secondary La_2CO_5 phase (red diffractogram, Figure 3.9b). In order to improve the film purity at this temperature, several films were prepared by varying R values from 4.00 to 5.00 (blue dots in Figure 3.8). The La/Ni ratios in thin film of these samples obtained by EPMA, together with the GI-XRD patterns of the different films are shown in Figure 3.12a and Figure 3.12b, respectively. By reducing R from 5.00 to 4.50, it is possible to eliminate the presence of impurities, which is confirmed by the decrease in intensity and absence of the La_2CO_5 peaks. Only the reflections of the L2NO4 tetragonal phase are observed in the films deposited at 600 ºC using R values of 4.25 and 4.00. However, the film deposited at the R of 4.00 in the source exclusively gives a La/Ni ratio of 1.95 in the L2NO4 film, which is close to the desired value of 2.00 for the highly pure L2NO4 phase. Therefore, the optimized conditions which allowed preparing high-quality polycrystalline and flat L2NO4 films on Pt, without dewetting, are: deposition temperature of 600 °C and R of 4.00. These deposition conditions were selected for the film growth and subsequent vertical memristive device fabrication.

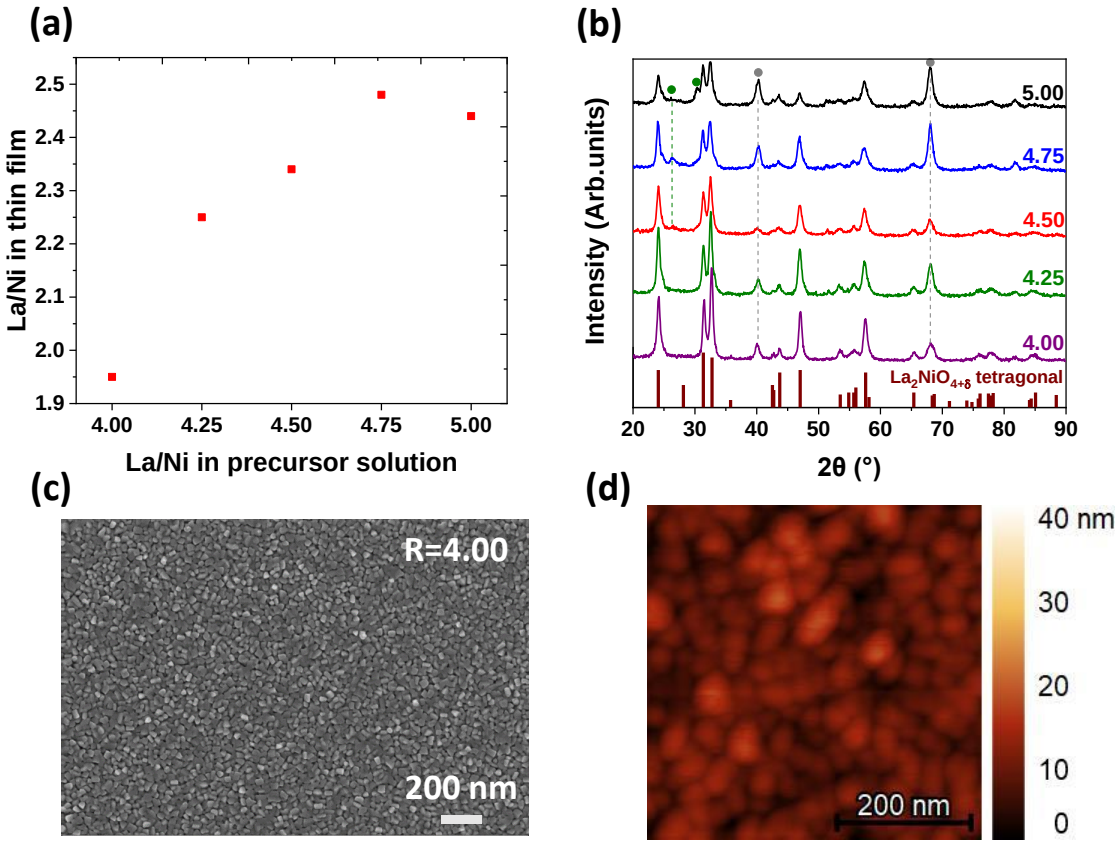

Figure 3.12. a) La/Ni atomic ratio in the L2NO4 films grown at 600 °C vs La/Ni atomic ratio in the precursor solution. b) GI-XRD patterns of L2NO4 films deposited on Pt substrate at different precursor concentration ratios. The position of the tetragonal *I4/mmm* peaks for $La_2NiO_{4+\delta}$ (ICDD: 00-034-0314) has been added at the bottom for comparison. The positions for Pt peaks (gray dots) and for the peaks corresponding to the La_2CO_5 phase (green dots) are indicated. c) SEM and d) AFM top-view image of optimized L2NO4 film deposited on Pt substrate (at 600 °C with R of 4.00).

In terms of morphology, by decreasing the R-value, no major difference is observed between the samples, as shown in the SEM images of those samples, displayed in Figure 3.13a-d.

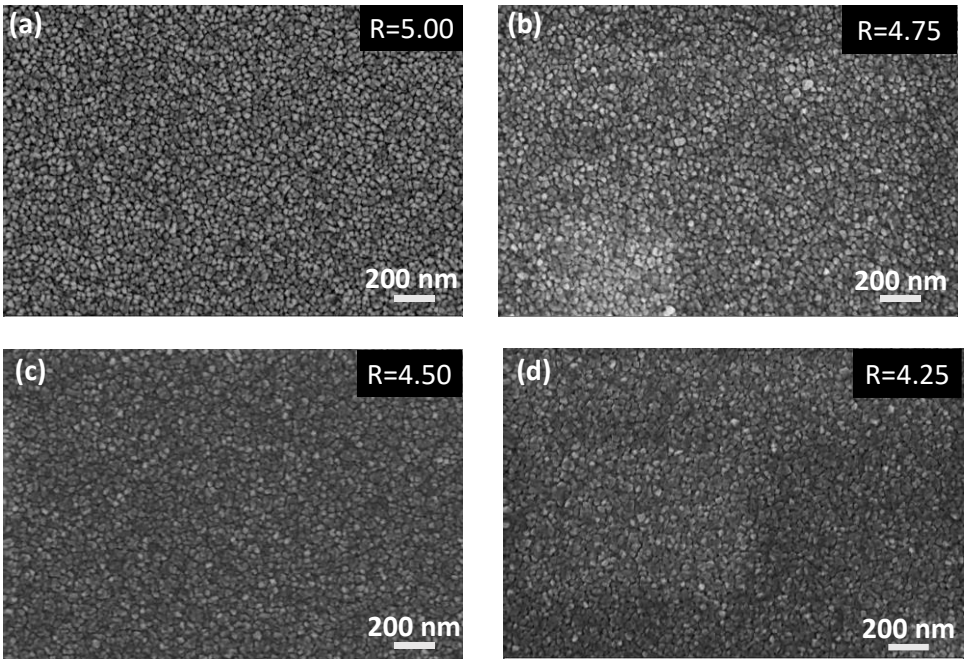

Figure 3.13: SEM top-view images of four L2NO4/Pt samples deposited varying the La/Ni ratio (R) in the precursor solution. a) R = 5.00, b) R = 4.75, c) R = 4.50, d) R = 4.25.

The optimized film (i.e., deposition temperature at 600 °C with R of 4.00) was then used to construct the L2NO4-based memristive devices. SEM and AFM top-view images of the optimized film are shown in Figure 3.12c and Figure 3.12d, respectively. The morphology observed by SEM is similar to that of the film grown at 600 °C with R of 5.00 (shown in Figure 3.11c), suggesting that the La/Ni ratio in the precursor solution does not have an effect on the morphology of the film. An RMS value of 2.8 nm and average grain size of 23.7 nm are calculated from the AFM measurements, which are in agreement with those reported for the films deposited at 600°C (Table 3.2).

3.2.2. Microstructural characterization of the Ti/L2NO4/Pt memristive devices in vertical configuration

To build the memristive devices, electrodes consisting of a 25 nm of Ti covered by a 75 nm of Pt, were evaporated on top of the optimized L2NO4 film. In order to study the quality of the device heterostructure, a lamella across the whole stack (from the Pt layer of the top electrode to SiO_2 layer of the substrate) was prepared by focused ion beam (FIB) milling and the STEM image of the lamella is shown in Figure 3.14a. Continuous dense Ti and Pt layers on top of the L2NO4 thin film can be observed, with sharp L2NO4/Ti and Ti/ Pt interfaces, and without dewetting nor Pt diffusion. The grains of the L2NO4 layer increase in size with increasing film thickness (V-shaped grains, as indicated by the red dashed-line in Figure 3.14a). Therefore, as can be observed in the image, the number of grains per

100 nm in-plane length increases from approximately 6-8 grains at the bottom part to 4-5 grains at the top region. The size of the top grains is thus in good agreement with the AFM results (i.e., 23.7 nm) shown in Figure 3.12d. Besides, 1 to 2 grains of varying length can be measured along the surface normal direction within 43-nm thick L2NO4 layer. The chemical composition of the lamella was characterized by energy-dispersive X-ray spectroscopy (EDX), as shown by the EDX atomic depth profile (Figure 3.14b) and EDX maps (Figure 3.14c) of the lamella cross-section. These results show, from top to bottom, a clearly-delimited Pt capping layer, a continuous Ti top electrode, the L2NO4 memristive oxide layer and the Pt bottom electrode, with sharp interfaces between the layers of the heterostructure and a uniform La and Ni composition within the L2NO4 film thickness. In addition, the presence of oxygen within the Ti layer can be detected. This observation suggests the spontaneous formation of a TiO_x interlayer when Ti electrode is put in contact with L2NO4 film, prior to any thermal treatment process.

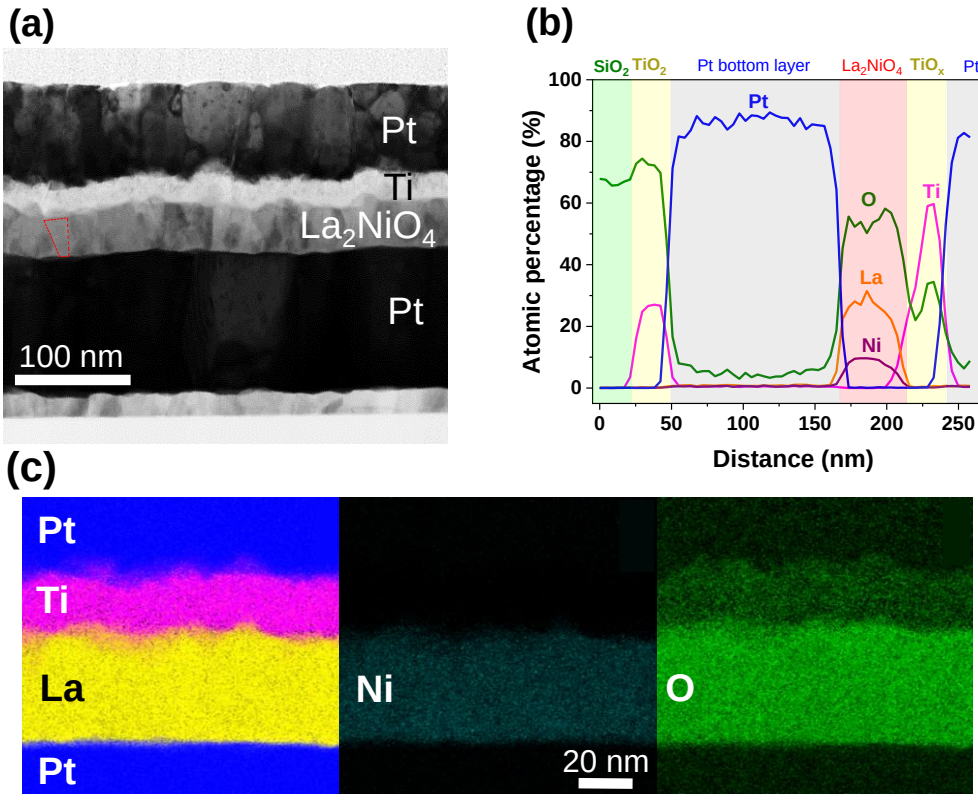

Figure 3.14. Cross-sectional transmission electron microscopy of Ti/L2NO4/Pt memristive device: a) STEM image, b) EDX atomic depth profile, c) EDX elemental maps for Ti (pink), O (green), La (yellow), Ni (cyan) and Pt (blue) showing the presence of oxygen within the top Ti electrode.

STEM cross-section characterization of Ti/L2NO4/Pt device before the optimization (Figure 3.15) proves the L2NO4 roughness has been improved by decreasing the deposition temperature. Besides, the

film roughness also strongly depends on the substrate used. When comparing the crossectional STEM images of non-optimized L2NO4 thin films prepared by the same conditions on different substrates (L2NO4/SN in Figure 3.2 vs L2NO4/Pt in Figure below), the L2NO4/SN sample seems to be flatter, and the roughness could be transferred from Pt to L2NO4 as Pt starts being unstable at 600 °C [78] even though the dewetting was not detected.

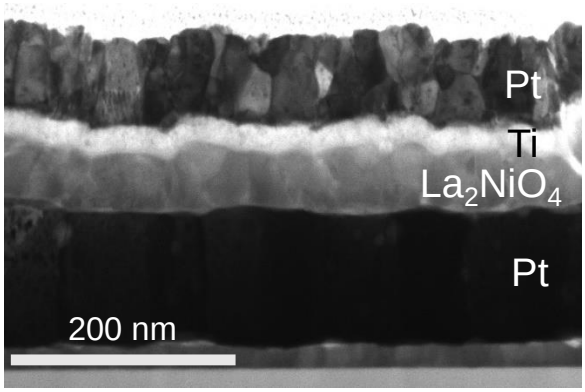

Figure 3.15: STEM cross-sectional image of the Ti/L2NO4/Pt heterostructure before the optimization (i.e., deposition temperature of 650 °C and R of 5.00) showing a rough L2NO4 film.

3.2.3. Memristive characteristics of the Ti/L2NO4/Pt devices in vertical configuration

To study the RS behavior of the Ti/optimized L2NO4/Pt devices, beforehand the initial resistance states (IRSs) were measured, giving an average value of 434 Ω for the 20^2 μm^2 devices. The I-V characteristics were recorded by applying symmetric bipolar voltage sweeps (0 V → +Vmax → 0 V → -Vmax → 0 V). The HRS and LRS were read at +0.01 V after each half-sweep. Firstly, an initialization process consisting of DC sweeps of increasing voltage amplitude (Figure 3.16a-d, plotted as R-V curves) was carried out to increase the Ti/L2NO4/Pt device to a higher resistance state. Then the device operates at ±3 V, as shown in Figure 3.16e (R-V plot). The first three sweeps at ±1 V show non-linear and rectifying electrical properties (see Figure 3.16a) with a resistance of 1 kΩ (read at low voltage).

b shows that the resistance increases during the next three sweeps at $|V_{max}|$ = 2 V and a small hysteresis starts to appear, however, the two resistance states are not clearly distinguishable. A larger hysteresis with two noticeably different states is obtained for the Ti/L2NO4/Pt device when cycled between ±2.5 V (Figure 3.16c). Figure 3.16d and Figure 3.16e show continuous R-V curves with gradual transitions between states at $|V_{max}|$ = 2.75 V and $|V_{max}|$ = 3 V, respectively, with a HRS/LRS ratio of around 11 for both working voltages. Thus it can be concluded that the Ti/optimized L2NO4/Pt devices can operate using $|V_{max}|$ in the range of 2.5-3 V. In all cases, the RESET process takes place at positive voltages and

the SET process at negative voltages. A continuous gradual change in resistance during both the SET and RESET processes is observed, without any abrupt jumps, which is considered as a prerequisite of analogue-type device operation.

The observed RS is also compatible with a valence change mechanism taking place at the L2NO4/Ti interface. By the application of a positive voltage to the Ti electrode, the drift of oxygen ions would induce the further oxidation of the TiO_x interlayer, and the concomitant resistance increase. This oxidation would be reversed by the application of a negative voltage, leading to the reduction of the TiO_x interlayer and re-oxidation of the L2NO4 film. In addition, these results are in good agreement with the gradual memristive behavior previously obtained on Pt/(epitaxial) L2NO4\Ti planar devices [43, 45], which has now been successfully reproduced in vertical configuration for reduced dimensions devices and using lower operation voltages.

To verify the interfacial switching observed on Ti/optimized L2NO4/Pt devices, the electrode area dependence test was carried out. The HRS and LRS states were read at 0.01 V after +3 V sweep and -3 V sweep, respectively, for different electrode sizes (i.e., 20^2 µm^2, 50^2 µm^2, 100^2 µm^2). Three devices were measured for each pad size, except for the 100^2µm^2 electrode, for which only one device was measured because most of the 100^2 µm^2 suffered a breakdown at this operation voltage. This is most likely due to the presence of a leakage current resulting from the presence of larger amount of defects in the larger device size, as often observed in the literature for other materials [79]. The average value of HRS and LRS are plotted as a function of contact area in Figure 3.16f. This plot shows a clear decrease in HRS and LRS when increasing the pad size. The slopes are -1.66 and -1.05 for HRS and LRS, respectively. As the resistance-dependence of electrode area is a typical characteristic of interfacial RS, the Ti/optimized L2NO4/Pt memristors thus present interface-type RS.

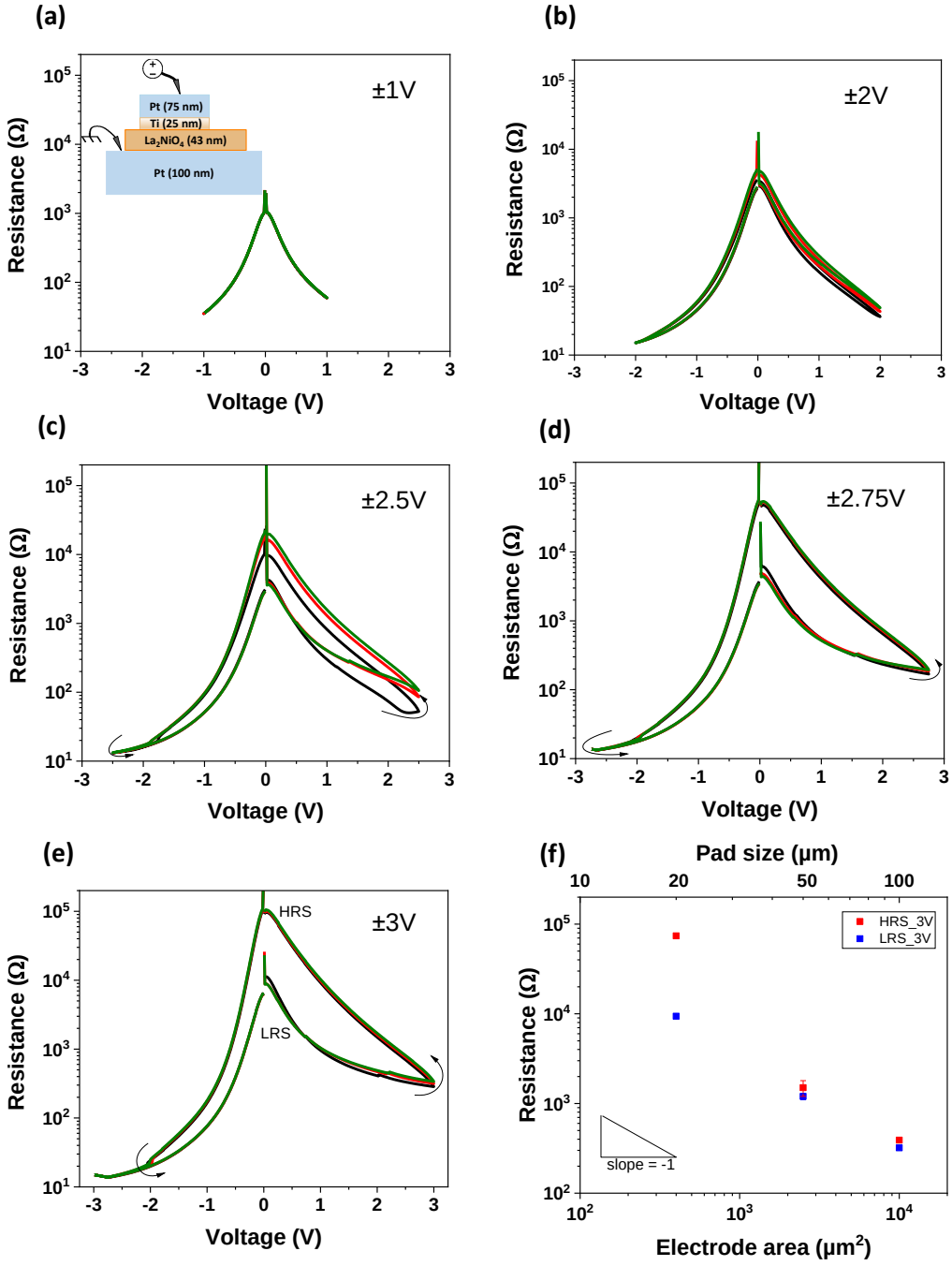

Figure 3.16: R-V characteristics of a Ti/optimized L2NO4/Pt device (size of device: 20^2 μm^2, sketch shown as an inset) during the initialization process: sweep cycles sequence 0 V → +V_{max} → 0 V → -V_{max} → 0 V for a) $|V_{max}|$ = 1 V, b) $|V_{max}|$ = 2 V, c) $|V_{max}|$ = 2.5 V, d) $|V_{max}|$ = 2.75 V. e) R-V characteristics at $|V_{max}|$ = 3 V after the initialization process of the same Ti/L2NO4/Pt device and f) Electrode-area dependence resistance for $|V_{max}|$ = 3 V (average of 3 devices for the small pad sizes, while only 1 device is presented for the largest pad size). 1st sweep: black, 2nd sweep: red, 3rd sweep: green.

To compare the switching properties of memristive devices based on non-optimized L2NO4 films and the previously shown results on the optimized L2NO4 films, beforehand, the IRS of the 20^2 μm^2 devices was measured, giving the average value of 48.8 kΩ. Then, standard I-V sweeps with different $|V_{max}|$ were carried out on the Ti/non-optimized L2NO4/Pt devices. Figure 3.17a presents the non-linear electrical properties with a resistance of roughly 87 kΩ. Next, the sweeps at ±2 V, ±2.5 V, ±2.75 V, ±3 V were carried out. The sweeps at ±3 V are displayed (Figure 3.17b), showing that, by increasing the $|V_{max}|$, the device resistance decreases. In the positive branch, the hysteresis starts to appear with eightwise switching sense. An abrupt change in resistance to lower values hereafter referred to as "forming" step, can be observed at ±3.25 V sweep, as indicated in Figure 3.17c. After the "forming", the device can operate at a lower working voltage range ($|V_{max}|$ = 2.75 V) as shown in Figure 3.17d, with a HRS/LRS ratio of 6 in this case. We propose that, the much higher IRS measured for the non-optimized L2NO4 devices compared to the optimized L2NO4 devices (48.8 kΩ vs 434 Ω, respectively) could be due to the presence of the La_2CO_5 impurity phase observed by XRD, and that the abrupt resistance change could be due to the breakdown of this impurity blocking layer, reaching then the standard operation cycles of the optimized L2NO4-based devices. It should be noted that this process is not the classical electroforming occurring in filamentary VCMs, where a conducting filament is created within the switching layer.

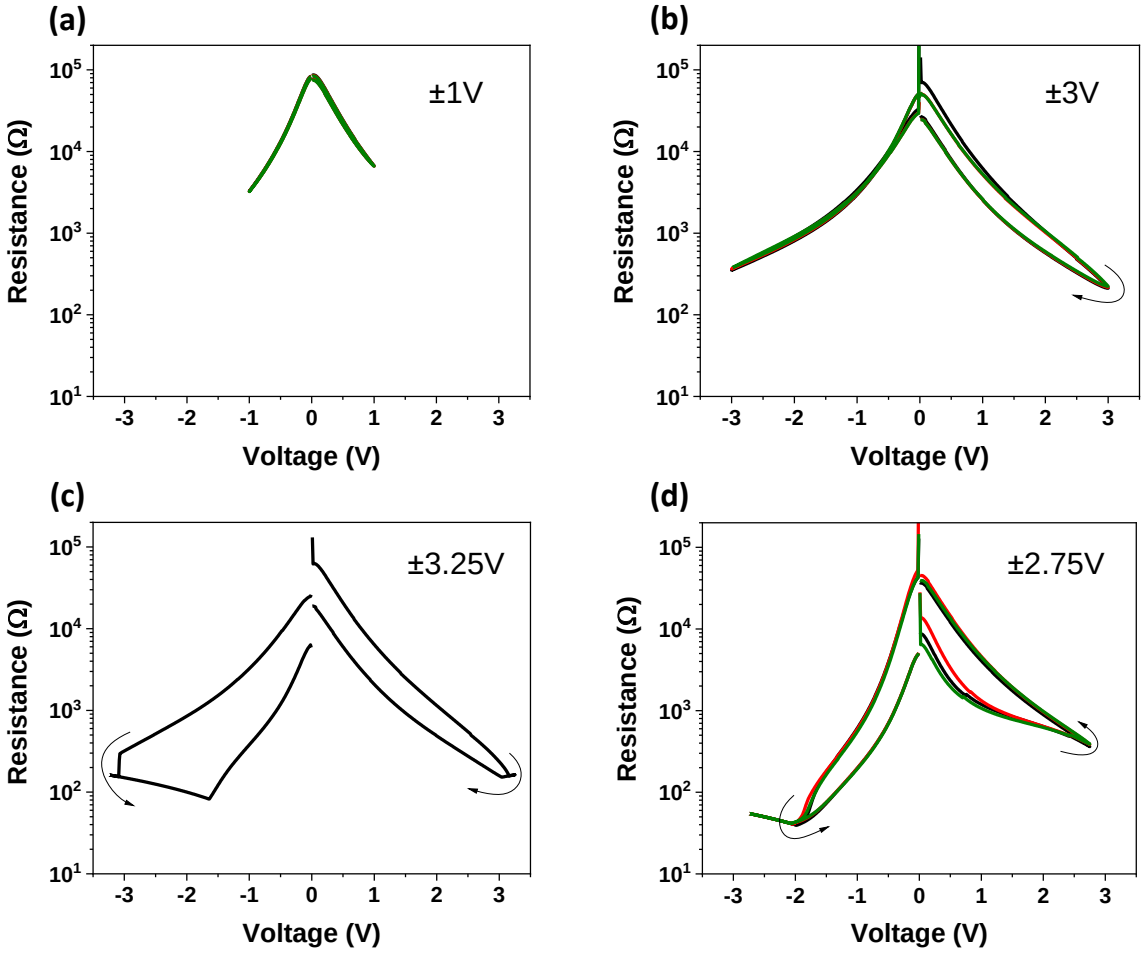

Figure 3.17. R-V characteristics of Ti/non-optimized L2NO4/Pt device in 20^2 μm^2 size a-b) before the forming, c) at the forming, d) after the forming. Sweep cycles following the sequence 0 V → $+V_{max}$ → 0 V → $-V_{max}$ → 0 V for a) $|V_{max}|$ = 1 V, b) $|V_{max}|$ = 3 V, c) $|V_{max}|$ = 3.25 V, d) $|V_{max}|$ = 2.75 V. 1st sweep: black, 2nd sweep: red, 3rd sweep: green.

In order to study the RS performance, another 20^2 μm^2 Ti/optimized L2NO4/Pt memristor was selected to test the data retention and the endurance. Figure 3.18a shows the retention of the device measured after an initialization process followed by 5 cycles at ±2.5 V. A decrease of the HRS from 43.4 to 24.2 kΩ (56%) and an increase of LRS from 5.9 to 10.0 kΩ (169%) are observed after 12 hours. The dynamic resistance relaxation of HRS was previously observed in Ti\200µm-L2NO4/Pt devices and is attributed to the oxygen mass transport between p-type L2NO4 and n-type TiO_x [43]. Figure 3.18b shows the resistances (read at 0.01V after ±2.5 V sweep) as a function of the number of sweeps (500 consecutive sweeps) showing no overlap of the HRS and LRS states.

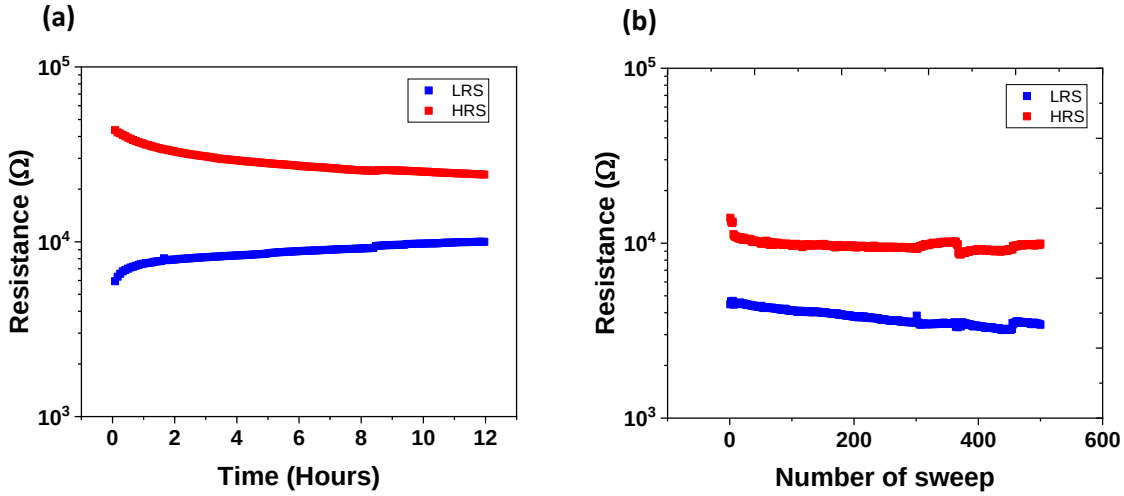

Figure 3.18. a) Resistance vs time measured for the HRS (red square dot) and the LRS (blue square dot) with a reading amplitude of 0.01 V. Resistance were measured every 5 minutes. b) Endurance plot recorded by measuring 500 consecutive sweeps. The HRS and LRS were programmed by the sweeps at ±2.5 V.

3.3. Role of a rapid thermal annealing (RTA) on the Ti/L2NO4/Pt vertical devices

In Section 3.1, the memristive characteristics obtained on L2NO4-based memristive devices in planar configuration using Ti as top electrode were described, for which a RTA was required prior to operation. Only one sample of planar devices was fabricated.

Section 3.2, on the other hand, presented the standard memristive characteristics of the smallest vertical devices (20x20 μm^2), without an additional RTA. In this subsection, the role of RTA will be discussed for the case of the standard vertical Ti/L2NO4/Pt devices in which the L2NO4 films were prepared in optimized deposition conditions (600 °C, R=4.00). Three standard samples (45 nm of L2NO4) were fabricated using Ti as top electrodes to study the effect of the RTA. For all of these samples, only the small devices (20x20 μm^2 and 50x50 μm^2) have high enough initial resistance values (from a few hundred ohms to a thousand ohms) with rectifying behavior in pristine state. Therefore, typically there is no need for a RTA process to trigger the RS on small devices, as seen in section 3.2.3. However, the rest of the devices (larger sizes) exhibited ohmic-like behavior and their initial resistances were very small (a few tens of ohms). We aimed to activate these large devices (increase their IRs) and further obtain RS characteristics on them. Thus, the RTA strategy was carried out for the three standard samples.

3.3.1. Electrical characteristics of the Ti/L2NO4/Pt devices after RTA

The detailed conditions of RTA carried out on these samples are reported in Table 3.3.

Table 3.3: Details of RTA conditions used to activate the Ti/L2NO4/Pt devices

Sample	**RTA conditions (T, t) (°C, s)**	**Results after the last RTA for 50^2 μm^2 size devices**
L2NO4-03-Ptd	(334, 30) (325, 45) (340, 45) (375, 45) (370, 45) (400, 45) (400, 120)	IR : increased Hysteresis : yes
L2NO4-08-Pta	(400, 120) (325, 180) (375, 180) (375, 600)	IR : increased Hysteresis : no
L2NO4-09-Ptb	(325, 300) (325, 300) (325, 300) (357, 300) (357, 600)	IR : increased Hysteresis : no

Unfortunately, none of the large devices (100^2, 150^2 and 200^2 μm^2) presented hysteretic behavior after the RTA. Thus, in this section, we again focus on the memristivity behavior of the small devices. The I-V and R-V characteristics of one of the 50^2 μm^2 Ti/L2NO4/Pt devices (45 nm of L2NO4) from sample L2NO4-03-Ptd, which was exposed to a fast anneal at approximately 400 ºC for 120 s in Ar atmosphere, are shown in Figure 3.19a-b. It can be observed that the IR of the device increased by three orders of magnitude (from 0.2 kΩ to 2 MΩ) after the RTA process, which can be attributed to the further oxidation of the TiO_x interlayer and possible reduction of the L2NO4 film. The RS response of the Ti/L2NO4/Pt devices after the RTA process was confirmed by symmetric bipolar voltage sweeps, 0 V → +2.75 V → 0 V → -2.75 V → 0 V (see Figure 3.19b). Bipolar anti-clockwise I-V characteristics were obtained. Gradual RESET and SET processes take place at +2.75 V and -2.75 V, respectively. Two discernable resistance states were obtained with a HRS/LRS ratio of 5.

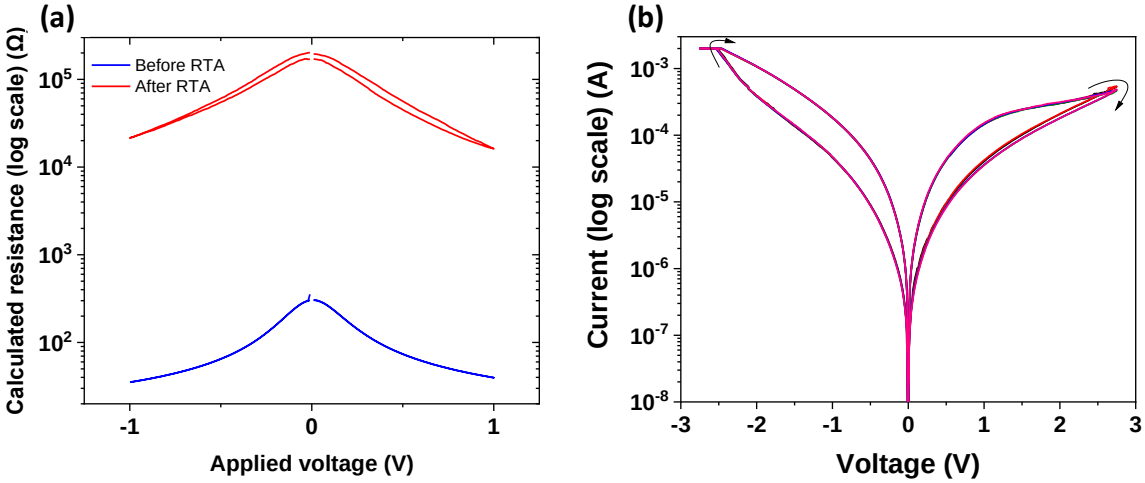

Figure 3.19: a) R-V curves showing the resistance increase after the RTA process of an annealed Ti/optimized L2NO4/Pt device. b) Five consecutive I-V cycles showing highly reproducible analogue RS characteristics obtained for Ti/L2NO4/Pt devices after the RTA process.

Despite these first promising results, unfortunately, we found that the RTA effect carried out in our furnace is not reproducible, as by using the same (or even higher and longer) annealing conditions (T, t) that worked for another sample, higher resistances were not always reached. In other words, each sample has different conditions (T, t) of RTA to trigger the RS, which could be due to small differences in oxygen stoichiometry in the as-deposited samples, but mainly due to a not well-controlled RTA temperature/time/atmosphere with the old furnace used.

With the furnace used, we had to repeat the process many times: RTA (with T and t reported in Table 3.3) and measure the resistance until the devices reached higher resistance, which led to a time-consuming and complicated process. The T and t should be carefully controlled because, as explained in the following section, over-annealed samples can have higher resistance and rectifying behavior, but no distinguishable resistances can be obtained (no programming window).

The RTA effect was also studied for Ti/L2NO4/Pt sample where the thickness of L2NO4 is 90 nm. The large devices (100x100 μm^2 and 150x150 μm^2) on the sample presented IRs of around 200 Ω (see black squares in Figure 3.20) and linear I-V characteristics. In this study, RTA process with T = 330 °C, t = 300 s was carried out. Figure 3.20 shows the area dependence of resistance measured before and after this RTA process. In this sample, the IR of all devices with different sizes increases one order of magnitude after the RTA. This observation can be considered an advantage to avoid the leakage current thanks to the higher resistance. However, even if higher IR and rectifying characteristics were reached, no hysteresis nor distinguishable resistance states were obtained for this sample (Figure 3.19b-c). This

behavior could be attributed to a fully oxidized TiO_x interlayer (TiO_2), which will be structurally and chemically characterized in the next section.

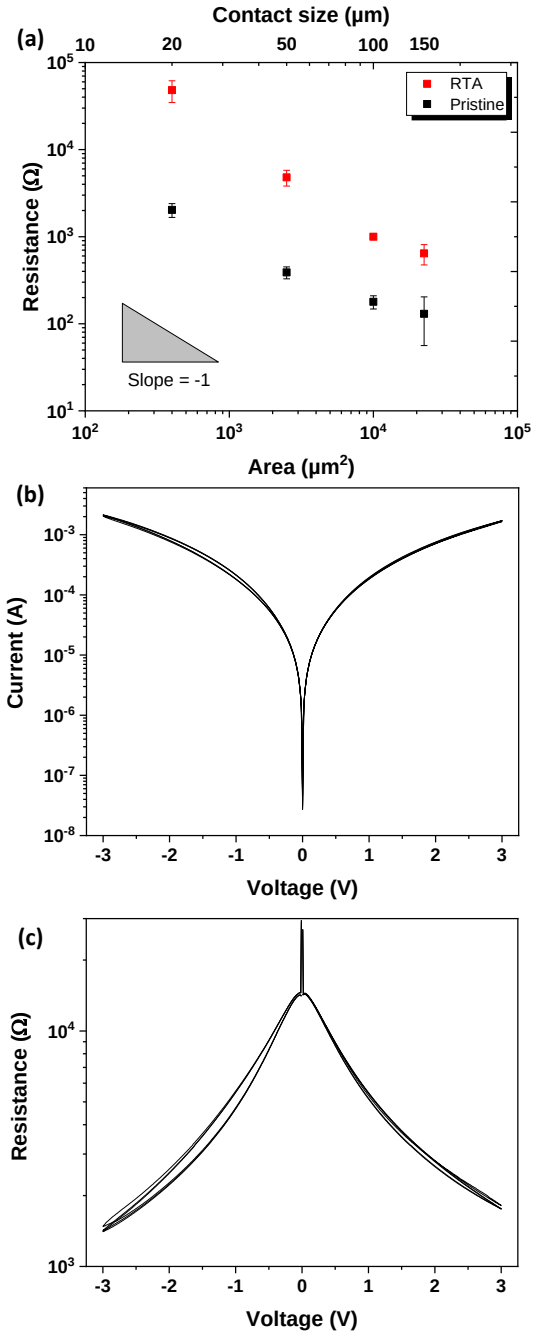

Figure 3.20: Electrical properties of Ti/90nm-L2NO4/Pt memristive devices: a) Evolution of resistances with respect to device areas. Black squares and red squares represent initial resistance before and after the rapid thermal annealing (RTA) at T = 330 °C for 300 s, respectively. b) I-V and c) R-V characteristics of a Ti/90nm-L2NO4/Pt device after the RTA.

3.3.2. Study of the TiO_x interlayer by TEM

In this subsection, the Ti/L2NO4/Pt device with a 90 nm thick L2NO4 film (prepared by a deposition using 4000 pulses) presented in the previous subsection (Figure 3.20) is studied by TEM. The top electrode is the same as for the standard devices (25 nm of Ti covered by 75 nm of Pt). Two devices were chosen to prepare the lamellae for TEM *ex situ* observations, e.g., before RTA and after RTA. The RTA process was carried out at T = 330 °C for t = 5 minutes. Figure 3.21a and c reveal a considerably rough surface of L2NO4 thin films due to the presence of nano-columnar microstructure when growing thin film with high thickness [80]. Consequently, the Ti layer is not flat, as can also be observed in the EDX elemental maps in Figure 3.21b, d. However, a larger oxygen concentration is clearly detected within the Ti layer (brighter) after the RTA, compared to the pristine sample.

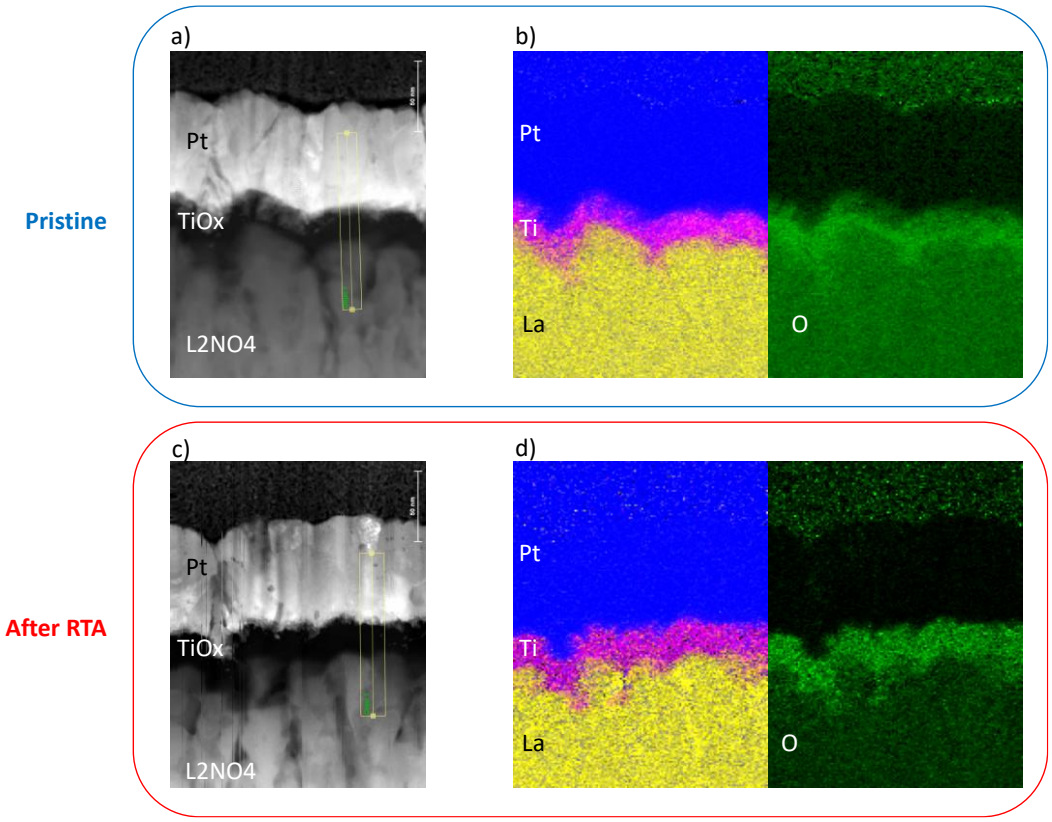

Figure 3.21: Ti/L2NO4/Pt device with a 90 nm thick L2NO4 film a, c) STEM images and b, d) EDX elemental maps for Pt (blue), Ti (pink), La (yellow) and O (green) of devices in a, b) pristine state and c, d) annealed state.

The EDX chemical depth profile of a selected flat region of the lamella prepared from a pristine device (Figure 3.22a) shows a gradient of oxygen content in Ti layer, suggesting the gradual diffusion of oxygen into Ti electrode in pristine state, spontaneously forming a TiOx interlayer during the evaporation of Ti.

After the RTA, the oxygen concentration is much higher (approximately 67%) and doubles the Ti concentration (approximately 35%) within the top electrode, revealing the complete oxidation of Ti, resulting in a TiO_2 layer, due to the relatively long duration of the RTA (5 minutes).

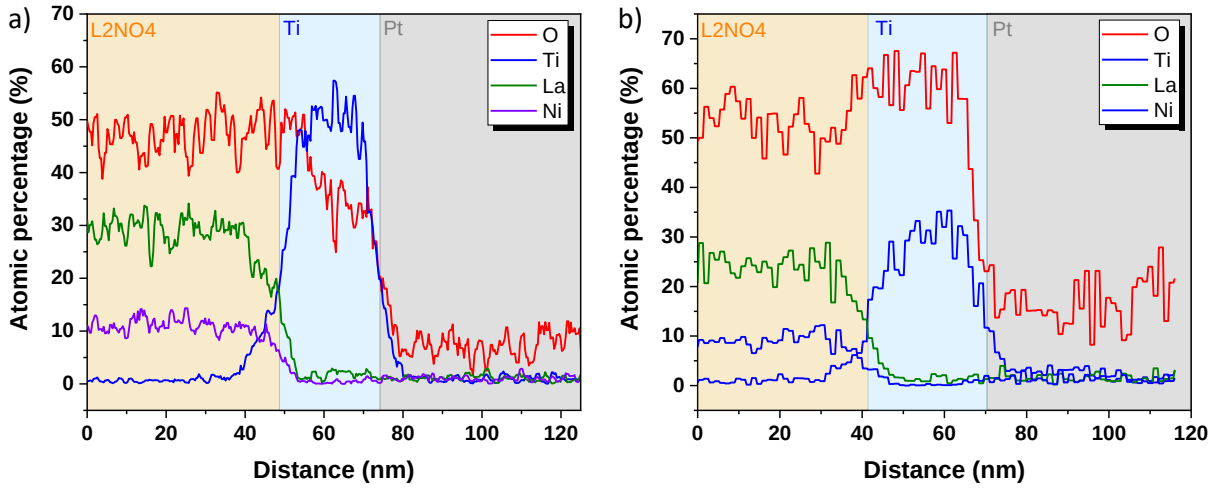

Figure 3.22: EDX chemical depth profiles of flat regions within the lamellae prepared from Ti/L2NO4/Pt devices with a 90 nm thick L2NO4 film a) before RTA and b) after RTA.

3.3.3. Study of the TiO_x interlayer by XANES

To better study the Ti oxidation process, a series of RTA (with small steps of T and t) was carried out using several standard samples (45 nm of L2NO4), until the initial resistances of the devices increased and the rectifying characteristics were obtained. Initially, the large devices (50x50, 100x100, 150x150, 200x200 μm^2) on these three samples showed linear I-V characteristics with low initial resistance values (see Table 3.4). Hence, a series of RTAs (with small steps of T and t) was carried out until the resistance of the devices increased and rectifying characteristics were obtained. The conditions of the final RTAs for these two annealed samples are reported in Table 3.4. Figure 3.23a-b show the I-V characteristics of 20x20 μm^2 devices from two different samples after RTAs in which the last step was a 3-min RTA at 395 °C (Figure 3.23a), showing hysteretic characteristics and two distinguishable resistances states, and in which the last step was a 10-min RTA step at 375 °C (Figure 3.23b), which does not show a reproducible hysteresis nor distinguishable HRS and LRS states.

We then assessed by XANES the Ni-K edge of three samples with different annealing using a large beam size, and the Ti-K edge of 20x20 μm^2 memristive devices located on each of these samples (using a small beam size of 50x50 μm^2). The beam focused at the center of a vertical memristive device for each sample: one as-deposited sample and two samples annealed at different temperatures (T) and durations (t).

Table 3.4: Conditions of the final RTAs of the Ti/L2NO4/Pt samples and the corresponding resistance values of 20x20 μm^2 devices, Nì-K edge position, Ni oxidation state and oxygen off-stoichiometry (δ) of the devices located on these samples.

	Pristine	**3-min RTA**	**10-min RTA**
Initial resistance (Ω)	-	5300	200
Resistance after RTA (Ω)	-	24400	42000
Temperature (°C)	-	400 °C	375 °C
Time (minutes)	-	3	10
Ni-K edge (eV)	8346.0 ± 0.1	8345.9 ± 0.1	8345.7 ± 0.1
Estimated Ni oxidation state	2.25 ± 0.03	2.22 ± 0.03	2.15 ± 0.03
Estimated oxygen off-stoichiometry (δ)	0.125 ± 0.015	0.110 ± 0.015	0.075 ± 0.015

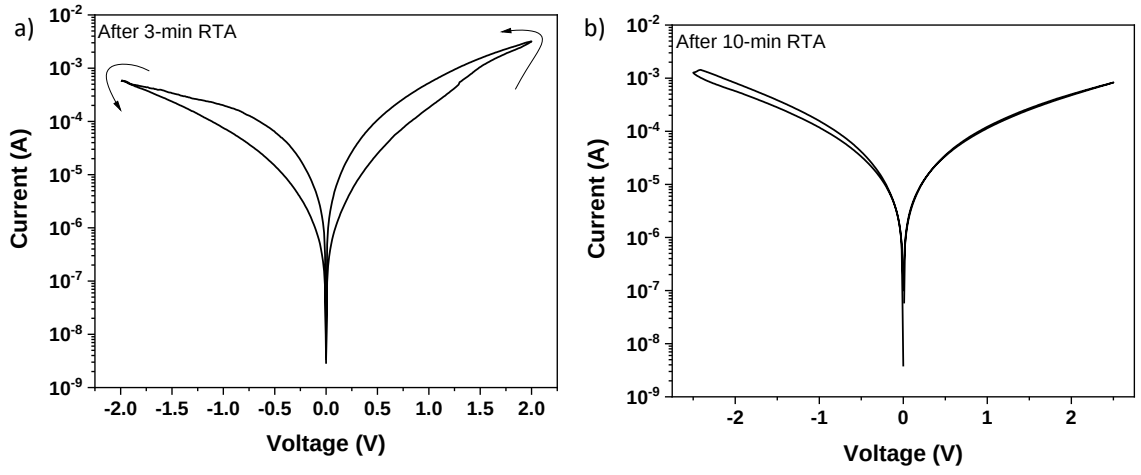

Figure 3.23: I-V characteristics of 20x20 μm^2 Ti/L2NO4/Pt devices with a 45 nm thick L2NO4 film: a) after RTA at 395 °C for 3 minutes and b) after RTA at 375 °C for 10 minutes.

Figure 3.24a shows the Ni-K edge XANES spectra of the three samples used in this subsection. The XANES spectra of a Ni foil and NiO powder measured to be used as references to estimate the Ni oxidation state are added for comparison (see calibration curve in subsection 2.2.7 of chapter 2 for more

details). The measured Ni-K edge energy, estimated oxidation state and oxygen off-stoichiometry for the as-deposited, 3-min RTA and 10-min RTA devices are also reported in Table 3.4, showing that the Ni in the L2NO4 film is reduced when increasing T and t of the RTA process. However, it is important to be aware that, in these Ni-K edge XANES spectra, the full 1x1 cm^2 samples were exposed to the beam (see the illustration at the right of Figure 3.24a). Thus, the Ni oxidation states revealed by the measured Ni-K edges are representative of the regions with Ti electrode and electrode-free. In the other word, it is difficult to conclude that all of the oxygen atoms diffused into Ti layer thanks to the RTA, but they could also go to the Ar gas flow during the process.

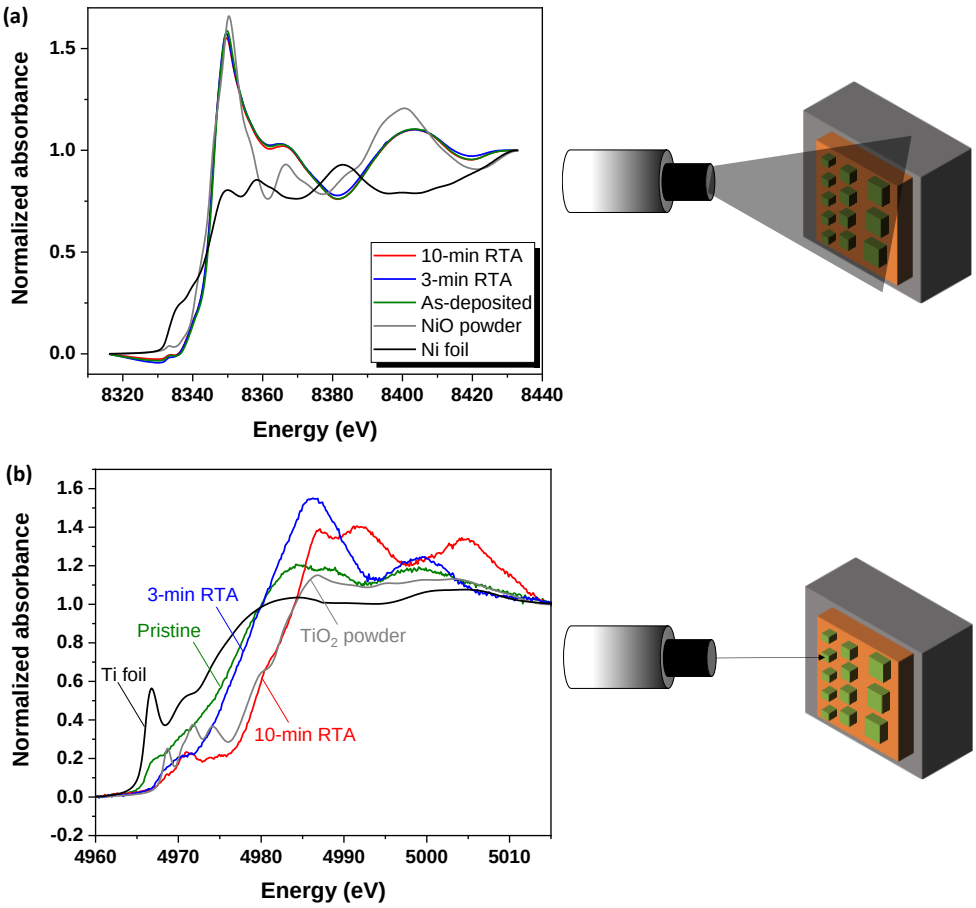

Figure 3.24: a) Ni-K edge XANES spectra measured on as-deposited sample and samples annealed in different RTAs with memristive devices of Ti/45 nm-L2NO4/Pt. b) Ti-K edge XANES spectra measured on 20x20 μm^2 devices located on as-deposited sample and for samples annealed in different RTAs. The Ni-K edge XANES spectra of Ni foil and NiO as well as Ti-K edge XANES spectra of Ti foil and TiO_2 powder are added for comparison. Illustrations of each type of measurement are present at the right of each figure.

Figure 3.24b presents the Ti-K edge XANES spectra of three selected devices located on these three samples (only the devices were exposed to the beam, as sketched at the right of the figure) and references (Ti foil and TiO_2 powder). It is also worth noting that a TiO_2 adhesion layer is present under all devices, under the Pt, and thus the signal of this TiO_2 layer might be included in the collected signal. Hence, a Ti-K edge XANES spectrum at the region that is electrode-free was also performed and we assume that such 20-nm layer of TiO_2 is uniform. Thus, this "electrode-free" spectrum has been subtracted from the spectra of the three devices shown in Figure 3.24b. All spectra have been calibrated (shifted) to the Ti foil theoretical position (4966 eV). As can be observed, the Ti-K edges of the pristine device and 3-min RTA device are close. The Ti-K edge of 3-min RTA is shifted to higher energy, suggesting a higher oxidation state of Ti is obtained thanks to the RTA at 395°C for 3 minutes. Comparing the observed XANES features and Ti-K edge positions to those of the other research [81, 82] Ti oxidation state of pristine device and 3-min RTA device is around 3+. The Ti-K edge of the 10-min RTA device (at 375 °C) is very close to that of TiO_2 powder (Ti^{4+}), suggesting the possible presence of the fully oxidized TiO_x ($x \approx 2$), even though small steps of T and t were used.

In a nutshell, the over-heated or too-long RTA process leads to the full oxidation of Ti electrode (TiO_2). This TiO_2 is stable, and it is thus not easy to reduce. This is why the measured resistance of the device after RTA is higher than the initial value and no hysteresis was obtained. In the ideal cases, i.e. a non-stoichiometric and continuous TiO_x interlayer formed after appropriate RTA conditions (or even without RTA) allows for further oxidation/reduction of TiO_x and L2NO4, facilitating the RS with distinguishable HRS and LRS.

3.4. Conclusions

The conclusions of this chapter are summarized below and organized according to the corresponding sections.

Section 3.1: Ti\L2NO4/Pt planar memristive devices

- L2NO4 thin films have been reproduced on a Si_3N_4 (SN) substrate in polycrystalline form using the same deposition conditions as for the growth of epitaxial L2NO4 on single crystal substrates (650°C, R=5.00)
- The L2NO4/SN sample was mainly composed of $La_2NiO_{4+\delta}$ tetragonal *I*4/*mmm*. However, the presence of a La_2CO_5 phase was confirmed by GIXRD and EPMA (La/Ni ratio in thin film = 2.75). The films are formed by small grains (average size of 15.8 ± 0.4 nm) with a relatively flat surface (RMS = 2.23 ± 0.02 nm)

- The microfabrication of Pt/Ti and Pt electrodes was successful. HRTEM images reveal the polycrystalline nature of Pt and L2NO4. Oxygen was detected at L2NO4/SN and Ti/L2NO4 interfaces suggesting the SiO_x and TiO_x interlayers are formed during the deposition and the microfabrication, respectively.
- Ti\L2NO4/Pt memristive devices initially exhibited ohmic I-V characteristics and a fast thermal treatment (RTA) is always required to trigger the RS. The operation voltages are very high, with small HRS/LRS ratio of around 2
- Although the Ti\L2NO4/Pt planar devices were successfully fabricated, high operation voltages with small programming window are considered as drawbacks of device performance for planar devices.

Section 3.2: Ti/L2NO4/Pt vertical memristive devices:

- Optimization of L2NO4 on platinized substrates:
    - The deposition of L2NO4 at 650 °C led to films with a relatively rough surface. However, no Pt dewetting nor pinholes were observed. When decreasing the deposition temperature, a smaller grain size with a flatter surface can be obtained (at 600 °C). At 500 °C, the L2NO4 thin films became amorphous.
    - The La/Ni ratio in precursor solution (R) was optimized at 600 °C. When decreasing R, the presence of the La_2CO_5 impurity can be discarded. There is no clear effect of R on the thin film morphology.
    - Pure, relatively-flat and dense polycrystalline L2NO4 thin films (43 nm thick) have been deposited by PI-MOCVD on a platinized silicon substrate using the optimal deposition conditions (600 °C, R = 4.00).
- Ti/L2NO4/Pt memristive devices have been fabricated in vertical configuration for the first time, using L2NO4 thin films deposited under the previously optimized conditions. A TiO_x interlayer was observed by STEM-EDX analysis whenever Ti is deposited on top of L2NO4.
- The Ti/L2NO4/Pt devices present gradual transitions between the HRS and LRS states, suggesting bipolar analogue RS can be obtained. Interface-type RS is likely related to the Ti/L2NO4/Pt switching, confirmed by the electrode-area dependence of the resistance.
- The Ti/optimized-L2NO4/Pt memristive devices are forming-free with dynamic resistance relaxation during 12 hours and good cyclability, whereas the Ti/non-optimized L2NO4/Pt devices have a higher initial resistance and require a “forming” step before exhibiting similar RS characteristics to the optimized ones.

Section 3.3: Role of the RTA step

- RTA allows us to i) bring the initial resistance of L2NO4-based devices to higher values, which is considered as an advantage and ii) obtain rectifying behavior of the devices, which leads to hysteresis in the I-V curves. The RTA is thought to supply additional energy to either further oxidize or homogenize the TiO_x interlayer. However, the RTA process with our furnace is not reproducible.
- *Ex situ* TEM images of device maps after RTA combined with EDX confirm a significantly increased oxygen concentration within the Ti electrode.
- Complementary *ex situ* XANES spectra at the Ni-K edge and at Ti-K edge show that Ni in L2NO4 (at both regions: electrode and electrode-free) is generally reduced and Ti is oxidized after the RTA process, suggesting that the oxidation occurred by the migration of (partial) oxygen from L2NO4 to Ti, favored by the heat energy supplied by the RTA.
- Overlong RTAs lead to the completely oxidized TiO_2 layer, as measured both by EDX profiles and by XANES, which is detrimental as it is related to high resistance states, lack of hysteresis and lack of memristance of the devices. Good switching characteristics are obtained when a non-stochiometric TiO_x is present, however, its presence is difficult to control with our very-old furnace.

Chapter 4: TiN/$La_2NiO_{4+\delta}$/Pt, a Memristive Device for Artificial Synapse Applications

The current chapter focuses on the characterization of L2NO4-based vertical memristive devices grown on platinized substrates in combination with TiN as top electrode. The chapter is divided into three sections. In the first one, the structural characterization of optimized L2NO4 thin films and TiN/L2NO4/Pt vertical devices with different oxygen stoichiometries is present. The second section focuses on the electrical characterization of the TiN/L2NO4/Pt memristive devices based on L2NO4 films with varying oxygen contents. The conclusions section, which serves as a summary, sums up the main findings of the chapter.

4.1. The TiN/L2NO4/Pt memristive devices

L2NO4 films grown on Pt (L2NO4/Pt) using the optimized temperature and precursor solution composition, as described in section 3.2.1, were used to build vertical TiN/L2NO4/Pt memristive devices.

4.1.1. Structural characterization of the L2NO4 thin films annealed in different atmospheres

Three L2NO4/Pt samples with different oxygen stoichiometries were used to evaluate the effect of oxygen content on the films' structural properties. One sample was synthesized by PI-MOCVD using the optimized deposition conditions with no further heat treatment (as-deposited film). The other two samples was deposited simultaneously in the reactor and were then separately annealed at 500 °C for 1 hour in in oxygen and argon atmosphere, respectively. These two films are hereafter referred to as O_2 sample and Ar sample, respectively. For phase identification, XRD in grazing incidence mode (GI-XRD) has been chosen to reduce the XRD intensity from the substrate peaks (Pt/TiO_2/Si). Figure 4.1a shows the GI-XRD pattern of these three L2NO4/Pt samples. The Pt diffraction peaks are marked by gray circles. The rest of the main diffraction peaks can be assigned to either the tetragonal phase *I4/mmm* (ICDD: 00-034-0314, presented at the bottom) or the orthorhombic phase *Fmmm* (ICDD: 01-086-8663, presented at the top) of $La_2NiO_{4+\delta}$. The patterns of both structures are very similar and, therefore, it is extremely difficult to discriminate between them based on GI-XRD exclusively. However, it can be seen that all the films are polycrystalline, confirmed by the match of the peak positions between L2NO4/Pt samples and those of the database plotted by drop lines in Figure 3.1a. Moreover, no decomposition of L2NO4 is observed after being exposed to the thermal treatment. To determine the cell parameters of

L2NO4 on these three samples, their XRD patterns (Figure 4.1a) were refined using the TOPAS software. Despite the possibility of having two phases, for simplicity, only the orthorhombic *Fmmm* structure was chosen to obtain the lattice parameters. The values obtained are: as-deposited sample (a = 5.439 ± 0.002 Å, b = 5.490 ± 0.001 Å, c = 12.643 ± 0.008 Å), O_2 sample (a = 5.405 ± 0.007 Å, b = 5.467 ± 0.002 Å, c = 12.681 ± 0.014 Å) and Ar sample (a = 5.439 ± 0.005 Å, b = 5.492 ± 0.002 Å, c = 12.583 ± 0.009 Å). In addition, the Raman spectra of these three samples (as seen in Figure 4.1b) show similar modes without major differences. The most intense mode is observed at 442 cm^{-1} for all samples, where the A_{1g} mode is found in the literature due to the out-of-plane stretching of oxygen octahedral and the corresponding bending mode is found at 226 cm^{-1}. Low-frequency modes (84 and 150 cm^{-1}) are also found for La-O stretching and bending modes [83, 84]. These modes are present in both structures (orthorhombic and tetragonal) and therefore, the coexistence of both phases can not be ruled out. The contribution of the tetragonal phase might be largest in the oxidized film and gradually decreases in the other two samples because the intensity of the broad peak around 650 – 700 cm^{-1} is normally found very high in the orthorhombic phase [83, 84] is highest in Ar-sample, becomes less in the pristine sample and disappears in O_2-sample.

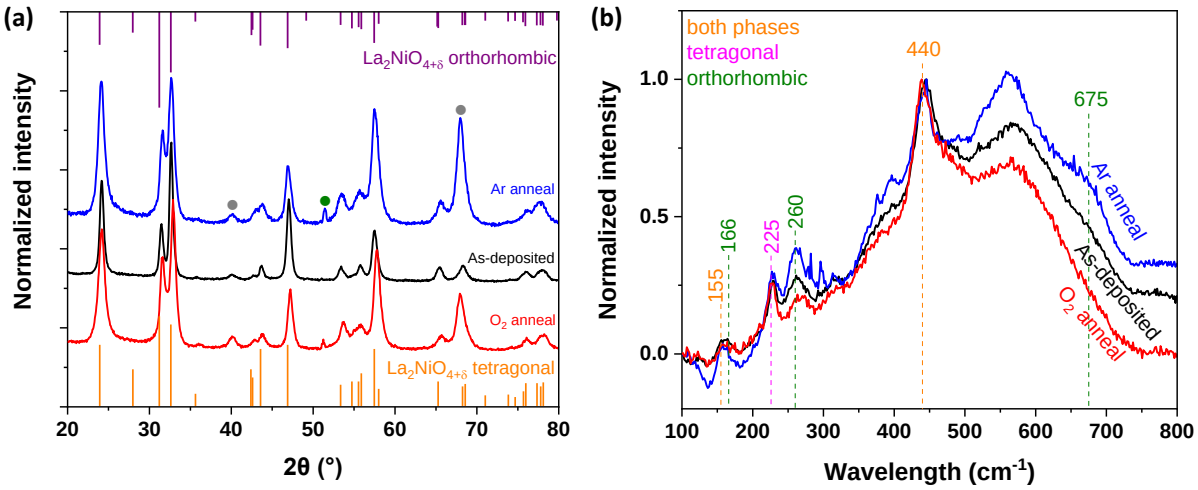

Figure 4.1: Structural characterization of the L2NO4 films obtained after annealing in different gas atmospheres: a) GI-XRD pattern, Pt peaks are marked by gray circles. The orange and purple droplines correspond to the positions of the $La_2NiO_{4+\delta}$ XRD reflections for the tetragonal *I*4/*mmm* structure (ICDD: 00-034-0314) and for the orthorhombic *Fmmm* structure (ICDD: 01-086-8663), respectively. b) Raman spectra with active modes marked by colors according to the phases: orange (both phases), pink (tetragonal phase) and green (orthorhombic phase).

The SEM top-view images of the three samples are presented in Figure 4.2a-c show that no cracks have appeared in the two annealed samples. In terms of morphology, grain coarsening is observed for the

annealed samples. Indeed, the average grain size of the as-deposited sample is between 25 and 28.6 nm, while the average grain size of the Ar-annealed and O_2-annealed samples are 30.3 to 40.0 nm, respectively.

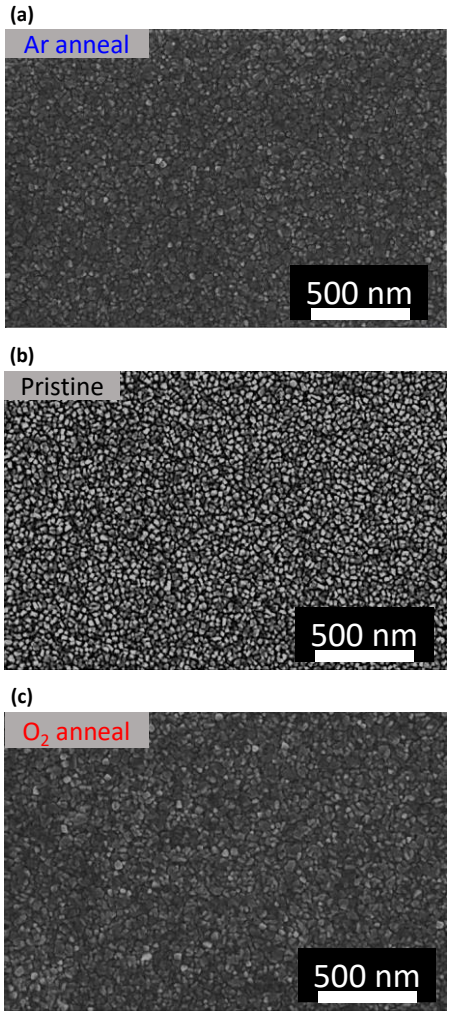

Figure 4.2: Top-view SEM images in the backscattering mode of the a) argon annealed, b) as-deposited and c) oxygen annealed L2NO4/Pt samples, showing the grain coarsening in the annealed samples.

4.1.2. Characterization of the L2NO4 thin films by X-ray Absorption Near-Edge Spectroscopy (XANES)

These three samples were then measured by X-ray Absorption Near-Edge Spectroscopy (XANES) performed on the ID12 beamline at the European Synchrotron Radiation Facility (ESRF). Figure 4.3a shows XANES spectra of the three samples together with the reference samples (Ni foil and NiO powder). The self-absorption correction was applied to the reference samples. Then, their Ni-K edge positions were used as references for Ni(0) and Ni (+2), respectively, to estimate the oxidation state of

the other three samples (see subsection 2.2.7). The Ni-K edge positions of the three samples equal to 8345.9, 8346.0 and 8346.3 ± 0.1 eV for the Ar-annealed, as-deposited and O_2-annealed samples, respectively, which were determined by the first derivative method. As expected, the Ni-K edge shifts slightly towards lower energy when the sample is exposed to Ar (reducing atmosphere) and to higher energy when exposed to O_2. The Ni oxidation state can then be estimated from the measured Ni-K edge energy and allows for the estimation of the oxygen off-stoichiometry (δ). The δ presents 0.110, 0.125 and 0.170 ± 0.015 for Ar, as-deposited and O_2 sample, respectively. The cell parameters estimated by XRD as a function of the oxygen off-stoichiometry are shown in Figure 4.3b. A trend is observed for the out-of-plane lattice parameter *c*, which increases when the sample is oxidized. This observation can be related to the increase in interstitial oxygen content, which is in agreement with the previous studies in powders [85] and L2NO4 epitaxial thin films [45]. The in-plane lattice parameters (*a* and *b*) slightly decrease with increasing δ, which might be due to the shrinking of the unit cell when the sample loses oxygen; similar observations of *a* and *b* were also reported in the reference [85]. The results presented in sections 4.1.1 and 4.1.2 confirm that the oxygen content is tunable by post-thermal treatments and that it influences the structure and oxidation state of L2NO4.

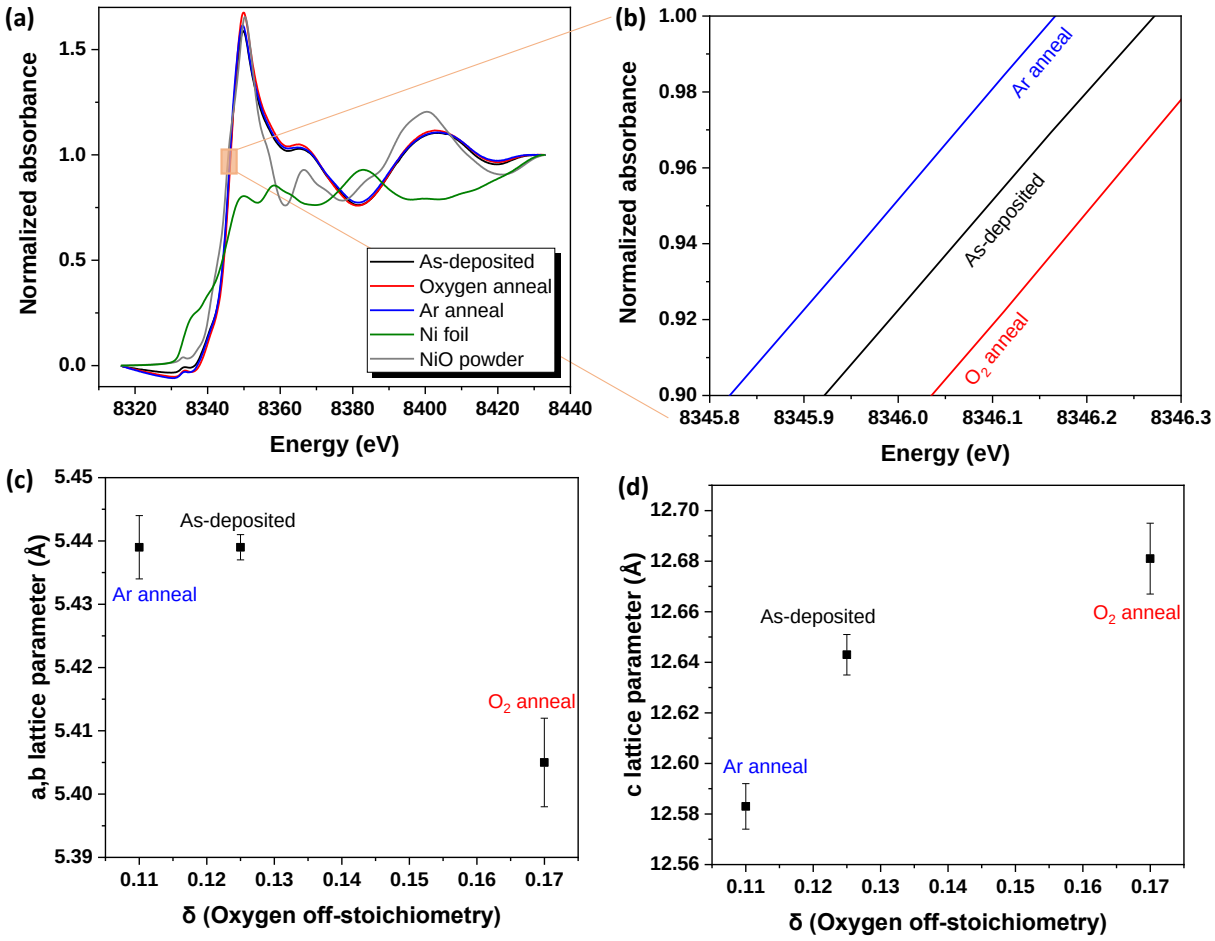

Figure 4.3: a) Ni-K edge XANES spectra obtained for L2NO4 films with different gas annealings (500 °C for 1 hour) and for reference samples (Ni foil and NiO powder). (b) An additional inset of a) focuses on the edge area. Evolution of c) in-plane *a*, *b* and d) out-of-plane *c* lattice parameters as a function of oxygen off-stoichiometry δ. The δ value was estimated by the Ni-K edge position measured by XANES. The *a*, *b* and *c* lattice parameters were fitted by TOPAS software, and diffractograms in (Figure 4.1a) were used as input data for the fittings.

4.1.3. Characterization of the TiN/L2NO4/Pt heterostructures

To build the TiN/L2NO4/Pt memristive devices for each L2NO4/Pt sample, the electrodes were first patterned by laser lithography, followed by the sputtering of 100 nm of TiN, and completed by a lift-off process (see section 2.3 for more details). It should be noted that although in chapters 4 and 5, we talk about "TiN" for simplicity, the exact stoichiometry of the sputtered TiN has not been measured. However, it is thought to be slightly off-stoichiometric (e.g. $TiN_{x<1}$), as its nominal resistivity is of 88

μΩ.cm (value measured by the PTA cleanroom engineers), higher than the theoretical value of 20 μΩ.cm expected for stoichiometric TiN.

Some of the devices were structurally/chemically analyzed by TEM combined with EDX. Figure 4.4a shows the STEM image of a TiN/L2NO4(as-deposited)/Pt/TiO_2/SiO_2 lamella prepared from a device in pristine state, showing that L2NO4 and TiN films grow conformally. All the layers of the stack are continuous and dense. The thickness of the L2NO4 switching layer was measured to be 33.8 ± 1.7 nm. The EDX elemental maps displayed in Figure 4.4b show the TiN top layer, the L2NO4 switching layer below and the Pt bottom electrode. A uniform distribution of La, Ni and O atoms within the L2NO4 thin film is observed. The EDX in-depth profile extracted from the map (Figure 4.4c) confirms the presence of relatively sharp interfaces between the layers. No cation element diffusion is observed between them. However, a small amount of oxygen is detected at the bottom part of the TiN electrode. It is worth noting that the lamella of the device was taken in pristine state prior to any electrical measurements. Therefore, the presence of oxygen at the TiN/L2NO4 interface suggests it is likely a TiN_xO_y interlayer that was spontaneously formed during the sputtering of TiN. The presence of a TiN_xO_y layer has been reported in other oxide systems using TiN electrode [38, 86]. It should also be noted that fully stoichiometric TiN is a metal with a relatively high work function and a relatively low oxygen affinity often used in the industry [25], similar to Pt, Ir or Au. On the other hand, $TiN_{x<1}$ is often obtained in research labs as a stoichiometric nitride, and can act as an oxidizable electrode, such as Ti, Ta, W and Hf, due to the excess of Ti in the structure.

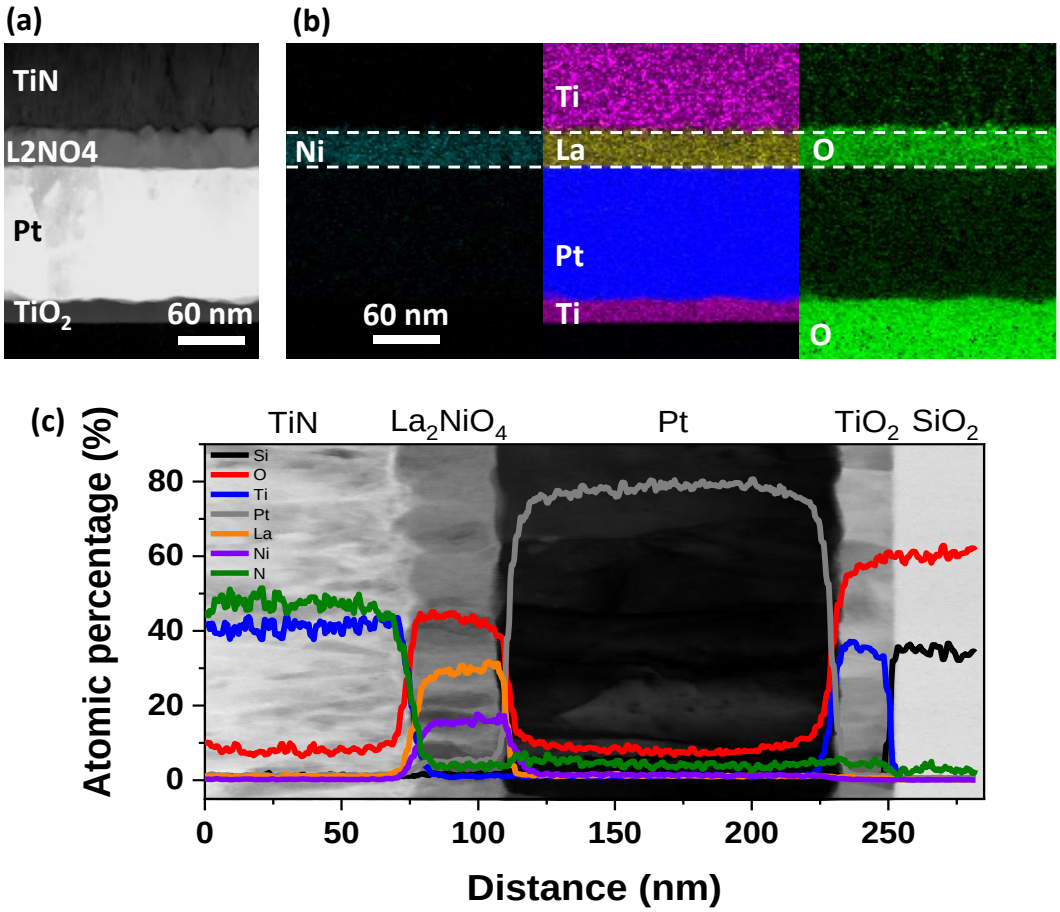

Figure 4.4: Cross-section TEM analysis of a TiN/L2NO4(as-deposited)/Pt memristive device: a) STEM image showing the layer stack of the device, b) EDX elemental maps for Ti (pink), La (yellow), Pt (blue), Ni (cyan) and O (green), c) EDX atomic depth profile showing a small amount of oxygen at the TiN/L2NO4 interface.

Another lamella of TiN/L2NO4(Ar-annealed)/Pt stack prepared from a pristine device was also characterized by high-resolution TEM. In Figure 4.5a, the STEM image reveals a thin interlayer at TiN/L2NO4 interface, which is brighter than the TiN electrode (TiN_xO_y). The device is in pristine state (prior to any electrical bias). The HRTEM image confirms the presence of an amorphous TiN_xO_yinterlayer (a few nm thick) at the TiN/L2NO4 interface. It also reveals the polycrystalline nature of L2NO4 film and TiN electrode. The L2NO4 (Ar-annealed) film consisted of grains of different orientations of about 15-20 nm size in width.

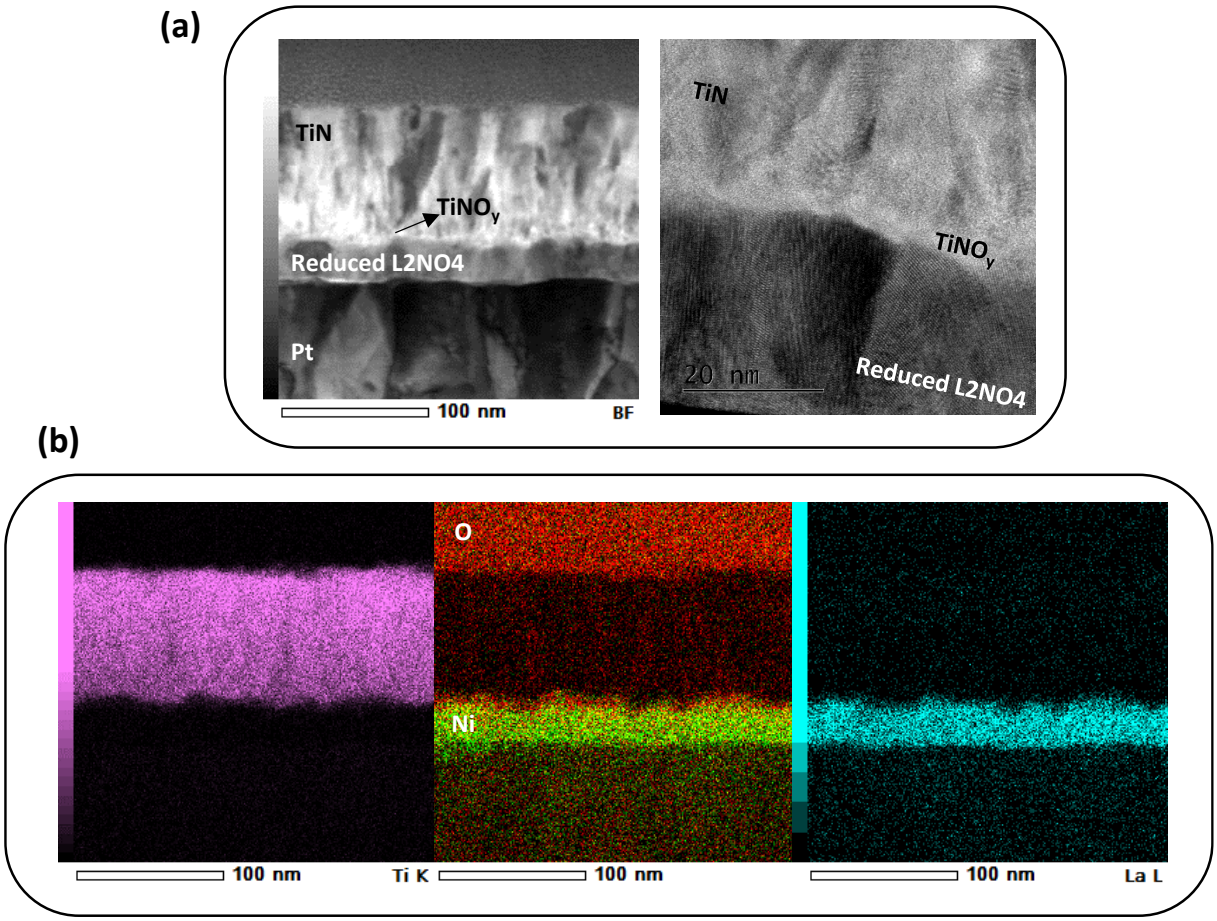

Figure 4.5: a) STEM image and high-resolution TEM (HRTEM) image focus at TiN/L2NO4/Pt stack and TiN/L2NO4 interface, respectively, showing the TiN_xO_y interlayer spontaneously formed after the microfabrication. b) EDX elemental maps integrated on the STEM image for Ti (pink), Ni (green), La (cyan) and O (red) showing the overlap of Ni and O elements at TiN/L2NO4 interface.

4.2. Electrical characterisation of the TiN/L2NO4/Pt memristive devices

4.2.1. Initial Resistance State

For each sample, the initial resistance (IR) of at least ten devices per pad size was measured. Then average values were calculated for each electrode size and represented in Figure 4.6 by circles with error bars. In all samples, the measured IR decreases when increasing the electrode area. The IR is expected to decrease with the electrode area with a slope of -1 (black dashed line added at the bottom), in the case the IR is dominated by the L2NO4/electrode contact resistivity. The slopes measured for these three samples are relatively close to -1, suggesting the IR strongly depends on the device geometry and in particular, on the area of the electrode. In general, the Ar-annealed sample shows the highest IR values for all device sizes, with the exception of the 200x200µm^2 devices. The IR decreased by about one order

of magnitude between the Ar sample and O_2 sample. The higher IR observed in the Ar-sample (compared to the oxygen-rich sample) can be attributed to the higher hole carrier concentration and expected higher work function of the oxygen-deficient L2NO4 film. Indeed, in the L2NO4 structure, interstitial oxygen serves as a negative charge defect and it has to be compensated by electronic holes to keep the charge neutrality. In other words, the lower the interstitial oxygen concentration in L2NO4, the lower the electronic carrier concentration, leading to higher resistivity in the Ar-annealed sample [45, 68]. However, as previously mentioned, the device resistance is also governed by the contact resistance, which depends on the difference in work function between L2NO4 and the electrode material. Indeed, the work function of L2NO4 was reported at 4.1 and 4.3 eV for the δ of 0.04 and 0.08, respectively. This result is exciting as it shows that the device's IR can be tuned (increased) when subjected to a reducing atmosphere, resulting in a higher resistance, which could help prevent the memristive devices from leakage current.

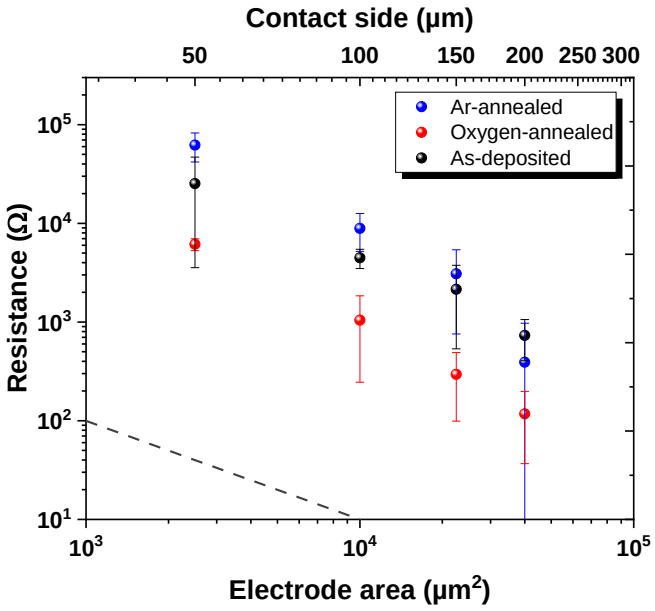

Figure 4.6: Initial resistance values of TiN/L2NO4/Pt devices as a function of the electrode area for Ar, as deposited and O_2-annealed samples. For each sample, four different electrode pad sizes have been measured. Their side dimensions are indicated on top of the graph. Black dashed line with a slope of -1 is added at the left-bottom corner for comparison.

Figure 4.7a, b and c present the variability of the IR with the electrode area for these three samples (for each sample, 14 devices were measured for each electrode size). It can be observed that, in all cases, the smallest electrode size (50x50 μm^2, plotted in blue) shows the smallest variability, which increases with device size. This effect can be attributed to the presence of defects in L2NO4 films and/or the

inhomogeneities of TiN_xO_y interlayer and L2NO4 film deposited on Pt substrates (variation in thickness). Indeed, within a larger electrode size, the probability of having more defects is higher. The 50x50 μm^2 TiN/L2NO4/Pt devices were thus selected as standard devices for the in-depth characterization of their electrical performance.

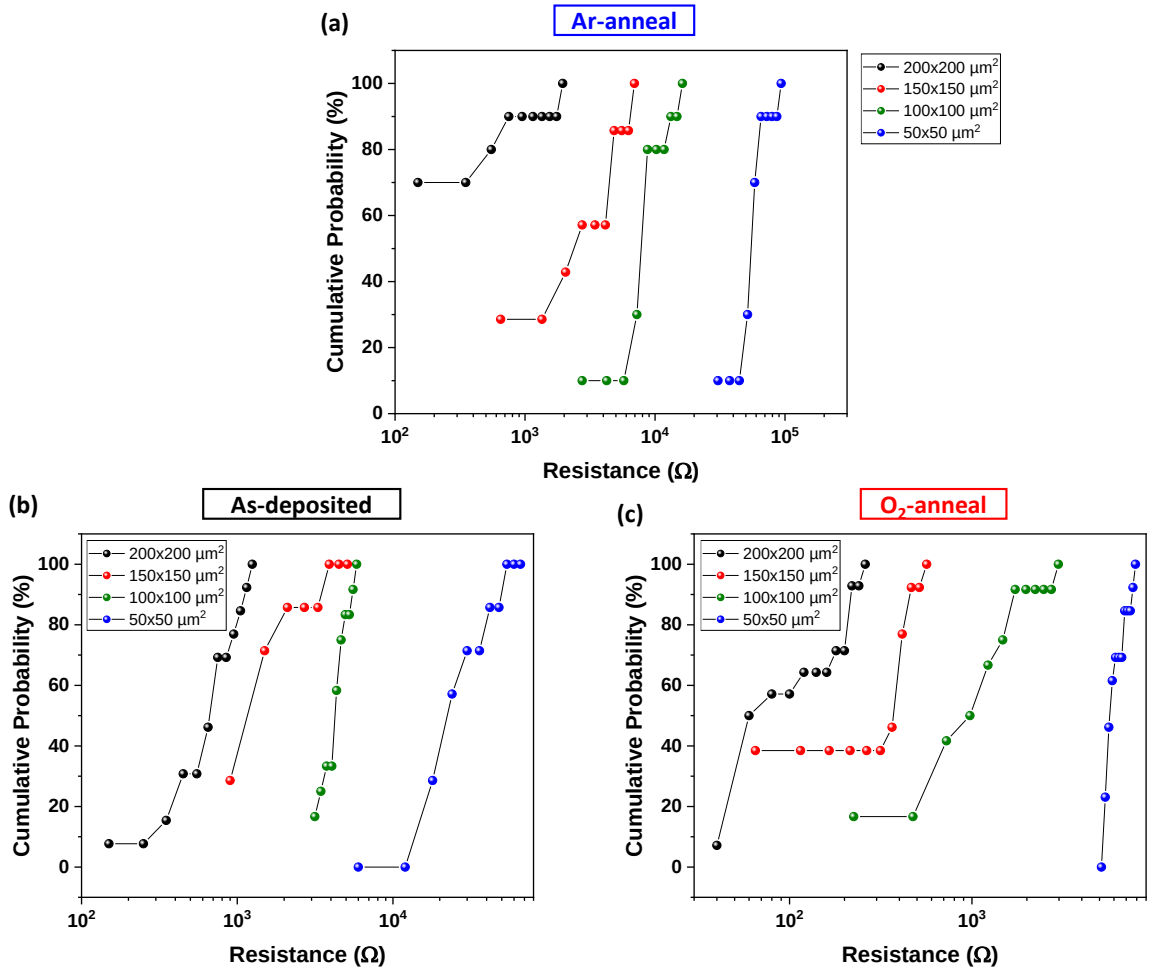

Figure 4.7: Cumulative probability representation of the initial resistance (IR) values for different electrode-size TiN/L2NO4/Pt devices annealed in different gas of L2NO4/Pt samples: a) Ar annealing, b) as-deposited and c) O_2 annealing (14 devices were measured for each electrode size for each sample).

4.2.2. The 'soft-forming' step

There are typically two ways of activating valence change memristive devices, namely the 'initialisation' and the '(electro)forming', which are a prerequisite for a reliable operation. An 'initialisation' process is known as a stabilization procedure, which is carried out at voltages near the device's operation ones. A 'forming' process is described as a 'soft breakdown' step to create a filament (or filaments) between the electrodes, creating the devices in LRS.

Before exhibiting RS in the standard regime, a 'soft-forming' process is required in TiN/L2NO4/Pt memristive devices. For this, the standard TiN/L2NO4/Pt devices were electrically stressed under bipolar voltage sweeps (0 V → $+V_{max}$ → 0 V → $-V_{max}$ → 0 V) with increasing V_{max} amplitude every five cycles as presented in Figure 4.8a-c. The first five sweeps at $|V_{max}|$= 1.5 V show rectifying I-V characteristics from the TiN/L2NO4 interface, knowing that the L2NO4/Pt is an ohmic contact (linear response of Pt/L2NO4/Pt devices was observed), with no clear separation of the HRS and LRS. Already at $|V_{max}|$= 2 V, the HRS and LRS start to appear with the HRS/LRS ratio of 2, suggesting a possible dynamic phenomenon starts appearing at the TiN/L2NO4 interface. At the first cycle of the $|V_{max}|$ = 2.5 V sweeps, a sudden decrease in resistance occurs (black line in the bottom panel), reaching the current compliance of 100 mA, while the following four cycles show two stable and reproducible resistance states with a HRS/LRS of 36. The jump in the first cycle is considered as a 'soft-forming' of the devices.

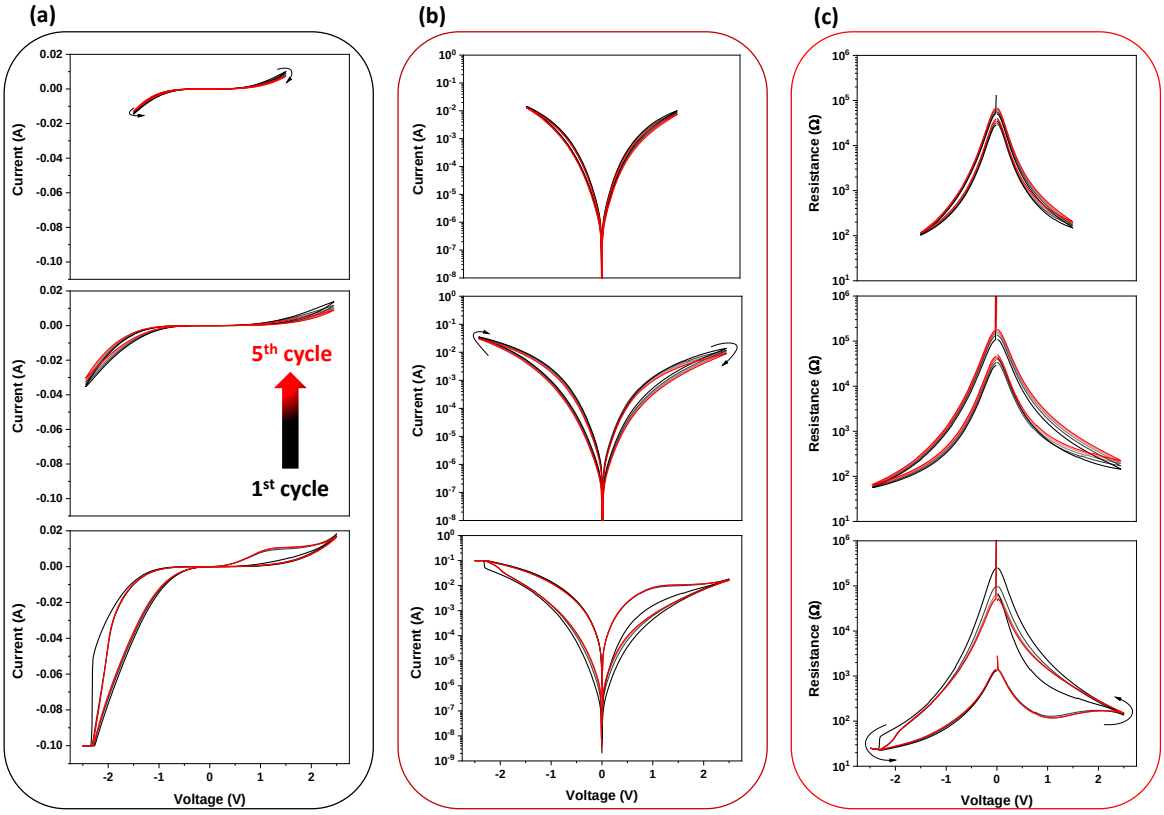

Figure 4.8: a) I-V characteristics of a TiN/L2NO4/Pt device during the initialization process, the solid line in the bottom panel shows the soft-forming. Each panel shows five cycles performed following the same sequence (0 V → $+V_{max}$ → 0 V → $-V_{max}$ → 0 V). $|V_{max}|$ = 1.5, 2, 2.5 V, from the top panel to the bottom panel, respectively. b) log (I)-V characteristics. c R-V characteristics. The sense of the switching is always counter-eightwise in I-V (marked with arrows).

4.2.3. Quasi-static hysteretic *I-V* characteristics

Further electrical measurements were performed on the standard device mentioned in subsection 4.2.2, by applying voltage and measuring the current. The TiN top electrode is biased while the Pt bottom electrode is grounded and the current compliance (CC) in the negative branch was set at 100 mA to avoid the device breakdown. As seen in the last panel of Figure 4.8a, the current in positive polarity is generally small and thus, a smaller CC of 30 mA is used. The sweep cycles followed the sequence: 0 V → $+V_{max}$ → 0 V → $-V_{max}$ → 0 V, with a step of 0.01 mV. After each half cycle, a read-sweep (0 V → 0.01 V, step of 0.001 V) is applied and the corresponding current at 0.01 V is used to calculate the read resistance. Figure 4.9a and b present ten sweeps at $|V_{max}|$ = 2.5 V, showing that these ten cycles are perfectly overlapped, thus, suggesting the highly reproducible cycle-to-cycle switching behavior. A HRS/LRS ratio of 36 is observed. In both polarities, gradual transitions between HRS and LRS can be observed, showing the counter-eightwise analogue RS can be obtained on TiN/L2NO4/Pt memristive devices. Multilevel HRS states can be obtained by varying the applied voltage amplitude. As shown in Figure 4.9c and d, the higher the voltage amplitude used, the higher the resistance states obtained. These results suggest the highly multilevel resistances can be programmable in such TiN/L2NO4/Pt memristive devices.

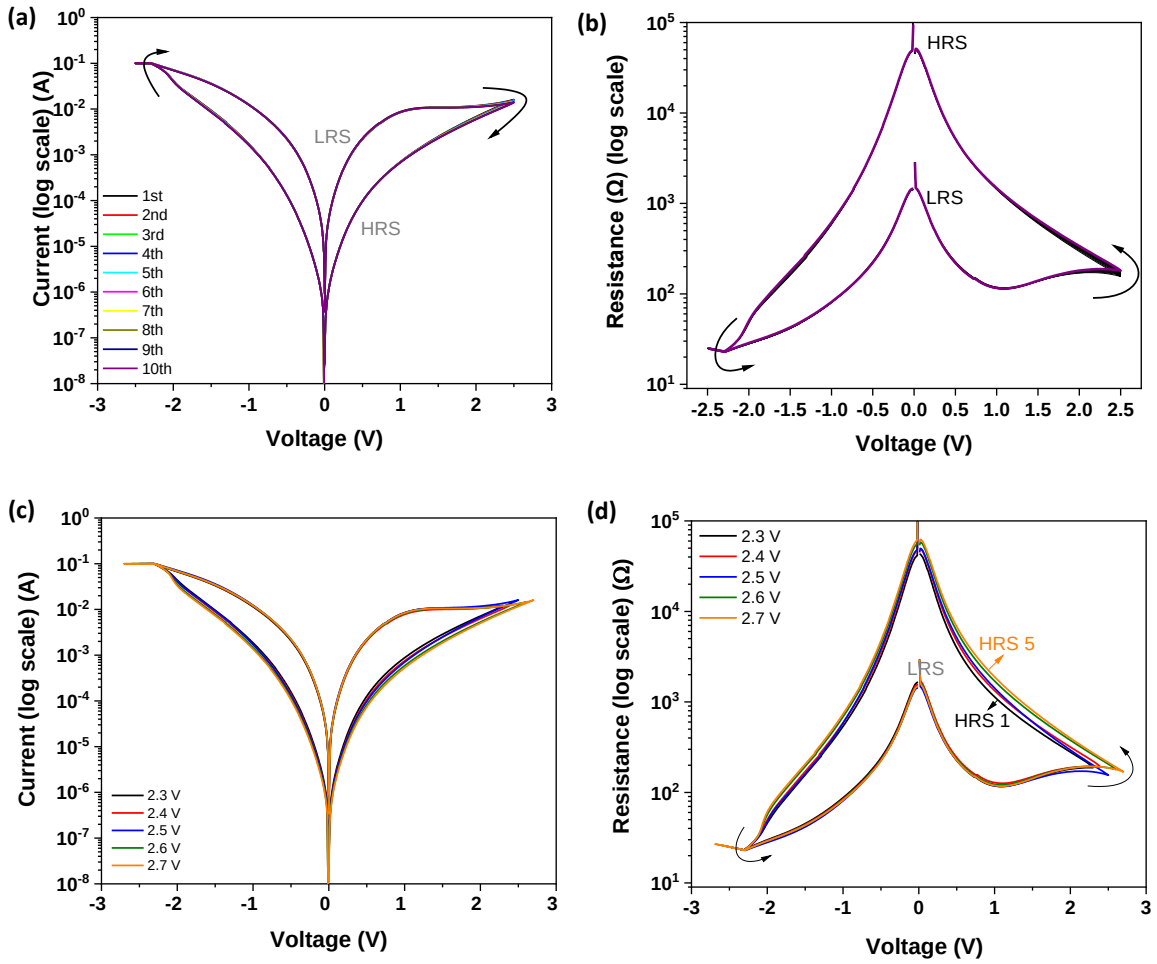

Figure 4.9: Memristivity of TiN/L2NO4/Pt devices recorded by continuous sweeps using the sequence: 0 V → $+V_{max}$ → 0 V → $-V_{max}$ → 0 V. a) I-V and b) R-V characteristics of ten consecutive cycles using $|V_{max}|$ = 2.5 V showing the high cycle-to-cycle reproducibility of the device. c) I-V and d) R-V characteristics obtained using $|V_{max}|$ = 2.3 V, 2.4 V, 2.5 V, 2.6 V, 2.7 V, one cycle for each V_{max} amplitude, showing multiple HRS states.

In order to study the effect of electrode area on the obtained RS, HRS and LRS of as-deposited memristive devices with different electrode areas were statistically measured, as seen in Figure 4.10. Five devices for each electrode area (20^2 µm^2 and 50^2 µm^2), except for the 100^2 µm^2 electrode, only three devices were measured. The averaged HRS and LRS are plotted with their error bars, showing that they are independent of electrode area and far away from the slope of -1 shown at the bottom. This feature strongly supports the presence of filament-type RS in TiN/L2NO4/Pt memristive devices.

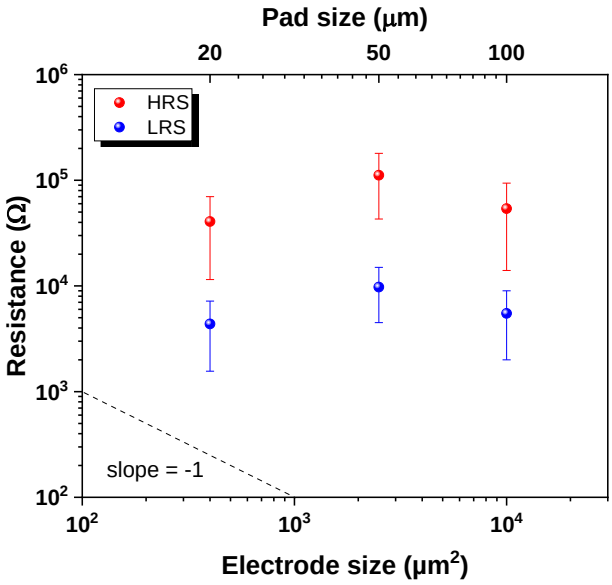

Figure 4.10: Pad-size area independence resistance of the HRS (red) and LRS (blue). Their averaged values are reported for each contact area with error bars (five devices for small pad sizes and three devices for 100^2 μm^2 pad size).

To study the memristivity of the devices with different oxygen content (δ), three devices located on three samples with different δ were submitted to a sequence of bipolar voltage sweeps (0 V → $+V_{max}$ → 0 V → $-V_{max}$ → 0 V), five cycles for each V_{max}. At $|V_{max}|$ = 2.5 V, the Ar-annealed sample and the pristine sample show a 'soft-forming' process in the first cycle (black lines in Figure 4.11a and Figure 4.11b). The I-V and R-V characteristics of the O_2-annealed device using $|V_{max}|$ = 2.5 V are not shown. Instead, the measurements using $|V_{max}|$ = 2.75 V are plotted in Figure 4.11c. As can be observed, contrary to the other two samples, the oxidized devices do not show the large jump in the first cycle (soft-forming), and do not reach current compliance, even if a higher $|V_{max}|$ (compared to the ones where the soft-forming usually occurs) is used. Before the forming, resistances of devices located on Ar-anneal and pristine samples were relatively high (100-200 kΩ, see black R-V curves in Figure 4.11b-c). After the soft forming, in general, the gas annealing does not considerably affect the memristive characteristics. As seen in Table 4.1, comparing the HRS and LRS of the three devices after the forming, LRSs are the same level, even though the HRSs (and thus ratio of HRS/LRS) are relatively higher in TiN/O_2-annealed L2NO4/Pt memristive device. Therefore, the post-annealing in oxygen can be a pre-treatment done to the sample before depositing the electrodes to avoid the soft-forming in the memristive devices and to have lower device-to-device variability.

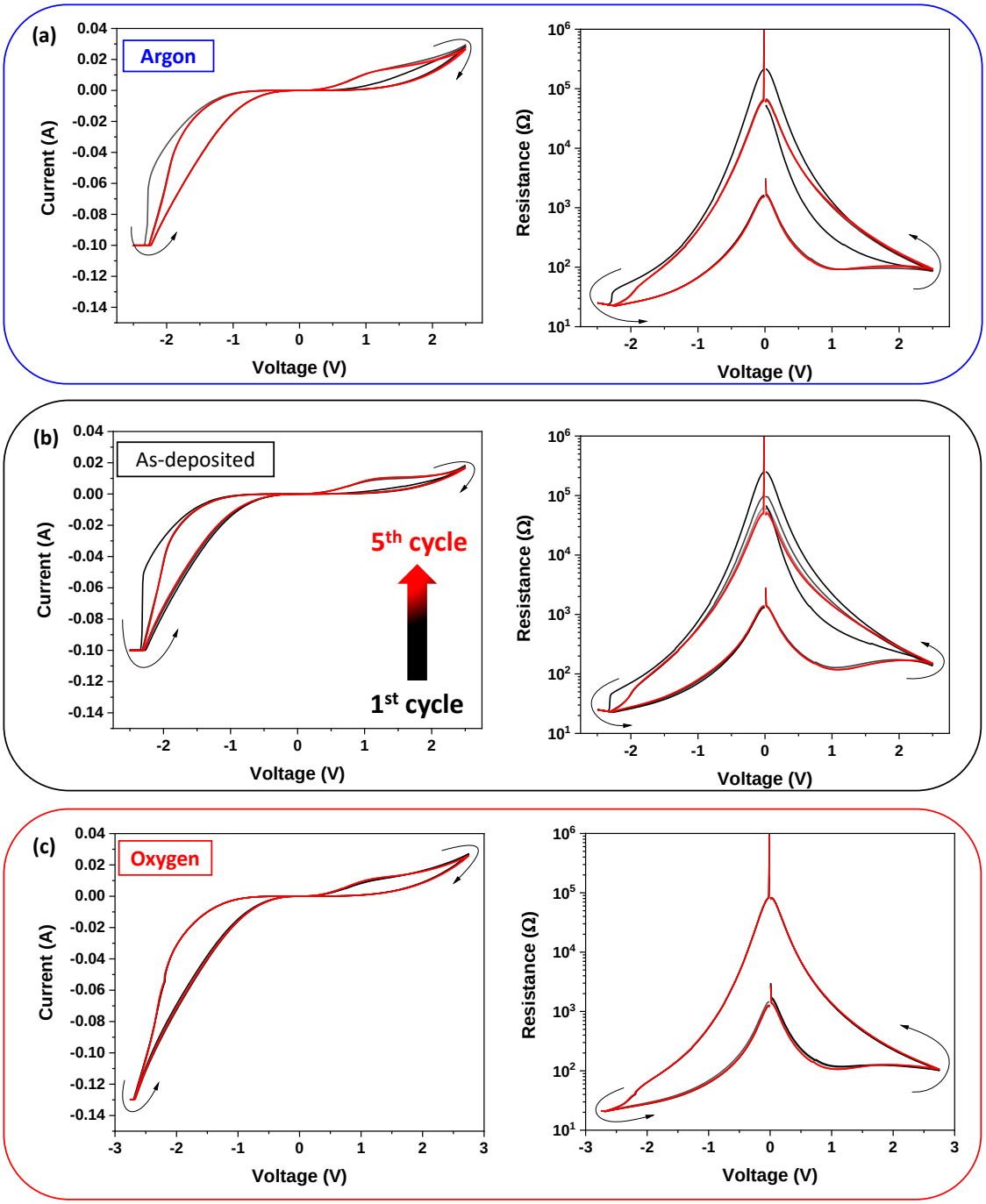

Figure 4.11: I-V and R-V characteristics of three different TiN/L2NO4/Pt memristive devices (a) annealed in argon, (b) kept as-deposited and (c) annealed in oxygen, showing the 'soft-forming' process observed in argon annealed and as-deposited samples.

Table 4.1: Resistances extracted at 0.02 V of the I-V sweeps of three TiN/different annealing L2NO4/Pt devices after the soft forming

	Argon anneal	**As-deposited**	**Oxygen anneal**
HRS (kΩ)	63.9	50.7	81.7
LRS (kΩ)	1.6	1.4	1.4
Ratio of HRS/LRS	40	36	58

4.2.4. Resistance hysteresis switching loops (RHSL)

For use in realistic memory chips and for the application of artificial synapses in spiking neural networks (SNNs) where the synaptic weights are controlled by spikes, pulsed input signals are greatly preferred. For that purpose, measurements using pulses were carried out to study the responses of standard TiN/L2NO4(as-deposited)/Pt memristive devices (Figure 4.12a). A staircase of write pulses (red pulses) was applied, followed by consecutive read pulses, as shown in the Resistance hysteresis switching loop (RHSL) measurement sketch in Figure 2.8b (subsection 2.4.1). The write pulse amplitude $|V_{max}|$ varied from 0.25 V to 2.5 V with the step of 0.25 V, whereas the read pulse amplitude was kept at 0.01 V. The duration of the write pulse was 250 ms and that of the read pulse was 50 ms. Figure 4.12b shows the I-V plots (3 cycles) of the points obtained in the write pulses. The measurements from the continuous I-V normal sweep are added as a black line in the same plot for comparison. The I-V data are perfectly consistent between both measurements, suggesting that the TiN/L2NO4/Pt memristive cells can be used in two modes (pulse and sweep). Moreover, the three RHSL cycles measured are highly reproducible. Figure 4.12c presents the resistance values taken from reading pulses, showing a wide operating window. The obtained HRS/LRS ratio is 35, which is comparable to that of continuous sweeps in Figure 4.9a. Moreover, in addition to two stable resistance states: HRS ≈ 27.5 kΩ and LRS ≈ 0.8 kΩ, multiple intermediate resistance states can be observed in between. This observation is reproducible throughout the three RHSL loops. These results show the good response of TiN/L2NO4/Pt memristive devices under pulse input and confirm the high cycle-to-cycle reproducibility switching observed in the previous section with multiple resistance states.

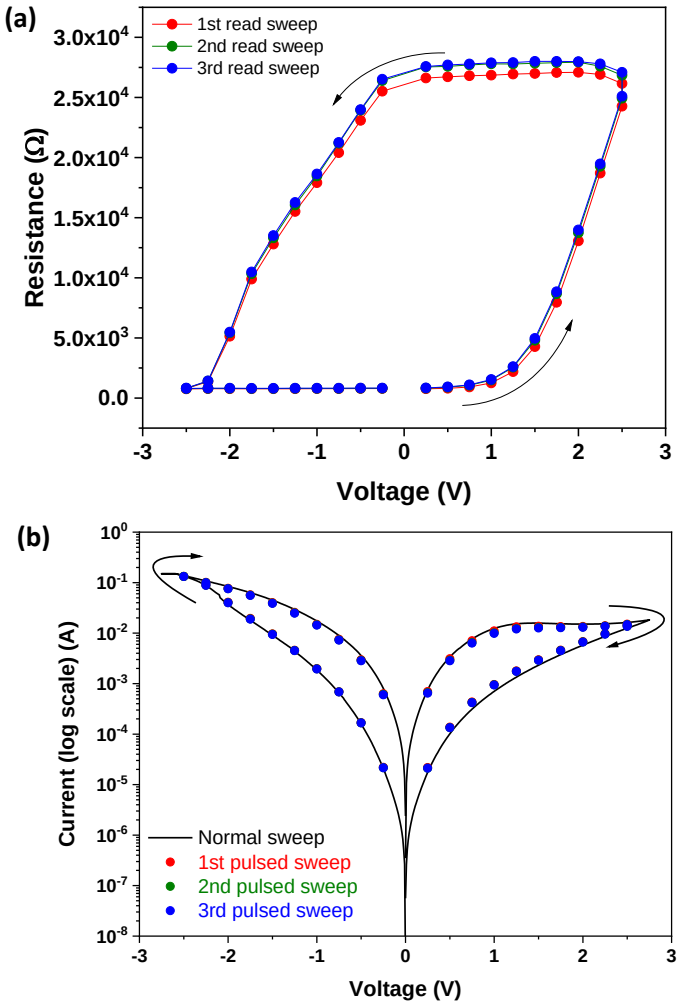

Figure 4.12: Resistance hysteresis switching loop (RHSL) tests performed on a TiN/L2NO4/Pt memristive device. a) I-V plot comparing the data obtained by the write pulses and the continuous sweep mode. b) Read resistance values obtained by the read pulses show multilevel resistance states.

4.2.5. Retention characteristics

Another standard as-deposited device was chosen to study the retention characteristics. HRS of 40 kΩ and LRS of 0.7 kΩ were programmed by the sweeps of $|V_{max}|$ = 2.75 V. Then their resistance states were measured (every 5 minutes) for 6 hours by read measurements. The evolution of the HRS and LRS states vs time is shown in Figure 4.13a. A small relaxation (slight increase) of resistance at the beginning of the measurements (the first 15 minutes) is observed both for the HRS and LRS. When the states reach their stable values, they remain constant until the end of the measurement (6 h). Figure 4.13b shows the evolution during 15 minutes of different HRS states programmed by pulses. The HRSs programmed by +2.25 V and +2.5 V sweeps slightly increase during the first 5 minutes and then remain constant till the

end of the measurement (15 minutes). These preliminary results suggest good data retention characteristics and, thus, the suitability of using TiN/L2NO4/Pt as a long-term artificial synapse.

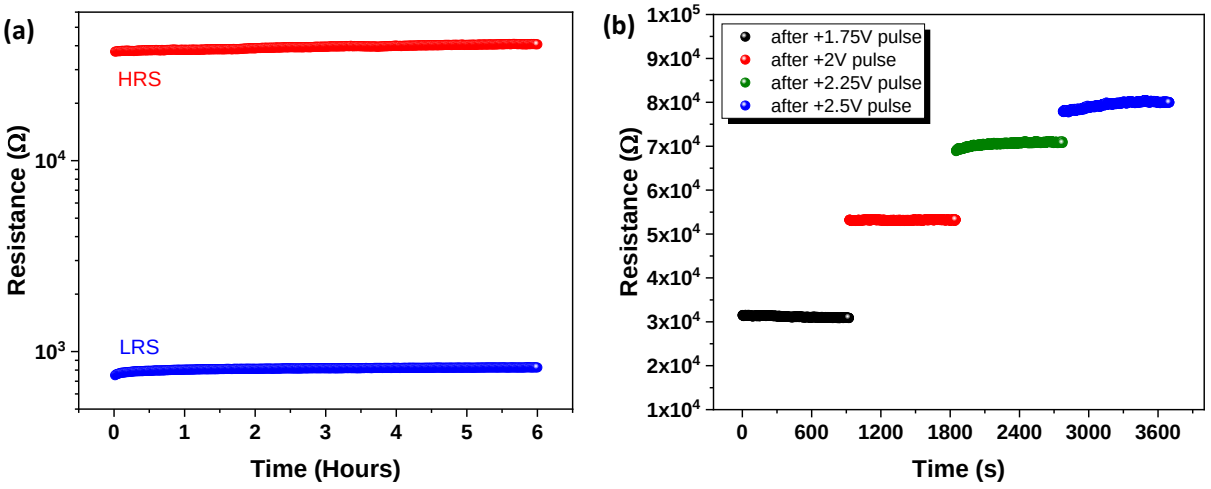

Figure 4.13: Retention characteristics of TiN/L2NO4/Pt memristive devices a) HRS and LRS programmed by the sweeps of $|V_{max}|$ = 2.5 V and measured for 6 hours. b) Multiple HRSs programmed by +1.75 V, +2.00 V, +2.25 V, +2.5 V pulses and measured for 15 minutes.

4.2.6. Long-term depression-potentiation measurements

It is commonly believed that the learning and memory processes are linked to synaptic weights between neurons and synaptic weights can be regarded as the conductance of electronic artificial synapses [87]. The increase in conduction is called potentiation, and depression stands for the decrease in conductance. In our TiN/L2NO4/Pt devices, stepwise RESET and SET pulsed measurements (RPM and SPM) were carried out for three standard TiN/L2NO4/Pt memristive devices with different L2NO4 oxygen stoichiometry to investigate the potentiation-depression plasticity of such devices.

First, the effect of pulse duration was studied on a device of an as-deposited sample by RPM measurements (50 pulses of +2.5 V) with three different pulse durations (50, 250 and 1250 ms). After each write pulse, a read pulse (0.1 V/50 ms) was applied. Figure 4.14a shows that the longer the pulse duration, the higher the resistance obtained at the last RPM pulse (50^{th} pulse). This observation is consistent with the effect of pulse height, where higher pulse amplitudes can reach higher resistances in the depression processes. Figure 4.14a is replotted as a function of the total applied pulse duration in Figure 4.14b showing a quite linear behavior. This trend suggests the total change in resistance strongly depends on the total applied time of the pulses and not only on the number of pulses. The results prove that, by combining different pulse amplitudes and pulse durations, the resistance (conductance or

synaptic strength) of TiN/L2NO4/Pt memristive devices can be controlled and programmable in a flexible way. Thus, it allows for flexible adaptation when being used for SNN simulations.

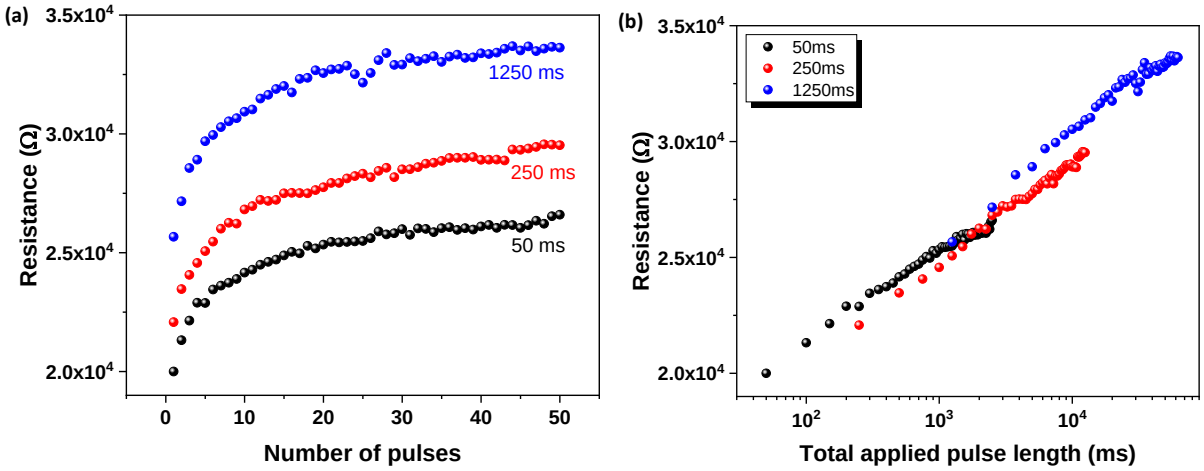

Figure 4.14: a) RPM measurements on a TiN/L2NO4/Pt memristive device using three different pulse durations (50 ms, 250 ms and 1250 ms). b) Resistance obtained from the RPM measurements plotted as a function of the total applied pulse duration.

Next, depression/potentiation measurements were carried out for the three samples. They consisted in applying 50 consecutive positive RESET pulses followed by 50 consecutive negative SET pulses (intercalated by read pulses). Write pulses of 250 ms of duration and varying amplitude were applied, alternated with read pulses of 0.1 V with 50 ms duration. The effect of the pulse amplitude was studied by varying the positive and negative pulse amplitude for each device independently. First, six positive voltage amplitudes were tested, where the $-V_{max}$ was fixed at -3.4 V and $+V_{max}$ varied from 1.6 V to 2.8 V, with a step of 0.2 V. Secondly, $+V_{max}$ was kept at +1.8 V while $–V_{max}$ varied from -1.8 V to -3.4 V, with a step of -0.2 V. After each pair of stepwise SET/RESET measurement (RPM/SPM or depression/potentiation, respectively), the device was set to the LRS (approximately 2 kΩ for these three devices) by a negative half voltage-sweep cycle of -2.75 V (0 V → -2.75 → 0 V).

As shown in Figure 3.20a-c the RPM takes the devices to a HRS, while the SPM takes devices to LRS. From the RPM it can be concluded that, in general, by applying a higher $+V_{max}$ amplitude, a higher final resistance (after the 50^{th} pulse) can be obtained. Similar trends are observed for the SPM, the lower the $-V_{max}$ the higher the resistance obtained, except for the SPM in the Ar sample. In all cases, saturation resistance state can be reached, suggesting more numbers of pulses (or longer pulse duration) cannot open larger the programming window with more numbers of resistance levels. Up to 50 multilevel HRSs can be programmed by different numbers of pulses in the RPM, while the number of LRS in SPM is generally not larger than 25. The increase or decrease in resistance, in all cases, is non-linear. However,

the non-linearity and the gap between potentiation-depression can be resolved by identical pulse pairs (large pulses followed by small pulses in opposite polarity) or non-identical pulse pairs (small pulses followed by large pulses in the same polarity) [88, 89], as seen in Figure 4.12c of RHSL measurement. It should be noted that some of these preliminary measurements are quite noisy, particularly those in which a high resistance was measured, probably due to very low currents measured and short measurement times. Better quality data are expected for longer read measurements or by measuring at larger reading voltages.

By cross-comparison between the different sample's behaviour, the role of oxygen content in the L2NO4 film can be highlighted. Firstly, a change in the shape of the synaptic update can be seen in the depression processes (Figure 3.20a-c). In Figure 3.20b, the as-deposited sample shows noisy RPM values for V_{max} = +2.2 V and larger, due to relatively high resistance values. The O_2-annealed sample and the as-deposited sample seem to be better in terms of programming window, compared to the Ar-annealed sample. Thus, ±2.8 V pulses seem to be the best voltage amplitudes for RPM and SPM with the largest window and number of resistance states.

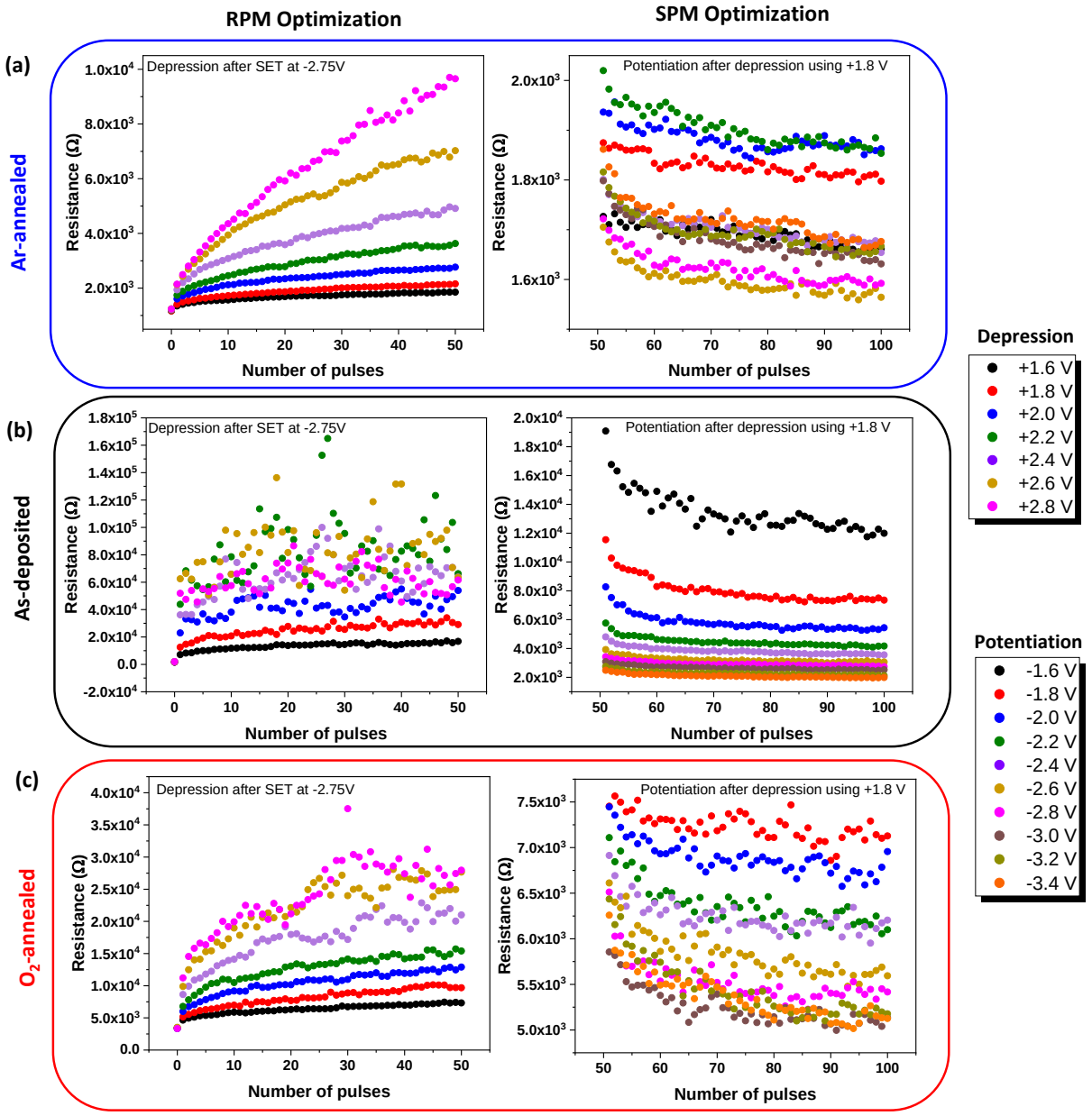

Figure 4.15: Evolution of resistance with the number of pulses during the RPM and SPM (depression/potentiation) for TiN/L2NO4/Pt memristive devices annealed in Ar (a and b), as-deposited (c and d) and annealed in O_2 (e and f). For RPM optimization, $+V_{max}$ varied from +1.6 V to +2.8 V, with a step of +0.2 V, a half voltage sweep of -2.75 V was applied prior to the RPM to set the device to LRS. For SPM optimization, RPM using 50 pulses of +1.8 V was applied prior to the SPM with $-V_{max}$ varied from -1.8 V to -3.4 V, with a step of -0.2 V.

4.3. Conclusions

In this chapter, we showed the structural properties of L2NO4/Pt samples submitted to different annealing treatments and the electrical properties of the corresponding TiN/L2NO4/Pt memristive devices built on those films. The main results are summarized below:

Structural characterization:

- Three L2NO4/Pt samples with different oxygen stoichiometries were obtained by post-thermal treatments. All of them consisted of continuous dense films composed of polycrystalline grains (from 25 – 40 nm) without decomposition but with grain coalescence of L2NO4 after the annealings, as confirmed by XRD and SEM surface imaging.
- By combining the information obtained by GI-XRD and Raman spectra, there seems to be a coexistence of tetragonal I4/*mmm* and orthorhombic *Fmmm* phases in the L2NO4 films
- By TEM observations combined with EDX on standard TiN/as-deposited L2NO4/Pt and TiN/Ar-annealed L2NO4/Pt memristive devices, it was possible to confirm the successful fabrication of the devices and the presence of a TiN_xO_y interlayer between the film and the electrode. The oxygen content in L2NO4 can be tuned, modifying the cell parameters consequently. The out-of-plane parameter *c* increases and the in-plane parameters *a* and *b* slightly decrease when the oxygen content δ increases. The XANES measurements confirm the important role of post-annealing treatment on the change of Ni-K edge position and, thus on the Ni oxidation state and oxygen content to compensate.

Electrical characterization:

- Initial resistance: Ar annealing allows for the highest IR obtained on TiN/L2NO4/Pt memristive devices, while the IR is smaller for the pristine sample and the smallest for the O_2-annealed sample. The influence of the post-annealing treatment on the electrical properties of L2NO4 and, thus, on the IR of the devices has been confirmed.
- TiN/L2NO4/Pt memristive devices based on as-deposited L2NO4 and reduced L2NO4 require a ‘soft-forming’ process before starting to operate the RS in the standard regime, while devices based on oxidized L2NO4 are forming-free directly exhibiting the standard RS. Generally, the post-thermal treatment affects the IR but not the ultimate RS of the TiN/L2NO4/Pt devices. Post-annealing in oxygen can be considered as an advantage to avoid the ‘soft-forming’ step in the operation of the devices.

- TiN/L2NO4/Pt devices showed gradual transitions for the SET and RESET processes, suggesting analogue RS can be obtained. The electrode area independence of HRS and LRS strongly suggests the switching scenario is filamentary.
- Multilevel resistance states can be programmed by different voltage amplitude in both sweep mode and pulse mode. RPM and SPM measurements show that it is possible to artificially mimic the depression-potentiation plasticity of bio-synapses on TiN/L2NO4/Pt devices with long-term data retention of at least four different resistance states. Moreover, the resistance change during the depression depends on the total pulse time applied to the devices, confirming the suitability of using TiN/L2NO4/Pt devices as artificial synapses and programming them in a flexible way.

Chapter 5: Study of the Electrochemical Changes during Switching in $TiN/La_2NiO_{4+\delta}/Pt$ Memristive Devices

The current chapter focuses on advanced characterization to gain a better understanding of the resistive switching (RS) mechanisms occurring on TiN/optimized-L2NO4/Pt vertical memristive devices. The first section is dedicated to transmission electron microscopy (TEM) and X-ray absorption near-edge spectroscopy (XANES) measurements in *ex situ, in situ* and *operando* modes under atmospheric conditions. The second section focuses on *in situ* TEM observations of a TiN/L2NO4/Pt lamella device under ultra-high vacuum conditions. The final section summarizes the main findings of the chapter.

5.1. Study of the switching mechanisms in standard devices under atmospheric conditions

5.1.1. Structural and chemical characterization by *ex situ* TEM

Throughout this subsection, five 100x100 μm^2 devices with different electrical histories were chosen from an as-deposited (non-annealed) sample (TiN/45-nm L2NO4/Pt) to prepare the lamellae for *ex situ* TEM observations. Table 5.1 summarizes the electrical history and resistance state of each of these devices. In order to allow for a meaningful comparison, the devices were selected so that their initial resistances (IRs) are relatively similar. A reading test consisting of a voltage sweep from 0 → 10 mV was applied to each device, and the current measured at 10 mV was taken to calculate the IRs, giving values between 3.5 kΩ and 6.4 kΩ for the different devices, as detailed in Table 5.1. One device was kept in its pristine state, and its lamella is hereafter named as lamella P. Two devices were programmed to HRS and LRS before the 'soft-forming' step, namely lamella H and lamella L, respectively. The two last devices were also programmed to HRS and LRS but after the forming, namely FH and FL, respectively. The resistance states measured after the programming steps are detailed in Table 5.1.

Table 5.1: Initial and programmed resistance of the five devices used to prepare the lamella for *ex situ* TEM observations

	Lamella P	**Lamella H**	**Lamella L**	**Lamella FH**	**Lamella FL**
Specimen description	Pristine state	Before forming, programmed in HRS	Before forming, programmed in LRS	After forming, programmed in HRS	After forming, programmed in LRS
IR (kΩ)	3.5	4.5	4.3	6.4	5.3
HRS (kΩ)	-	50	-	34.2	-
LRS (kΩ)	-	-	6	-	0.9

These five lamellae were used for TEM observations. Figure 5.1a represents the schematic of a TiN/L2NO4/Pt memristive device showing the region of interest (i.e., L2NO4/Pt and TiN/L2NO4 interfaces). The TEM images (Figure 5.1b-f) in scanning mode (STEM) show no major structural differences between the five states of the devices. The stack is formed by the three well-delimited layers: TiN (dark top layer), L2NO4 (sandwiched film formed by columnar grains) and Pt (light bottom layer). A thickness of 33.8 ± 1.7 nm was statistically measured for the L2NO4 film through the five STEM images. A very small roughness is observed for the bottom L2NO4/Pt interface, which becomes larger (RMS = 2.8 nm) at the top TiN/L2NO4 interface due to the columnar morphology of the film consisting of randomly-oriented grains. The rough surface of L2NO4 at some regions can result in the inhomogeneity of the TiN_xO_y interlayer (incontinuous).

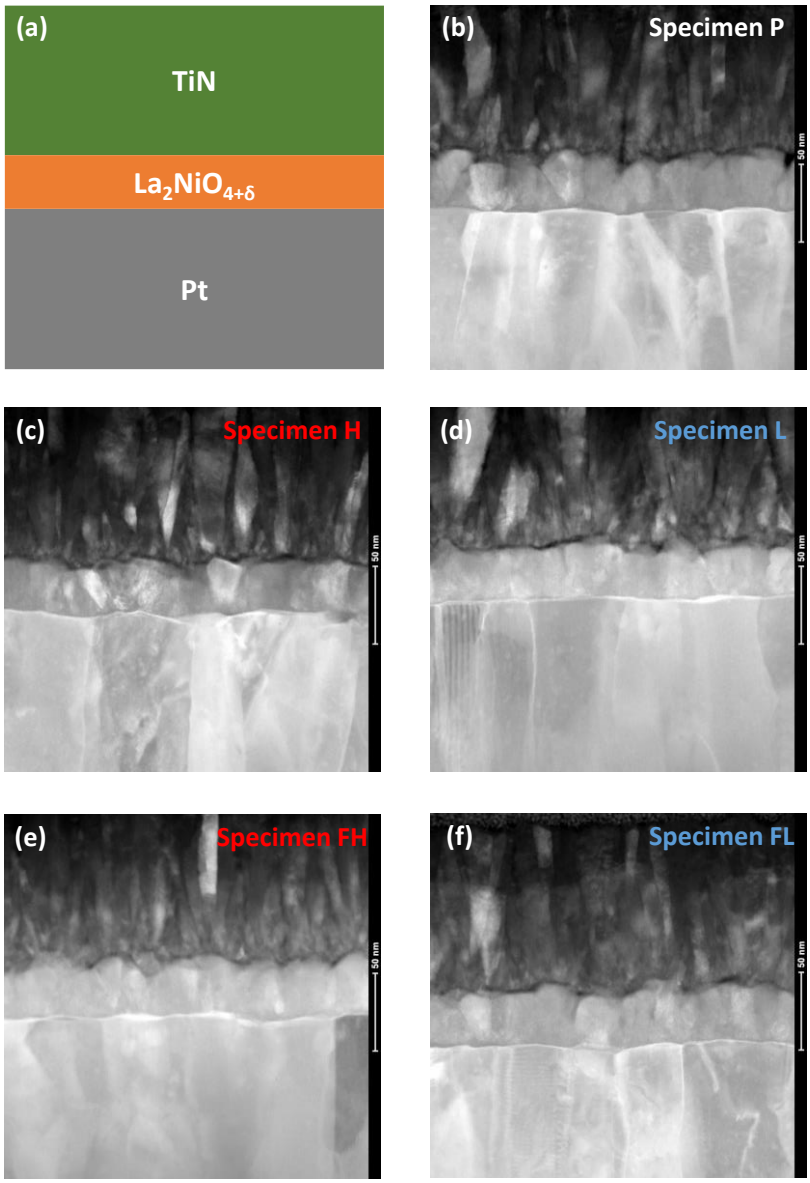

Figure 5.1: (a) Schematic illustrating the TiN/L2NO4/Pt stack of the lamellae prepared for *ex situ* TEM measurements. STEM images of (b) pristine device (specimen P), (c) device in HRS, no forming (specimen H), (d) device in LRS, no forming (specimen L), (e) formed device in HRS (specimen FH) and (f) formed device in LRS (specimen FL).

The EDX mapping analysis of the five lamellas is shown in Figure 5.2a-e. In each panel, a TEM image (high-angle annular dark field, HAADF) and its corresponding EDX elemental maps are shown. In general, three layers: the TiN top electrode, the L2NO4 switching layer and the Pt bottom electrode are observed, with clearly defined interfaces between them. A number of nano-inclusions can be observed at the L2NO4/Pt bottom interface. These regions contain Ni and O elements, but no La nor Pt, as seen in Figure 5.2a, b, c and e. In fact, NiO_x nano-clusters seem to form during the growth of the L2NO4 film

in regions where the Pt layer is not totally flat, but where there is a shallow "valley" instead, which might be formed by an incipient dewetting step of the Pt due to the high deposition temperatures used. The aggregation of NiO_x cannot be attributed to the electrical field used to program the devices since the NiO_x is present already in lamella P (the lamella in the pristine state prior to any electrical measurements). It should be noted that the NiO_x impurities are present locally at some places at the top part of Pt substrate but not everywhere within the L2NO4. NiO_x diffraction peaks have not been observed in the XRD patterns of the L2NO4/Pt samples, which can be attributed to the very small size of the nano-inclusions. As the resistivity of NiO_x is larger than that of L2NO4, these regions are not expected to act as "hot points" for filament formation. On the contrary, their global effect is expected to result in small inactive/less active switching regions. Instead of being totally vertical, the electric field lines would be expected to curve in the L2NO4 film around the nano-inclusions.

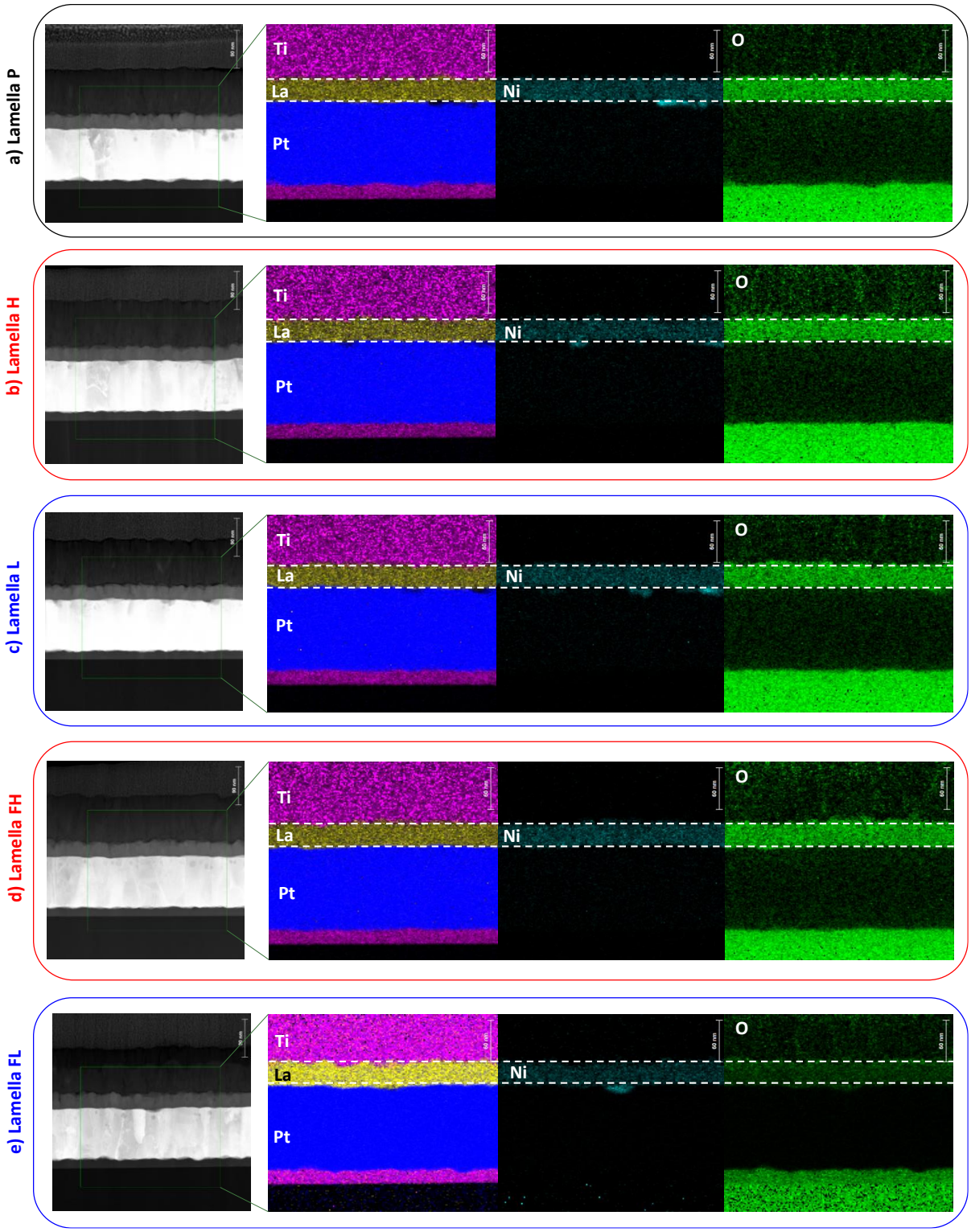

Figure 5.2: TEM (HAADF) images and their corresponding EDX elemental mapping for Ti (pink), O (green), La (yellow), Ni (cyan) and Pt (blue) of five lamellae: a) device in pristine state (P), b) device in HRS, no forming (H), c) device in LRS, no forming (L), d) formed device in HRS (FH) and e) formed device in LRS (FL). The white dotted lines serve as a guidelines.

To assess the evolution of the elements within the device stacks in five different resistance states, the EDX chemical profiles have been extracted from the EDX images (Figure 5.3a-e). The analysis was integrated on the whole area of the specimens, from the bottom SiO_2 layer to the the TiN top electrode (background of Figure 5.3a-e). It should be pointed that the oxygen atom is very light, thus, the quantification of oxygen by EDX becomes extremely difficult. In addition, surface oxidation on the free sides of the lamella during its preparation cannot be avoided in any FIB milling process. Thus, one should be very careful when analyzing the EDX oxygen profiles to avoid misinterpretations, particularly for the inter-comparison between different lamellas. If the thickness between lamellas is different, this can lead to different surface-to-volume ratios, and thus to different levels of surface oxidation during the FIB preparation. This seems to be the case of lamella FL (Figure 5.3e) in which a higher oxygen concentration has been measured in all the oxidizable layers: TiO_2, Pt, L2NO4, and TiN. It can be concluded that this "apparent" higher oxygen content probably comes from having a thinner lamella or a longer exposure to air. As this oxidation is expected to be homogenous within a particular lamella, we have limited the comparison of the oxygen profiles to a qualitative comparison of the shape of the profiles within different regions of the lamella.

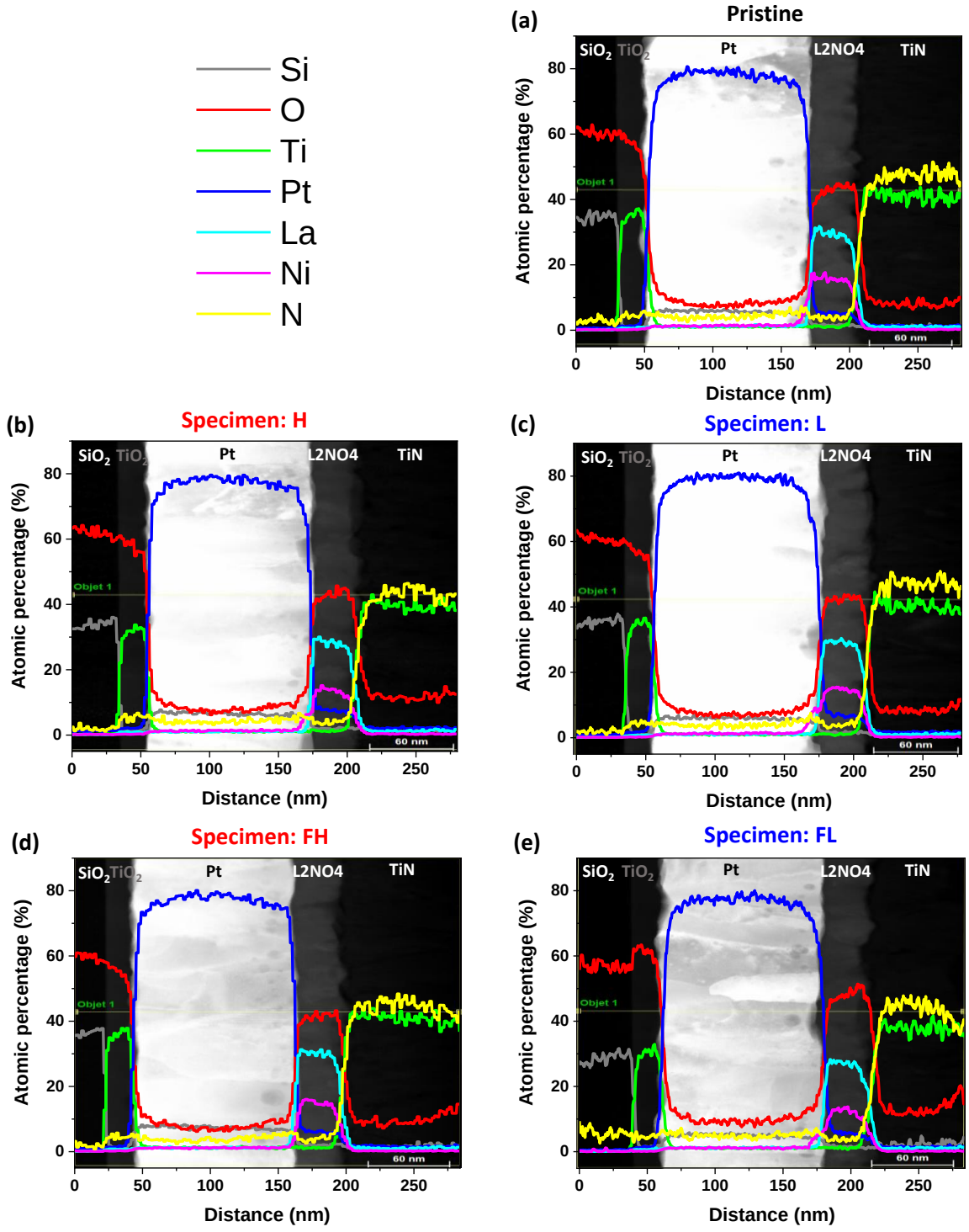

Figure 5.3: EDX chemical depth profiles (bottom to top) of the five specimens: a) pristine state (P), b) unformed device in HRS (H), c) unformed device in LRS (L), d) formed device in HRS (FH) and e) formed device in LRS (FL).

The EDX analysis confirms that no observable Pt, La nor Ti drift takes place within the device stack after the I-V sweeps nor after the 'soft-forming' step in standard laboratory conditions. Concerning the O element, a TiN_xO_y interlayer seems to be present in EDX profiles for all the lamellas measured. For a better comparison and in order to avoid artifacts due to the surface roughness, the EDX profiles have been replotted (see Figure 5.4a-e) by selecting only the L2NO4 region including its interfaces, and integrating in small regions where the film is relatively flat. The presence of oxygen within the TiN_xO_y interface is confirmed, at the L2NO4/TiN interface the La and Ni element counts start decreasing before the O counts (see red background corresponding to the O concentration). By comparing the five lamellas, small differences in oxygen accumulation at the L2NO4/TiN interface can be observed. In addition, except for the pristine lamella, it seems that oxygen might also be present within Pt at the bottom interface, particularly for the formed lamella. However, as only one region of each device has been measured it is not possible to distinguish if these small differences come from the electrical history of the devices, or from morphological differences. It should also be mentioned that if the 'active' regions governing the RS take place at localized positions in the sample (for example conductive filaments), such *ex situ* TEM measurements equipped with EDX could not reveal the differences.

Thus, to go deeper into the analysis an *in situ* experiment was designed, in order to analyse always the same lamella but for different resistance states. The results from this experiment are explained in detail in section 5.2.

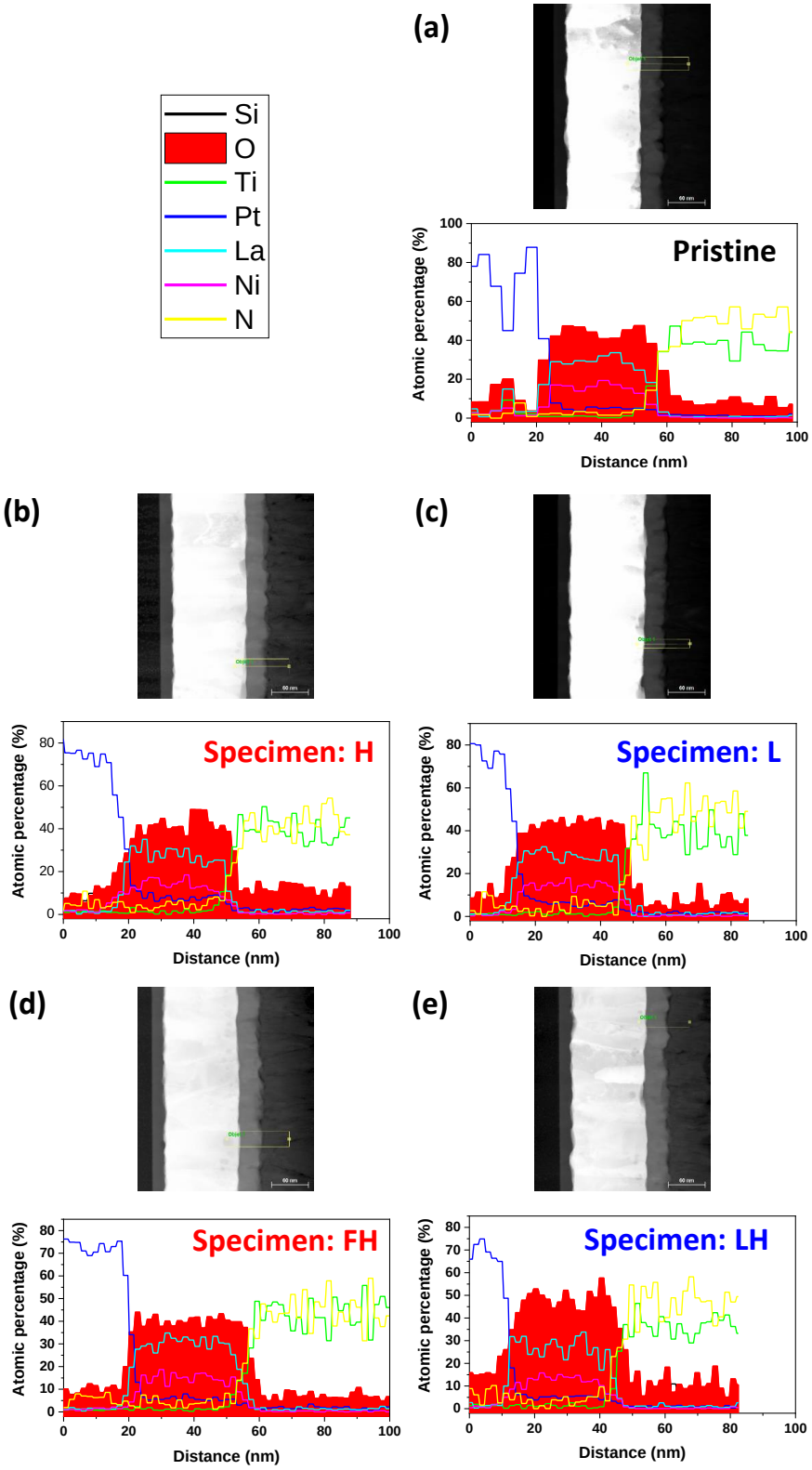

Figure 5.4: EDX chemical depth profile across the Pt/L2NO4/TiN stack for five specimens: a) pristine state (P), b) unformed device in HRS (H), c) unformed device in LRS (L), d) formed device in HRS (FH) and e) formed device in LRS (FL)

5.1.2. Characterization by X-ray absorption near edge structure (XANES)

5.1.2.1. XANES measurements in localized regions

The Ni K-edge position was measured to evaluate the differences in Ni oxidation state in different regions of an as-deposited L2NO4/Pt sample with TiN patterned top electrodes, and using a X-ray beam size of 50x50 μm^2. Two regions of interest (ROIs) were chosen: ROI 1 corresponding to a TiN electrode (50x50 μm^2 TiN/L2NO4/Pt device) and ROI 2 corresponding to an electrode-free region (bare L2NO4 film), as illustrated in Figure 5.5a. Two scans for ROI 1 and four scans for ROI 2 were carried out and averaged to improve the statistics. An enlargement of the region close to Ni-K edge is shown in the inset. It can be observed that the Ni-K edge of ROI 1 is shifted towards lower energy (8346.1 eV) compared to ROI 2 (8346.3 eV), suggesting the Ni in the L2NO4 film under the TiN (ROI 1) is more reduced. This reduction is expected to occur due to the diffusion of oxygen from the L2NO4 layer to the TiN electrode to form the $TiNO_x$ interlayer at the TiN/L2NO4 interface during the deposition of the TiN electrode. Similarly a reduction of the L2NO4 layer (shift of 0.10 eV) had been also previously observed under Ti electrodes compared to regions without electrode in a previous PhD thesis in the group [68]. The estimation of the Ni oxidation state and oxygen off-stoichiometry at ROI 1 and ROI 2 are reported in Table 5.2. The measurements in this subsection were performed during beamtime MA-4802 and were shifted to lower energy by $\Delta E = 2.3$ eV. The reader is referred to subsection 2.2.7 for more details and the calibration curve to determine the Ni oxidation state.

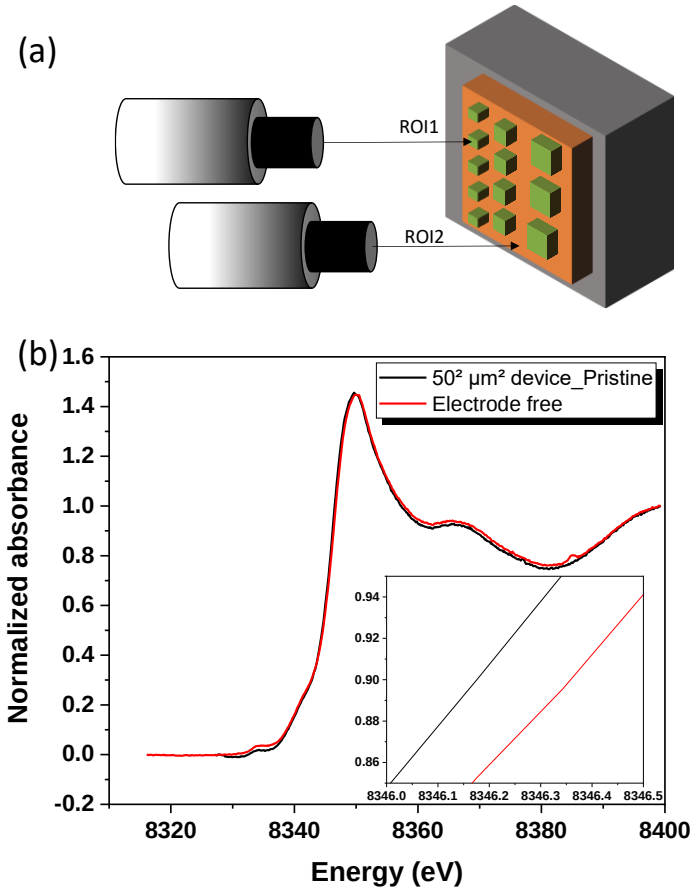

Figure 5.5: a) Measurement setup schematic showing the beam focused on the regions with a TiN electrode (ROI 1) and without electrode (ROI 2), b) the corresponding Ni-K XANES spectra (MA-4802) obtained at these two positions, the inset shows the shift of Ni-K edge.

Table 5.2: Measured Ni-K edge, estimation of Ni oxidation state and oxygen off-stoichiometry at ROI 1 and ROI 2

Beamtime	**MA-4802**	
Region	ROI 1 (TiN electrode)	ROI 2 (electrode-free)
Ni-K edge energy (eV)	8346.1 ± 0.1	8346.3 ± 0.1
Estimated Ni oxidation state	2.28 ± 0.03	2.34 ± 0.03
Estimated oxygen off-stoichiometry (δ)	0.14 ± 0.02	0.17 ± 0.02

Next, we performed XANES measurements at the Ni-K edge for the pristine devices and devices programmed *ex situ* at different resistance states (HRS and LRS). The electrical properties of these three devices are reported in Table 5.3. It should be noted that the programmed resistance states were before the 'soft-forming' step. The device is identified C12 (or pristine) corresponds to ROI 1 in the previous measurements.

Table 5.3: Electrical properties and measured Ni-K edge position of devices used in *ex situ* XANES

	Pristine	**LRS (no forming)**	**HRS (no forming)**
Identification	C12	C13	C2
Initial resistance (kΩ)	326	91	566
Programmed resistance (kΩ)	-	10	938
Ni-K edge (eV)	8346.1 ± 0.1	8346.1 ± 0.1	8346.0 ± 0.1
Estimated Ni oxidation state	2.28 ± 0.03	2.28 ± 0.03	2.25 ± 0.03
Estimated oxygen off-stoichiometry (δ)	0.14 ± 0.02	0.14 ± 0.02	0.12 ± 0.02

For each device, two scans from 8316 to 8400 eV were carried out. The XANES spectra of the three devices are presented in Figure 5.6, where each spectrum is an average of the two scans. The energy values obtained for the three devices are detailed in Table 5.3, and the differences measured between devices are rather small (0.1 eV). In order to extract conclusions from this comparison, there are some considerations that should be taken into account. Firstly, the IR state variation between these three devices is relatively large (between 91 and 566 kΩ), suggesting their Ni oxidation states might be already different at their pristine states. In other words, the Ni-K edge values of the devices obtained after being programmed might not only be related to the device's electrical history but also to differences in the pristine state. In addition, the variation of the beam over time should also be taken into account. Indeed, we have shown in table 2.1 (subsection 2.2.7) that the energy position at the Ni edge for a NiO powder sample measured in the same beamtime has different values for two different measurements (shift 1: 8347.3 eV, shift 2: 8347.4 eV, time between two shifts: 2 days). Furthermore, to have enough statistics, we performed two XANES full scans for each resistance state (around 2 hours of measurement). Because the XANES measurements were carried out in fluorescence mode, the counting times are long, making each XANES full scan took approximately 50 min to record. In other words, the small differences in the estimated Ni-K edge values of the devices obtained after being programmed might not only be related only to the device's electrical history, but also to device-to-device differences already in the pristine

state. Thus, it is difficult to extract rigorous conclusions on such *ex situ* XANES measurements where the difference between states is of 0.1 eV. In order to overcome these limitations, we designed an *in situ* XANES, which was carried out for one single device, to avoid the device-to-device variation. The results are presented in the next subsection.

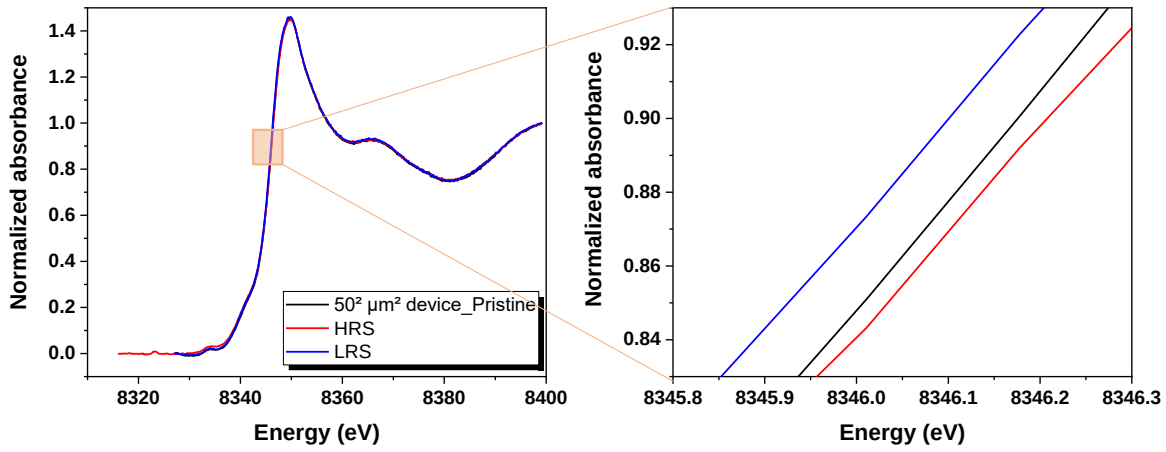

Figure 5.6: Ni-K edge XANES spectra measured on three TiN/L2NO4/Pt devices in three different resistance states (no forming): pristine (black line), HRS (red line) and LRS (blue line). The enlargement corresponds to a higher magnification focusing at the region close to the Ni-K edge.

5.1.2.2. In situ XANES full scan measurements

Two different XANES modes were carried out for devices operated in the beam hutch, which correspond to *in situ* and *operando* modes. The *in situ* mode consisted of four full scans XANES from 8316 to 8400 eV on a device performed after programming it in HRS or LRS (results presented in this subsection). The XANES measurements presented were carried out in beamtime MA-4802. The *operando* mode will be shown in the next subsection and consisted in measuring the intensity at a precise energy position corresponding to the Ni-K edge (or Ti-K edge) while the device was being electrically biased. *Operando* experiments were carried out both in beamtime MA-4802 and in beamtime MA-5230, although only the latter are presented in this chapter.

Figure 5.7a shows the results of the *in situ* XANES measurements, each spectrum is an average of four full XANES scans. The device was programmed to HRS and LRS (steps 1-2 and steps 4-5, respectively). The XANES spectra were recorded after the programming sweeps (steps 3 and 6) and are shown in Figure 5.7b. The Ni-K edges position obtained by the 1st derivative/fitting method is of 8346.1 eV for both LRS and HRS, with a slightly lower energy edge position obtained for HRS (see the inset). Since the difference between two Ni-K edge positions is very small (in the error range) and the RS observed in Figure 5.7a is forming-free (voltages used in this case are lower than those of standard RS), we

consider that the results are not conclusive, as the changes are close to the detection limit of the technique. This suggests that, as expected, the changes between the HRS and LRS are very small and another methodology is required to track the Ni-K edge changes. In addition, the XANES measurements show that the spectra maintain the same shape after having been electrically biased, suggesting a good starting point for *operando* XANES, which will be discussed in the next subsection.

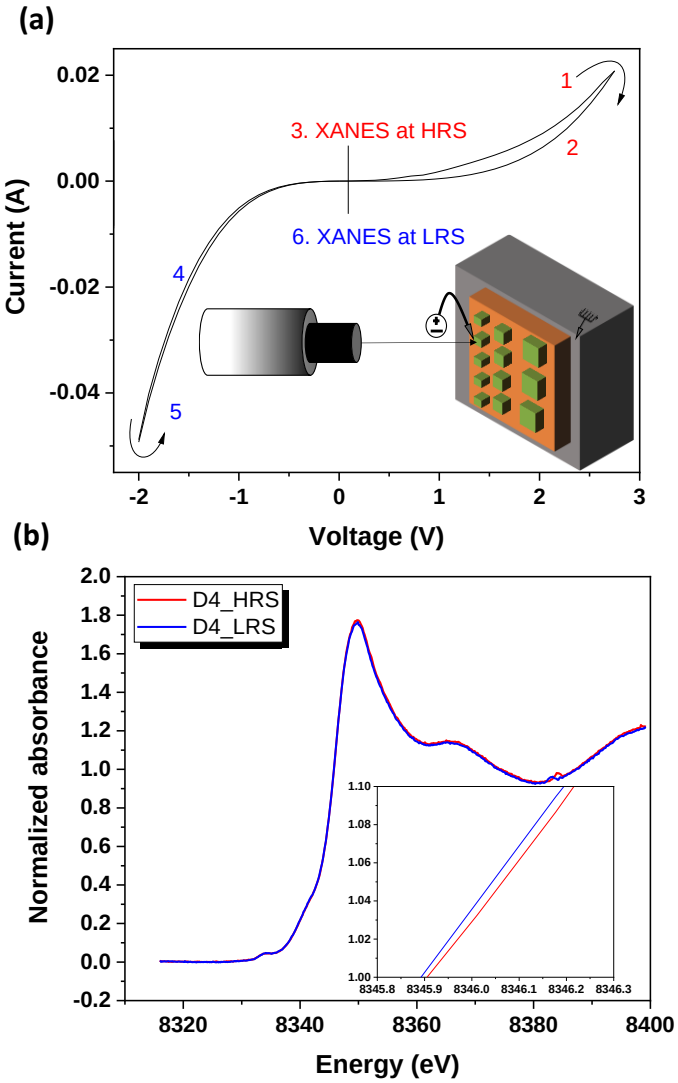

Figure 5.7: a) I-V sweep obtained for TiN/L2NO4/Pt device in the *in situ* XANES, voltage sweep sequence: 0 V → 2.75 V → 0 V → -2 V → 0 V (no forming). The inset showing a sketch of the *in situ* XANES setup where the TiN top electrode was biased while the Pt electrode was grounded. b) Ni-K edge XANES spectra obtained after each half cycle.

Table 5.4: Measured Ni-K edge energy, estimated Ni oxidation state and oxygen off-stoichiometry of HRS and LRS for *in situ* XANES measurements

	HRS (no forming)	**LRS (no forming)**
Ni-K edge energy (eV)	8346.1 ± 0.1	8346.1 ± 0.1
Estimated Ni oxidation state	2.28 ± 0.03	2.28 ± 0.03
Estimated oxygen off-stoichiometry (δ)	0.14 ± 0.02	0.14 ± 0.02

5.1.2.3. Operando XANES measurements at the edge position

During beamtime MA-4802, we carried out *operando* XANES measurements at the Ni K-edge, , which served as a preliminary results. In this subsection, the *operando* XANES measurements carried out during the following beamtime MA-5230 are presented, during which both the Ni-K and Ti-K edges were measured. The results regarding the Ni K-edge were similar for both experiments, confirming that the XANES measurements in *operando* mode are reproducible for different devices and samples.

It should be noted that in standard measurements (beamline and laboratory) the TiN electrode is always biased while the Pt electrode is grounded. However, during beamtime MA-5230 the biasing electrode was the opposite one: the Pt electrode was biased while the TiN electrode was grounded. This was initially done inadvertently at the beginning of beamtime MA-5230, and then for consistency we decided to keep the same configuration for all measurements throughout the beamtime. Hence, it should be noted that the switching sense of the I-V curves and pulses during MA-5230 (results presented below) is opposite to the normal operation presented in the rest of the thesis, although the shape is the same (symmetric).

Assessing Ni valence changes during operation

The concept of the *operando* XANES measurements with standard RS is illustrated in Figure 5.8a and b. The high-energy X-ray beam was focused on a selected TiN/L2NO4/Pt device, which initial resistance was of 43.6 kΩ. The device was then operated by the initialization process and 'soft-forming' step. The XANES spectrum of the pristine state is shown in Figure 5.8b and the Ni-K edge position was calculated to be 8345.5 eV. Next, the beam energy was fixed at 8345.5 eV and the intensity at this energy was continuously measured (Figure 5.9a) while the device was electrically biased by bipolar voltage sweeps (R-V characteristics of these sweeps shown in Figure 5.9c). Based on the obtained R-V curves and compared to those observed in the previous chapter, it is important to confirm that the memristivity

obtained in such *operando* XANES measurements are exactly similar to those we regularly obtain in the laboratory's measurements for the standard device. In Figure 5.9a an absorbance intensity vs voltage loop can be observed for each individual I-V cycle. However, the measurement is rather noisy as it is superimposed to a continuous absorbance intensity increase (drift) from cycle 1 to cycle 10 (from about 0.0101 to about 0.0106). In order to eliminate possible X-ray energy-drift perturbations, the combined I-V cycle and simultaneous X-ray absorption measurement at the edge position were consecutively measured ten times, and the averaged intensity values for each applied voltage are shown in Figure 5.9b. To interpret the meaning of the observed intensity changes by cycling, in the inset of Figure 5.8b, we observe that an intensity increase (from A to B) corresponds to a shift of the spectrum to lower energies (from A to F). As the shape of the spectrum does not change upon the electrical bias, as proven in Figure 5.7b, a rigid energy shift of the spectra can be considered. Reversely, a decrease in the Ni-K edge intensity (from A to C) corresponds to a Ni-K edge shift to higher energies (from A to G when a negative is applied to the device).

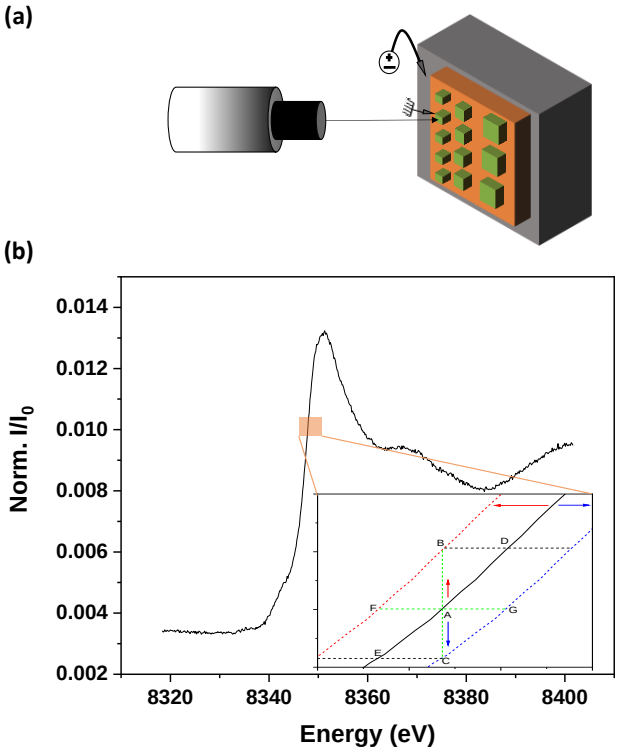

Figure 5.8: *Operando* XANES measurement for a TiN/L2NO4/Pt device. a) Scheme of the setup where the Pt electrode was biased while TiN electrode was grounded. b) Ni-K edge XANES spectrum measured in the pristine state to determine the Ni-K edge position prior to any electrical bias.

The device switches from HRS to LRS under positive polarity (see Figure 5.9d), with an abrupt change in resistance (SET) occurring around 2.25 V. As observed in Figure 5.9b, when a positive voltage sweep

is applied to the Pt bottom electrode, Ni is oxidized (revealed by the increase in Ni-K edge position or Ni oxidation state), which is coherent with the increase of oxygen concentration in L2NO4. It should be noted that the oxidation of L2NO4 occurs as soon as a small voltage is applied to the device, in a continuous manner from 0 to +2.7 V (maximum voltage applied), and then the Ni oxidation remains quite stable, while the device is biased back from +2.7 to 0 V. This could occur due to an oxygen ion drift from the $TiNO_x$ layer into the L2NO4 film, as the oxygen ions are attracted by the positive bottom Pt electrode. It can be observed that the abrupt change in resistance at 2.25 V is not accompanied by an abrupt change in oxidation state and could thus be related to the creation of a filament through the TiN_xO_y layer.

In opposite polarity (negative) the device gradually switches from LRS to HRS (RESET), while the Ni-K edge progressively shifts back to lower energy, corresponding to the reduction of Ni (loss of oxygen in the L2NO4 film). In this case, the oxygen ions from the L2NO4 would be re-incorporated into the $TiNO_x$ layer, blocking the filament and re-creating a continuous insulating layer. Again, the Ni oxidation state change is gradual from 0 to -2.7 V (minimum voltage applied), while it then remains quite stable when sweeping back from -2.7 to 0 V. These processes (resistance switching and Ni-K edge shift) are reversible, proving that L2NO4 acts as an oxygen exchange layer, and confirming that a valence change mechanism governs the RS in TiN/L2NO4/Pt devices. The change of Ni-K edge between HRS and LRS is very small (0.07 eV), which corresponds to an average change in the oxidation state of approximately $\Delta x \approx 0.02$ and a change in oxygen content of $\Delta\delta \approx 0.01$. These very small changes explain the difficulty related to the *ex situ* and *in situ* XANES measurements previously mentioned, and thus *operando* XANES plays a crucial role in proving the resistive switching mechanisms in this context.

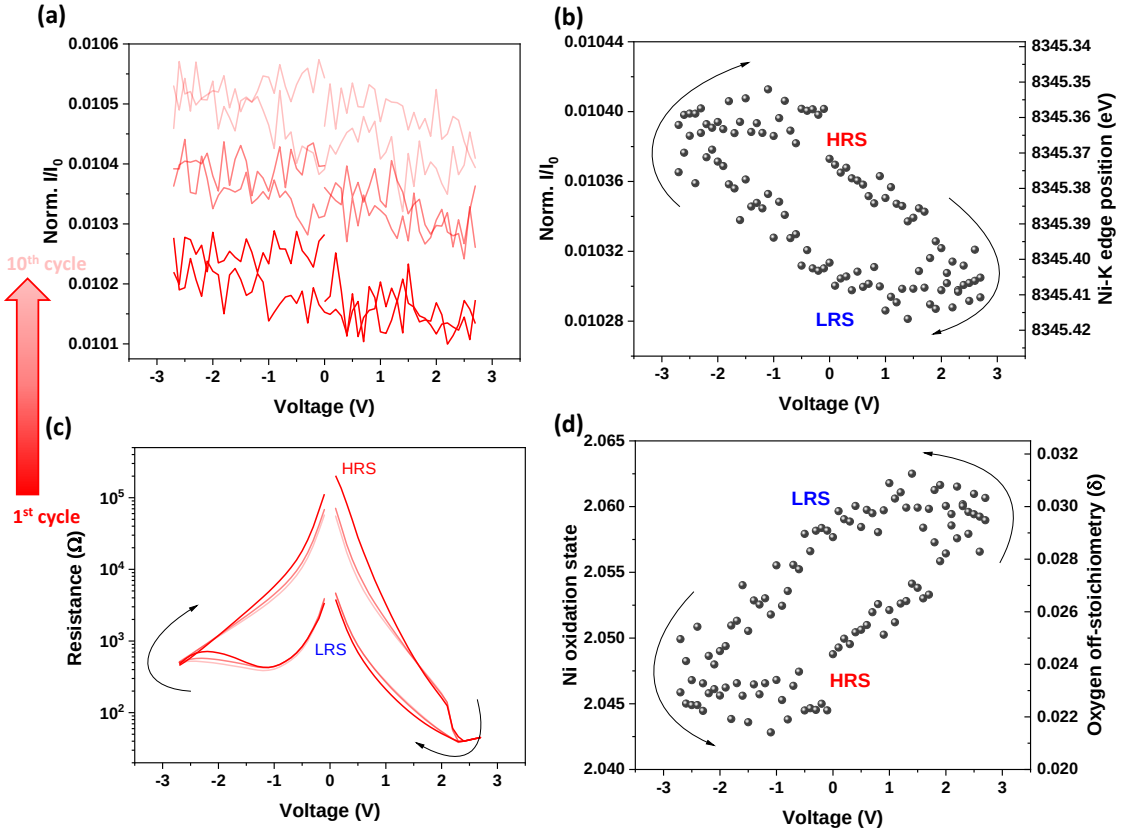

Figure 5.9: *Operando* XANES measurement for a TiN/L2NO4/Pt device. a) recorded intensity at the Ni-K edge (8345.4 eV), showing three of the ten voltage sweeps cycles. b) an average of ten cycles measured in a) and the calculated Ni-K edge position. c) Three over ten cycles of R-V characteristics were obtained after forming. d) evolution of Ni oxidation state and oxygen off-stoichiometry as a function of voltage, estimated by the Ni-K edge in b).

After the *operando* XANES with standard RS, the device was stabilized by a bipolar voltage sweep of ±2.7 V and was left at HRS_0 of 54.6 kΩ (resistance at time 0) prior to the *operando* XANES with potentiation/depression characteristics. Figure 5.10a shows the profile of the positive and negative sweeps used to control the resistance modulation (representing the potentiation/depression characteristics) of the TiN/L2NO4/Pt device. Ten consecutive positive sweeps (0 V → +2.2 V → 0 V, step of 0.1 V) followed by ten consecutive negative sweeps (0 V → -2.7 V → 0 V, step of -0.1 V) were applied to the device while the intensity of the Ni-K edge of 8345.5 eV was simultaneously recorded. The values of current (resistance) and intensity were taken at +0.1 V/-0.1 V of the positive/negative sweeps, respectively. Figure 5.10b presents the calculated resistance as a function of the number of cycles, showing that the application of repetitive electrical bias changes the device's resistance. It should be noted that the change from HRS_0 of 54.6 to LRS_1 of 7.0 kΩ (and from LRS_10 of 6.0 to HRS_11 of 62.3 kΩ) resistance is abrupt and occurs mainly after the first sweep. While the first positive/negative

voltage sweep induces a large change in resistance, the following nine sweeps only slightly decrease/increase the resistance value measured. As for the absorbance intensity, it can be observed that it initially decrases (quite linearly) after each positive sweep, and seems to stabilize after about 7 sweeps, corresponding to an increase in Ni oxidation state, and thus an increase in oxygen stoichiometry in the L2NO4 film. As for the change in Ni oxidation state during the RESET (LRS to HRS), it abruptly decreases after the first 3 sweeps, reaching a stable value of about 2.03. The smaller positive voltage (+2.2 V) applied allowed for a more gradual change in the Ni oxidation state (gradual incorporation of oxygen into the film), while the larger negative voltage applied (-2.7 V) allowed for a faster oxygen excorporation (in only 2 to 3 sweeps a stable Ni oxidation state is reached). Thus, it seems that the oxidation/reduction of Ni in L2NO4 is not the only factor governing the switching, and that two processes could occur simulatenously: oxido-reduction of Ni probably along the whole surface/volume and creation/dissolution of a conducting filament in the $TiNO_x$ interlayer. The shift of the Ni-K edge between the highest HRS and lowest LRS (≈ 0.2 eV) is larger than for the single sweeps presented in the previous section. This corresponds to an average change in oxidation state of approximately $\Delta x \approx 0.06$ and a change in oxygen content of $\Delta\delta \approx 0.03$.

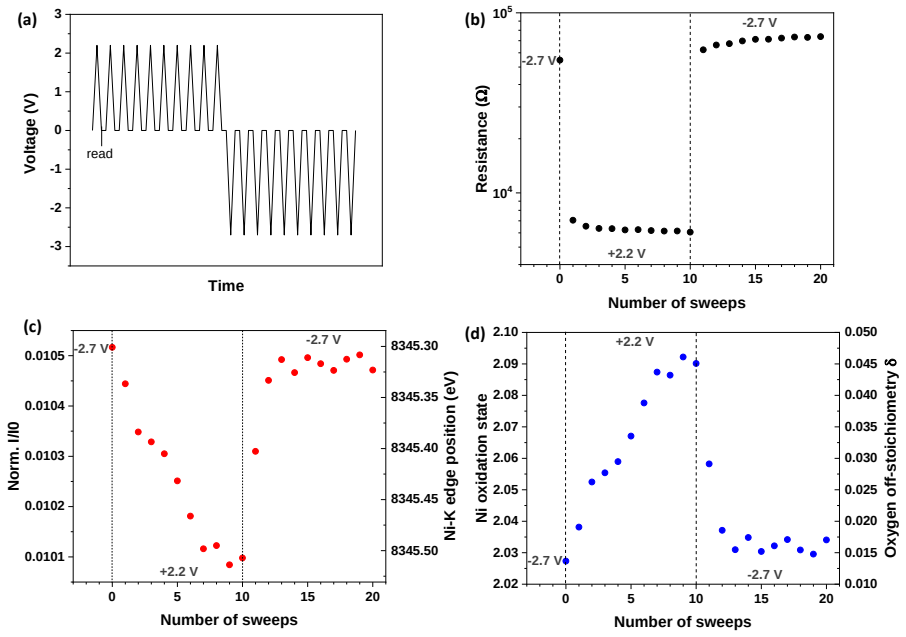

Figure 5.10: TiN/L2NO4/Pt memristive device: a) programming consequence where ten consecutive sweeps of +2.2 V/-2.7 V were applied for potentiation/depression measurements, respectively. b) measured resistance, c) absorbance intensity and estimated position of Ni-K edge, as well as d) estimated Ni oxidation state and oxygen off-stoichiometry (δ) as a function of the number of sweeps. The measured resistance shown in and absorbance intensity were taken at +0.1 V/-0.1 V of the positive/negative sweeps, respectively.

Assessing Ti valence changes during operation

In order to try to observe the oxidation/reduction of the $TiNO_x$ electrode while cycling the TiN/L2NO4/Pt device, Ti-K edge XANES measurements in *operando* mode were carried out, similar to *in situ* Ni-K edge XANES reported in the previous results (see Figure 5.11a). The Ti-K edge position of the XANES spectrum in Figure 5.11b is determined by the first derivative method and gave a value of 4978.5 eV. The Ti-K edge energy was kept constant while the device was electrically stressed by ten cycles of voltage sweeps, as shown in the R-V curves of Figure 5.12a. As in the previous measurements, the Pt electrode was biased while the TiN electrode was grounded.

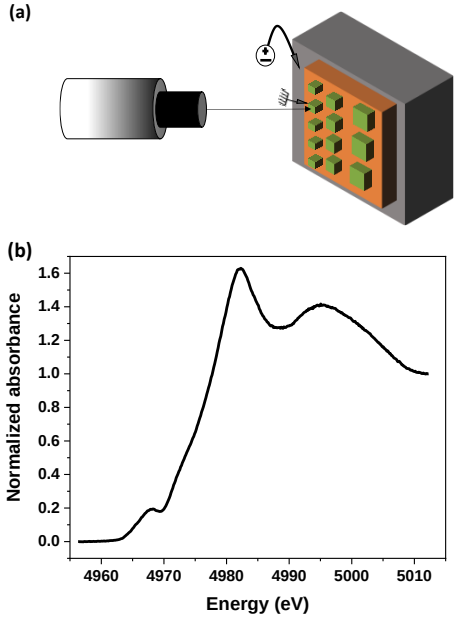

Figure 5.11: *Operando* XANES measurements focused at the TiN/L2NO4/Pt device. a) illustration of the setup where the Pt electrode was biased while TiN electrode was grounded. b) Ti-K edge XANES spectrum measured in the pristine state to determine the Ti-K edge position prior to any electrical bias.

Figure 5.12b shows the intensity as a function of the voltage for the three first I-V cycles as an example of the intensity evolution during cycling. The shape of each of the cycles is different and somewhat chaotic. While during the first cycle the intensity continuously increases with time leading to an open cycle, during the second and third the evolution is different, with a closed and an open cycle, respectively. We thus belive that the average values of several cycles is unreliable for the Ti K-edge measurements as, contrary to what occurred when measuring the Ni K-edge, in this case the averaged shape will depend on which exact cycles are selected. This observation might be because of the noise and/or the electron injection which happened every hour during the beamtime, as the intensity variation

due to the beam seems to be larger (or in the same range) than those due to the voltage application. Unfortunatley it is not possible to disentagle both contributions.

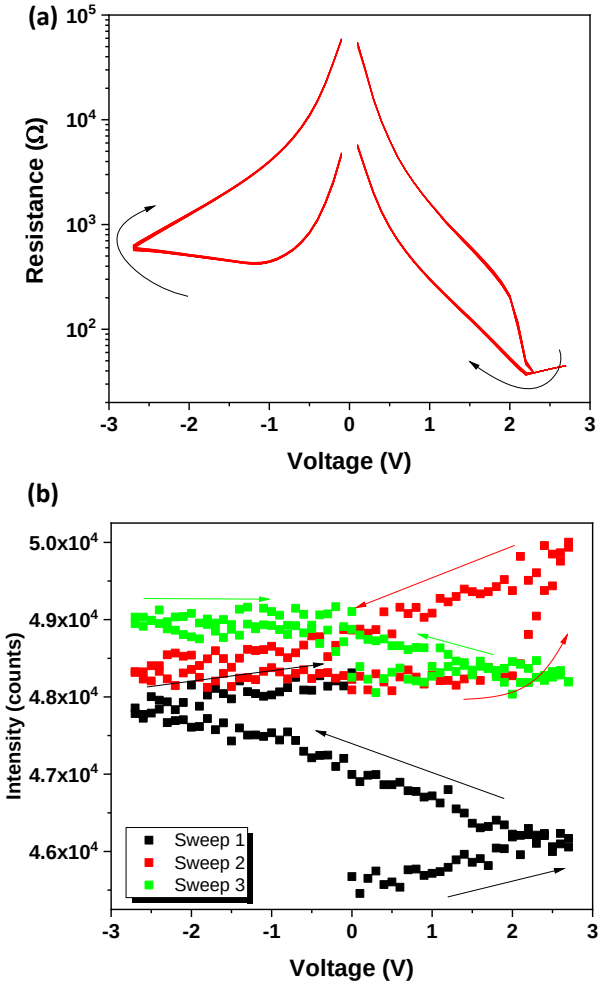

Figure 5.12: *Operando* XANES focused on Ti-K edge: a) Obtained R-V characteristics for ten switching cycles showing the standard switching and the high reproducibility of switching b) measured intensity of Ti-K edge for the first three switching cycles showing the variation and unclosed loops.

5.2. *In situ* study of the switching mechanisms in a TEM lamella device under ultra-high vacuum conditions

As discussed in subsection 5.1.1, it is very challenging to compare *ex situ* TEM observations for different lamellas which have been programmed *ex situ* to HRS and LRS. Moreover, it is not possible to quantify reliably the oxygen content of a sample by EDX, as this technique is not very sensitive to light elements. Thus, a lamella device (about 10 µm long and about 140 nm thick) was prepared for *in situ* measurements using an STEM microscope equipped with electron energy loss spectrocopy (EELS). The

N-K edge, Ti-K edge and O-K edge were measured at the region of interest for different resistance states. Beforehand, STEM images and EELS spectra were taken in the pristine state prior to any electrical bias (see sketch showing history of the measurements in Figure 5.13). Next, a series of voltage sweeps were applied to the TiN/L2NO4/Pt specimen to perform the initialization and soft-forming with careful control of the current compliance, until the standard RS was achieved (see R-V measurements in Figure 5.13).

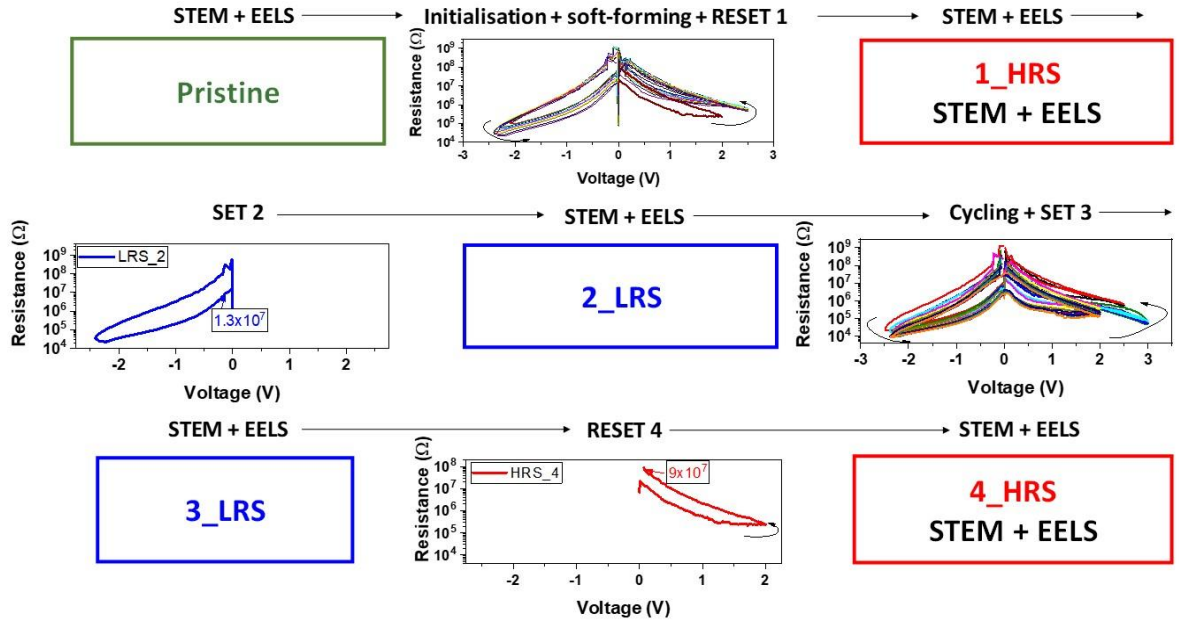

Figure 5.13: Sketch showing the history of the *in situ* TEM measurements. STEM images and EELS spectra in pristine state were carried out beforehand. STEM images and EELS spectra for HRS_1, LRS_2, LRS_3 and HRS_4. Initialisation, forming and RESET were acquired between pristine state and HRS_1. The lamella was cycled 13 times between LRS_2 and LRS_3.

In this subsection, the results corresponding to the lamella at four resistance states, programmed by half-voltage sweeps (as seen in Figure 5.14a and b), will be presented. It should be mentioned that, as shown in R-V curves of Figure 5.13, cycles (HRS_1 and LRS_2) and cycle 2 (LRS_3 and HRS_4) do not correspond to consecutive cycles, as there lamella device was cycled 13 times in between, progressively changing the voltage range and current compliance values. The current compliance for the SET process in negative polarity was increased for the second cycle (from 0.1 to 0.27 mA).

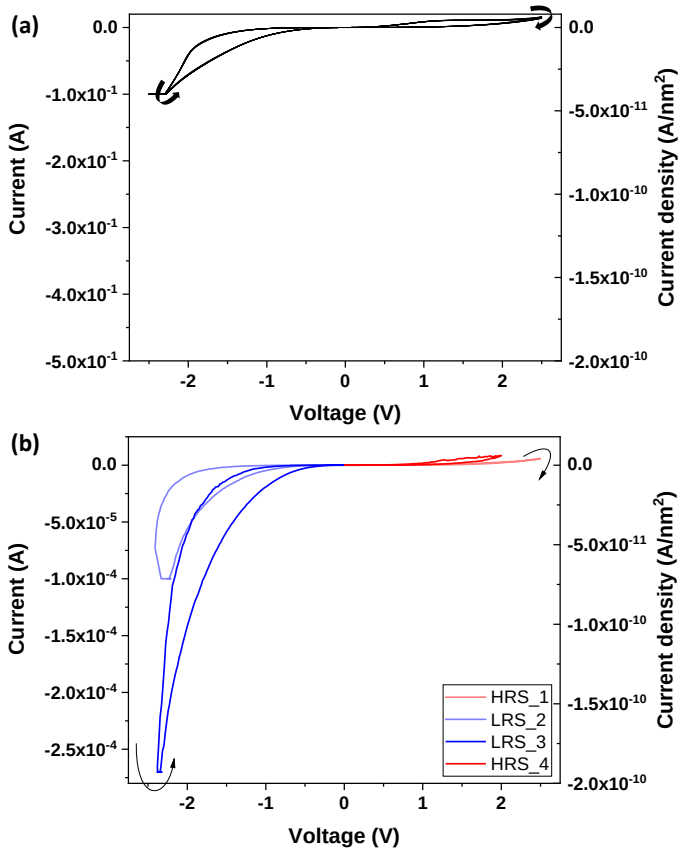

Figure 5.14: I-V characteristics of TiN/L2NO4/Pt devices, as examined in a) 50x50 μm^2 device (standard conditions) and b) 10x0.14 μm^2 during the *in situ* TEM measurements (ultra-high vacuum).

STEM images and EELS spectra were acquired for five lamella in different resistance states, as specified in Table 5.5 (details of the last electrical sweep prior to the observations shown in the table). The HRS/LRS ratios are around 10 (HRS_2/ LRS_1) and 37.5 (HRS_2/ LRS_1) for 1st and 2nd cycle, respectively, which are comparable to that of the standard memristive device (around 37). It should be noted that the I-V curves corresponding to cycle 1 (HRS_1 and LRS_2) are very similar and reach similar current densities to those measured for standard 50 μm^2 devices (see Figure 5.14a), while those corresponding to cycle 2 (LRS_3 and HRS_3) reach a much larger current density during the negative half-cycle (see Figure 5.14b).

Table 5.5: Electrical information of the examined lamella devices during the *in situ* TEM measurements

		Cycle 1		**Cycle 2**	
	Pristine	**HRS_1**	**LRS_2**	**LRS_3**	**HRS_4**
$-V_{max}$ (V) SET	-		-2.5	- 2.5	-
$+V_{max}$ (V) RESET	-	+2.5		-	+ 2.0
Current compliance (mA)	-	0.1	0.02	0.27	0.02
Measured resistance (MΩ)	275	130	13	2.4	90

Figure 5.15 shows the STEM images and oxygen and titanium EELS maps for the five different states. The blue horizontal lines added in each panel of Figure 5.15 serve as a visual indication of where the L2NO4 film interfaces are initially observed by STEM imaging (in pristine state). Small differences were observed in the EELS maps between the pristine state and the first two resistance states (HRS_1 and LRS_2). The O K-edge EELS maps for the HRS_1 and LRS_2 show a quite homogenous oxygen content throughout the L2NO4 film. However, the interfaces do not seem as sharp as the pristine lamella. Indeed, it seems that the interfaces become broader; some titanium has drifted from the top TiN electrode into the L2NO4 film, and some oxygen has drifted from the L2NO4 film into the top region of the Pt electrode. In addition, larger differences are observed for the last two resistance states (LRS_3 and HRS_4 states), after many I-V cycles with a final SET operation at a large negative voltage (-2.5V) and a large current compliance (0.27 mA). An oxygen gradient is observed within the L2NO4 film, with an oxygen depletion at the top surface. Both interfaces have become broader. Ti is clearly present in the top 10 nm of the L2NO4 film (see the column of Ti K-edge maps in Figure 5.15), and oxygen is also present at the top part of Pt bottom electrode (5-6 nm), as shown in the O K-edge maps in Figure 5.15). These observations suggest that the RS mechanism under these operation conditions is more intricate than a simple oxygen ion movement, as here both an anionic (oxygen) and a cationic (titanium) ion drift occurs over the whole electrode surface upon voltage application. It is also worth noting that Ti drift is not expected to occur to this extent in standard devices and standard operation conditions, as it has not been observed by *ex situ* TEM subsection 5.1.1. This observation has only been detected in lamella devices when a high current compliance of 0.27 mA was used, reaching high current densities of about 1.8×10^{-10} A/nm^2. Joule heating effects are expected to occur during the SET process. The high temperatures reached might lead to titanium diffusion and to oxygen gas being formed, and thus in oxygen being removed from the L2NO4 material. We expect these processes to occur primarily for lamella devices with a very large exposed area and inside the TEM in ultra-high vacuum conditions. Nevertheless, Ti drift in a much shorter length scale cannot totally be discarded in standard devices.

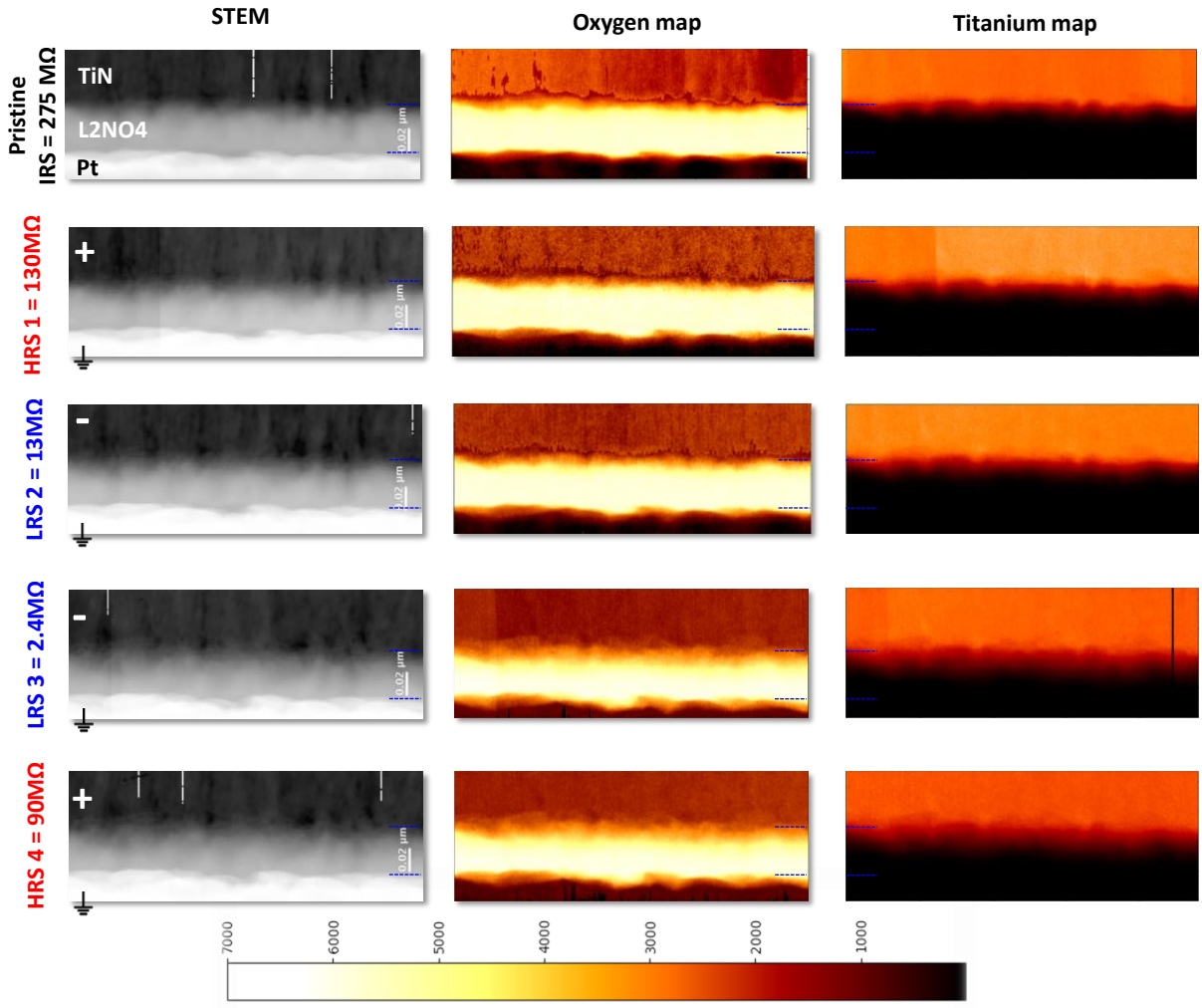

Figure 5.15: STEM images (first column), EELS oxygen maps (second column) and EELS titanium maps (last column) for five resistance states (pristine, HRS_1, LRS_2, LRS_3 and HRS_4). Their resistance values are added at the left part.

Figure 5.16 presents the STEM image of TiN/L2NO4/Pt device stack, showing the region of interest (ROI) where EELS spectra were integrated for five resistance states. The ROI consists of a number of lines in a row, separated by either 1.0 nm (for pristine state) or 1.2 nm (for the other four states). Thus, 25 and 21 corresponding EELS spectra were obtained for pristine state and the other four states, respectively.

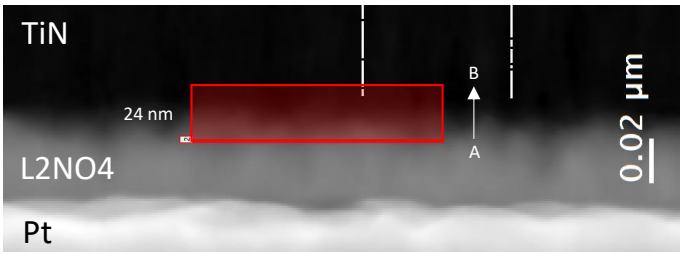

Figure 5.16: STEM image showing the geometry of the device and the region of interest (ROI) marked by a red rectangle, which is 24-nm high and is centered at the TiN/L2NO4 interface. EELS spectra were integrated in lines, from point A to point B. Along the AB side, the ROI is divided into 25 lines (step of 1.0 nm) for the pristine state and into 21 lines (step of 1.2 nm) for the HRS_1, LRS_2, LRS_3 and HRS_4, respectively. Each line corresponds to an EELS spectrum shown in the figures below.

The EELS spectra at the ROI (TiN/L2NO4 interface) are shown in Figure 5.17, Figure 5.18, Figure 5.19, Figure 5.20 and Figure 5.21, corresponding to the pristine state, HRS_1, LRS_2, LRS_3 and HRS_4, respectively. In general, the EELS spectra show that the N-K edge intensity is highest at point B, gradually decreases from B to A, and mostly disappears at point A, suggesting that nitrogen is obviously present within the TiN top electrode. A small amount of N is present at point A in LRS_3 and HRS_4, which could be due to the expansion of the TiN_xO_y interface, since the device had been cycled many times.

Similar observations are obtained for titanium: the Ti-$L_{2,3}$ edge intensity is highest at point B, then slowly decreases, and is barely visible at point A, for the pristine state, HRS_1 and LRS_2. However, titanium is present deep in the L2NO4 film (point A) in LRS_3 and HRS_4, revealing the Ti drift/diffusion into L2NO4 and thus confirming the extension of the TiN_xO_y interlayer because high current passed through the lamella. Clear changes of the Ti-$L_{2,3}$ edge are observed for the different positions and states, which will be replotted and discussed in the next paragraph.

Although the oxygen spectra are relatively noisy (compared to the Ti spectra) in the five resistance states, it can be observed that the O-K edge becomes visible and broader along the BA direction (from the TiN layer to the L2NO4 film), suggesting the presence of oxygen within the interlayer and L2NO4 film.

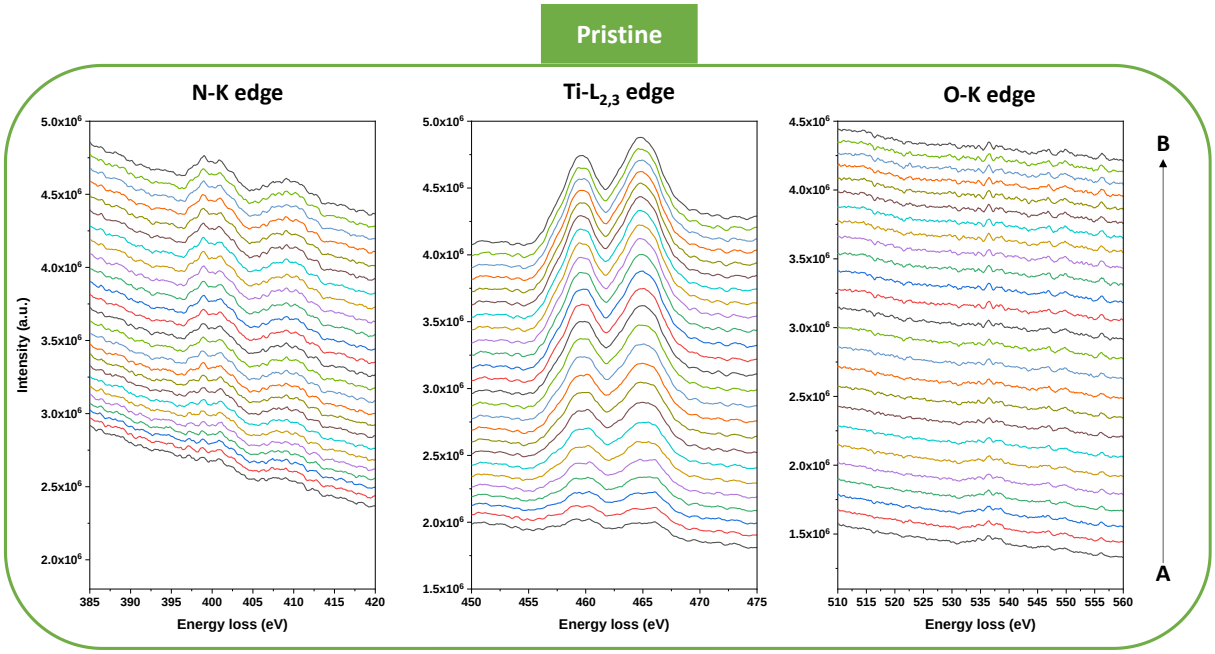

Figure 5.17: Integrated EELS spectra at the TiN/L2NO4 interface in pristine state. From left to right: N-K edge, Ti-$L_{2,3}$ edges, O-K edge. The bottom of the ROI marked by A and the top marked by B correspond to the ROI height (AB) of 24 nm shown in Figure 5.16.

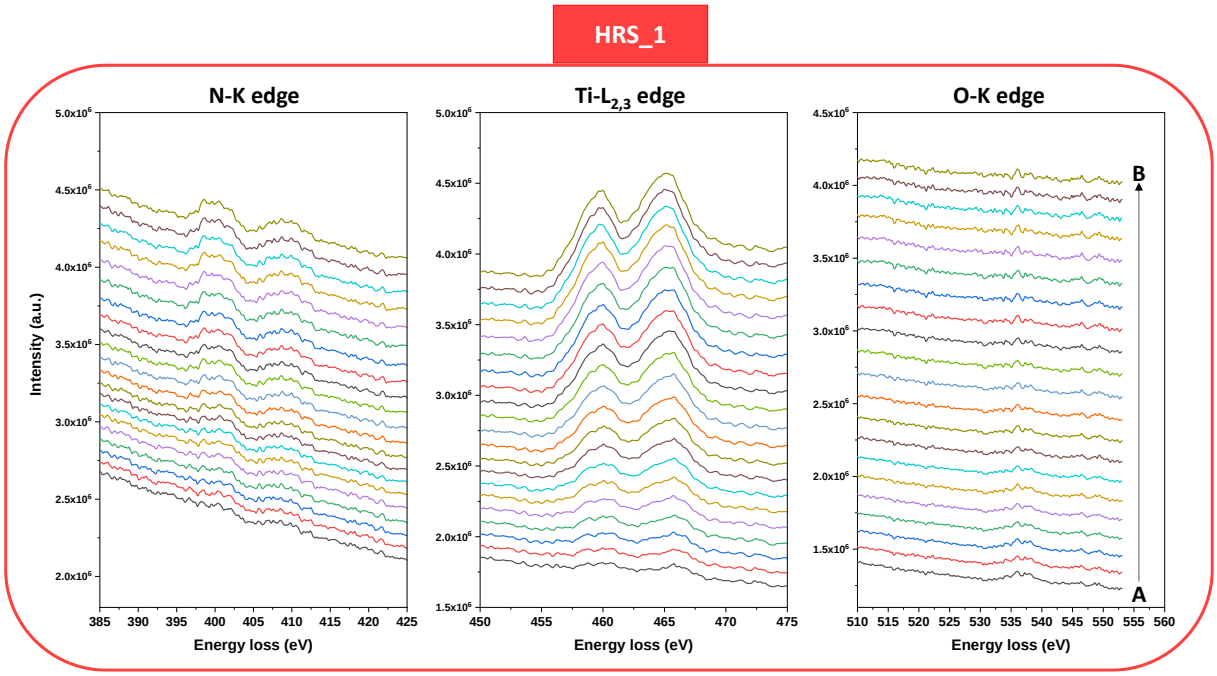

Figure 5.18: Integrated EELS spectra at the TiN/L2NO4 interface in HRS_1. From left to right: N-K edge, Ti-$L_{2,3}$ edges, O-K edge. The bottom of the ROI marked by A and the top marked by B correspond to the ROI height (AB) of 24 nm shown in Figure 5.16

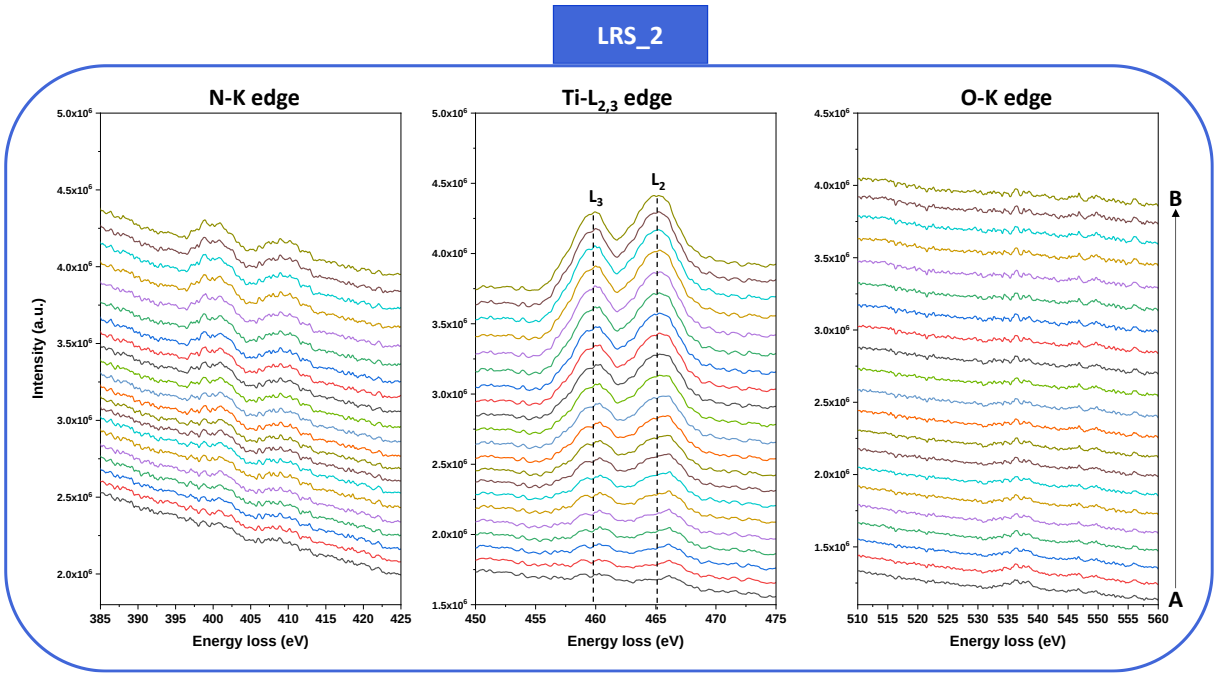

Figure 5.19: Integrated EELS spectra at the TiN/L2NO4 interface in LRS_2. From left to right: N-K edge, Ti-$L_{2,3}$ edges, O-K edge. The bottom of ROI marked by A and the top marked by B correspond to the ROI height (AB) of 24 nm shown in Figure 5.16.

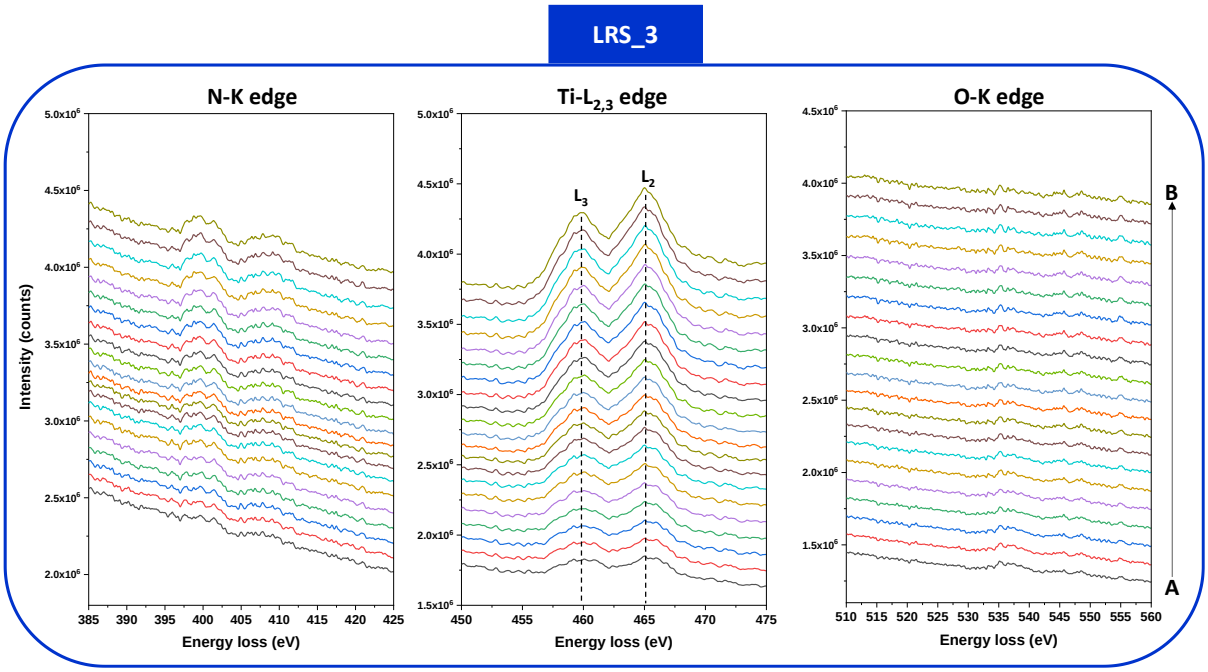

Figure 5.20: Integrated EELS spectra at the TiN/L2NO4 interface in LRS_3. From left to right: N-K edge, Ti-$L_{2,3}$ edges, O-K edge. The bottom of the ROI marked by A and the top marked by B correspond to the ROI height (AB) of 24 nm shown in Figure 5.16.

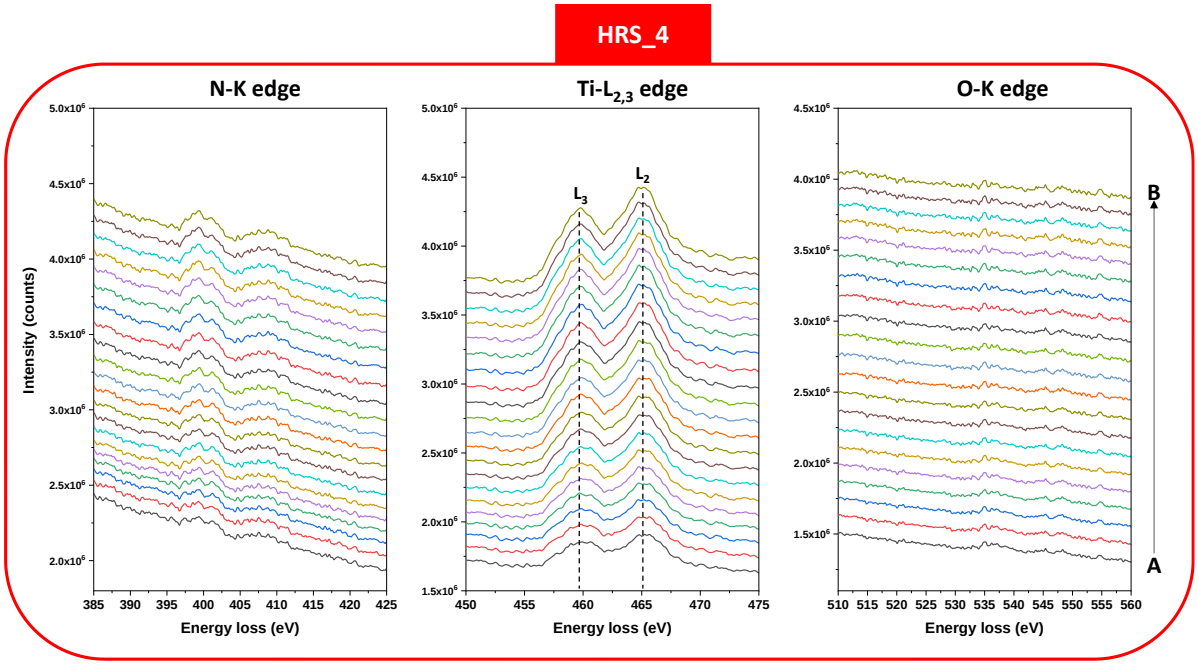

Figure 5.21: Integrated EELS spectra at the TiN/L2NO4 interface in HRS_4. From left to right: N-K edge, Ti-$L_{2,3}$ edges, O-K edge. The bottom of the ROI marked by A and the top marked by B correspond to the ROI height (AB) of 24 nm shown in Figure 5.16.

Thus, an energy shift in EELS spectrum or changes in the fine structure can idicate the change in crystallographic structure or in chemical compositions [90]. L_2 and L_3 edges are mainly studied as the main features to analyze EELS spectra of transition metals (such as Ti). Indeed, due to spin-orbit splitting of the 2p core hole, when an electron is excited, its transition from the 2p to the 3d states is known as the Ti-L_3 edge ($2p_{3/2} \rightarrow 3d$) and Ti-L_2 edge ($2p_{1/2} \rightarrow 3d$) [91]. The Ti-$L_{2,3}$ edges are marked as dashed lines in the Ti EELS spectra (Figure 5.22a). Abdallah *et al.* studied the chemical shift of the EELS Ti-$L_{2,3}$ edges to determine the composition at different regions of a sample through an oxide-alloy interface consisting of: oxide, titanium oxynitride interface, titanium nitride and Ti-based alloy ($Ti_6Al_2Sn_4Zr_2Mo_{0.1}Si$) (see spectra in Figure 5.22a) [90]. In that study, the Ti-L_3 edge and Ti-L_2 edge in the alloy (brown spectrum) were found at 457.0 eV and 462.5 eV, respectively. They are shifted to higher energy when entering to TiN_x region, then to higher energies and showing broader peak in the titanium oxynitride interface and, finally, start splitting into four peaks (t_{2g} + e_{2g} for each L_3 and L_2) when reaching oxide region. The shifts of Ti-$L_{2,3}$ edges towards higher energy with their "flattening" are used as typical signs to detect the oxidation of Ti (presence of Ti^{4+}) in this thesis. Indeed, depending on the Ti valence and the atomic surrounding (in TiO_2 rutile or anatase, six-fold coordination of Ti ions by surrounding O ions) degeneracy of Ti^{4+} can occur by the octahedral crystal field, leading to the splitting of unoccupied 3d into lower t_{2g} and higher e_g bands [92], as illustrated in Figure 5.22b.

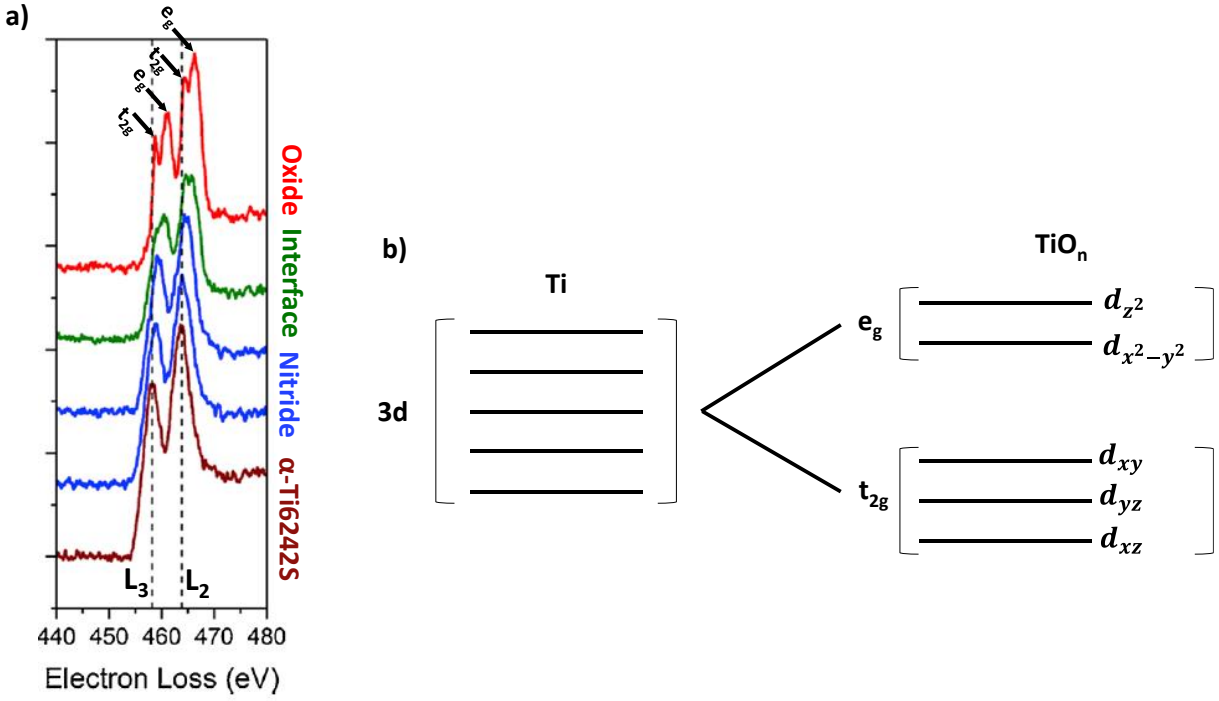

Figure 5.22: a) EELS spectra showing the evolution of the Ti-$L_{3,2}$ edges at different regions of interest: α-Ti6242S alloy, nitride, interface and oxide. Reprinted and adapted from reference [90]. b) Crystal field spitting of the degenerated Ti 3d electronic structure.

For a careful comparison of the oxidation state changes, the EELS spectra at the Ti-$L_{2,3}$ edges of these five resistance states are replotted in Figure 5.23. Only the representative spectra at 0 nm (point A), 6 nm, 12 nm, 18 nm and 24 nm (point B) within the ROI are shown. In pristine state at the top part of the ROI (positions: 24 nm, 18 nm and 12 nm), the Ti-$L_{2,3}$ edges are at 459.6 eV and 464.8 eV, respectively, which are shifted to higher energies compared to those reported for the Ti-based alloy (Figure 5.22a). This suggests that the top part of ROI is mainly TiN_x. At the bottom part of the ROI, the Ti-$L_{2,3}$ edges are broad and shifted to higher energies (compared to the top part of the ROI), suggesting the TiN_xO_y interlayer is present.

In HRS_1, the Ti-$L_{2,3}$ edges are split into four peaks at 0-nm and 6-nm positions, and they already seem to start splitting at the 12-nm and 18-nm positions (with relatively "flat" peaks observed). Visibly, the e_g-L_2 peaks of 6 nm and 12 nm increase in intensity (marked by red arrows), compared to those in the pristine state. This observation suggests that the TiN_xO_y interface is further oxidized thanks to the drift of oxygen from L2NO4 to TiN (triggered by the positive voltage sweep). It should be noted that between the pristine state and the HRS_1, many voltage sweeps had been applied to the lamella for its initialisation, soft-forming and RESET 1. In LRS_2, these peaks slightly decrease in intensity, and are slightly flatter and less asymmetric compared to HRS_1 (peaks marked by blue arrows), suggesting that

the ratio of Ti^{4+}/Ti^{3+} decreases. This can be explained by the reduction of the TiN_xO_y, which is related to oxygen ions drifting back into the L2NO4 film by RESET 1. However, it can be seen that the Ti-$L_{2,3}$ edge EELS spectra of the pristine state and those of the LRS_2 are very different, suggesting that the structure and chemical composition of the ROI has changed, and the device never come back to the same structural and chemical characteristics of the pristine state.

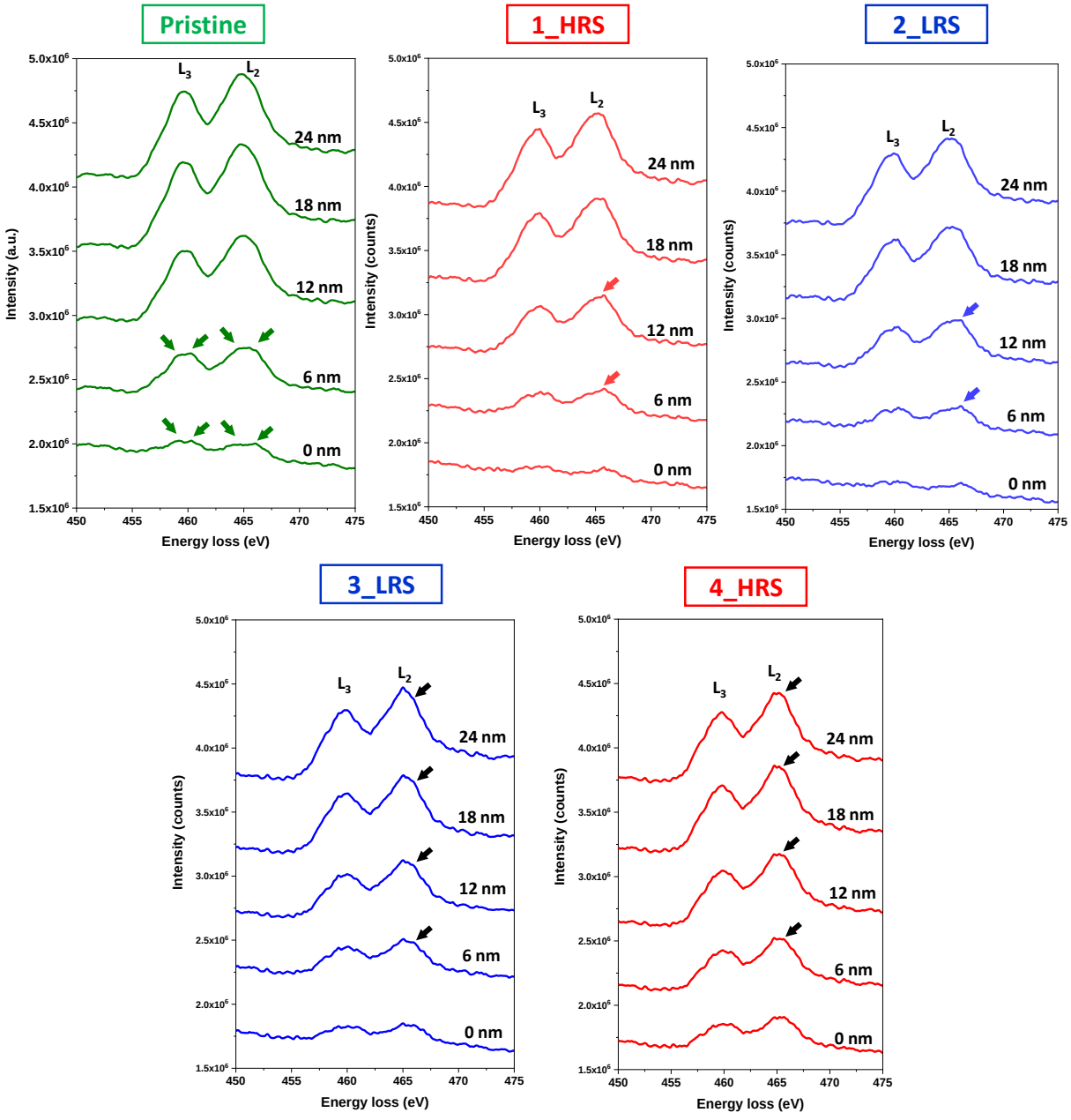

Figure 5.23: *In situ* resistive switching in a TiN/L2NO4/Pt TEM device lamella: Ti-$L_{2,3}$ edge EELS spectra at five different positions of a selected ROI at the TiN/L2NO4 interface for five different resistance states: pristine, HRS_1, LRS_2, LRS_3 and HRS_4.

The lamella was then electrically biased by 13 voltage sweeps with increasing current compliance up to 0.27 mA, before reaching LRS_3. By comparing the EELS spectra between LRS_3 and HRS_4, the main changes are observed in the e_g-L_2 peak at every position (marked by black arrows). It can be seen that the peak disappears/decreases in intensity for LRS_3 and appears/increases in intensity for HRS_4, being in agreement with that previously observed in HRS_1 and LRS_2. Moreover, in this second examined cycle (HRS_3 and LRS_4), the changes take place at all positions, including the 18 nm and 24 nm positions, where the splitting of Ti-$L_{2,3}$ is barely seen in the pristine, HRS_1 and LRS_2 states. This observation strongly suggests that more oxygen is incorporated within the interlayer (due to the high current applied). However, in the two last sweeps, the diffusion of cations (such as Ti, La, etc) due to Joule heating effect cannot be ruled out. In 2016 Baek *et al* [93] reported similar observations of Ti diffusion on TiN/PCMO/Pt devices, where they proposed an increase in the TiO_xN_y interlayer thickness with increasing voltage amplitude, as reprinted in Figure 5.24a-b.

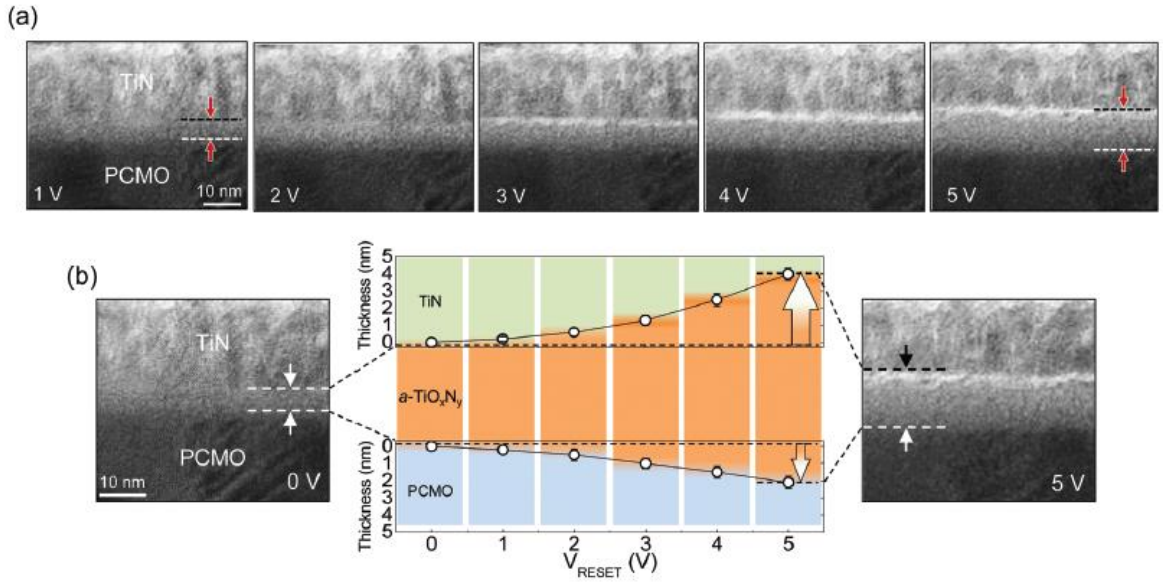

Figure 5.24: *In situ* TEM resistive switching of a TiN/PCMO/Pt junction device to the HRS. (a) A series of TEM snapshots captured at V_{RESET} during sequential positive bias sweeps by applying V_{RESET} from 1 V to 5 V in 1 V increments. Changes in the thickness of the a-TiO_xN_y reaction layer are indicated by red arrows. (b) Movement of the two reaction fronts of the a-TiO_xN_y layer, i.e., the a-TiO_xN_y/TiN (upper) and the PCMO/a-TiO_xN_y (lower) interfaces, traced with the increase in V_{RESET}. The a-TiO_xN_y/TiN interface moves faster than the PCMO/a-TiO_xN_y interface indicating that the drift of not only oxygen but also Ti ions contribute to the growth process with stronger influence of the oxygen ions. Reproduced from literature reference [93].

For a direct comparison, the EELS spectra of pristine, HRS_1 and LRS_2 in the five selected positions are replotted and displayed in the same graphs, as shown in Figure 5.25. The loss in intensity of HRS_1

(compared to pristine) might be related to the extension of the TiN_xO_y interface (due to Ti drift/diffusion during initialization process and RESET 1). However, the signs of Ti oxidation can be observed in HRS_1 by the shift of Ti-$L_{2,3}$ peaks of HRS_1 towards higher energy and their asymmetry (higher intensity at higher energy). When compared to HRS_1, the EELS spectra of LRS_1 present a flatter or more rounded shape and slightly lower intensity, being in agreement with the reduction of the TiN_xO_y interface.

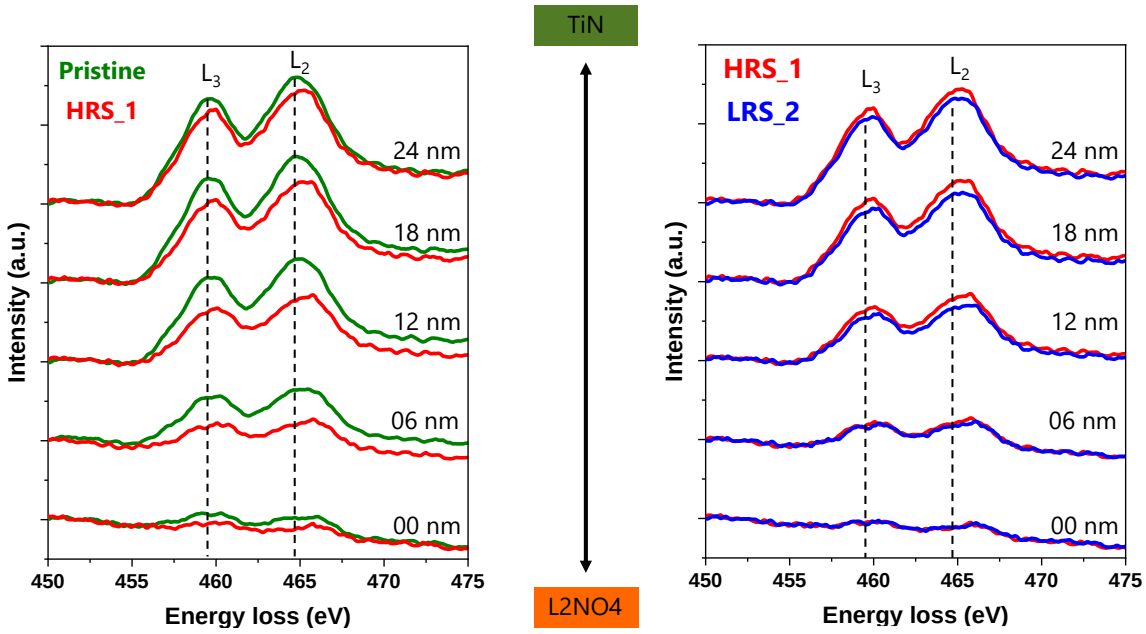

Figure 5.25: Ti-$L_{2,3}$ edge EELS spectra at five different positions of a selected ROI at the TiN/L2NO4 interface for pristine, HRS_1 and LRS_2 of in situ TEM observations. Data is replotted in the same graphs and similar to the one in figure 5.24. EELS spectra of pristine and HRS_1 are in the left graph. EELS spectra of HRS_1 and LRS_2 are in the right graph.

5.3. Proposed simplified model of the RS mechanisms in TiN/L2NO4/Pt devices

Based on the combination of all the XANES and TEM observations presented in this chapter, in addition to the electrical characteristics of the TiN/L2NO4/Pt devices presented in the previous chapter, a simplified RS model is presented in Figure 5.26a-b. The proposed model shows the coexistence of a filament-based and an interface-based valence change switching mechanism.

During the deposition of titanium nitride, when the TiN gets in contact with L2NO4, a TiN_xO_y interlayer is naturally formed between the L2NO4 and the electrode by the intake of oxygen, resulting in a thin and poorly-conductive $La_2NiO_{4+\delta'}$($\delta' < \delta$) interlayer. This assumption is supported by the experimental

obsevation of STEM images coupled with EDX (Figure 4.4), the *ex situ* TEM measurements coupled with EDX chemical profiles of five devices (subsection 5.1.1), the reduction of the Ni oxidation state in L2NO4 under the TiN region (subsection 5.1.2.1) and by the *in situ* TEM/EELS observations (section 5.2).

Considering firstly the soft-forming process (Figure 5.26a), when the negative voltage is applied to TiN, an electrochemical redox reaction takes place to reduce the TiN_xO_y and oxygen ions are re-incorporated into L2NO4, which gets oxidized. At a certain voltage (-2.2 V in the R-V graph of Figure 5.26a), the conducting paths (filaments in the form of TiN and $La_2NiO_{4+\delta}$, assuming that δ is high enough to be conductive) can be created, and thus the LRS is reached. From the second cycle on, the standard RS is highly-reproducible, which is believed to be related to the formation/dissolution of TiN filament(s). It is worth emphasizing that the initial HRS (IRS) is never reached again, once the filament is created. Thus, it is believed that the structure (and chemical composition) of the reduced L2NO4 and of the adjacent films have changed and could not be re-established to their initial state.

Next, considering the standard RS, we propose a coexistence of filament-type and interface-type switching. Indeed, as seen in chapter 4, the HRS and LRS do not scale with electrode area, which is a typical characteristic of filamentary RS. This type of switching is also strongly suggested by the abrupt decrease in resistance (switch from HRS to LRS), which is not accompanied by a large change in Ni oxidation state in *operando* XANES. In addition, the *in situ* TEM results (section 5.2) reveal electrochemical redox reactions associated with the switching of resistance. As observed by TEM (Figure 4.4, Figure 4.5, Figure 5.1 and Figure 5.16), in the observed devices the TiN/L2NO4 interface is not perfectly flat and sharp, and the thickness of the interlayer is not completely uniform, as presented here in the proposed model for simplicity. At some regions where the interface is thinner, the high electric field present could lead to a local soft-breakdown. Therefore, the L2NO4 film in standard RS would act as an oxygen reservoir layer, where the oxygen entering or coming out from the L2NO4 can be indirectly measured by the change in Ni oxidation state in *operando* Ni-K edge XANES measurements. Under positive bias, oxygen migration from L2NO4 into TiN would take place, firstly reducing the oxygen ion concentration within the L2NO4 (and thus more resistive L2NO4 is obtained), secondly further oxidizing the TiN_xO_y interlayer, and ultimately disconnecting the conductive filaments of TiN (reaching a HRS). Reversibly, LRS is achieved when the TiN filaments are re-connected (favored by the reduction of TiN_xO_y and the drift of oxygen ions back into the L2NO4 film).

This model is also in agreement with the long data retention which is usually observed in the RS based on filaments. Thus, the multiple resistance states obtained in potentiation/depression can be due to the

fine modulation (in size or composition) of either a single filament or several filaments thanks to the capacity of L2NO4 of in- and ex-corporating a wide range of oxygen stoichiometry.

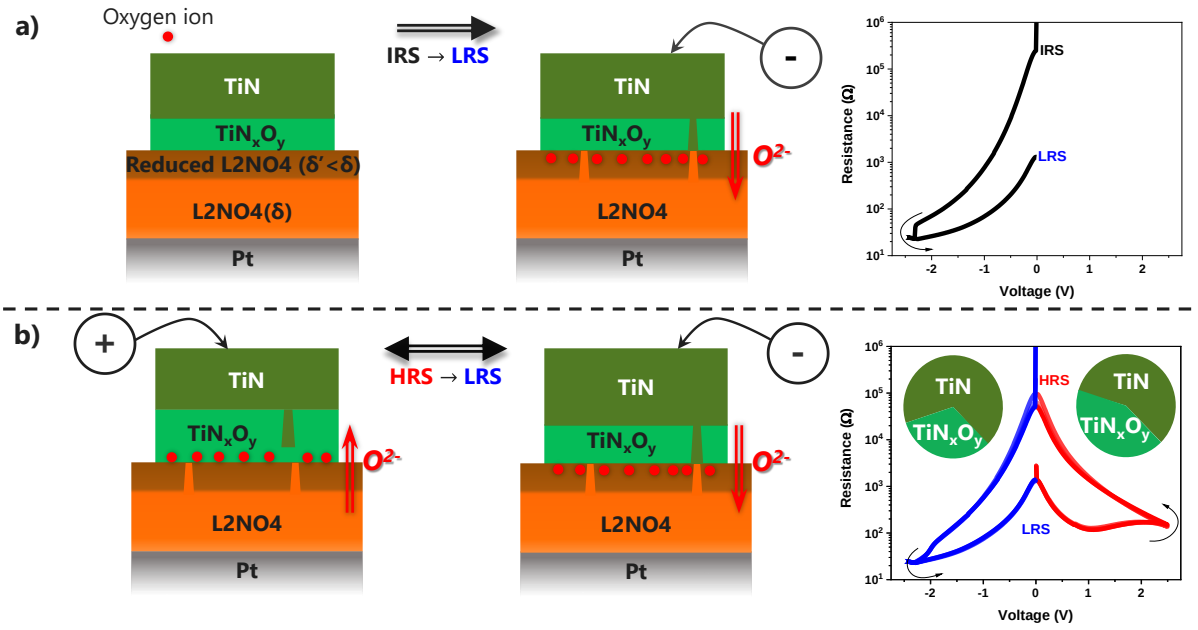

Figure 5.26: Simplified phenomenological model of a) the soft-forming process and b) standard switching mechanism observed in TiN/L2NO4/Pt vertical devices. The corresponding R-V characteristics are added for a better understanding.

5.4. Conclusions

In this chapter, we aim to get better insights underlying the memristivity obtained on TiN/L2NO4/Pt devices by using TEM and XANES techniques in different modes and conditions. The main points can be summarized below:

Characterization technique acquired in atmospheric conditions:

- *Ex situ* TEM: STEM images showed that no major structural differences between five memristive devices, which were in five different resistance states, were observed. The L2NO4 film thickness of 33.8 ± 1.7 nm was statistically measured by these five specimens of memristors. In general, the roughness was found to be relatively small at the bottom interface of L2NO4/Pt and becomes larger at the top interface of TiN/L2NO4. The columnar structure of polycrystalline L2NO4 film and grain boundaries are observed, which are probably the places where the filaments could be present if they govern the observed RS. EDX elemental maps reveal the aggregation of nickel oxide at the top part of Pt substrate, which is expected to not strongly affect on the memristivity of such devices. EDX depth profiles, even though they show

small differences in oxygen concentration at the TiN/L2NO4 interface and/or electrodes (TiN and Pt) in different resistance states, make it turns into the difficulty of extracting conclusions without artifacts as oxygen is insensitive to such characterization technique and the obtained RS could be governed by filaments.

- *Ex situ* XANES: Ni-K edge at the region under TiN shifts to lower energy by 0.2 eV (compared to the electrode-free region) confirming the reduction of Ni in L2NO4, strongly suggesting the presence of the interlayer. The difference between Ni-K edge energies of three devices (pristine, HRS and LRS without forming) was too small (in the range of 0.1 eV). In addition, the initial resistances of these three devices were largely different. Thus, the small change of Ni-K edge in such measurements is not reliable.
- *In situ* XANES: reveals the same Ni-K edge in HRS and LRS. It should be noted that the measurements were done on a 100x100 μm^2 device and the I-V characteristics obtained were before forming, which are not the standard device and regular memristivity of interest. This is tricky and difficult to study the valence change of Ni during the observed RS so far.
- *Operando* XANES in RS: the recorded intensity of Ni-K edge increased/decreased with changing the polarity of electrical bias applied on TiN/L2NO4/Pt. From the obtained intensity, the shift of Ni-K edge energy, Ni oxidation state and oxygen off-stoichiometry can be estimated. Thus, the valence change of Ni corresponding to the observed RS on TiN/L2NO4/Pt device can be confirmed. Under positive voltage sweep, Ni oxidation state decreases linked to the loss of oxygen in L2NO4, the device is in HRS at the end of the sweep. Reversely, the increase of Ni oxidation state is found when negative voltage sweep is applied, suggesting the re-oxidation of L2NO4; at this point, the device is in LRS. A difference of 0.07 eV is observed in Ni-K edge energy between HRS and LRS. Similar *operando* measurements were carried out at Ti-K edge, but chaotic and unclosed individual loops were observed, thus no conclusions can be established on Ti oxidation state because the drift of intensity was present during the beamtime and the oxidation/reduction of Ti (if it really happens and involves in the obtained memristivity of TiN/L2NO4/Pt) could not be distinguished.
- *Operando* XANES in potentiation/depression gives a hint about the RS mechanism. Large change in Ni-K edge energy while the resistance keeps unchanged, strongly suggesting the oxygen vacancy-based filaments are disconnected while oxygen ions keep migrating from L2NO4 to TiN

***In situ* TEM equipped with EELS carried out in ultra-high vacuum:**

- STEM images show no clear differences observed between pristine state and biased states. However, EELS elemental mapping shows the broadening of TiNxOy interface between

pristine and (HRS_1 and LRS_2) cycles with a small current compliance due to the diffusion of titanium and oxygen in Pt bottom electrode are detected. With increasing current compliance up to 0.27 mA, the presence of Ti at top part of L2NO4, the loss of oxygen in L2NO4 and the presence of oxygen at top part of Pt are seen.

- EELS spectra: reveal the oxynitride TiNxOy is present at the TiN/L2NO4 interface. In operating with moderate current compliance, further oxidation of this interface is observed when the device is programmed to HRS_1 under positive voltage applied to TiN (confirmed by the presence and/or increase in the intensity of e_{2g} and t_{2g} peaks of Ti-L2,3 edges). Reduction of the TiNxOy interlayer takes place when applying negative voltage sweep to TiN to bring the device to LRS_2 (confirmed by the decrease in intensity of e2g and t2g peaks of Ti-L2,3 edges when comparing to HRS_1). When working with higher current compliance, a complex process including the diffusion of Ti through the device stack is detected (confirmed by the presence of the non-split Ti-L2,3 edges) and of the other cations/anions likely takes place. This comes to the fact that it is difficult to interpret clearly the composition of the interlayer in LRS_3 and HRS_4. However, such observations with massive diffusion (LRS_3 and HRS_4) are not expected to be the regular mechanisms underlying the memristivity in standard TiN/L2NO4/Pt device, especially since such measurements were carried out in the ultra-high vacuum.

Chapter 6: Conclusions and Prospects

General conclusions:

The exponential development of artificial intelligence (AI) in parallel to the presence of the von Neuman bottleneck in computation architecture and to the end of Moore's law is giving rise to neuromorphic computing as a new computing paradigm. To build neuromorphic computing on solid-state platforms, new electronic elements with bio-realistic behavior (i.e., artificial neurons and synapses) are being studied and developed. In this context, analogue-type resistive switching devices whose resistance can be tuned and regarded as a synaptic weight have attracted many researchers' attention. Among the many types of existing memristive devices, valence change memories (VCM), which are electrochemical systems based on a metal-oxide-metal (MOM) structure, are one of the most promising candidates for artificial synapse applications.

In this thesis, we chose a mixed ionic-electronic conductor, $La_2NiO_{4+\delta}$ (L2NO4), as a memristive layer to construct VCM-based memristive devices. This material possesses interesting properties as VCM material, including oxygen storage and oxygen transport capabilities without decomposing and electronic properties, which vary with its oxygen stoichiometry.

The L2NO4 thin films in this thesis were synthesized by PI-MOCVD on $Si_3N_4/SiO_2/Si$ (SN) and $Pt/TiO_2/SiO_2/Si$ (Pt) substrates. Two types of deposition conditions were used:

- Non-optimized conditions: temperature of 650 °C and La/Ni ratio in precursor solution of 5.00 used for Ti\L2NO4/Pt planar memristive devices built on SN substrate and for Ti/L2NO4/Pt vertical devices.
- Optimized conditions: temperature of 600 °C and La/Ni ratio in precursor solution of 4.00 used for Ti/L2NO4/Pt and TiN/L2NO4/Pt vertical memristive devices.

Ti\L2NO4/Pt planar memristive devices built on $Si_3N_4/SiO_2/Si$ substrates

Inspired from the previous work in the group on Ti\epitaxial-L2NO4/Pt (on $SrTiO_3$ substrate), here Ti\polycrystalline L2NO4/Pt devices, where the L2NO4 film was deposited on SN, were successfully reproduced. L2NO4/SN samples were prepared using non-optimized deposition conditions. Thus, the presence of a small amount of La_2CO_5 impurity phase was detected by GI-XRD and EPMA. TEM equipped with EDX showed that the 25 nm of Ti electrode was partially oxidized to TiO_x ($x < 2$). The concentration of oxygen within the Ti layer was highest at the Ti/L2NO4 interface and gradually decreased towards the top Pt/Ti interface. The migration of oxygen into the Ti layer occurred

spontaneously when evaporating the Ti metal. For the memristive properties, an activation step of rapid thermal annealing (RTA) is required to trigger the rectifying I-V curve and, eventually, the resistance hysteresis. Analogue-type I-V characteristics could be obtained when cycling the 200x200 μm^2 devices from V_{max}= ±15 V to ±40 V. However, small ratios of HRS/LRS were obtained (1.24 – 1.66). **The low performance of Ti\L2NO4/Pt memristive devices with the large operation voltage and requirement of a RTA step is considered unsuitable for further hardware implementation in realistic memory arrays**, and for this reason, we moved to vertical devices for the rest of the thesis.

Optimization of the deposition of L2NO4 films on platinized substrates

The optimization of the film roughness and purity was carried out by varying the PI-MOCVD deposition temperature (T) and precursor solution concentration (La/Ni ratio, R) for depositions of L2NO4 on Pt substrate.

- R was kept at 5.00 while decreasing the temperature: at relatively high temperatures (650-700 °C), the surface of L2NO4 thin films was very rough. A RMS of 6.6 nm for T = 650 °C was experimentally measured without the dewetting of Pt. Decreasing the temperature resulted in a decrease in the RMS value (3.4 nm for T = 600 °C), while the crystallinity of the polycrystalline L2NO4 was preserved. At lower temperatures, the presence of the $La_3Ni_2O_7$ phase, in addition to L2NO4 (at 550 °C) was detected. At T = 500 °C, the obtained L2NO4 film was amorphous nature, which study is out of the scope of this thesis. Thus the trade-off between the lowest temperature to obtain a relatively-flat film surface with small grains and a polycrystalline film is selected at T = 600 °C. In general, the temperature affects the roughness and the average grain size of L2NO4/Pt samples.
- At the fixed T = 600 °C, the R parameter has an effect on the purity of the material of interest. R in the range of 4.50-5.00 leads to the presence of the undesired phase La_2CO_5, while that in the range of 4.25-4.00 this phase does not appear. Pure L2NO4 is obtained at R = 4.00 with a La/Ni ratio of 1.95 in L2NO4 thin film (measured by EPMA). Basically, R in the range from 4.00 to 5.00 does not influence the morphology of the films. **Therefore, the optimized conditions for the deposition of high-quality L2NO4 thin films on Pt by PI-MOCVD are T = 600 °C, R = 4.00.**

Ti/L2NO4/Pt vertical memristive devices built on platinized substrates

The vertical configuration of device Ti/L2NO4/Pt was chosen with the expectation of lowering the operating voltages. Ti electrodes of five different sizes (200^2, 150^2, 100^2, 50^2 and 20^2 μm^2) were deposited on top of the L2NO4 film. In general, STEM cross-section images of selected TiN/non-optimized/Pt and Ti/optimized L2NO4/Pt devices showed that the device stack was well constructed

without Pt dewetting. The presence of TiO_x was again observed at the Ti/L2NO4 interface. There is no significant difference in structure between the two types of devices, except that the Ti/L2NO4 interface was improved (lower toughness) after the optimization.

In terms of memristivity, while Ti/non-optimized L2NO4/Pt requires a 'soft-forming' step before exhibiting RS characteristics, the Ti/optimized L2NO4/Pt is forming-free. Their electrical memristive characteristics are quite comparable after the forming. Only the small devices (50^2 and 20^2 μm^2) had enough high initial resistance and rectifying I-V curves in the pristine state. **Ti/optimized L2NO4/Pt devices showed relatively reproducible analogue-type I-V characteristics between ±2.75 V and ±3.00 V with a HRS/LRS ratio of 11** (while non-optimized devices had a ratio of 6). **HRS and LRS were area-dependent, suggesting interface-type RS**. The HRS decreased to 56% of its initial value, while the LRS increased by 169% during 12 hours. These characteristics could be interesting for short-term artificial synapses as they can be used to perform 'forgetting' behavior (volatility) in certain neural networks. The Ti/L2NO4/Pt device's ability to withstand 500 voltage sweeps without degrading was another positive sign of its durability.

Rapid thermal annealing (RTA)

The observed TiO_x interlayer is believed to play a key role in the switching of Ti/L2NO4/Pt devices. Indeed, the resistance change in such devices is based on the p-n junction between L2NO4 and TiO_x (p-type L2NO4 and n-type TiO_x), where the oxygen exchange between the two materials is responsible for the change in the junction properties. In this context, RTA is expected to supply additional energy to partly oxidize or homogenize the TiO_x layer for large devices (100^2, 150^2 and 200^2 μm^2), thus activating them for memristive properties. We found that the RTA allowed small devices to increase their resistances (from 1 to 3 orders of magnitude). This could be an advantage in avoiding leakage currents when implementing such devices in memory crossbar arrays. However, unfortunately, we also found that this resistance increase with our RTA furnace was not reproducible. By TEM observations combined with XANES, the diffusion of oxygen from L2NO4 to TiO_x under RTA process was confirmed. The longer the RTA step, the more oxidized the TiO_x interlayer. In addition, too long RTAs led to fully oxidized TiO_x (TiO_2), which is stable and difficult to be reduced, explaining the non-distinguishable HRS and LRS states.

TiN/L2NO4/Pt vertical memristive devices built on platinized substrates

The oxygen content of the L2NO4 films was successfully modified post-thermal treatments in different gas atmospheres without L2NO4 decomposition. The influence of the oxygen content δ on the structural and chemical characteristics was highlighted by combining GI-XRD and XANES. The as-deposited sample showed intermediate values of the cell parameter and Ni oxidation state. When the sample is

exposed to an oxidizing environment at a high temperature, the L2NO4 film incorporates more oxygen (confirmed by the increase in cell parameter and Ni oxidation state). Reversely, when being exposed to an inert gas (Ar) for a long time, L2NO4 is slightly reduced with a decrease in cell parameters and Ni oxidation state. **These results confirm the ability to store a wide range of oxygen content (δ) in L2NO4, which is easily tunable by thermal treatments**.

The three different annealed L2NO4 films were used to prepare three types of TiN/L2NO4/Pt memristive devices. TiN electrodes were fabricated similarly to the Ti electrodes (square contacts of five different sizes). The presence of a TiN_xO_y interlayer at the TiN/L2NO4 interface was observed for the TiN/as-deposited L2NO4/Pt and TiN/Ar-annealed L2NO4/Pt in their pristine states (for the TiN/O_2-annealed L2NO4/Pt it is also expected although it has not been experimentally measured due to time limitation). This interlayer formed spontaneously when sputtering TiN on L2NO4, similar to the case of the TiO_x interlayer in Ti/L2NO4/Pt devices. In addition, NiO_x nano-clusters were found at some localized regions at the L2NO4/Pt interface of the TiN/as-deposited L2NO4/Pt sample, probably due to the defects of the surface in the incipient dewetting of Pt at 600 °C.

In terms of electrical properties, the initial resistance (IR) of the devices with different δ was found to be highest for the Ar-annealed L2NO4/Pt sample, an intermediate value for the as-deposited L2NO4/Pt sample and smallest for the O_2-annealed sample. This trend is inversely proportional to the oxygen content in the L2NO4 thin films and confirms the IR of devices could be tuned by post-annealing treatment in different gas atmospheres (by controlling δ).

In terms of memristivity, a 'soft-forming' step is required before the devices start presenting reproducible memristive characteristics for the Ar-annealed sample and for the as-deposited sample. This 'soft-forming' process is not the traditional forming usually observed in other oxide systems, as the applied voltage is not higher than the operational one. **Highly reproducible I-V characteristics have been achieved when cycling between ±2.50 V and ±2.75 V with gradual transitions between the HRS to LRS and vice versa for all the different annealed samples.**

In the **TiN/as-deposited L2NO4/Pt devices, multilevel resistance states could be obtained by using different voltage amplitudes in the I-V sweeps**. What is more, highly multilevel and bipolar memory characteristics can be performed in pulsed mode by resistance hysteresis switching loops (RHSL). Stable resistances can retain for at least 6 hours. **Potentiation/depression plasticity was artificially performed also by trains of pulses in the same polarity. The modulation of potentiation/depression plasticity can be controlled by pulse amplitude and pulse duration**. We also found a linear trend between total applied pulse duration and resistance change, suggesting the synaptic weight updating

strongly depends on the total applied pulse duration but not on the number of pulses. **These exciting results pave the way for using TiN/L2NO4/Pt in long-term artificial synapse applications**.

Advanced characterization to study the switching mechanisms in TiN/L2NO4/Pt memristive devices

The switching mechanisms were studied by TEM and XANES in *ex situ, in situ* and *operando* modes.

Confirming the *ex situ* TEM results, XANES spectra measured at regions with and without TiN electrode (bare L2NO4 film) confirm the presence of a TiN_xO_y interlayer in the pristine TiN/L2NO4/Pt devices, as a reduction in the Ni oxidation state under TiN could be deduced by the shift of the Ni K-edge position.

A new and pioneering methodology based on Ni-K edge XANES measurements in *operando* mode is presented. This measurement mode enables tracking the changes of Ni-K edge energy under electrical polarization, highlighting that an oxygen transport between the TiN_xO_y interlayer and the L2NO4 film occurs during the switching. These results, combined with the *operando* XANES measurements during potentiation/depression, strongly suggest a mixed interfacial and filamentary valence change mechanism occurring in such devices.

In situ **TEM/EELS observations on a TiN/L2NO4/Pt specimen proved to be a unique complementary technique which was used to confirm the oxidation/reduction of TiN_xO_y during the switching.** When relatively low current densities were used, the oxidation and reduction of the TiN_xO_y interlayer upon positive and negative voltage was observed. When higher current compliance was used, a complicated process consisting of both cation and anion drift/diffusion and an expansion of the interlayer thickness, probably caused by Joule heating, was detected.

Hence, a simplified switching model has been proposed. **Before forming (low current passing through the device), interface-type RS is dominant due to the oxygen drift under the external electric field. After being formed, the standard switching in TiN/L2NO4/Pt devices would be mainly controlled by the formation/dissolution of TiN_x filament(s) in the TiN_xO_y interlayer.**

Prospects:

In this section, a number of future prospects are proposed, going from the material deposition to the integration of these devices in simple synaptic networks.

For the future, to be able to produce L2NO4-based memristive devices in an industrial scale, lower deposition temperatures compatible with CMOS technology would be required. Lower deposition temperatures would help avoid the instability of Pt bottom electrode, reducing the L2NO4 film

roughness. However, using lower deposition temperatures by PI-MOCVD will result in the amorphous nature of the L2NO4 films. Thus, in this case, an additional step of crystallization (such as laser treatment with localized heating) might be necessary.

For further development of the proposed devices, a better comprehension of the effect of the L2NO4 thickness and of the TiN thickness on the device performance would be the next step. It is known that thick films of L2NO4 deposited by PI-MOCVD have rough surface because of the nano-columnar growth at relatively low temperatures (600-650 ºC). Thus, a decrease in the L2NO4 thickness is expected to result in a smoother surface. Moreover, the TiN_xO_y interlayer could be therefore flatter. The TiN thickness could also be optimized (decreased), because the voltage drop likely happens at the very thin TiN_xO_y interlayer.

To be embedded in real devices, additional memristive properties devices should be studied for the TiN/L2NO4/Pt, such as data retention (for multilevel resistance states) as a function of temperature (85 °C), data retention for longer times, device endurance with a higher number of cycles (> 10^5 cycles), the evolution of resistance as a function of environmental humidity and p_{O2}, etc. Moreover, smaller electrode areas (smaller than 50^2 μm^2) should be used, as the memristivity properties were better for the small devices (for Ti/L2NO4/Pt and TiN/L2NO4/Pt). This is also consistent with the memory cell integration into microchips.

Depending on the desired plasticity, optimization of pulse height, pulse duration and number of pulses could be carried out to better control the synaptic weight updating in the potentiation/depression processes and to improve the linearity of the response.

Based on the simplified model that has been proposed, simulations on switching mechanisms, memristivity and plasticity in artificial neural networks would be future steps to be carried out. Expanding the memory and plasticity performance into a crossbar array with multiple TiN/L2NO4/Pt devices instead of a single memory cell, as in this study, is proposed for future studies.

References

1. del Valle, J., et al., *Challenges in materials and devices for resistive-switching-based neuromorphic computing.* Journal of Applied Physics, 2018. **124**(21): p. 211101.
2. Moore, G.E., *Cramming More Components Onto Integrated Circuits.* Proceedings of the IEEE, 1998. **86**(1): p. 82-85.
3. Schuller, I.K., et al., *Neuromorphic Computing – From Materials Research to Systems Architecture Roundtable*. 2015: United States.
4. Bi, G.Q. and H.X. Wang, *Temporal asymmetry in spike timing-dependent synaptic plasticity.* (0031-9384 (Print)).
5. Kuzum, D., S. Yu, and H.S.P. Wong, *Synaptic electronics: Materials, devices and applications.* Nanotechnology, 2013. **24**: p. 382001.
6. Yu, S. and P.-Y. Chen, *Emerging Memory Technologies: Recent Trends and Prospects.* IEEE Solid-State Circuits Magazine, 2016. **8**: p. 43-56.
7. Chen, A., *A review of emerging non-volatile memory (NVM) technologies and applications.* Solid-State Electronics, 2016. **125**: p. 25-38.
8. Zidan, M.A., J.P. Strachan, and W.D. Lu, *The future of electronics based on memristive systems.* Nature Electronics, 2018. **1**(1): p. 22-29.
9. Yu, S., *Neuro-Inspired Computing With Emerging Nonvolatile Memory.* Proceedings of the IEEE, 2018. **PP**: p. 1-26.
10. Di, J., et al., *Recent advances in resistive random access memory based on lead halide perovskite.* InfoMat, 2020. **3**(3): p. 293-315.
11. Yu, S., et al. *Binary neural network with 16 Mb RRAM macro chip for classification and online training*. in *2016 IEEE International Electron Devices Meeting (IEDM)*. 2016.
12. Zhang, W., et al., *Analog-Type Resistive Switching Devices for Neuromorphic Computing.* physica status solidi (RRL) – Rapid Research Letters, 2019. **13**(10): p. 1900204.
13. Burr, G.W., et al., *Neuromorphic computing using non-volatile memory.* Advances in Physics: X, 2016. **2**(1): p. 89-124.
14. Waser, R. and M. Aono, *Nanoionics-based resistive switching memories.* Nature Materials, 2007. **6**(11): p. 833-840.
15. Chua, L., *Memristor-The missing circuit element.* IEEE Transactions on Circuit Theory, 1971. **18**(5): p. 507-519.
16. Herpers, A., et al., *Spectroscopic proof of the correlation between redox-state and charge-carrier transport at the interface of resistively switching Ti/PCMO devices.* Adv Mater, 2014. **26**(17): p. 2730-5.
17. Borgatti, F., et al., *Chemical insight into electroforming of resistive switching manganite heterostructures.* Nanoscale, 2013. **5**(9): p. 3954-60.
18. Shono, K., et al., *Origin of Negative Differential Resistance Observed on Bipolar Resistance Switching Device with Ti/Pr0.7Ca0.3MnO3/Pt Structure.* Applied Physics Express, 2008. **1**: p. 055002.
19. Kanegami, N., Y. Nishi, and T. Kimoto, *Unique resistive switching phenomena exhibiting both filament-type and interface-type switching in Ti/Pr0.7Ca0.3MnO3−δ/Pt ReRAM cells.* Applied Physics Letters, 2020. **116**(1): p. 013501.

20. Muenstermann, R., et al., *Coexistence of filamentary and homogeneous resistive switching in Fe-doped SrTiO3 thin-film memristive devices.* Adv Mater, 2010. **22**(43): p. 4819-22.

21. Kim, H.J., et al., *Digital versus analog resistive switching depending on the thickness of nickel oxide nanoparticle assembly.* RSC Advances, 2013. **3**(43): p. 20978.

22. Shi, T., R. Yang, and X. Guo, *Coexistence of analog and digital resistive switching in BiFeO3-based memristive devices.* Solid State Ionics, 2016. **296**: p. 114-119.

23. Sawa, A., *Resistive switching in transition metal oxides.* Materials Today, 2008. **11**(6): p. 28-36.

24. Bagdzevicius, S., et al., *Interface-type resistive switching in perovskite materials.* Journal of Electroceramics, 2017. **39**(1-4): p. 157-184.

25. Dittmann, R., S. Menzel, and R. Waser, *Nanoionic memristive phenomena in metal oxides: the valence change mechanism.* Advances in Physics, 2021. **70**(2): p. 155-349.

26. Ielmini, D., *Resistive switching memories based on metal oxides: mechanisms, reliability and scaling.* Semiconductor Science and Technology, 2016. **31**(6): p. 063002.

27. Asif, M. and A. Kumar, *Resistive switching in emerging materials and their characteristics for neuromorphic computing.* Materials Today Electronics, 2022. **1**: p. 100004.

28. Zahoor, F., T.Z. Azni Zulkifli, and F.A. Khanday, *Resistive Random Access Memory (RRAM): an Overview of Materials, Switching Mechanism, Performance, Multilevel Cell (mlc) Storage, Modeling, and Applications.* Nanoscale Res Lett, 2020. **15**(1): p. 90.

29. Waser, R., *Redox-based resistive switching memories.* J Nanosci Nanotechnol, 2012. **12**(10): p. 7628-40.

30. Waser, R., et al., *Redox-Based Resistive Switching Memories - Nanoionic Mechanisms, Prospects, and Challenges.* Advanced Materials, 2009. **21**(25-26): p. 2632-2663.

31. Dittmann, R. and J.P. Strachan, *Redox-based memristive devices for new computing paradigm.* APL Materials, 2019. **7**(11): p. 110903.

32. Derry, G.N. and Z. Ji-Zhong, *Work function of Pt(111).* Physical Review B, 1989. **39**(3): p. 1940-1941.

33. Borgatti, F., et al., *Chemical insight into electroforming of resistive switching manganite heterostructures.* Nanoscale, 2013. **5**(9): p. 3954-3960.

34. Vitale, S., et al., *Work-Function-Tuned TiN Metal Gate FDSOI Transistors for Subthreshold Operation.* Electron Devices, IEEE Transactions on, 2011. **58**: p. 419-426.

35. Lefevre, G., et al., *Nano-analytical investigation of the forming process in an*

HfO2-based resistive switching memory. Journal of Applied Physics, 2021. **130**(24): p. 244501.

36. Yamamoto, T., et al., *Formation of transition layers at metal/perovskite oxide interfaces showing resistive switching behaviors.* Journal of Applied Physics, 2011. **110**(5): p. 053707.

37. Liao, Z., et al., *Electroforming and endurance behavior of Al/Pr0.7Ca0.3MnO3/Pt devices.* Applied Physics Letters, 2011. **99**(11): p. 113506.

38. Meunier, B., et al., *Resistive switching in a LaMnO3 + δ/TiN memory cell investigated by operando hard X-ray photoelectron spectroscopy.* Journal of Applied Physics, 2019. **126**(22): p. 225302.

39. Bruchhaus, R., C.R. Hermes, and R. Waser, *Memristive Switches with Two Switching Polarities in a Forming Free Device Structure.* MRS Online Proceedings Library (OPL), 2011. **1337**: p. mrss11-1337-q08-03.

40. Bagdzevicius, S., et al., *Superposition of interface and volume type resistive switching in perovskite nanoionic devices.* Journal of Materials Chemistry C, 2019. **7**(25): p. 7580-7592.

41. Bagdzevicius, S., et al., *Bipolar "table with legs" resistive switching in epitaxial perovskite heterostructures.* Solid State Ionics, 2019. **334**: p. 29-35.

42. Rodriguez-Lamas, R., et al., *Integration of LaMnO3+delta films on platinized silicon substrates for resistive switching applications by PI-MOCVD.* Beilstein J Nanotechnol, 2019. **10**: p. 389-398.

43. Maas, K., et al., *Using a mixed ionic electronic conductor to build an analog memristive device with neuromorphic programming capabilities.* Journal of Materials Chemistry C, 2020. **8**(2): p. 464-472.

44. Gonzalez-Rosillo, J.C., et al., *Engineering Oxygen Migration for Homogeneous Volume Resistive Switching in 3-Terminal Devices.* Advanced Electronic Materials, 2019. **5**(9): p. 1800629.

45. Maas, K., et al., *Tuning Memristivity by Varying the Oxygen Content in a Mixed Ionic–Electronic Conductor.* Advanced Functional Materials, 2020. **30**(17): p. 1909942.

46. Maas, K., et al., *Role of pO2 and film microstructure on the memristive properties of La2NiO4+δ/LaNiO3−δ bilayers.* Journal of Materials Chemistry A, 2022.

47. Hayashi, A., H. Tamura, and Y. Ueda, *Successive structural phase transitions in stoichiometric La2NiO4 observed by X-ray diffraction.* Physica C: Superconductivity, 1993. **216**(1): p. 77-82.

48. Rice, D.E. and D.J. Buttrey, *An X-Ray Diffraction Study of the Oxygen Content Phase Diagram of La2NiO4+δ.* Journal of Solid State Chemistry, 1993. **105**(1): p. 197-210.

49. Rodriguez-Carvajal, J., M.T. Fernandez-Diaz, and J.L. Martinez, *Neutron diffraction study on structural and magnetic properties of La2NiO4.* Journal of Physics: Condensed Matter, 1991. **3**(19): p. 3215.

50. Tranquada, J.M., et al., *Oxygen intercalation, stage ordering, and phase separation in La2NiO4+ delta with 0.05 <~ delta <~ 0.11.* Phys Rev B Condens Matter, 1994. **50**(9): p. 6340-6351.

51. Tamura, H., A. Hayashi, and Y. Ueda, *Phase diagram of La2NiO4+δ (0 ≤ δ ≤ 0.18): I. Phase at room temperature and phases transition above δ = 0.15.* Physica C: Superconductivity, 1993. **216**(1): p. 83-88.

52. Demourgues, A., et al., *Electrochemical Preparation and Structural Characterization of La2NiO4+δ Phases (0 ≤ δ ≤ 0.25).* Journal of Solid State Chemistry, 1993. **105**(2): p. 458-468.

53. Jorgensen, J.D., et al., *Structure of the interstitial oxygen defect in La2NiO4+d.* Physical Review B, 1989. **40**(4): p. 2187-2199.

54. Skinner, S.J., *Characterisation of La2NiO4+δ using in-situ high temperature neutron powder diffraction.* Solid State Sciences, 2003. **5**(3): p. 419-426.

55. Burriel, M., et al., *Anisotropic oxygen diffusion properties in epitaxial thin films of La2NiO4+δ.* J. Mater. Chem., 2008. **18**(4): p. 416-422.

56. Minervini, L., et al., *Oxygen migration in LaNiO.* Journal of Materials Chemistry, 2000. **10**(10): p. 2349-2354.

57. Burriel, M., et al., *Enhanced High-Temperature Electronic Transport Properties in Nanostructured Epitaxial Thin Films of the Lan+1NinO3n+1 Ruddlesden−Popper Series (n = 1, 2, 3, ∞).* Chemistry of Materials, 2007. **19**(16): p. 4056-4062.

58. V. Kharton, V., et al., *Oxygen ion transport in La2NiO4-based ceramics.* Journal of Materials Chemistry, 1999. **9**(10): p. 2623-2629.

59. Bassat, J.M., P. Odier, and J.P. Loup, *The Semiconductor-to-Metal Transition in Question in La2-xNiO4+δ (δ > 0 or δ < 0).* Journal of Solid State Chemistry, 1994. **110**(1): p. 124-135.

60. Demourgues, A., et al., *Transport and Magnetic Properties of La2NiO4+δ(0 ≤ δ ≤ 0.25).* Journal of Solid State Chemistry, 1996. **124**(2): p. 199-204.

61. Vashook, V.V., et al., *Oxygen nonstoichiometry and electrical conductivity of the solid solutions La2−xSrxNiOy (0≤x≤0.5).* Solid State Ionics, 1998. **110**(3): p. 245-253.

62. Sayer, M. and P. Odier, *Electrical properties and stoichiometry in La2NiO4.* Journal of Solid State Chemistry, 1987. **67**(1): p. 26-36.

63. Bassat, J.M., J.P. Loup, and P. Odier, *Progressive change with T from hopping to random phase propagation in La2-xNiO4- delta (delta >or=0).* Journal of Physics: Condensed Matter, 1994. **6**(40): p. 8285.

64. Ishikawa, K., et al., *Metal–Semiconductor Transition of La2NiO4+δ.* Journal of Solid State Chemistry, 1997. **131**(2): p. 275-281.

65. Amow, G. and S.J. Skinner, *Recent developments in Ruddlesden–Popper nickelate systems for solid oxide fuel cell cathodes.* Journal of Solid State Electrochemistry, 2006. **10**(8): p. 538-546.

66. Aguadero, A., et al., *In situ high temperature neutron powder diffraction study of oxygen-rich La2NiO4+δ in air: correlation with the electrical behaviour.* Journal of Materials Chemistry, 2006. **16**(33): p. 3402-3408.

67. Tarancón, A., et al., *Advances in layered oxide cathodes for intermediate temperature solid oxide fuel cells.* Journal of Materials Chemistry, 2010. **20**(19): p. 3799.

68. Maas, K., *La2NiO4+d, a Mixed Ionic-Electronic Conductor for Interface-Type Valence Change Memories*

La2NiO4+d, un conducteur mixte ionique-électronique pour les mémoires à changement de Valence. 2019, Université Grenoble Alpes.

69. Lanza, M., et al., *Recommended Methods to Study Resistive Switching Devices.* Advanced Electronic Materials, 2019. **5**(1): p. 1800143.

70. Khuu, T.-K., et al., *La2NiO4+δ-Based Memristive Devices Integrated on Si-Based Substrates.* Advanced Materials Technologies, 2022: p. 2200329.

71. Sénateur, J.-P., et al., *Pulsed injection MOCVD of functional electronic oxides.* Advanced Materials for Optics and Electronics, 2000. **10**(3-5): p. 155-161.

72. Villepreux, E.d., *Characterization of oxygen ions in biased resistive memory by advanced TEM*

Caractérisation des ions d'oxygène dans les mémoires résistives soumises à polarisation électrique par techniques de TEM avancées. 2020, Université Grenoble Alpes [2020-....].

73. Woolley, R.J., et al., *In situ determination of the nickel oxidation state in La2NiO4+δ and La4Ni3O10−δ using X-ray absorption near-edge structure.* Journal of Materials Chemistry, 2011. **21**(46): p. 18592.

74. Moncasi, C., et al., *Structural Defects Improve the Memristive Characteristics of Epitaxial La0.8Sr0.2MnO3-Based Devices.* Advanced Materials Interfaces, 2022. **9**(23): p. 2200498.

75. Jeon, T., et al., *Laser Crystallization of Organic-Inorganic Hybrid Perovskite Solar Cells.* ACS Nano, 2016. **10**(8): p. 7907-14.

76. Izawa, Y., et al., *Ultra fast melting process in femtosecond laser crystallization of thin a-Si layer.* Applied Surface Science, 2009. **255**(24): p. 9764-9769.

77. Choi, T., D. Hwang, and C. Grigoropoulos, *Ultrafast laser-induced crystallization of amorphous silicon films.* Optical Engineering, 2003. **42**(11).

78. Lee, J.-M. and B.-I. Kim, *Thermal dewetting of Pt thin film: Etch-masks for the fabrication of semiconductor nanostructures.* Materials Science and Engineering: A, 2007. **449-451**: p. 769-773.

79. Jana, D., et al., *Observation of Resistive Switching Memory by Reducing Device Size in a New Cr/CrO x /TiO x /TiN Structure.* Nanomicro Lett, 2015. **7**(4): p. 392-399.

80. Stangl, A., et al., *Tailored nano-columnar La2NiO4 cathodes for improved electrode performance.* Journal of Materials Chemistry A, 2022. **10**(5): p. 2528-2540.

81. Lin, K.-S., et al., *Synthesis and Characterization of Metal Hydride/Carbon Aerogel Composites for Hydrogen Storage.* Journal of Nanomaterials, 2012. **2012**: p. 1-9.

82. Simon, P., et al., *X-ray absorption investigation of titanium oxynitride nanoparticles obtained from laser pyrolysis.* Chemical Physics, 2013. **418**: p. 47-56.

83. Bates, F.E. and J.E. Eldridge, *Normal modes of tetragonal La2NiO4 and La2CuO4, isomorphs of the hight Tc superconductor La2-xSrxCuO4.* Solid State Communications, 1989. **72**(2): p. 187-190.

84. Sugai, S., et al., *Separation of Spin and Charge Densities in La 2NiO 4+δ.* Journal of the Physical Society of Japan, 1998. **67**(9): p. 2992-2995.

85. Tamura, H., A. Hayashi, and Y. Ueda, *Phase diagram of La2NiO4+δ (0 ≤ δ ≤ 0.18) II. Thermodynamics of excess oxygen, phase transitions (0.06 ≤ δ < 0.11) and phase segregation (0.03 ≤ 6 < 0.06).* Physica C: Superconductivity, 1996. **258**(1): p. 61-71.

86. Kyungjoon, B., et al., *In situ TEM observation on the interface-type resistive switching by electrochemical redox reactions at a TiN/PCMO interface.* Nanoscale, 2017. **9**(2).

87. Yang, R., H.M. Huang, and X. Guo, *Memristive Synapses and Neurons for Bioinspired Computing.* Advanced Electronic Materials, 2019. **5**(9): p. 1900287.

88. Yu, S., *Neuro-inspired Computing Using Resistive Synaptic Devices*. 2017.

89. Wang, Z., et al., *Engineering incremental resistive switching in TaOx based memristors for brain-inspired computing.* Nanoscale, 2016. **8**(29): p. 14015-22.

90. Abdallah, I., et al., *STEM-EELS identification of TiOXNY, TiN, Ti2N and O, N dissolution in the Ti2642S alloy oxidized in synthetic air at 650 °C.* Corrosion Science, 2019. **153**: p. 191-199.

91. Leapman, R.D., L.A. Grunes, and P.L. Fejes, *Study of the ${L}_{23}$ edges in the $3d$ transition metals and their oxides by electron-energy-loss spectroscopy with comparisons to theory.* Physical Review B, 1982. **26**(2): p. 614-635.

92. Fischer, D.W., *Molecular-Orbital Interpretation of the Soft X-Ray LII,III Emission and Absorption Spectra from Some Titanium and Vanadium Compounds.* Journal of Applied Physics, 2003. **41**(9): p. 3561-3569.

93. Baek, K., et al., *In situ TEM observation on the interface-type resistive switching by electrochemical redox reactions at a TiN/PCMO interface.* Nanoscale, 2017. **9**(2): p. 582-593.